

**NSF/REU  
RESEARCH EXPERIENCE  
FOR UNDERGRADUATES  
IN PHYSICS**



**STUDENT RESEARCH PAPERS**

**SUMMER 2010**

**VOLUME 21**

**REU DIRECTOR  
UMESH GARG, PH.D.**

**REU Student Research Papers – Summer 2010**  
**University of Notre Dame – Department of Physics**

Student	Research Title	Page No.
Samia Bouzid Rutgers University	High Time Resolution Photometry of V458 Vul	1
Ke Cai Bard College	Computer Code for Calculating Matrix Elements and Overlaps of States for the Generalized Seniority Scheme via Recurrence Relations	11
Lidens Cheng Illinois Institute of Technology	Project GRAND: Modifying Data Acquisition System	23
Patrick Copp University of Wisconsin – La Crosse	Nuclear Alpha Cluster and Accelerators	31
Louis Didio Indiana Univ. of Pennsylvania	Guided Inquiry and the Brain	39
Evan Figg Bob Jones University	Simulation of the Accretion of Matter onto a White Dwarf Star	53
Angela Galvez American River College	Identifying Particle Trajectories in CMS using the Long Barrel Geometry	63
Kathryn Gerbich University of Notre Dame	Measurement of W + Charm Production in CDF II Data	73
Christina Gower Loyola Marymount	Progress toward a Monte Carlo Simulation of the Ice VI-VII Phase Transition	85
Valerie Gray St. Norbert College	Detecting and Suppressing Background Signal	95
John Hinnefeld Cornell University	Reconstruction of Semileptonic $K^0$ Decays at BaBar	107

<b>Student</b>	<b>Research Title</b>	<b>Page No.</b>
Alexander Kocurek University of Notre Dame	Determining the Existence of a Radiation Amplitude Zero in W $\gamma$ Events	117
Sandra Liss Swarthmore College	Guided Inquiry and the Brain	39
Omar Magana St. Mary's University Texas	Development of a Low-Level Counting Station	131
Andrew Miller University of Dallas	The Segmented Universe: Identifying Cosmic Voids with a Multi-Scale Geometric Flow	141
Alexander Moncion Florida International University	Measurement of the $^{12}\text{C} + ^{12}\text{C}$ Fusion Cross Section at Sub-Barrier Energies	153
Dakota O'Dell University of Notre Dame	MBE Growth and Characterization of ZnTe and Nitrogen-doped ZnTe on GaAs(100) Substrates	163
Robert Schaefer University of Notre Dame	A Study of Gold Nanoparticles Using Laser Transmission Spectroscopy	175
Kimberly Schlesinger University of Notre Dame	Critical Current and Vortex Lattice Properties in Superconducting MgB <sub>2</sub>	187
Adam Siegel Stony Brook University	Diffusion as a Rate Limiting Effect On Microtubule Dynamic Instability	197
Nathan Smith Indiana University, South Bend	Detectors and Data Acquisition for the St. George Recoil Mass Separator	205
LaTianna Sturrup Arizona State University	Modeling and Visualizing Social Networks	217
Andrei Vajiac Indiana University, South Bend	Distribution of Delay Times in Laser Excited CdSe-ZnS Core-Shell Quantum Dots	227
Taiyo Wilson Illinois Wesleyan University	Project GRAND's Search for Sub-TeV Gamma Rays Coincident with Swift Gamma Ray Bursts	237

# High Time Resolution Photometry of V458 Vul

Samia Bouzid  
2010 NSF/REU Program  
Physics Department, University of Notre Dame  
Advisor: Dr. Peter Garnavich

## ABSTRACT

We observed the nova V458 Vul over the course of June 7 to June 10, 2010 at the Vatican Advanced Technology Telescope (VATT) on Mt. Graham, Arizona. The star erupted on August 8, 2007, reached its 8.1 magnitude peak in the following days (Rodríguez-Gil et al. 2010), and has since begun to evolve toward quiescence. We explore the properties of its current evolutionary state to identify quasi-periodic oscillations (QPOs) and the possibility of other variability. Our data reveal a 0.1-magnitudes variation that occurs over an approximately 20 minute period and strongly suggests quasi-periodic oscillation. The irregularity of the signal, particularly the difference between consecutive sets of data, provides evidence for this noncoherent variability. The orbital period is not evident in our observations, whose 2-4 hour spans do not favor the 98-minute period, too weak in amplitude to be distinguishable from random variations. Furthermore, visible light emitted from the system is dominated by the disk, which masks the signal from the systems orbital motion. We focus on investigating the pronounced signal from speculated QPOs.

### 1. Introduction

Nova V458 Vul is a cataclysmic variable star (CV). CV are binary systems comprising a white dwarf primary paired with a less compact secondary or donor star. The donor star is so named because it regularly loses a part of its mass to the white dwarf. The secondary exceeds its Roche lobe, the gravitational potential surface that takes a teardrop shape because of the systems distribution of gravity, and mass escapes through the Lagrangian point  $L_1$ . This escaped mass falls onto an accretion disk around the white dwarf at a distance dependent on its angular momentum. Dwarf nova outbursts occur when temperature rises in the disk and viscosity-slowed matter falls from the disk onto the star (La Dous 1993).

V458 Vul is peculiar in that it is surrounded by a planetary nebula, which indicates that the white dwarf primary formed in the last 14,000 years (Wesson et al. 2008). The existence of this

nebula is not implausible, only statistically surprising.

Currently, V458 Vul is in a “nova-like” stage of evolution, its disk in a continuous bright state that resembles a dwarf nova outburst. This optically thick accretion disk radiates brightly, principally in the optical, to counteract the unrestrained temperature rise resulting from viscosity and ionization that increases with mass accretion (Rodríguez-Gil & Torres 2005). V458 Vul may eventually evolve into a dwarf nova but at this point in its evolution it has not yet reached quiescence. Its current “nova-like” state is a result of high mass transfer rate after the nova explosion rather than from a true dwarf nova outburst (Misuzawa et al. 2010). Often smaller scale flickering occurs during this phase (La Dous 1993). Material that falls from the disk onto the star can cause erratic surges in brightness. In some cases the spin of the white dwarf can contribute to small, precise variation frequencies. Other moderately consistent variations in magnitude that occur during this phase are often attributable to QPOs. QPOs have periods in the range of seconds to several minutes, which exhibit sizeable variations in amplitude and frequency over time. They are more regular than the erratic flickering that is always present in “nova-like” stars but less uniform than coherent oscillations. In this study, we probe our data for evidence of these small scale variations, finding strong evidence for the existence of QPOs.

## 2. Observations

Image data were obtained at the Vatican Advanced Technology Telescope (VATT) at the Mt. Graham International Observatory (MGIO) on the nights of June 7-10, 2010. Data was filtered in the *V* band on June 7 and 9, in the *B* band on June 8, and in the *R* band on June 10, with all image exposures between 10 and 20 seconds. We read out a selected 1026x512 pixel portion of the chip to reduce readout time to 10 seconds. Using the VATTs 4K CCD and 2 $\times$ 2 pixel binning, we obtained a field of view of 0.376 ”/pixel. The average airmass over all four nights was 1.5.

### 3. Data Reduction

We used the standard IRAF photometry packages for the bias subtraction and flat-field reduction of the data. We combined biases, omitting those whose mean values fell in the upper and lower 5 percent. We subtracted the combined bias from each flat-field and applied *implot* to the overscan regions to evaluate the success of the bias subtraction. In the *R* and *V* bands there remained nonzero values in the overscan region, which we subtracted interactively. We combined the flat fields with the same standards for omission and normalized the results.

We specified an aperture of 4 pixels in the package *photpar* in approximate agreement with the full-width at half-maximum measurement (in pixel units), comprising roughly 80 percent of the starlight. Using *imexam* we identified coordinates for three stars: the variable star, a bright (noise-resistant) comparison star, and a third check star to evaluate the stability of the comparison star. We performed aperture photometry with *phot*, run non-interactively with the centering algorithm set to centroid and a maximum shift of 5 pixels. We used the magnitude and error from the output to create a light curve.

## 4. Results

### 4.1. Light Curves

We derived two light curves from each dataset. The relevant data is displayed in the first, which plots the difference in magnitude between variable and comparison stars against the observation time extracted from the image header. The second curve compares the magnitudes of the comparison and check stars to verify that the comparison star does not vary.

The light curve in the *V* band from the first night of observation is the clearest indicator of a QPO, showing a nearly sinusoidal variation of  $\sim 0.1$  magnitudes with an oscillation period of  $\sim 20$  minutes. The light curves resulting from the following nights of data display variation on about the same order, though considerably less regularly. In the data taken in the *R* and *B* bands, sinusoidal oscillation is not easily discernable. This is unlikely to be a consequence of filter choice

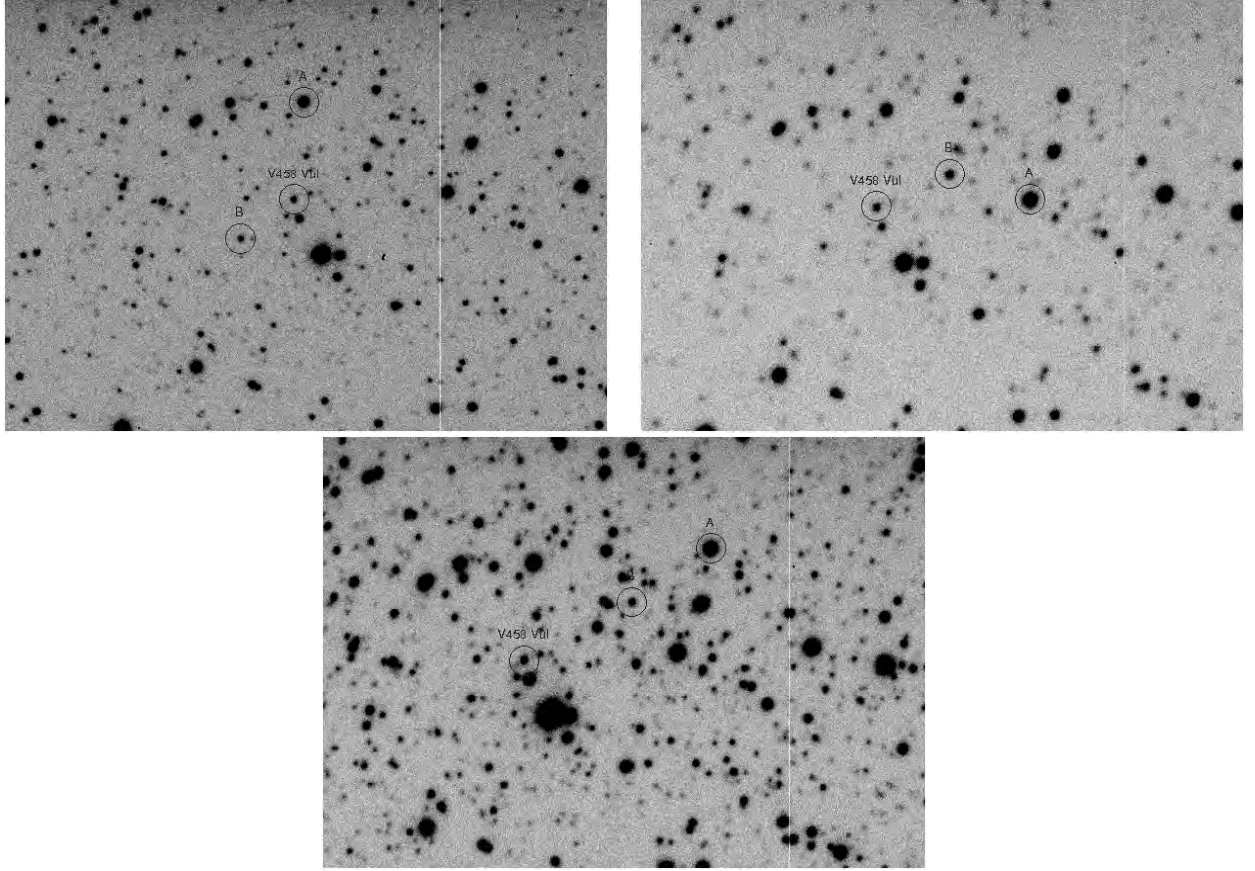


Fig. 1.— V458 Vul in the V, B, and R bands, respectively. ‘A’ identifies the comparison star, ‘B’ the check star.

and is probably a temporal effect, because the results of the power spectrum analysis that follows provide evidence for oscillation at the same frequency, though not obvious in the light curve. This suggests that some of the random variation characteristic of cataclysmic variables may have had some role in cluttering the signal from the primary QPO. Moreover, the noncoherence of the oscillation at this frequency over time broadens the peaks and lowers their strength. The power spectrum analysis, extended to all our data, further explores the nature of the speculated QPO.

#### 4.2. Power Spectrum Analysis

The system’s approximately 98-minute orbital period is not apparent in our observations, yet the star exhibits an irregular variation on all four nights that is suggestive of quasi-periodic oscillation (QPO). As a diagnostic, we created a power spectrum for each light curve to analyze

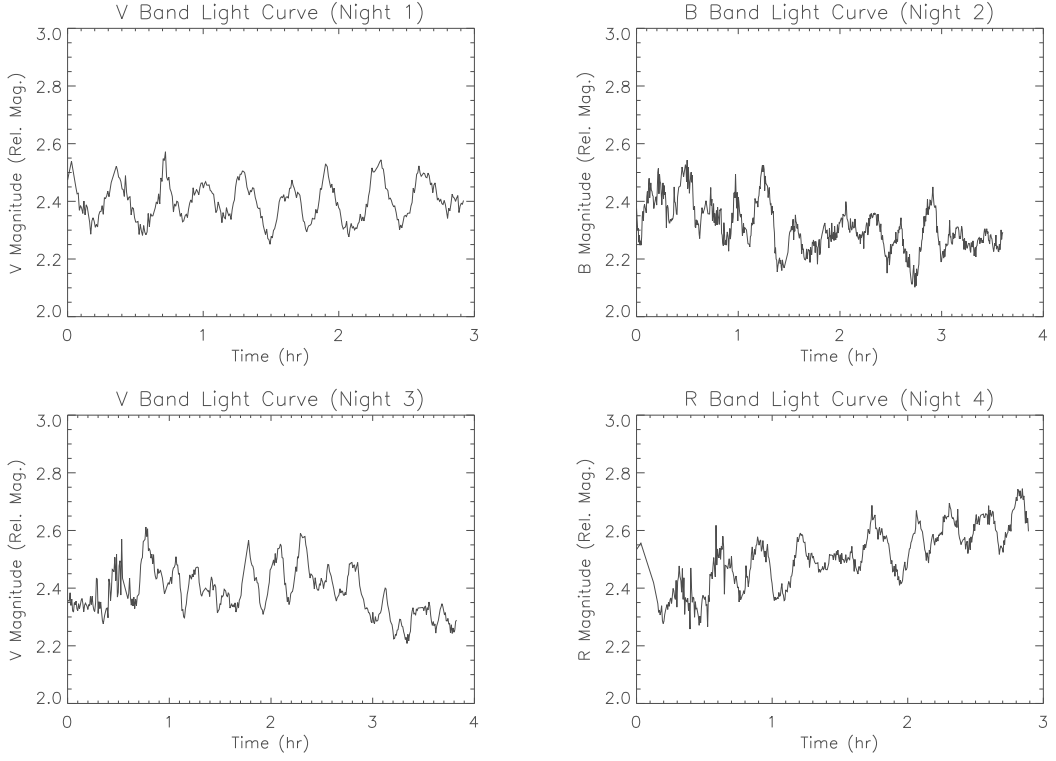


Fig. 2.— Light curves in V, B, and R bands relative to comparison star A.

the variation. We read the light curve data into a program that performed a Fourier transform and output a plot of power against frequency, its spikes indicating frequencies of oscillation.

Each set of data exhibited a prominent spike at a frequency of  $\sim 0.001$  Hz. To evaluate the amplitude of the variation by the magnitude of the spike, we simulated the oscillation of the star with a sine curve at this frequency, adjusting its amplitude such that the spike produced by the simulation had the same value as that produced by the data. This amplitude represents the percent change in magnitude of the variable star over a cycle.

Speculating that lower frequency oscillations would become more apparent over the longer duration of the combined observations, we combined all the datasets for simultaneous analysis. When this dataset was finely resolved (with 1600 data points), the  $\sim 0.001$  Hz spike resolved into two narrowly separated spikes of like size. This further supports the argument for QPOs, characterized by small temporal instabilities in the frequency of oscillation. This refutes the possibility of the white dwarfs spin being a factor in this variability, since its spin frequency is necessarily perfectly coherent.

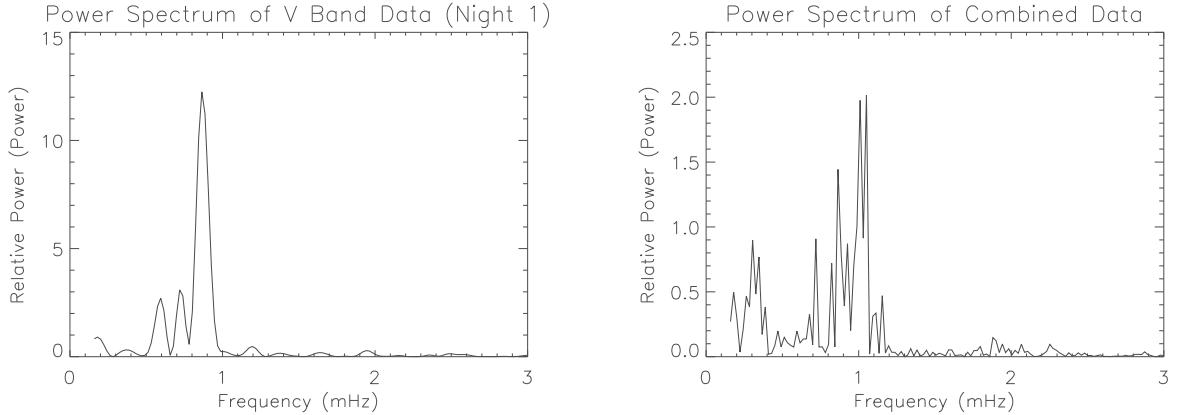


Fig. 3.— Two power spectra. The left frame shows the broad peak at 0.83 mHz obtained in the V band from one night. The right frame shows a higher resolution spectrum of the combined data from four nights and indicates two equal-amplitude frequencies of oscillation at 1.00 mHz and 1.05 mHz.

## 5. Other Considerations

In addition to QPOs, CVs of this type are also sometimes found to exhibit dwarf nova oscillations (DNOs), high-frequency oscillations that occur in the range of 5-15 times the QPO frequency (Warner et al. 2002). Our data do not support DNOs but do not eliminate the possibility. Because these data are susceptible to noise, a greater number of data points may be necessary to reveal a spike in the power spectrum. Our data is at a particular disadvantage given that the postulated frequency of oscillation of a DNO has a period in the range of the time between images. It is possible then that DNOs are not apparent or do not exist currently but will become observable later.

Our merged images reveal a nebula that surrounds the nova, including a region that appears somewhat more extensive than the planetary nebula emission seen before the outburst. The nebula is seen in all three bands, raising the possibility that V458 Vul has produced a light echo scattering off of dust originally in the planetary nebula. We make the geometrical assumption that nova and planetary nebula lie on a line in the plane of the sky at a separation of 0.28 pc (Wesson et al. 2008), or  $8.6 \times 10^{13}$  km and calculate that in the 1035 days between the nova explosion and our observations, light traveled  $2.68 \times 10^{13}$  km. This rough calculation supports the possibility of

observing a light echo, which may be interesting to re-examine in later observations.

## 6. Conclusions

Variations in magnitude of nova V458 Vul in this early, “nova-like” state of its evolution are strongly suggestive of quasi-periodic oscillation. The rough oscillatory variation detectable in each light curve is unambiguously defined in the resultant power spectrum. Evidence for QPOs arises from the night-to-night variation in frequency. Since the QPO wobbles about a small range of frequencies, it appears in the power spectrum as a broad curve, which would be a delta function in the case of fixed frequency. QPO is further supported by the higher resolution power spectrum of the combined data, in which the broad spike resolves into two equal-magnitude spikes of near-equal frequency.

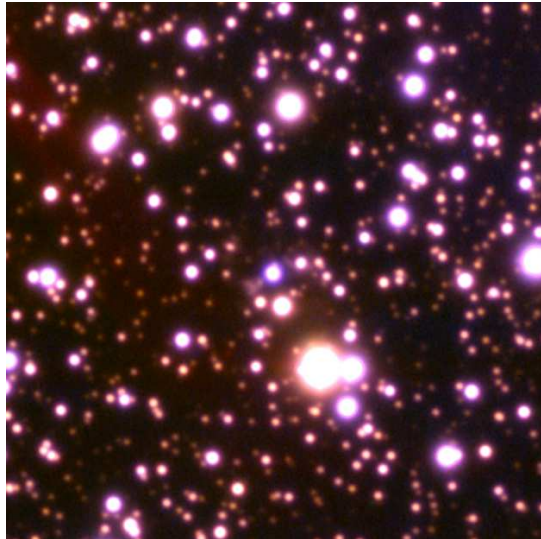


Fig. 4.— This combined color image of V458 Vul shows that the star appears rather blue. The image is scaled logarithmically to bring out the nova’s faint planetary nebula, which appears just to the left of the nova.

Table 1. Magnitudes of comparison stars are calibrated to standard values for apparent magnitude found at [www.aavso.org](http://www.aavso.org). Magnitudes are measured in three bands and listed for each night of observation. The varying magnitude of V458 Vul can be extrapolated from these values and the relative magnitudes used to plot the light curves.

Star	V Magnitude	B Magnitude	R Magnitude
V Star A	14.36	15.27	13.91
B Star A	14.96	15.98	14.39
R Star A	14.77	16.12	14.07

Table 2. Frequency and amplitude of spike obtained from each power spectrum.

Date	Filter	Duration (hr)	Frequency (mHz)	Amplitude (mag)
June 7, 2010	V	2.9	0.84	0.088
June 8, 2010	B	3.6	1.05	0.045
June 9, 2010	V	3.8	1.05	0.050
June 10, 2010	R	2.9	1.00	0.060

**REFERENCES**

- La Dous, C. 1993, Space Science Journal, 67, 1
- Wesson et al. 2008, ApJ, 688, L21
- Warner et al. 2002, Royal Astronomy Society
- Misuzawa et al. 2010, Astronomical Society of the Pacific, 122, 299
- Rodríguez-Gil et al. 2010, arXiv:1006.1075v1

Computer Code for Calculating Matrix Elements and  
Overlaps of States for the Generalized Seniority Scheme  
via Recurrence Relations

Ke Cai

Bard College

2010 NSF/REU Program  
Physics Department, University of Notre Dame  
Advisor: Mark Caprio

August 6th, 2010

## Abstract

The generalized seniority approximation provides a truncation scheme for the nuclear shell model based on building the states of the nucleus from nucleon pairs. We present a computer code to calculate matrix elements of one-body and two-body operators between generalized seniority states and overlaps of these states based on a set of recurrence relations.

## 1 Introduction

The generalized seniority approximation provides a truncation scheme for the nuclear shell model. The nuclear interaction tends to induce nucleons to form pairs coupled to angular momentum zero. This approximation considers the ground state of an even-even nucleus to be consisted of collective  $S$  pairs, which are constructed from like nucleons coupled to angular momentum zero. Then the low-lying excited states of a nucleus are obtained from breaking one or more of these pairs. The generalized seniority,  $v$ , of the state of a nucleus, is defined to be the number of nucleons not participating the collective  $S$  pairs. To perform calculations based on the generalized seniority scheme, it is first necessary to compute the matrix elements of one-body and two-body operators between basis states of low generalized seniority. It is also necessary to calculate the overlaps between these states in order to construct an orthogonal basis. In this paper, we present a computer code to calculate such quantities. The main algorithm is based on a set of recurrence relations recently derived [1]. In Sec.2, we go over some essential definitions. In Sec.3, we briefly introduce the recurrence relations<sup>1</sup>. We present the structure of the code in Sec.4 and 5. In Sec.6, we present validations we have performed. In Sec.7, we summarize the paper and propose future applications of the code.

---

<sup>1</sup>For detailed discussion involving the contents of Sec.2 and Sec.3, please refer to [1]

## 2 Definitions

We first review some of the necessary definitions of generalized seniority scheme and notations used in the recurrence relations. Working in a single major shell, one can uniquely specify a single-particle level. Let  $C_{c,\gamma}^\dagger$  be the creation operator<sup>2</sup> for a particle in the state of angular momentum  $c$  and  $z$ -projection quantum number  $\gamma$ . The angular-momentum coupled product of two spherical tensor operators is defined by  $(A^a \times B^b)_\gamma^c = \sum_{\alpha\beta} (aab\beta|c\gamma) A_\alpha^a B_\beta^b$ [3]. Then the angular-momentum coupled pair creation operator is defined by

$$A_{ab}^{e\dagger} = (C_a^\dagger \times C_b^\dagger)^e, \quad (1)$$

and the collective  $S$  pair is defined as the following linear combination of pairs of nucleons coupled to angular momentum zero:

$$S^\dagger = \sum_c \alpha_c \frac{\hat{c}}{2} A_{cc}^{0\dagger}, \quad (2)$$

with  $\hat{c} = (2c + 1)^{1/2}$ . The amplitudes  $\alpha_c$  are conventionally taken subject to the normalization condition  $\sum_c (2c + 1)\alpha_c^2 = \sum_c (2c + 1)$ . The state of zero generalized seniority and consisted of  $N$   $S$ -pairs is defined by the  $S$ -pair successively acting on the vacuum  $N$  times:  $|S^N\rangle = S^{\dagger N}|0\rangle$ . In general, a state of generalized seniority  $v$  is constructed as as  $|S^N F^f\rangle = S^{\dagger N} F^{f\dagger}|0\rangle$ , where  $F^{f\dagger}$  is a cluster of  $v$  fermion creation operators coupled to angular momentum  $f$ .

To calculate matrix elements of one-body and two-body operators, quantities of immediate interest are reduced matrix elements  $\langle S^N G^g \| T_{rs}^t \| S^N F^f \rangle$ , taken between generalized seniority states, where  $T_{rs}^t$  is the elementary one-body multipole operators, and  $F^f$  and  $G^g$  represent clusters of  $v$  nucleons not participating in the  $S$  pairs. Since generalized seniority states are not orthonormal, we also need to calculate the overlaps between states :

---

<sup>2</sup>Here we do not distinguish between the level  $c$  and its angular momentum  $j_c$ . However, when we start to work with the code, we labeled single particle levels using integers and store corresponding angular momenta elsewhere, for simplicity of storing information. For definition and further discussion of creation and annihilation operators, see [2]

$\langle S^N G^f | S^N F^f \rangle$ . In [1],  $\Gamma_N^{(v)}[\dots]$  is used for the one-body operator matrix elements between states of equal generalized seniority, *e.g.*,

$$\Gamma_N^{(4)}[(cd)^f(kl)^{n,h} | (rs)^t | (ab)^e(ij)^{m,g}] \equiv \langle S^N (A_{cd}^f A_{kl}^n)^h \| T_{rs}^t \| S^N (A_{ab}^e A_{ij}^m)^g \rangle, \quad (3)$$

and  $\Phi_N^{(v)}[\dots]$  for the overlaps, *e.g.*,

$$\Phi_N^{(4)}[(cd)^f(kl)^{n,g} | (ab)^e(ij)^{m,g}] \equiv \langle S^N (A_{cd}^f A_{kl}^n)^g | S^N (A_{ab}^e A_{ij}^m)^g \rangle. \quad (4)$$

We will follow the same notations in this paper.

Since a state with any generalized seniority and N number of  $S$  pairs ( $N > 0$ ) can be expressed as a linear combination of states with higher generalized seniority by expanding one or more  $S$  pairs in terms of  $A_{kk}^0$ , matrix elements or overlaps involving states of different generalized seniority can be calculated using states with the same generalize seniority, *e.g.*,

$$\langle S^N A_{cd}^g | S^{N-1} (A_{ab}^e A_{ij}^m)^g \rangle = \sum_k \alpha_k \frac{\hat{k}}{2} \langle S^{N-1} (A_{kk}^0 A_{cd}^g)^g | S^{N-1} (A_{ab}^e A_{ij}^m)^g \rangle. \quad (5)$$

It is noteworthy that  $\Gamma_N^{(v)}$  and  $\Phi_N^{(v)}$  obey some symmetry relations under permutation of arguments, *e.g.*,

$$\begin{aligned} \Gamma_N^{(4)}[(cd)^f(kl)^{n,h} | (rs)^t | (ab)^e(ij)^{m,g}] &= -\theta(abe) \Gamma_N^{(4)}[(cd)^f(kl)^{n,h} | (rs)^t | (ba)^e(ij)^{m,g}] \\ &\quad \xleftrightarrow{\qquad\qquad\qquad} \\ &= \theta(emg) \Gamma_N^{(4)}[(cd)^f(kl)^{n,h} | (rs)^t | (ij)^m (ab)^{e,g}]. \end{aligned} \quad (6)$$

or complex conjugation, *e.g.*,

$$\Gamma_N^{(4)}[(cd)^f(kl)^{n,h} | (rs)^t | (ab)^e(ij)^{m,g}] = -\theta(rsgh) \Gamma_N^{(4)}[(ab)^e(ij)^{m,g} | (sr)^t | (cd)^f(kl)^{n,h}]. \quad (7)$$

### 3 The Recurrence Relations

In [1], the reduced matrix elements of the one-body operator and overlaps between generalized seniority states are written as vacuum expectation values, *e.g.*,

$$\langle S^N G^g \| T_{rs}^t \| S^N F^f \rangle = (-)^{f-t-g} \langle 0 | (\tilde{G}^g \tilde{S}^N \times T_{rs}^t \times S^{\dagger N} F^{f\dagger})^0 | 0 \rangle, \quad (8)$$

and

$$\langle S^N G^f | S^N F^f \rangle = \hat{f}^{-1} \langle 0 | (\tilde{G}^f \tilde{S}^N \times S^{\dagger N} F^{f\dagger})^0 | 0 \rangle. \quad (9)$$

The recurrence relations for the matrix elements are derived by first commuting the one-body operator  $T$  to the right and then a pair creation operator  $A$  to the left to annihilate the vacuums (shown by the arrows), resulting in terms due to commutators (shown beneath the arrows), which now involve states with lower generalized seniority or lower  $N$ , schematically:

$$\begin{aligned} \Gamma_N^{(v)} &\sim \langle 0 | (\tilde{G} \tilde{S}^N) \xrightarrow[A^\dagger S^{\dagger N-1}]{\longrightarrow} T (S^{\dagger N} F^\dagger) | 0 \rangle \\ &\sim \langle 0 | (\tilde{G} \tilde{S}^N) \xrightarrow[H^\dagger \sim [T, F^\dagger]]{\longrightarrow} (S^{\dagger N} T F^\dagger) | 0 \rangle + \langle 0 | \tilde{G} \tilde{S}^N A^\dagger S^{\dagger N-1} F^\dagger | 0 \rangle \\ &\sim \langle 0 | (\tilde{G} \tilde{S}^N) (S^{\dagger N} H^\dagger) | 0 \rangle + \langle 0 | \tilde{G} \tilde{S}^N A^\dagger S^{\dagger N-1} F^\dagger | 0 \rangle. \end{aligned} \quad (10)$$

and then

$$\begin{aligned} &\langle 0 | \tilde{G} \tilde{S}^N A^\dagger S^{\dagger N-1} F^\dagger | 0 \rangle \\ &\sim \langle 0 | (\tilde{G} A^\dagger \tilde{S}^N) (S^{\dagger N-1} F^\dagger) | 0 \rangle + \langle 0 | (\tilde{G} \tilde{S}^{N-1}) (S^{\dagger N-1} F^\dagger) | 0 \rangle \\ &\quad + \langle 0 | (\tilde{G} T \tilde{S}^{N-1}) (S^{\dagger N-1} F^\dagger) | 0 \rangle + \langle 0 | (\tilde{G} \tilde{S}^{N-1}) T (S^{\dagger N-1} F^\dagger) | 0 \rangle \\ &\sim \langle 0 | (\tilde{I} \tilde{S}^N) (S^{\dagger N-1} F^\dagger) | 0 \rangle + \langle 0 | (\tilde{G} \tilde{S}^{N-1}) (S^{\dagger N-1} F^\dagger) | 0 \rangle \\ &\quad + \langle 0 | (\tilde{E} \tilde{S}^{N-1}) (S^{\dagger N-1} F^\dagger) | 0 \rangle + \langle 0 | (\tilde{G} \tilde{S}^{N-1}) T (S^{\dagger N-1} F^\dagger) | 0 \rangle. \end{aligned} \quad (11)$$

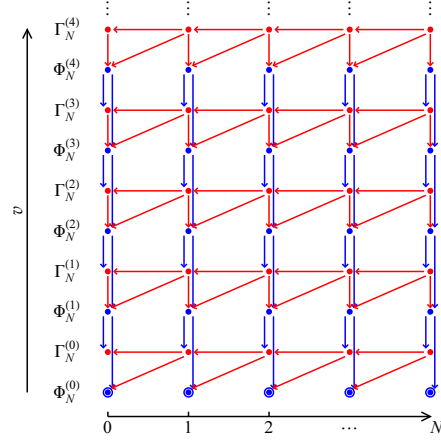
The recurrence relations for  $\Phi_N^{(v)}$  are derived along the same line. The resulting recurrence relations have the following forms:

$$\Gamma_N^{(v)} \sim \Phi_N^{(v)} + \Gamma_{N-1}^{(v)} + \Phi_{N-1}^{(v)}. \quad (12)$$

and

$$\Phi_N^{(v)} \sim \Gamma_N^{(v-1)} + \Phi_N^{(v-1)}. \quad (13)$$

The recurrence network of  $\Gamma_N^{(v)}$  and  $\Phi_N^{(v)}$  are shown below.



The base case of the recurrence network – the overlaps  $\Phi_k^{(0)}$  ( $k = 0, 1, \dots, N$ ), have been calculated, using combinatorial methods[4][5]:

$$\Phi_N^{(0)} = (N!)^2 \sum_{(M_c) \in \mathcal{P}(N, D)} \left[ \prod_c \alpha_c^{2M_c} \binom{\Omega_c}{M_c} \right]. \quad (14)$$

## 4 Structure of the Code

To preserve the algebraic structure of our problem, we construct various classes to represent objects we work with. The following classes are key to the structure of the code.

## 4.1 The `halfint` Class

As shown by Eq.(3) and (4), all the calculations of matrix elements and overlaps between states are carried out using angular momenta of individual or coupled nucleons, which can only have integer or half-integer values (e.g.,  $-1, -\frac{1}{2}, 0, \frac{1}{2}, 1$ , etc.). Since the C++ standard library does not define a data type for fractions, we first construct the class `halfint` , which includes both integers and half-integers (an integer is considered a half-integers with an even numerator). `halfint` only defines one member, the `numerator`, which is of type `int`, in C++. Without defining a denominator, we assume that the denominator of any object is 2. We then define appropriate operations of `halfint` type, such as addition, subtraction, comparison, etc., in terms of `numerator` of `halfint`, i.e. twice the actual value of `halfint` objects. Now a user of the code can easily preserve half-integer properties of angular momenta during computation and perform calculations involving them intuitively. In addition to the operations above, a series of other functions associated with angular momenta are defined. Variables of `halfint` type can now be used as building blocks for the classes to follow.

## 4.2 The `cluster` Class

We now construct the `cluster` class to represent clusters, in consistency with their physical definition in Sec.2. The `cluster` class has four members, for storing four kinds of information of the nucleons being created or annihilated: their species (neutrons or protons), the single particle levels on which they are created or annihilated, intermediate angular momenta resulting from coupling pairs of nucleons and total angular momentum of all particles created or annihilated. In particular, intermediate and total angular momenta are declared to be of type `halfint`.

In order to use the symmetric property mentioned in Sec.2, we define the canonical ordering of a cluster and a function to arrange a cluster into such an order and multiplying the cluster with a phase factor. The canonical order of a cluster is defined such that the single particle indices are in ascending order within pairs, pairs of indices of single particle levels are in ascending order lexicographically, i.e.  $(ab) < (cd)$  (where  $(ab)$  and  $(cd)$  are ordered pairs)

if  $a < c$  or if  $a = c$  and  $b < d$ . If two pairs of single particle indices are equal, these two pairs are then arranged such that their coupled angular momenta are in ascending order. Then using the symmetries in Eq(6), clusters with arguments permuted with respect to each others can be related by a simple phase factor.

Other important functions defined for `cluster` include those that check the physical validity of grouped clusters, such as one that checks triangularity of coupled angular momenta. When an object of `cluster` is found to be "invalid", these functions either make the term involving such an invalid cluster zero, or terminate the program, which cut down the amount of calculation or avoid calculating physically impossible quantities. Using `cluster`, we construct the two following classes.

### 4.3 The `tensorOp` Class

`tensorOp` is constructed for spherical tensor operators. `tensorOp` has members `creation`, `annihilation` (of type `cluster`, defined for the creation-operator-cluster and annihilation-operator-cluster) and `opTotalAm` (of type `halfint`, defined for the coupled angular momentum of total angular momenta `totalAm` of `creation` and `annihilation`. One important operation defined for a `tensorOp` is taking it's adjoint, realized by swapping `creation` and `annihilation` and multiplying with an appropriate phase.

### 4.4 The `state` Class

Different from `tensorOp`, which uses `cluster` type as members, the class `state`, constructed for representing a generalized seniority state, is a derived class of `cluster`, with an additional member, `pairnumber`, which indicates the number of collective  $S$  pairs of the state. Since a generalized seniority state is defined as  $N S$  pair creation operators and a cluster of  $v$  creation operators acting on  $|0\rangle$ . our construction of a generalized seniority state is consistent with its physical definition in the way that  $S^{\dagger N}$  is simplified as  $N$ , indicated by `pairnumber` and the notion of  $|0\rangle$  is suppressed. As a derived class of `cluster`, `state` inherits a number of functions defined for `cluster`, while some other functions need to be

overloaded or redefined to take `pairnumber` into account. One function specially defined for `state` is `raiseSeniority` based on Eq(5), which returns a series of states with higher seniority, lower `pairnumber` and appropriate coefficients. With this function, the code is able to calculate matrix elements and overlaps between states of different generalized seniority. It also provides means to internal consistency checks.

## 4.5 The `phiEnsemble` and the `gammaEnsemble` Classes

In recurrence calculations, some quantities of lower seniority or lower N come up repeatedly. To take advantage of this, we use the C++ container, `map`, to cache those values. Each entry in a `map` is consisted of a unique `key`, and a corresponding value to the `key`. In our case, the value is any intermediate calculation of a matrix element or the overlap between two states. In order to uniquely identify quantities with `key`, we construct the classes `phiEnsemble` and `gammaEnsemble`, used to identify values of  $\Phi$ 's and  $\Gamma$ 's, respectively. A `phiEnsemble` contains two members of type `state`, namely, `bra` and `ket`. This way, an object of `phiEnsemble` uniquely labels the overlap between its `bra` and `ket`. `gammaEnsemble` is defined and used in the same way, except it contains an additional member of type `tensorOp`, to indicate the spherical tensor operator involved in the calculation. To utilize symmetries due to complex conjugation, and provide a rule for C++ to look up values, we define the canonical form of an ensemble and a function to set an ensemble to "canonical form". The canonical form of an ensemble is a form such that both of the states involved are in "canonical order", and `bra` is "less" than `ket` (defined by lexicographically comparing each member of the two states). In the case of a `gammaEnsemble`, if `bra` and `ket` were the same, and `creation` were "greater than" `annihilation` in the spherical tensor operator (again, "greater than" is defined by lexicographical comparison), the adjoint of the spherical tensor operator would be taken, resulting in an appropriate phase.

The above five classes are the foundations of our code. With these classes, we are now able to perform specific calculations of matrix elements and overlaps in a straightforward

way.

## 5 Calculations and Caching

We used the recurrence relations as our main algorithm for calculating the matrix elements and overlaps. We developed two sets of functions. One set consists of specific functions, `Phi0`, `Phi1`, `Gamma0`, `Gamma1`, etc., defined for each seniority, calculating matrix elements and overlaps of states using the corresponding formulae provided by the recurrence relations. The other set consists of two general functions, `Gamma` and `Phi`, which perform preliminary works, such as checking the validity of states and operators, arranging ensembles into "canonical form", looking up existing values in the `map`'s, etc. After all the preliminary works are done, if , it calls the specific functions according to seniority of the states involved and finally caches the values in the map.

In side the specific set of functions, recurrence relations are realized by constructing new states of lower  $N$  or lower seniority, using the information in the original arguments, and calling the general functions with the newly constructed states or operators as arguments. These two sets of functions are related by calling each other in the recurrence network until both  $v$  and  $N$  reduce to 0.

## 6 Validations

Some of the formulae provided by the recurrence relation have many arguments and are error-prone. To check both the correctness of the code and of the formulae themselves, we are able to perform some validations.

### 6.1 Comparing with Combinatorial Methods

Overlaps between states of generalized seniority 2 were evaluated as sums over overlaps between states of generalized seniority 0 using combinatorial methods [1]. We compared our

results calculated by the recurrence formulae, to those given by the explicit formulae. The results agreed – this proves that both the derivation of the recurrence relations and the code are correct up to  $v = 2$ .

## 6.2 Internal Consistency Checks

As mentioned in Eq.(5), a state with  $N$  number of  $S$  pairs and generalized seniority  $v$  can be expanded as a linear combination of states with  $(N-1)$  number of  $S$  pairs generalized seniority  $v - 2$ . Based on this, we compared results calculated by upgrading both of the states involved in a specific calculation, *e.g.*,

$$\langle S^N A_{cd}^g | S^N A_{ab}^e \rangle = \sum_i \sum_j \alpha_i \alpha_j \frac{\hat{i}}{2} \frac{\hat{j}}{2} \langle S^{N-1} (A_{ii}^0 A_{cd}^g)^g | S^{N-1} (A_{jj}^0 A_{ab}^e)^e \rangle. \quad (15)$$

## 7 Summary

Based on the recurrence relations, the computer code we present here is able to calculate matrix elements and overlaps. We can use the results of the code to calculate matrix elements of tensor operators of physical interest, *e.g.* Hamiltonian and the electromagnetic transition operators. Planned applications of the code include testing pair structures and extending shell model calculations to nuclei which cannot easily be reached by conventional calculations, and studying the mapping of shell model onto the Interactive Boson Model[Reference!], which treats pairs of nucleons as composite bosons.

## 8 Acknowledgements

This work was supported by the US DOE under grant DE-FG02-95ER-40934.

## References

- [1] F.Q. Luo and M.A. Caprio, Nucl. Phys. A (2010).
- [2] J. Suhonen, *From Nucleons to Nucleus* (Springer-Verlag, Berlin, 2007).
- [3] D. A. Varshalovich, A. N. Moskalev, and V. K. Khersonskii, *Quantum Theory of Angular Momentum* (World Scientific, Singapore, 1988).
- [4] Y. K. Gambhir, A. Rimini, and T. Weber, Phys. Rev. 188, 1573 (1969).
- [5] S. Pittel, P. D. Duval, and B. R. Barrett, Ann. Phys. (N.Y.) 144, 168 (1982).

# **Project GRAND: Modifying Data Acquisition System**

**Lidens Cheng**

**2010 NSF/REU Program  
Physics Department, University of Notre Dame**

**Advisor: John Poirier**

## **Abstract:**

The Data Acquisition System (DAS) running at Project GRAND's experimental site is currently on its 22<sup>nd</sup> edition. In DAS16, this C program identifies both single muon hits and large air showers. The wire coordinates are then recorded to the computer's fast memory. After storing 900 tracks in fast memory, the computer then writes the data to the IDE disk. Furthermore, a transfer program copies this data from IDE to a USB disk hourly as a backup. Several of the changes made to DAS17-DAS22 include a feature to free memory allocated at the beginning of the program, a feature to transition from an older version of DAS to a newer version with a 2 second time loss, and a feature to write 900 tracks of data from the computer's fast memory to both IDE and USB disks.

Among the 64 huts at the experiment, several huts operate less efficiently in the winter compared to the rest of the year. In order to determine these huts, one of the necessary steps is calculating the ratios of the total muon counts for two weeks in March to the total muon counts for two weeks in September for each of the 64 huts. The huts with the lowest ratios for March 2010 to September 2009 and March 2009 to September 2008 and the results from other tests are compiled to produce a list of inefficient huts.

## **Introduction:**

A DAS is a system that acquires data from an aspect of the physical world for the purpose of controlling a process, measuring a process, or understanding a process. It usually involves gathering signals from sensors and digitalizing the signals for storage and analysis on a PC. A DAS for a PC usually consists of sensors, which convert physical parameters to electrical signals [1]. A circuit board containing a signal conditioning feature and an analog-to-digital converter will convert the sensor signals into analog waveforms and the analog waveforms into digital values respectively [1]. Since the circuit board is normally the interface between the sensor signals and the PC, it is connected to the bus of the PC. A DAS software program, which is commonly written in a general-purpose programming language, controls the entire operation of a DAS.

The DAS at Project GRAND (Gamma Ray Astrophysics at Notre Dame) works similarly to the general description of a DAS

above. The experiment is an array of detectors in 64 stations. Each of the 64 stations contains 4 proportional wire chambers (PWC). Each chamber consists of 2 horizontal planes of signal wires; one plane of 80 wires runs north-south and another plane of 80 wires runs east-west [2]. In each of the 64 huts, a mixture of Ar and CO<sub>2</sub> flows through all four chambers. In addition, the 160 wires in each chamber are held at 2600V [2]. When a charged particle such as a muon or an electron passes through a chamber, the gas is ionized. These ions accelerate toward the closest wire, a small current forms on this wire, and the electronic signal gives away the position of the charged particle that passed through the wire [2]. In order to distinguish between a muon and an electron, there is a steel plate positioned between the 3<sup>rd</sup> and 4<sup>th</sup> chambers. Since electrons are scattered, showered, or stopped by the steel plate 96% of the time, muons are the particles that pass through all 4 pairs of planes [3]. Each wire has a circuitry that consists of an amplifier, a shift register, and a summer used in coincidence to form a self-trigger for a particular station.

This trigger causes information from the 640 wires to be stored in its respective shift register memory. The trailer receives a timing signal from a hut that is triggered and a train of clock pulses are sent to all 64 stations in order for the data in each station to shift serially to the trailer [2]. The bus (VMEBus) of the associated computer (5100) records the data from the stations and the wire coordinates of the successful muon. After 900 successful muons, the 5100's fast memory writes data to the IDE disk of another computer (PC1) and the IDE disk copies data to an external USB disk hourly. The DAS software program, which is written in C, controls the whole procedure.

Due to the effects of the Earth's atmosphere, there is a high correlation between the number of muons detected and temperature. When temperature increases, the atmosphere expands and rises. Due to a less dense atmosphere, pions are less likely to interact with air molecules and more likely to decay into muons [4]. When the atmosphere is cold and dense, pions are more likely to interact with air molecules before they can decay into muons. Therefore, the muon rate in a warmer atmosphere is higher than the muon rate in a colder atmosphere [5]. With this in mind, in order to determine the huts that are less efficient in the winter at Project GRAND, the muon rates in a colder month are compared to the muon rates in a warmer month.

### **Experiment:**

Prior to Summer 2010, the DAS software program was on its 16<sup>th</sup> version (DAS16). First, a muon file and a shower file are created on IDE disk with the current timestamp as their names. Next, DAS16 loops until there is data in the VMEBus. Once there is an event in the VMEBus, the program determines whether it is a shower

event or a muon event. A shower event is when multiple stations register a hit in coincidence and a muon event is when a station registers a single track of a successful muon [3]. The program defines a shower event to be an event where at least 6 huts had been hit. When this is the case, the data regarding this shower event is written to the shower file that was created in the beginning of the program. Otherwise, this is a muon event. In order to locate the muon event, the program cycles through all 64 huts. When searching through a particular hut, the program cycles through all 8 planes. When searching for a muon, the program searches for 1 hit on each plane. While searching on a particular plane, the program cycles through all 80 wires. A hit is defined to be when 1, 2, or 3 adjacent wires are struck. The coordinates of the wires are recorded in the 5100's fast memory and every event is processed in the same way. Every 10 minutes, a day file, which records the muon counts in each hut for that particular day, is updated. A file called "control" is also checked every 10 minutes. If "control" holds a 0, DAS16 would exit. If "control" holds a 1, the DAS program would continue running. If "control" holds a 2, DAS16 would execute a command file called "restart", which would enable a newer version of the DAS program (DAS17) to start running. However, this feature does not work properly in DAS16. After DAS16 records 900 muon events and the coordinates of their respective wires, the data regarding the muon events are written from the 5100's fast memory to the muon file that was created in the beginning of the program. Every hour, the muon file and the current shower file are closed and a new muon file and a new shower file are created.

The DAS program is currently on its 22<sup>nd</sup> version (DAS22). Several features that did not work or were not efficient in DAS16 are

modified. First, “control” is checked for a 0 and checked for a 1 every 10 seconds instead of every 10 minutes. In addition, allocated memory is never freed in DAS16. In DAS22, if “control” holds a 0, appropriate files are closed, allocated memory is freed, and DAS22 exits. Furthermore, “control” is not checked for a 2 every 10 minutes along with the other two “control” conditions. Instead, “control” is checked for a 2 every hour after the muon file and the shower file are closed. If “control” holds a 2, appropriate files are closed, allocated memory is freed, “control” is changed to a 1, and the command file “restart” is executed. Once “restart” is executed, there is a 2 second sleep that gives enough time for DAS22 to exit before DAS23 starts running. If “control” does not hold a 2, a new muon file and a new shower file are created with the current timestamp in DAS22. If there is a 2 in “control”, a new muon and a new shower file are created with the timestamp given at the beginning of DAS23.

One of the tests to assemble a list of huts that are less efficient in the winter is comparing the muon rates during a warmer month to the muon rates during a colder month. Figure 1 shows the muon rates throughout 2008 and Figure 2 shows the muon rates throughout 2009. The general trend in Project GRAND’s data is the presence of a maximum in September and the presence of a minimum in March. Since a day file holds the muon counts for all the huts in a day in 10-minute intervals, the day files are used to compare the muon rates in March to the muon rates in September. The comparison is conducted for D60-D75 (03/01/10-03/16/10) versus D250-D265 (09/07/09-09/22/09) and for D60-D75 (03/01/09-03/16/09) versus D250-D265 (09/06/08-09/21/08). First, a FORTRAN program is written to compute the total

muon count at the end of the day for each of the 64 huts for every day file selected for this comparison. Next, the ratios of the total muon counts of each hut for the respective days of 2010 to the total muon counts of each hut for the respective days of 2009 are computed. For example, the ratio of the total muon count of each of the 64 huts in D60 of 2010 to the total muon count of each of the 64 huts in D250 of 2009 is calculated and this same step is applied to the remaining selected days of March 2010 to the remaining selected days of September 2009. Afterwards, the 16 days worth of ratios for each of the 64 huts are averaged in order to produce the ratios of the muon rates in March 2010 to the muon rates in September 2009 for all 64 huts. These same steps are done to compute the ratios of the muon rates in March 2009 to the muon rates in September 2008.

## **Results and Analysis:**

In DAS22, a new muon file and a new shower file are only created hourly if “control” does not contain a 2. If “control” has a 2, a new muon file and a new shower file are created at the beginning of DAS23 in order to reflect more accurate timestamps. Compared to DAS16, when “control” holds a 2 in DAS21, the time loss for switching from an old muon file and an old shower file in DAS21 to a new muon file and a new shower file in DAS22 is minimized to 2 seconds. However, since a day file does not necessarily bear the same time down to the seconds as a muon file or a shower file, the time loss in a day file when transitioning from one DAS program to another DAS program is usually greater than 2 seconds. Moreover, allocated memory is never freed in DAS16. When allocated memory is freed at the end of a program, the memory is given back to the pool that it was taken from. In the transition from DAS21 to DAS22,

allocated memory is freed before DAS21 exited in order to prevent possible memory leaks.

Figure 3 is an example of an efficient hut in the winter. Hut 53 follows the general trend of possessing slightly higher muon rates for the days in September than the muon rates for the days in March. The average ratio of the muon rates for hut 53 for the days in March 2010 to the days in September 2009 is 0.96. Figure 4 is an example of an inefficient hut in the winter. Hut 33 shows a large deviation from the general trend, with the muon rates for the days in March being considerably lower than the muon rates for the days in September. The average ratio of the muon rates for hut 33 for the days in March 2009 to the days in September 2008 is 0.16. Table 1 shows the averaged ratios of the muon rates for March 2010 to September 2009 and the averaged ratios of the muon rates for March 2009 to September 2008 for every hut. The seven huts with the lowest ratios for both March 2010/September 2009 and March 2009/September 2008 are highlighted and recommended for new gas flow meters.

### Conclusion:

The current DAS software program (DAS22) at Project GRAND incorporates several new features that were not available prior to Summer 2010. In addition, some of the features in DAS16 were modified to improve time efficiency and the quality of the program. In DAS22, the feature to transition from the running DAS version to a newer DAS version is now functioning with a time loss of only 2 seconds. The timestamps of new files after a changeover from an old DAS program to a newer DAS program are also more accurate. Additionally, in order to prevent memory

leaks, allocated memory is freed before the DAS program exits.

As one of the tests to determine the huts that are less efficient huts in the winter, the ratios of muon rates for March 2010 to September 2009 and the ratios of muon rates for March 2009 to September 2008 are calculated. Seven huts with the lowest ratios for March 2010 to September 2009 and March 2009 to September 2008 make a list of potential candidates for new gas flow meters.

### Acknowledgments:

First and foremost, I would like to thank Dr. John Poirier. I thoroughly appreciated his guidance and advice throughout this summer. I would also like to thank Dr. Chris D'Andrea for his willingness to help. Finally, I would like to thank Dr. Garg, Shari Herman, and the Notre Dame Physics Department for this research opportunity.

### References:

- [1] Ozkul, Tarik. *Data Acquisition and Process Control Using Personal Computers*. New York: Marcel Dekker, 1996. Print.
- [2]"Project GRAND In-depth Description." *University of Notre Dame*. Web. 04 Aug. 2010. <<http://www.nd.edu/~grand/grand.html>>.
- [3] Poirier, J. and C. D'Andrea. Status Report on Project Grand. *30th International Cosmic Ray Conference*, 2007.
- [4] Chui, Glennda, and Tona Kunz. "Symmetry - March 2009 - Cosmic Weather Gauges." *Symmetry Magazine*. Web. 04 Aug. 2010. <<http://www.symmetrymagazine.org/cms/?pid=1000688>>.
- [5] Dominick, Rocco. *Seasonal Variations in Muon Rate with Ice Cube*. Tech. Madison: University of Wisconsin, 2009. Print.

## Appendix A: Tables and Figures

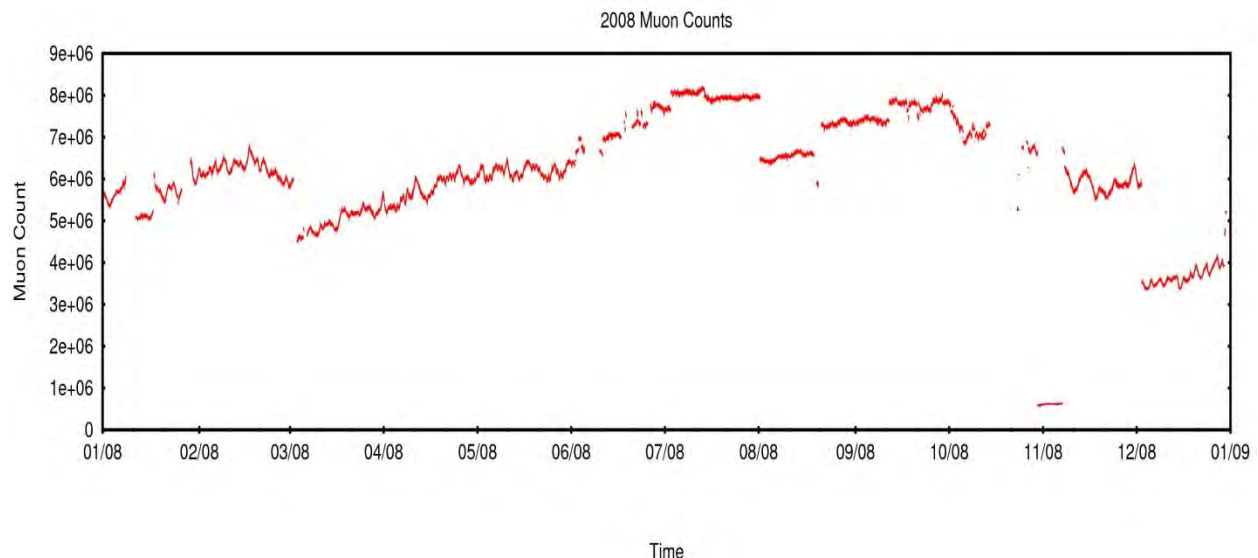


Figure 1: Muon counts throughout the year 2008

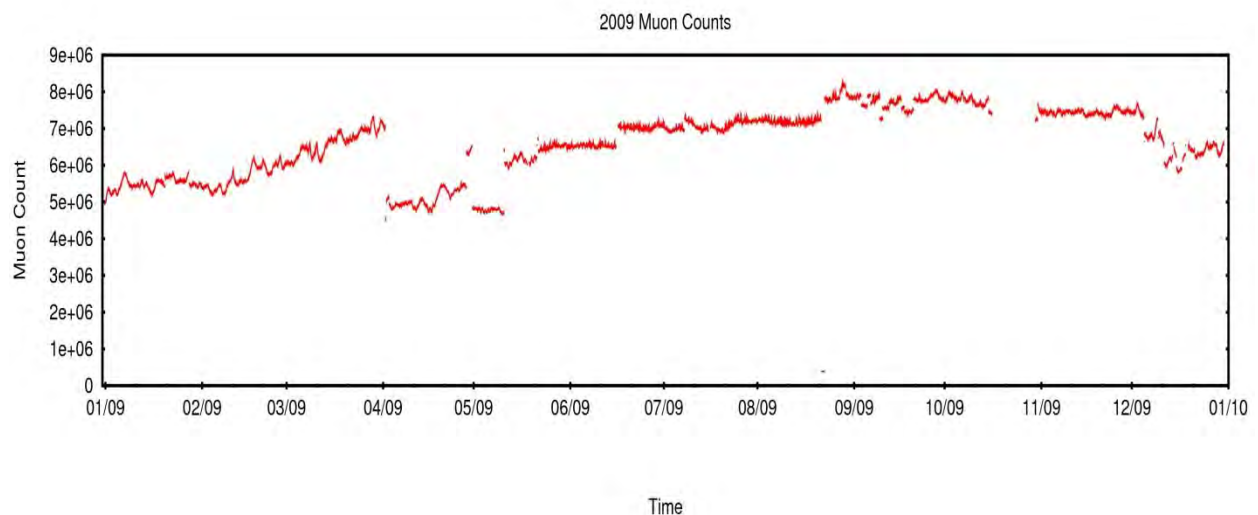


Figure 2: Muon counts throughout the year 2009

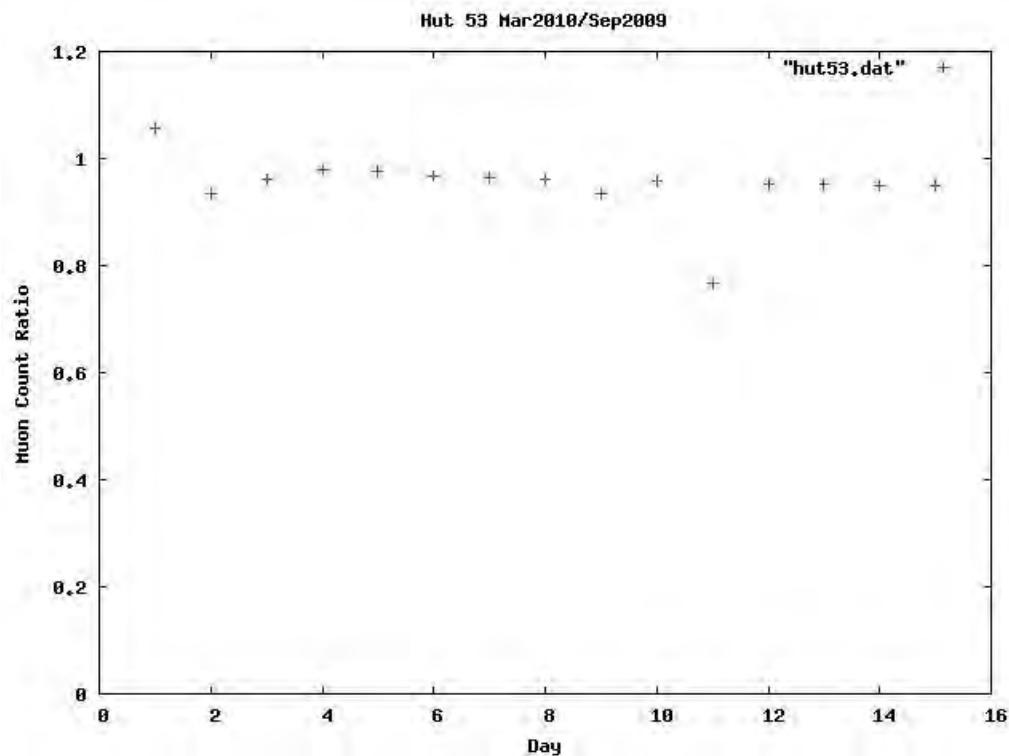


Figure 3: An example of an efficient hut shown through Hut 53

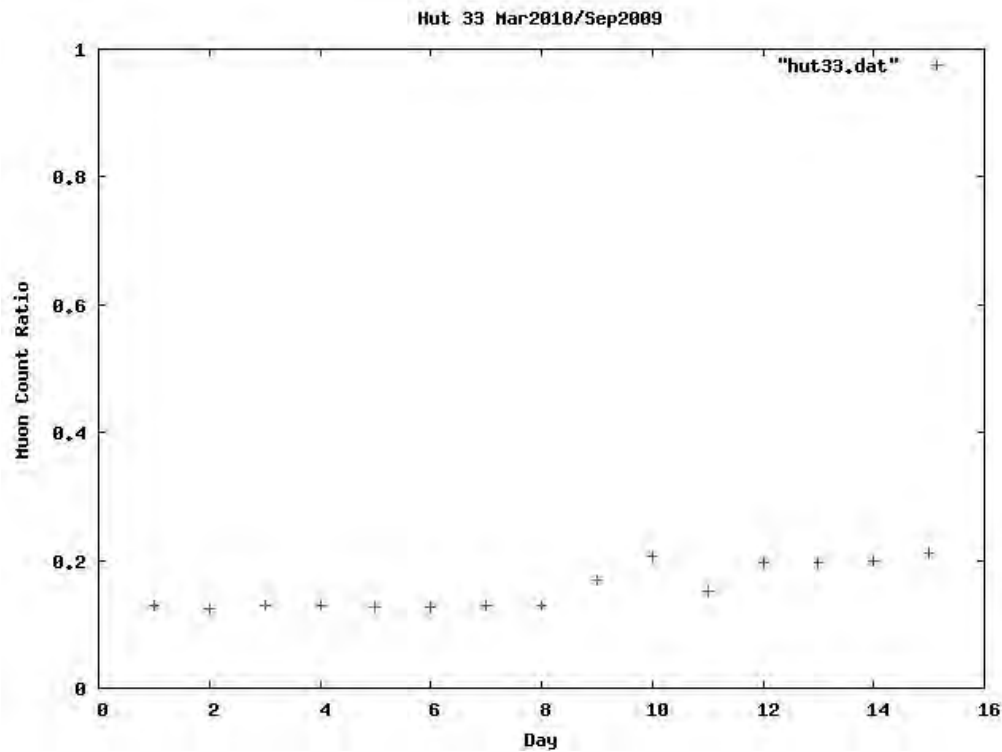


Figure 4: Example of an inefficient hut shown through Hut 33

Hut	Mar10/Sep09	Mar09/Sep08	Hut	Mar10/Sep09	Mar09/Sep08
1	1.04	1.58	33	<b>0.16</b>	<b>0.29</b>
2	1.02	1.55	34	1.49	0.28
3	0.71	1.44	35	1.03	1.55
4	1.02	1.57	36	0.92	0.27
5	1.01	1.59	37	1.01	1.57
6	1.02	1.58	38	0.95	1.10
7	DIV/0	DIV/0	39	1.00	1.23
8	DIV/0	DIV/0	40	1.00	1.52
9	DIV/0	DIV/0	41	DIV/0	0.28
10	1.02	1.58	42	<b>0.83</b>	<b>0.28</b>
11	1.02	1.58	43	0.77	0.40
<b>12</b>	<b>0.12</b>	<b>0.57</b>	44	1.00	1.57
13	0.89	1.58	45	1.00	1.47
14	1.05	0.90	46	<b>0</b>	<b>0.28</b>
15	1.05	1.80	47	0.89	1.19
16	DIV/0	DIV/0	48	DIV/0	DIV/0
17	DIV/0	DIV/0	49	DIV/0	DIV/0
18	1.00	DIV/0	50	0	0.28
<b>19</b>	<b>0</b>	<b>0.29</b>	51	1.00	1.52
20	0.42	1.40	52	0.99	0.35
21	2.09	0.28	53	0.96	2.56
22	1.04	1.58	54	<b>0</b>	<b>0.43</b>
23	0.99	1.56	55	0.88	0.27
24	1.03	1.58	56	DIV/0	DIV/0
25	0.82	DIV/0	57	1.07	DIV/0
26	1.01	DIV/0	58	0.31	1.72
27	0	DIV/0	59	<b>0.22</b>	<b>0.28</b>
28	1.02	0.68	60	1.01	1.54
29	1.03	1.00	61	DIV/0	DIV/0
30	1.02	1.55	62	1.04	1.68
31	1.03	1.59	63	0.99	1.54
32	1.00	1.56	64	0.99	1.53

Table 1: Huts and their muon rate ratios

# Summer REU Final Report

## Nuclear Alpha Cluster and Accelerators

Patrick A. Copp

8/6/2010

The following reports the activities of research during this summer's REU internship. Emphasis is aimed toward the first experiment and its corresponding events (due to length constrictions). Although the other experiments will be mentioned in conclusion.

### Theory and Introduction:

In stars fusion occurs between the elements, starting with Hydrogen then Helium and leading up to Beryllium, Carbon, and Oxygen. During this process it is extremely common for excess energy to form isotopes and excited states that can decay into lighter elements with the release of alpha particles and neutrons. An example of one unstable element that was studied this summer was  $^{16}\text{O}$  which has previously been theorized to contain a linear alpha structure at various excited states [1]. At the Notre Dame FN Tandem Accelerator a direct method was used to explore the reaction of  $^{12}\text{C} + \alpha \rightarrow ^{16}\text{O} \rightarrow ^8\text{Be} + ^8\text{Be}$ . By using a range of alpha energies from 12MeV to 20MeV it was possible to map an excitation curve to observe the  $0^+$ ,  $2^+$ ,  $4^+$ , and  $6^+$  rotational bands at discrete energy levels [2]. This is done by using an array of Si strip detectors [3] at the forward scattering angles. If the excited states do not match the predicted energies then it is most likely that a different structure has been observed.

The second, indirect method was to use a single alpha energy to bombard a  $^{13}\text{O}$  target and induce a transfer reaction [5]. Due to conservation of energy the energy of the system after collision must be split between an  $^{16}\text{O}$  nucleus and a neutron. The reaction causes the  $^{16}\text{O}$  nucleus to jump to an excited state while the neutron carries off the excess energy. Because  $^{16}\text{O}$  excited states can only exist at discrete levels the detection of the neutron energy can be used to deduce which state of  $^{16}\text{O}$  has been populated. For this set up neutron detectors were required to be arranged at the back scattering angles.

Why is the detection of neutrons important to the experiment? As mentioned above neutrons are the primary projectiles emitted by the unstable nuclei. By studying their respective energies it is possible to work backwards to find the populated levels of the excited states in the objective nuclei.

### Experimental Set Up:

The beginning of research consisted of experimental set up and overcoming technical problems. First, a metal rack and frame were constructed to hold six neutron detectors which had to be tested (via background and solid source radiation) before they could be used in the actual experiment. Afterwards the detectors were wired to the high voltage supply so that trigger levels could be established. The radiation levels were observed on an oscilloscope to show the energy induced voltages; this led to the determination of trigger levels to match the desired time scales for particle detection.

Equipment testing continued by connecting the target chamber to the beam line in the west target room. First the target holder was inserted into the chamber and vacuum pumping was started. Looking for leaks it was determined that the lid had been unequally screwed on, otherwise no other problems arose. Next the machine shop made two handles for opposite sides of the lid so it could be easily removed off the chamber. In addition, the voltage converter, from 110 V to 220 V, was tested for the UK equipment. They would be collaborating for the first experiment. Finally wires had to be soldered to the beam collimator tube and nylon screws were used to secure the collimator in place while insulating the connected electronics.

When vacuum was once again pumped a computer was booted up to analyze the background radiation spectrum which consisted of gamma rays and neutrons. The detector gates were then fine-tuned to read a filtered peak for the neutrons. In the experiment gamma rays result from Compton Scattering with electrons in the target and neutrons rebound from collisions with protons in the nucleus.

The target chamber was then moved to the east target room where the experiment actually took place. A faraday cup, which was used to detect the beam's charge at any given point in time, was placed before the chamber to block the beam from the target between runs.

Furthermore the beam had to be aligned almost perfectly before, through, and after the target chamber. To do this the chamber was disconnected from the beam pipe and a solid disk was inserted on the pipe's end. A permanent telescope already aligned with the beam pipe confirmed the alignment before the chamber. After that the chamber was reconnected and arranged such that it was level with the currently centered beam disk. Then the process of alignment through the chamber consisted of centering the collimator tube with the previously set disk. Adjustments were made in the xy plane perpendicular to the beam such that each target holder was also centered. The last step meant another disk needed to be inserted after the chamber and centered, the same way as previously mentioned above. Once alignment was complete a quartz window was inserted in place of the last disk after the chamber. This acted as a scintillation screen in order to view the beam through a camera which was then mounted level with the beam's alignment.

Everything was then ready to be wired to the control panel via BNC connectors except the quartz window which required a BNC to be soldered with a garter clip for attachment. The following were connected to the control board: collimator, target, faraday cup, quartz window, and camera. The neutron detectors were also positioned at the back scattering angles around the target chamber.

Soon afterwards Martin Freer and his team arrived from the UK, and he gave a short briefing of the experiment. There were three reactions to be studied during the following runs:  $^{12}\text{C}(\alpha, ^8\text{Be})^8\text{Be}$ ,  $^{13}\text{C}(\alpha, ^8\text{Be} + ^8\text{Be})\text{n}$ , and  $^9\text{Be}(\alpha, ^8\text{Be} + \alpha)\text{n}$  — where  $^8\text{Bd} + ^8\text{Be}$  forms the unstable excited states of  $^{16}\text{O}$ .  $20\mu\text{m}$  targets were used along with four Si strip detectors with a thickness of  $500\mu\text{m}$  each [3]. These detectors were used to observe the change in the angular distribution of the collisions. Afterwards Freer and his group inspected the set up and began mounting the Si strip detectors, wiring their high voltage electronics, and connecting computers. Once testing began it was discovered that several sets of wiring pin holes on the chamber were dysfunctional so new connectors were found as replacements.

Upon completion of the preparations a schedule was made to sit shifts at the control panel 24 hours a day for two consecutive weeks of run time. At first, the beam energy had to be changed every 20 minutes in  $100\text{KeV}$  intervals. An alpha beam was used to bombard a  $^{12}\text{C}$  target to observe the decay of  $^{16}\text{O}$  into  $^8\text{Bd} + ^8\text{Be}$ . An energy range of  $12\text{MeV}$  to  $17\text{MeV}$  was recorded by DAQ software to analyze the excited state levels  $2^+$ ,  $4^+$ ,  $6^+$  and  $8^+$  ( $8^+$  has never been experimentally verified [4]).

Sitting shifts at the control panel was a repetitive procedure, but also a great learning experience. First the beam was turned off after a run and the shutter (beam block) was put in. Then the frequency required for the analyzing magnet was tuned and the NMR peak aligned. Next the terminal voltage was set to the desired value that relates proportionally to the beam

energy. With the faraday cup in, the beam is turned back on and the shutter put out so that the beam current can be checked. Then the faraday cup is put out and the beam spot was checked on the camera aligned with the quartz window. Finally the cup is closed and the OK was given to begin data acquisition for the next run.

It was soon realized that the experiment was moving ahead of schedule so it was decided to focus on one beam energy for an extended period of time at 14.35MeV. This was done on the basis of observing the excitation of the Hoyle state which is related to the ground state of  $^{12}\text{C}$ [2]. It has been previously verified that this meta-stable  $2^+$  state is the main reaction for the formation of  $^{12}\text{C}$  in stars and is actually the only way  $^{12}\text{C}$  can be created in the universe. Afterwards the  $^{13}\text{C}$  target was ready to be inserted so the neutron detectors had to be repositioned to surround the entire target chamber and the experiment was continued.

#### Target Thickness Measurements:

A crucial part of the experiment was to measure the thickness of each of the targets used in the experiments. To do this a low energy alpha source was focused into a beam and calibrated at two energy peaks, 3183KeV and 5486KeV. At this calibration the centroid energy in KeV was recorded along the full width half maximum value and the net area (number of counts). The procedure was as follows: the alpha source is measure and the previously mentioned quantities were recorded. Then the first target was placed under the source and the new peaks were measured (for example Mylar, which composed the  $^{16}\text{O}$  target,  $P1=2743.23\text{KeV}$  and  $P2=5163.13\text{KeV}$ ) along with the corresponding quantities. Next the blank alpha energy is again measured. If the first peak shifts within three KeV of the original then the procedure continues for the next target. However, a shift more than three KeV implies an instability in the power supply and it is necessary to again measure the first target followed by the blank. When this process is done for all targets a table can be compiled as shown in table 1 which can be used to calculate the thickness.

Time	Target	Peaks	Centroid (KeV)	FWHM	Net Area
2:09	Empty	$P1=1123.06$	3183.00	27.36	2536
		$P2=1969.04$	5486.00	19.48	2030
2:17	Mylar	$P1=965.82$	2754.39	40.87	2002
		$P2=1856.54$	5179.75	36.63	2093
2:31	Empty	$P1=1117.89$	3168.92	16.91	1053
		$P2=1961.94$	5465.02	16.94	1739
2:44	$\text{New } ^{12}\text{C}$	$P1=1099.66$	3119.30	25.49	1676
		$P2=1946.40$	5424.38	22.41	1737
2:58	Empty	$P1=1117.58$	3168.06	19.98	1709
		$P2=1959.27$	5459.41	6.71	1178
3:15	Mylar	$P1=961.52$	2743.23	37.00	2305
		$P2=1850.44$	5163.13	36.49	3086

3:32	Empty	P1=1116.40	3164.87	19.33	1406
		P2=1956.99	5453.21	3.52	-140
3:39	Old $^{12}\text{C}$	P1=1096.18	3109.80	13.63	1553
		P2=1942.92	5414.91	8.09	1377
3:49	Empty	P1=1116.02	3163.81	16.94	1213
		P2=1956.93	5453.04	4.04	-275

Table 1 Measured quantities for thickness calculation.

In order to make a thickness calculation it was required to take the average of the blank centroid peaks (one with one and two with two) before and after the desired target (New  $^{12}\text{C}$  will be used as a example calculation).

$$\frac{(3168.92 + 3168.06)}{2} = 3168.49 \text{ KeV}$$

The change in energy is then needed between the average centroid and that of the desired target

$$\Delta E = 3168.49 - 3119.30 = 41.19 \text{ KeV}$$

Next the stopping power  $dE/dx$  (in units of  $\text{KeV}/(\mu\text{g}/\text{cm}^2)$ ) of the alpha beam energy (blank peaks) on the corresponding target is looked up in the SRIM program developed by James F. Ziegler.

$$dE/dx = 1.090 \text{ KeV}/(\mu\text{g}/\text{cm}^2)$$

Finally the thickness, in units of  $\mu\text{g}/\text{cm}^2$ , can be calculated by taking the quotient of the change in energy over the stopping power

$$\Delta x = \frac{\Delta E}{dE/dx} = \frac{41.19}{1.090} = 45.13 \mu\text{g}/\text{cm}^2$$

This result gives the simple approximation of the thickness. Checking this approximation can be done by integration, using the method of numerical summation, to find a more exact thickness. This is done by starting with the original blank energy  $E_0 = 3183 \text{ KeV}$  and its corresponding  $dE/dx$ . Then an arbitrary change in thickness ( $dx = 10$ ) is multiplied by the stopping power to find the first change in energy  $\Delta E_1$ . The difference between  $E_0$  and  $\Delta E_1$  gives the next energy  $E_1$  whose corresponding stopping power is used in conjunction with another arbitrary  $dx$  and the process is repeated. When the sum of the  $\Delta E_n$  is within one KeV of the original  $\Delta E$ , as calculated in the paragraph above, the  $dx_n$  are summed to give the

integrated thickness. This procedure must be completed for each target and was done as follows; the final thicknesses are presented after the calculation.

$$E_0 = 3183 \text{ KeV} \text{ and } \Delta E_1 = 1.090(10) = 10.9 \text{ KeV} \therefore E_1 = 3172.10 \text{ KeV}$$

$$\Delta E_2 = 1.093(10) = 10.93 \text{ KeV} \therefore E_3 = 3161.17 \text{ KeV} \dots$$

$$\sum \Delta E = 49.29 \text{ KeV} \text{ and } \sum \Delta x = 45 \mu\text{g/cm}^2$$

	Peak 1 Average Blank=3168.49 KeV	Peak 2 Average Blank=5462.22 KeV
$\Delta E$	49.19 KeV	37.84 KeV
$dE/dx$	$1.090 \text{ KeV}/(\mu\text{g/cm}^2)$	$0.7581 \text{ KeV}/(\mu\text{g/cm}^2)$
$\Delta x$	$45.13 (\mu\text{g/cm}^2)$	$49.91 (\mu\text{g/cm}^2)$

$$\therefore \sum \Delta x = 45.13 \mu\text{g/cm}^2 \text{ is confirmed.}$$

Table 2 New Carbon-12 Target

	Peak 1 Average Blank=3166.47 KeV	Peak 2 Average Blank=5456.31 KeV
$\Delta E$	423.24 KeV	293.18 KeV
$dE/dx$	$1.142 \text{ KeV}/(\mu\text{g/cm}^2)$	$0.7923 \text{ KeV}/(\mu\text{g/cm}^2)$
$\Delta x$	$370.62 (\mu\text{g/cm}^2)$	$370.04 (\mu\text{g/cm}^2)$

Table 3 Mylar Target

	Peak 1 Average Blank=3164.34 KeV	Peak 2 Average Blank=5453.13 KeV
$\Delta E$	54.54 KeV	38.22 KeV
$dE/dx$	$1.090 \text{ KeV}/(\mu\text{g/cm}^2)$	$0.7581 \text{ KeV}/(\mu\text{g/cm}^2)$
$\Delta x$	$50.04 (\mu\text{g/cm}^2)$	$50.42 (\mu\text{g/cm}^2)$

Table 4 Old Carbon-12 Target

Mylar	$356 (\mu\text{g/cm}^2)$
Old Carbon-12	$50.04 (\mu\text{g/cm}^2)$
New Carbon-12	$45.13 (\mu\text{g/cm}^2)$

Table 5 Final Thickness Measurements

Further calculations were then required to determine the statistical and systematical errors for each measurement. Assuming the centroid peaks were Gaussian in the form of  $e^{-\frac{(x-x_0)^2}{(2\sigma)^2}}$  (where  $\sigma$  is the error) the statistical error was found as follows. By taking the FWHM of the target's first peak and dividing it by 2.3,  $\sigma_t$  can be calculated. The same can be done for  $\sigma_0$  which corresponds to the blank peak

$$\sigma_t = \frac{25.49}{2.3} = 11.08 \text{ and } \sigma_0 = \frac{16.91}{2.3} = 7.35$$

Next,  $\sigma_{\Delta E}^2$  can be found by taking the sum of  $\sigma_t^2$  and  $\sigma_0^2$  each divided by their respective net areas. Then by taking  $\sigma_{\Delta E}$  divided by the known  $\Delta E$  of the target the statistical error can be found and converted into a percentage.

$$\sigma_{\Delta E}^2 = \frac{\sigma_t^2}{\text{net area}_t} + \frac{\sigma_0^2}{\text{net area}_0} = \frac{11.08^2}{1676} + \frac{7.35^2}{1053} = 0.1245$$

$\therefore \sigma_{\Delta E} = 0.00711 = 0.71\%$  for the New  $^{12}\text{C}$  target.

To find the systematic error simply set  $\sigma_{\Delta E}$  of the system equal to  $\left(\frac{1}{2}\Delta E_0\right)^2$ , where  $\Delta E_0$  is the difference between peak 1 of the blank measured before and after the target, and divide by the same  $\Delta E$  as determined during the first thickness measurements. Table six shows the error calculations for the old and new  $^{12}\text{C}$  as well as the mylar targets.

	Statistical - $\frac{\sigma_{\Delta x}}{\Delta x}$	Systematic - $\frac{\sigma_{\Delta x}}{\Delta x}$
New Carbon-12	0.71%	0.87%
Mylar	0.093%	0.37%
Old Carbon-12	0.49%	0.97%

Table 5 Experimental Error

Data analysis (SRIM) contributed dominate error of 3.9%

As an additional experiment, Martin and his group made four new  $20\mu\text{m}$  thick carbon targets, two of which were used in the experiment. This was done by taking a glass slide with a  $20\mu\text{m}$  film of carbon foil and transferring it onto a metal target holder with a circular hole cut in its center through which the beam could pass. In order to make the transfer, the film was cut into four equal sized squares on the glass slide. The slide was then mounted at an angel to be slowly lowered into a cup of water. As the slide entered the water the films separated from the glass and floated on the surface where it could be scooped up with the metal frame and adhere

over the hole, thus providing a sufficient target. The experiment was then rerun with the new targets at the interesting energies as determined by the previous experiment.

### Conclusion:

In summary the theory, experimental set up, and certain relevant measurements have been discussed in this report. It has been considered very important to find evidence for linear alpha clusters in the light elements formed in stars. The experiment consisted of preparations to induce reactions by colliding alpha particles with targets of Carbon and Oxygen. Setting up the target chamber, connecting it to the beam pipe, wiring the detectors, and sitting shifts at the control panel were the main technical feats to carry out the experiment. Afterwards the targets were measured and their thicknesses calculated

In addition to the experiment discussed in this report, an experiment was also conducted to study a similar transfer reaction and nuclear structure in  $^{24}\text{Mg}$ . A carbon beam was used to bombard carbon targets to induce this reaction. The formation of  $^{24}\text{Mg}$  in its excited state behaves in a comparable way to that of  $^{16}\text{O}$  since it rapidly decays into its constituent particles. It was observed that an alpha cluster is indeed one of these constituents which verify the reasoning for the experiment in the first place.

Other experiments are currently operating to study nuclear cluster structures in the mass range of 18-36 atomic mass units. One topic of great interest includes that of the transfer reactions between alpha particles and nuclei. Further aspects of research are also being pursued to study heavy nuclei structures by using rare isotope accelerators which have been developed in several places around the world [5].

### References

- [1] B.R. Fulton, *Contemporary Physics*, Vol. 4, 5, 299-311, (1999)
- [2] F. Hoyle, *Astrophys. J. Suppl. Ser.* **1**, 121, (1954)
- [3] P.J. Haigh et al *J. Phys. G: Nucl. Part. Phys.* **37**, (2010)
- [4] P. Chevallier et al, *Phys. Rev.* **160**, 827 (1967)
- [5] W. von Oertzen, Martin Freer, Yoshiko Kanada-En'yo, *Physics Reports* **432**, 43-113, (2006)

# Guided Inquiry and the Brain

Louis Didio

Indiana University of Pennsylvania

Sandy Liss

Swarthmore College

Dr. H. Gordon Berry

University of Notre Dame

Summer 2010

## Abstract

Guided inquiry (GI) is a constructivist teaching method that encourages students to become active participants in their own learning. This student-centered approach to the classroom focuses on the learning process in addition to pure academic content. It is particularly relevant to science education in that it allows students to learn science as science is practiced. Studies on learning have shown that in this type of classroom environment, students both retain information better and relate to the subject more than students in a traditional classroom environment. With that in mind, researchers in the field of science education are currently making connections between this phenomenon and brain research. Specifically, they are looking at how the brain gathers and processes information. We review past and current research in this area, especially as it pertains to best practice methods of creating long-term learning. We also suggest possible topics for future research.

## **Introduction and History**

In 1983, the National Commission on Excellence in Education (NCEE) released a report entitled *A Nation at Risk: The Imperative for Educational Reform*. It detailed the failings of the United States educational system, citing that among a series of nineteen academic achievement tests issued internationally, students from the US never scored among the top two nations. They did, however, fall last seven times when compared with other industrialized nations. In an age where technology was quickly and constantly revamping the responsibilities of the workforce, the committee feared the consequences of the next generation of United States citizens falling behind their international peers intellectually. Their goal in publishing the findings of this 18-month study was "to generate reform of our educational system in fundamental ways and to renew the Nation's commitment to schools and colleges of high quality throughout the length and breadth of our land" to ensure that this did not happen (*A Nation at Risk*).

The NCEE made four recommendations to those involved in the reform effort: (1) strengthen local and State high school graduation requirements; (2) adopt higher standards and expectations for student achievement at the high school, college, and university levels; (3) manage school time more efficiently or increase time spent in school; and (4) hold leaders responsible for funding and implementing the necessary changes. Though many have critiqued this report (Vik 1984, Stedman 1994, Berliner and Biddle 1995, etc.), there is little question that it was responsible for spurring a conscious and long-term effort to reform education in the United States.

In particular, many researchers began looking in to science, technology, engineering, and mathematics (STEM) education reform in an effort to explicitly confront the rise of technology use in the workplace. The National Research Council (NRC) headed one of these efforts.

The NRC, in line with the NCEEs second recommendation, released a series of standards to be used as a basis for the reform of science education in primary and secondary classrooms. These standards, published in 1996, stemmed from four guiding principles:

- All students are capable of learning science.
- Science education should be an engaging endeavor.
- Science should be taught as science is practiced.
- Improving science education is only one step in the process of a complete educational reform.

The NRC developed these principles after years of observation and research of the practices which led to the US's poor international performance. They found that science classrooms were primarily lecture-based with students copying formulae and examples from textbooks and chalkboards into notebooks. Students in such traditional classrooms are rewarded for reproducing what they have been told and for following predetermined procedures. This educational setting promotes the stereotypical image of a scientist: a lone white male battling to understand nature in an airy realm of abstraction (Michaels 3). This depiction of an individual who is so far removed from reality has been shown to discourage students from pursuing science in college (Handelsman 3). It is also in stark contrast to the reality of the scientific profession. Studies have shown that communication and collaboration, in addition to creativity and logical thinking characterize the work of scientists (Michaels 4). The NRC sought to rectify this discrepancy through the standards, which encourage educators to bring true science into their classrooms.

Guided inquiry (GI) is a pedagogical application of the NRC standards. In a GI classroom, science is taught in the manner it is practiced. Students, like scientists, seek to answer questions in a collaborative laboratory-like setting. They draw conclusions from their own data and subsequently share their findings with their peers. GI is what is referred to as a

constructivist method of teaching, whereby students' knowledge is derived from first hand experience with the phenomena in question (Handlesman 7).

There are five essential features of an inquiry approach (Bellina):

- It engages students with scientifically oriented questions.
- In responding to these questions, experimental evidence is the priority.
- Explanations come from the evidence.
- Explanations are compared to accepted scientific knowledge.
- Explanations are communicated and justified to peers.

What makes a lesson guided concerns the relative roles that the learner and instructor play in the learning process. GI falls in between a student-direct classroom, in which the questions, evidence, and analysis come solely from the student, and a teacher-directed classroom, which these aspects of the curriculum fall under the responsibilities of the teacher.

Recently, there has been a nationwide effort to encourage all science teachers in K-12 classrooms to incorporate this GI method into their classrooms because it has been shown to better support student understanding of the subject. In this paper, we first present the past and current research on learning and the brain that has led policy makers to support this method over traditional ones. Specifically, we focus on (a) how the brain gathers and stores information and (b) how internal and external stimuli affect these processes. We conclude by suggesting possible topics for future research in the area of science education and brain research.

# **Brain Research**

The brain is a very complex system, and the model by which it is said to gather and store information has changed many times over the years. Scientists are seeking to gain further insight into how the brain processes and stores memory by looking at how the different regions function in response to internal and external influences. The goal of this research is not only to learn more about the layout of the brain, but also to understand further how physiology and memory are affected by external stimuli. In particular, some researchers are studying the nature of the learning process and how it is either enhanced or inhibited by various teaching methods.

## **Background on the Brain**

**Physical Layout** The brain has four lobes, each one of which carries out a distinct set of functions. The frontal lobe is the region where higher-level thinking, language function, emotion, and problem solving take place. The occipital and temporal lobes focus primarily on the processing of visual and auditory stimuli, respectively. The parietal lobe allows a person to stand upright, perceive information, and balance. The lobes interact via neurons, which send electric impulses between the regions. The signal travels out along the axon of one neuron and through the synapse, which is the space between two neurons. It is received by the dendrite of the second neuron. This transfer of impulses forms pathways between the neurons. Research has shown that the more frequently these pathways are used, the stronger they become, allowing for faster transfer and processing of information (Sousa 78). Further research has shown that individuals whose jobs revolve around the completion of complex tasks develop more dendrites than those with lower level responsibilities. The addition of dendrites allows for more connections to form between neurons, which results in an increased

capacity for memory (Sousa 22).

**Sensory Input and Memory** The sensory register is responsible for filtering the information from the body's five senses. The selection process is determined by whether or not the brain perceives the stimuli as being important. The criteria of importance are set in a hierarchy (Sousa 43). First in the hierarchy is the concept of danger. If an individual is under stress, whether physical or mental, his or her brain will divert all of its rational information processing capacity to deal with the danger. This is known as the fight or flight response. Once the brain senses that the threat has passed, an individual may return to other forms of information processing. Under danger in the hierarchy is emotional input. Emotional response is controlled by the amygdala, which suspends complex processing and rational thought. Information that is relevant to previous experiences is given priority after danger and emotion. Finally, information pertaining to new learning falls last on the hierarchy, meaning that the previous levels must be addressed before the brain can attend to processing and storing new material. Once selected for processing, the information enters the short-term memory (STM). Here, the amount of information processed by the brain is significantly reduced. The information in the STM will either be discarded or transferred to the long-term memory (LTM). This is where the information is stored for future recall.

**Implications for Teaching** Because repeated use of neuron pathways makes them more efficient, an effective pedagogical method would constantly build on students prior knowledge. We are all scientists and begin exploring and modeling our environment as soon as we are born. All students come to the classroom with a set of preconceived notions based on these models, some of which agree with accepted scientific knowledge and some of which do not.

It has been found that unless students face their misconceptions head-on they are unlikely

to change their views (CSMEE 117). In a traditional classroom, students are typically told information and given answers. They rarely confront or are given the opportunity to reassess their beliefs, and therefore are unlikely to truly internalize the content or to correct misconceptions. Furthermore, content in a traditional classroom tends to be broken up into distinct units; once a lesson has been tested it is not needed to support the lessons that follow. This does not allow for repeated use of neuron pathways and therefore does not lead to the formation of new dendrites.

In a GI classroom, the curriculum builds on itself. Students are constantly encouraged to refer to lessons completed weeks prior to their current tasks. They constantly activate existing neuron connections while forming new ones. Additionally, students learn primarily through their own experience, the same manner in which they learned before beginning formal education. In this way, they are consistently referencing prior experience, which allows them to explicitly address misconceptions.

## Multiple Intelligences

Howard Gardners theory of multiple intelligences (MI) is based on a "pluralistic view of the mind," suggesting that the brain deploys several "discrete facets of cognition, acknowledging that people have cognitive strengths and contrasting cognitive styles" (Gardner 5). His original theory described seven distinct "intelligences": musical, body-kinesthetic, logical-mathematical, linguistic, spatial, interpersonal, and intrapersonal. Each intelligence has been linked to at least one part of the brain and every person is said to possess unique levels of all seven intelligences, which are responsible for processing different types of information (See figure 1), A person's individual cognitive make up will determine which of the intelligences will be most effective in his or her learning. It is important to note that the idea of MI is an open field in which progress continues to be made in the forms of new categories such as

naturalistic, spiritual, and moral (Mednick).

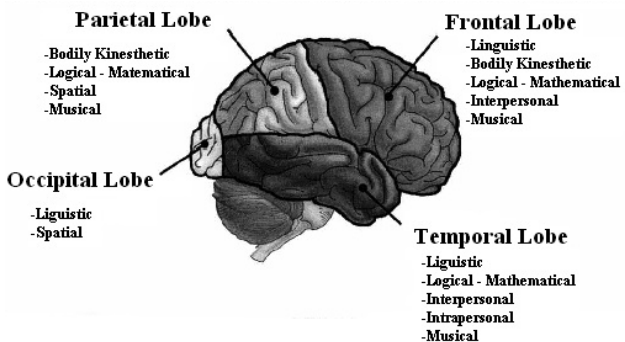


Figure 1: Conceptual model of lobe junctions correlated with characteristics of multiple intelligences.

**Implications for Teaching** The concept of MI has lent support to the methods of GI in several ways. A traditional classroom restricts student learning by catering to a limited number of intelligences, typically logical-mathematical and linguistic. For some students, the traditional classroom suits their learning needs because they connect well to those intelligences, but this is not the case for all students. An effective classroom is one in which the students can learn in the way that suits them, whether it is through visual, audio, or motion. GI classrooms allow students to explore content in a variety of ways, thus engaging more than students who are considered intelligent in the typical classroom.

## Emotion, Environment, and Learning

Emotions effect learning in two ways: (1) through the environment in which learning takes place, and (2) through an emotional connection to the content itself (Sousa 83). The emotional environment can have either a positive or negative effect on a student's learning. In a positive learning environment, the brain releases endorphins stimulating the frontal lobe, which is responsible for higher-level thinking and problem solving. In a stressful learning

environment, the brain releases cortisol rather than endorphins. This hormone activates the fight or flight response previously described. In other words, in a negative learning environment, students are not able to attend to learning new content because their brains are otherwise engaged. Instead of processing information, the frontal lobe must attend to the source of stress, which has been shown to impede memory formation and recall (Sousa 84).

An emotional investment in the content of a lesson makes information easier to recall. A memory is not stored in a single part of the brain; parts of the event are stored in various regions. An emotional aspect adds a dimension to the learning, making the memory of the lesson more easily accessible to the student. Emotional connections are one of many factors that affect retention and recall of information. For example, a study done by the National Training Laboratories in the 1960s (and supported by more recent research) showed that the teaching method used to present material has a large effect on the percentage of the content that makes it to the LTM (See figure 2).

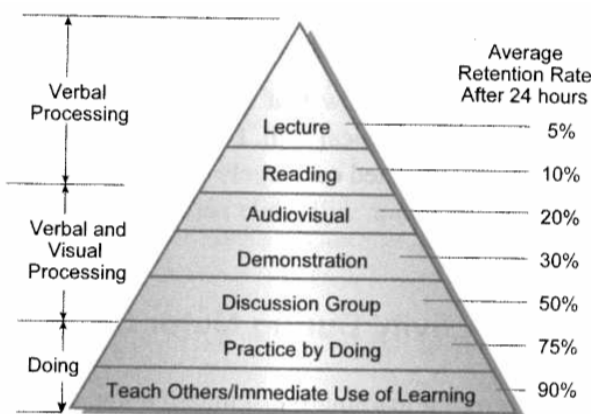


Figure 2: The average percentage of retention of material after 24 hours for each of the instructional methods.

**Implications for Teaching** It is very important that the environment in which learning takes places is well suited for retention and recall. The classroom must be a safe place where

students feel as if they can ask questions without the fear of being embarrassed by their peers or instructors. The teacher must be sure to guide students in a direction where their stress level does not overrule their intellectual curiosity. If the students become stressed, their brains will shut down, and the window for learning will be replaced by a focus on attending to a source of stress.

In a traditional classroom, the focus is on what students do not know and the teacher holds the key to learning. In contrast, in a GI classroom the teacher acts as a guide for the students to lean on during the learning process. The students have a personal investment in the course of their learning, as they are responsible for the outcome of each experience. Although the process of inquiry can be trying, the experimental nature of the classroom encourages students to see wrong answers as opportunities, thus taking the stigma out of sharing insights with a group. Thus, the GI environment is a naturally comfortable one for learning.

## Future Research

Our understanding of GI has come a long way since the introduction of the NRC standards in 1996, but there are still questions that have yet to be answered by both scientists and educators. Questions concerning psychology and neurological research have been a hot topic as of late.

One question that researchers are trying to answer is why children not responding to traditional methods of teaching and why reform is even needed. If change is to occur in the classroom, teachers need to know what already works and what does not in their current classroom. Researchers are looking at many aspects of this question such as psychological and social explanations for why children are not reaching expectations in a traditional

classroom.

A second question revolves around technology. As previously mentioned, we live in a technological world and it is affecting our lives on a daily basis. This begs the question of whether or not the amount of multimedia and technology that children are exposed to affect the brain's ability to focus attention. The availability of information on the internet and the speed at which it can be accessed has made it difficult for the traditional classroom to compete for the attention that every teacher desires from his or her students. If technology can be linked to learning, it could move education into a whole new realm of pedagogical theory.

The overlaying topic of research concerning GI and brain research has been on the question of whether there is any evidence suggesting physiological changes in the brain that occur when one learns via a constructivist style versus direct instruction. If a physical change can be observed when learning using one method over the other, and if this change can be linked to better classroom performance, administrators and educators can then make an argument as to which direction reform should go.

Though there are still many open questions concerning GI, there is still a lot of information out there that can be used to further advance education in the United States. There has been a growing effort to educate teachers, principals, and parents on the methods and practices of a GI classroom. In particular the Northern Indiana Science, Mathematics and Engineering Collaborative (NISMEC), has been running GI workshops at the University of Notre Dame for local middle school teachers. During these three part one-week sessions the teachers are introduced to GI, learn how to apply technology to a GI classroom, and finally develop their own GI lesson plans using this technology. These workshops are run with the hope that teachers will gather enough information about the method to incorporate it into their classrooms.

Workshop A: Introduction to Guided Inquiry, is based off of the work of Dr. Lillian Mc-

Dermott and colleagues from the University of Washington. Her group developed GI lesson plans based off of years of research. *Physics by Inquiry* was published in hopes that a students natural curiosity would drive the classroom lessons. During Workshop A, local middle school teachers become the students and are guided through one of *Physics by Inquiry*'s well known lessons, Bulbs and Batteries. Frustration turned into learning through the careful guiding of Dr. Joe Bellina and Dr. H Gordon Berry, and the teachers got a first hand look at the power of a GI lesson.

Workshop B: The Vernier Workshop, was used to shed light on technology in a GI classroom. Here, the teachers became accustomed to the Vernier Lab Quest, and the variety of probes that go along with it. Workshop C: Advanced Vernier, took what the teachers learned from the prior two weeks about GI and technology in the classroom and combined them. The goal of this work is to develop GI lesson plans using the Vernier probes. The teachers had to search for suitable State standards and then write objectives which were closely tied to the standards they selected. By the end of the week, the lessons were edited and tested. The teachers left with a better understanding of GI and technology in the classroom through experience with experts, along with ready made lesson plans to implement in their classrooms.

## Conclusion

NISMEC is just one example of the effort being made to educate science teachers on the methods of GI. This paper uses science education as an example, but GI has its roots in history, reading and mathematics as well. Education is in the hands of the entire community, schools, businesses, and families, and it up to them to pull the resources together to put the United States back on top as a leader in education.

## Bibliography

*A Nation at Risk: The Imperative for Educational Reform : a report to the Nation and the Secretary of Education, United States Department of Education.* Ann Arbor, Michigan: University Of Michigan Library, 1983. Print.

Berliner, David C., and Bruce J. Biddle. *The Manufactured Crisis: Myths, Fraud, and the Attack on America's Public Schools.* New York: Addison Wesley Publishing Company, 1995. Print.

Center for Science, Mathematics, and Engineering Education (CSMEE). *Inquiry and the National Science Education Standards: A Guide for Teaching and Learning.* Washington, D.C.: National Academies Press, 2000. Print.

Dickinson, Dee. "Questions to Neuroscientists from Educators by Dee Dickinson." *New Horizons for Learning.* N.p., n.d. Web. 30 July 2010.

Handelsman, Jo, Sarah Miller, and Christine Pfund. *Scientific Teaching.* 1 ed. New York: W. H. Freeman, 2006. Print.

*Human Learning: Biology, Brain, and Neuroscience, Volume 139 (Advances in Psychology).* UK: Elsevier Science, 2008. Print.

Bellina, Joe. "Integrating Inquiry into Text-based Science Instruction." The Guided Inquiry and Vernier Probes Science Teacher Institute. Northern Indiana Science, Mathematics, and Engineering Center. Jordan Hall of Science, Southbend, Indiana. 10 June 2010. Lecture.

Lawson, Anton E.. *Teaching Inquiry Science in Middle and Secondary Schools.* Thousand Oaks: Sage Publications, Inc, 2009. Print.

Mcdermott, Lillian C., Mark L Rosenquist, Peter S Shaffer, and Physics Education Group Univ. Washington. *Physics by Inquiry: An Introduction to Physics and the Physical Sciences, Vol. 2.* John Wiley and Sons, Inc., 1996. Print.

Michaels, Sarah, Heidi Schweingruber, and Andrew Shouse. *Ready, Set, Science!: Putting Research to Work in K-8 Science Classrooms.* Washington, D.C.: National Academies Press, 2007. Print.

"Multiple Intelligences - Course 1, Chapter 5." *Connexions - Sharing Knowledge and Building Communities.* Fred Mednick, n.d. Web. 20 July 2010. [jhttp://cnx.org/content/m13287/latest/](http://cnx.org/content/m13287/latest/).

National Research Council, and National Academy of Sciences. *National Science Education Standards: Observe, Interact, Change, Learn.* Washington D.C.: National Academy Press, 1996. Print.

Nibert, Marta, and S. Kay Ashworth. "Multiple Intelligences." *Pacific Crest Faculty Development.* N.p., n.d. Web. 10 June 2010. [jwww.pccrest.com/PC/FGB/index.html](http://www.pccrest.com/PC/FGB/index.html).

Rahmann, Hinrich, and Mathilde Rahmann. *The Neurobiological Basis of Memory and Behavior*. 1 ed. New York: Springer, 1992. Print.

Sousa, David A.. *How the Brain Learns*. Third Edition ed. Thousand Oaks, CA: Corwin Press, 2005. Print.

Stedman, Lawrence C.. "The Sandia Report and U.S. Achievement: An Assessment." *Journal of Educational Research* 87.3 (1994): 133-147. Print.

Vik, Phil. "A Response to A Nation at Risk: More Looking and Less Leaping ." *NASSP Bulletin* 68 (1984): 53-59. Print.

# Simulation of the Accretion of Matter onto a White Dwarf Star

Evan Figg

2010 NSF/REU Program

Physics Department, University of Notre Dame

Advisor: Dr. Dinshaw Balsara

## Abstract

White dwarf stars in binary systems can form a disk and accrete matter if the secondary star is overfilling its Roche lobe. In this case, material from the secondary star falls through the first Lagrangian point towards the white dwarf. Due to the conservation of angular momentum and energy, the material begins to orbit the white dwarf and eventually forms a disc around the star. When the base of the disk comes into contact with the star, a boundary layer forms as the star slows down the material from its Keplerian velocity. The boundary layer is defined as starting when a decrease in the radial distance from the star switches from resulting in an increase in the velocity to resulting in a decrease in velocity. There have been two competing models to explain the boundary layer. One model predicts that the material from the disk falls onto the star without moving toward the poles, while another predicts that the material will be pushed towards the poles. A computer simulation has been previously developed to determine that the second model is correct, but the simulation used a temperature of 300,000 K for the star. While a temperature this high is adequate for discerning between the two theoretical models, most white dwarf stars are cooler than 30,000 K. The code is currently being rewritten to be run with this lower temperature as the surface temperature of the star giving a more accurate picture of what happens at the boundary layer. At this time the code generating the initial parameters and environment is complete. Future work is necessary to finish the code that will run the simulation using the currently generated values.

## 1. Introduction

Stars in binary systems often have different masses. This difference causes them to have different lifetimes. In such a system, one star may become a white dwarf while the other is still on or near the main sequence. If the main sequence star then overfills its Roche lobe, material can be transferred through the first Lagrangian point to the white dwarf. However, since both stars are orbiting each other, the material will have a large quantity of angular momentum. This momentum causes the material to form into a disk which expands outward and inward as angular momentum is transferred between layers and other interactions such as that caused by a magnetic field interact with the disk (Warner 1995). When the base of the disk eventually comes into contact with the white dwarf, a boundary layer will form as the disk material slows from almost Keplerian velocities to the velocity of the star (Warner 1995). This layer causes fresh, unburnt material to mix with the atmosphere of the star. For nonmagnetic systems, nearly half of the energy released from material falling towards the white dwarf is released in the boundary layer (Balsara et al. 2009). This interaction between a white dwarf and its companion is the basis for cataclysmic variables. There are several different types of cataclysmic variables ranging from type Ia supernovae to highly magnetic polars to dwarf novae systems. The boundary layer is especially important to dwarf novae systems as an outburst releases much of its energy at this layer, and the layer can then be left heated up when the outburst is complete (Piro & Bildsten 2004). The energy release from the boundary layer means that an accurate knowledge of the boundary layer is necessary to correctly model the spectra observed from cataclysmic variables.

## 2. Previous Models

There have been two different types of theoretical models looking at the boundary layer. One model uses a radial, one dimensional analysis of the layer (Pringle 1981; Regev 1983; Popham & Narayan 1992, 1995). This model, however, lacks a consideration for any movement of the accreting material toward the poles as it comes into contact with the surface of the star. A two dimensional analysis of the boundary layer of a neutron star was done by Inogamov and Sunyaev (1999). This type of analysis was then applied to white dwarf stars by Piro and Bildsten (2004). The results from these studies showed that a significant portion of the boundary layer would move toward the poles especially when a dwarf nova system was in an outburst period. The effects of the expanded layer on the spectrum observed during and immediately following an outburst were also shown to quantitatively agree with the flux in the blue end of the spectrum that was unaccounted for in the radial model (Piro & Bildsten 2004).

A computer simulation of the boundary layer in an accreting white dwarf system was necessary to explicitly show that the layer does indeed spread toward the poles. This simulation was done previously using a 30° cross section of the star extending from the equator extending toward the poles and starting at five atmospheric scale heights below the surface of the star and extending three disk scale heights outside of the star and assuming that the layer would be symmetric around the equator (Balsara 2004; Fisker & Balsara 2005; Fisker, Balsara, & Burger 2006; Balsara et al. 2009). The simulations were run using an alpha viscosity parameter to adjust whether the system was in an outburst ( $\alpha = 0.1$ ) or a quiescent ( $\alpha = 0.001$ ) state. Alpha values of 0.03, 0.01, and 0.005 were also used to test middle values, and all of the simulations

used a  $0.6 M_{\odot}$ ,  $9 \times 10^8$  cm radius star. These simulations conclusively proved that the boundary layer would indeed spread out during an outburst but also that the boundary layer would not spread much if it were in quiescence. These simulations, however, used temperature of 300,000 K for the surface of the star. This temperature allowed there to be fewer cells in the computation of the simulation as features such as the scale heights of the disk and atmosphere were increased but is an entire magnitude over the maximum temperature normally seen for white dwarfs. While this temperature was sufficient to show that the boundary layer would spread toward the poles, a recoding using a more realistic temperature for the white dwarf was needed.

### 3. Current Adjustments to the Code

The major goal of this summer's research was updating the previously code that setup the initial parameters and the initial values in each of the cells in the computational domain. First, the temperature was changed from 300,000 K to 30,000 K. This new value is now on the upper end of the temperatures that white dwarfs are observed to have. The decrease in surface temperature also decreases the scale height of the disk which necessitated the recalculation of the number of zones that were needed to give enough resolution of the disk for the simulation to give accurate results. The halo temperature was dependent on the temperature of the star and had to be increased in order to maintain a reasonable pressure. The temperature increase also required an increase in the number of atmospheric scale heights below the surface of the star to simulate to keep a reasonable amount of surface material in the simulation. Second, the arc that the simulation covered was increased from  $30^\circ$  to  $84^\circ$ . This increase required more

zones to be added in the polar direction but will allow the flow of material to be tracked for higher latitudes. Third, since the new code has a different base, some of the variable names have changed which required all of the old code to be checked for changed variable names as it was added to the new code. Also, some of the variables had modifications to the type of data they held. For example, velocity in the azimuthal direction previously stored as angular momentum density but now it was changed to hold the actual velocity. Finally, the code was brought up to the current Fortran standards and commenting was improved to make it easier to understand what each piece of the code does. Density and pressure images of both the old code and the new code are given in figures 1-4.

Figure 1. Densities Produced by the Old Code



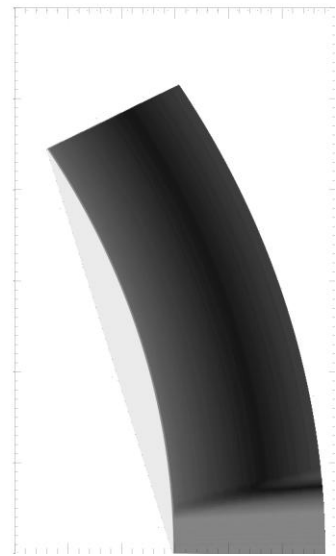
The densities produced by the old code are given with a logarithmic scaling with the lightest area as the densest. The light area is the densest and is the outer surface of the star, the medium area is the moderately dense disk, and the dark area is the very low density halo region.

Figure 2. Densities Produced by the New Code



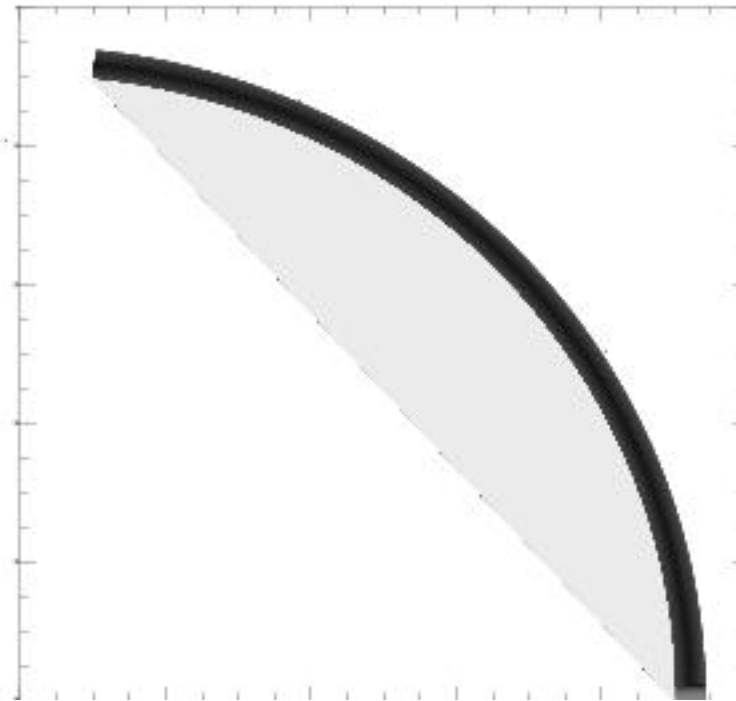
The densities produced by the new code are given with a logarithmic scaling with the lightest area as the densest. The regions are the same as those produced by the old code. Note that the disk is now thinner than what it was previously and the area being modeled is larger.

Figure 3. Pressures Produced by the Old Code



The pressures produced by the old code are given with a logarithmic scaling with the lightest area having the highest pressure.

Figure 4. Pressures Produced by the New Code



The pressures produced by the new code are given with a logarithmic scaling with the lightest area having the highest pressure.

#### 4. Conclusions and Acknowledgments

This code will help with the understanding of boundary layers and the effects that they have on the spectra of systems. The next step to be accomplished with the code is to update the old dynamical code to run the simulation on the new code that was created here. The effects seen from the new code should show further detail on what to expect from the non-magnetized dwarf novae. This code should also help in the understanding of turbulent mixing in classical novae and in understanding boundary layers in neutron stars and proto-stars. Further

updates to the code can be made to explore the effects of magnetic fields and radiative transfer.

I would like to thank my advisor Dr. Dinshaw Balsara for his help throughout the project. His help with learning Fortran and working with scientific programming was invaluable for this project and for future scientific work. Also, I would like to thank Dr. Garg and Shari Herman for organizing the REU and all of the events that went along with it.

#### REFERENCES

- Balsara, D. S. 2004, ApJS, 151, 149
- Balsara, D. S., Fisker, J. L., Godon, P., & Sion, E. 2009, ApJ, 702, 1536
- Fisker, J. L., & Balsara, D. S. 2005, ApJ, 635, L69
- Fisker, J. L., Balsara, D. S., & Burger, T. 2006, New Astronomy Reviews, 50, 509
- Inogamov, N. A., & Sunyaev, R. A. 1999, Astron. Lett., 25, 269
- Piro, A. L., & Bildsten, L. 2004, ApJ, 610, 977
- Popham, R., & Narayan, R. 1992, ApJ, 394, 225  
– 1995, ApJ, 442, 337
- Pringle, J. E. 1981, ARA&A, 19, 137
- Regev, O. 1983, A&A, 126, 146
- Warner, B. 1995, Cataclysmic Variable Stars (Cambridge: Cambridge Univ. Press)



# Identifying Particle Trajectories in CMS using the Long Barrel Geometry

Angela Galvez

2010 NSF/REU Program  
Physics Department, University of Notre Dame

Advisor: Kevin Lannon

## Abstract

The Compact Muon Solenoid (CMS) is a detector in the Large Hadron Collider (LHC), located in Geneva, Switzerland. CMS is used to study 7 TeV proton-proton collisions, which produce about 1000 particles per bunch-crossing. It consists of a pixel detector, inner and outer silicon tracker, electromagnetic and hadron calorimeters, and a 4-T superconducting solenoid. CMS has been designed to detect various particles, such as muons, electrons, pions, and kaons. An upgrade to LHC has been proposed which will increase the luminosity from  $1.0 \times 10^{34} \text{ cm}^{-2}\text{s}^{-1}$  to  $10^{35} \text{ cm}^{-2}\text{s}^{-1}$  allowing for an increased rate of particle detection. However, the upgrade to SuperLHC (SLHC) will affect the performance of CMS and a track trigger system is being considered. The trigger is separated into two levels, Level-1 and Higher-Level Trigger (HLT). Currently, tracking information is introduced into HLT. However, it is proposed that Level-1 should also use tracking information. Two other silicon tracker designs are being studied, Long barrel and a hybrid of the current tracker with Long barrel. A simulation of the Long Barrel geometry was used in this research with a focus on muon interactions with the detector. The goal of the research was to identify particle trajectories using patterns created by particle tracks using the trigger information of the silicon detectors. There are three layers of silicon sensors in the Long Barrel design at a distance of about 30, 50, and 100 cm from the beam line, with each layer consisting of two double-sided sensors, also known as a stack, separated by a distance of about 4 cm. When a particle, such as a muon, goes through one of the silicon strips, a hit is recorded. Two hits from the same stack form a stub and two adjacent stubs can form a tracklet. It is suspected that a specific pattern of stubs and tracklets will form depending on the particle that is being detected. In this study, we explore the feasibility of using silicon hit patterns to trigger on muons, electron, and photons.

## Introduction

Located at the European Organization for Nuclear Research (CERN) in Geneva, Switzerland, the Large Hadron Collider (LHC) is a proton and heavy ion accelerator that has a luminosity of  $1.0 \times 10^{34} \text{ cm}^{-2}\text{s}^{-1}$ . It is designed to produce 14 TeV proton-proton (pp) and 5.52 TeV/n lead ion (PbPb) collisions [4]. However, the LHC will only run at half energy for the next year. Various experiments are being conducted at LHC, such as ALICE, ATLAS, CMS, TOTEM, and LHCb, which address questions involving the Higgs boson, supersymmetry, CP violation, dark matter, the top quark, and extra dimensions.

Located 330 feet underground in Cessy, France, the Compact Muon Solenoid (CMS) is designed to identify particles produced from pp collisions, such as muons, electrons, neutral and charged hadrons, and photons. The 13 800 ton detector is 15 m in diameter and 21 m in length

and consists of a pixel detector, inner and outer silicon tracker, electromagnetic and hadron calorimeters, and a 4-T superconducting solenoid. Every 25 ns, proton bunches with an energy of 7 TeV collide producing about 20 collisions per bunch crossing and each bunch crossing produces about 1000 particles. As the particles radiate outward, their position and momenta are determined by the trigger and tracker systems. To further identify a particle, energy deposits in the electromagnetic calorimeter (ECAL) indicate the presence of either a photon or electron, while neutral and charged hadrons leave deposits in the hadron calorimeter (HCAL). Since muons have a much larger mass than electrons and lack the strong interaction of hadrons, they do not leave energy deposits in either ECAL or HCAL. Therefore, a muon system is located at the very edge of the detector, where other particles from the collisions are unlikely to reach [6, 7].

An upgrade to SuperLHC (SLHC) has been proposed, which will increase LHC luminosity from  $1.0 \times 10^{34} \text{ cm}^{-2}\text{s}^{-1}$  to  $10^{35} \text{ cm}^{-2}\text{s}^{-1}$ . This upgrade will result in a higher rate of particle production, thereby increasing the mass reach by 20-30%. SLHC will have a better chance of discovering physics beyond the Standard Model, such as SUSY extradimensions and the Higgs boson. However, the increase in luminosity will also increase the amount of data that CMS must process, and will therefore affect the performance of the CMS tracking and triggering systems. Due to a pileup of secondary particles and increased occupancy, a higher data readout rate will be necessary for the tracking system [7]. In addition, the higher rate of particle production in the SLHC will result in higher radiation doses and, therefore, higher radiation damage to the detectors. Some systems, especially the tracker, will have to be replaced with new hardware that can handle the higher amounts of radiation without breaking down.

## SLHC Tracker Upgrade

The tracking system is designed to provide the trajectories of charged particles using hits from silicon strips. The general idea behind charged particle detection using silicon sensors is that the collision between them creates a positively charged “hole” in the silicon where the electron originally was located. A voltage applied to the silicon causes these charges to drift through the silicon to the sensors, creating a current, which can be used to detect a signal. The tracking system consists of an inner and outer tracker, where hit rate density is  $1 \text{ MHz/mm}^2$  at  $r = 4 \text{ cm}$ ,  $60 \text{ kHz/mm}^2$  at  $r = 22 \text{ cm}$ , and  $3 \text{ kHz/mm}^2$  at  $r = 115 \text{ cm}$  [3]. The inner tracker is composed of three cylindrical layers of pixel detector modules at radii 4.4, 7.3, and 10.2 cm. At radii 20 to 116 cm, the outer tracker uses silicon micro-strip sensors and is further divided into the Tracker Inner Barrel (TIB) and Tracker Outer Barrel (TOB). TIB is composed of 4 barrel layers and TOB has 6 layers. On each side of the respective tracker, there are 2 disks for the inner and 3 disks for TIB. Tracker EndCaps (TEC), which extend to a pseudorapidity of  $|\eta| < 2.4$  and contain 9 disks, are on each side of the outer tracker [3].

An upgrade to the CMS tracking system has been proposed and two other tracker geometries are being studied, Long barrel (fig. 1) and the Hybrid structure (fig. 2), which is a combination of the current tracker and Long barrel. The Long Barrel geometry, which this research is based on, increases the number of layers of pixel detectors in the inner tracker and replaces TIB, TOB, TID, and TEC of the outer tracker with pixel sensors. The outer tracker would have three layers of pixel sensors at a distance of about 30, 50, and 100 cm from the beam line, with each layer consisting of two double-sided sensors, also known as a stack, separated by a distance of about 4 cm. Between layers 2 and 3, there are 2 shorter layers located at a radii of 65 and 80 cm and that cover the pseudorapidity range of about  $1.5 < |\eta| < 2.4$  on each side. These

additional layers allow for the removal of the disks without having to increase the lengths of the 2<sup>nd</sup> and 3<sup>rd</sup> layers. The Long Barrel design would increase the number of possible hits and therefore improve the event reconstruction capability of CMS. Another possible design for the CMS tracker would be to combine Long Barrel with the current tracker, creating the Hybrid structure. In this design, TIB and TID are replaced, and TOB are reduced to four single-sided sensors, which are 1/5 the original size [5].

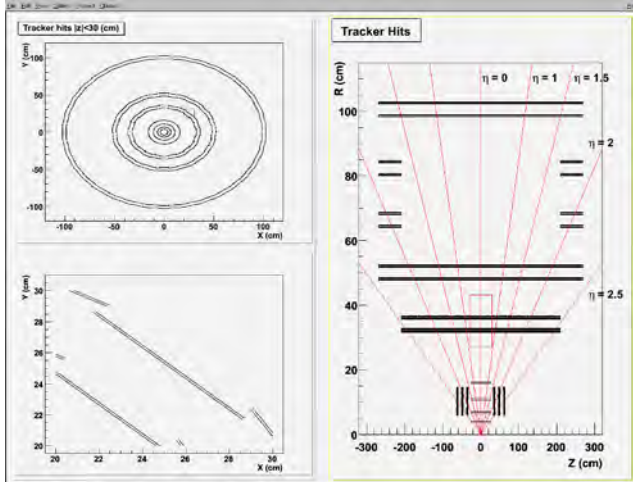


Figure 1: Long Barrel Geometry

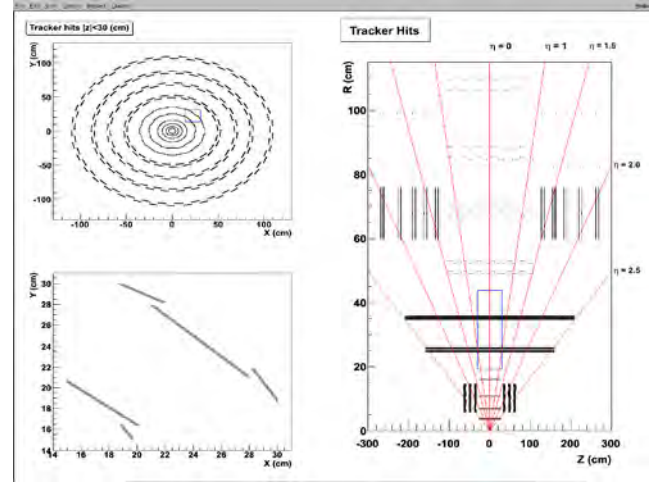


Figure 2: Hybrid Geometry

## SLHC Track Trigger

Currently, the trigger system is separated into two levels, Level-1 (L-1) and High Level Trigger (HLT). L-1 Trigger is made up of hardware in the form of FPGA technology and is designed to reduce the incoming data rate of 40 MHz to about 100 kHz. The information that passes through L-1 Trigger is further reduced to a rate of 100 Hz by HLT, which consists of software and has access to tracking information. L-1 Trigger is composed of the Calorimeter and Muon Triggers, which are further divided into local, regional, and global components. Using energy deposits, the Calorimeter Trigger determines which events should be sent to the Global Trigger. Likewise, the Muon Trigger, consisting of the Drift Tube (DT), Cathode Strip Chamber

(CSC), and Resistive Plate Chamber (RPC), searches for correlated hits based on drift time and forms track segments using position, angular direction, bunch-crossing information, timing, and number of layers hit. Once an event is sent to the Global Trigger, it is analyzed by HLT, which performs calculations, such as transverse momentum ( $P_T$ ), and filters events using tracking information [3].

A track triggering system has been proposed which would implement tracking information into the L-1 Trigger. This would allow L-1 to filter through events at a higher rate, thus, increasing the data readout rate. Since tracking information contains the particle trajectories through hits on the silicon strips, a track triggering system would identify particles through hit pattern recognition creating stubs, which could then form tracklets. By adding tracking in L-1, it will allow the system to distinguish between electrons, which form tracks, and photons, which do not. Currently, calorimeter information is used to trigger on electrons and photons. For muons, momentum is measured better in the tracker than the muon system, so we get a better momentum resolution in the trigger using the tracking information.

In the long barrel design, there are three layers, each containing two double-sided sensors. Using these sensors, also known as a stack, two hits located in the same general region and from the same stack would be recognized as a stub and two stubs from the same layer could form a tracklet. Specific stub and tracklet patterns could be used in the track trigger system to identify particles [1].

### Study of Muons, Electrons, and Photons in a Simulated Detector

In this study, we examined the behaviors of three different particles, muons, electrons, and photons, while interacting with a simulated CMS detector of long barrel geometry. Muons were determined to be a good starting point to test the Long Barrel design because they have a

larger mass and no strong interactions, which allows them to pass through the detector without producing secondary particles and maintain their initial  $P_T$ . In addition, they have a charge and would leave a track in the inner and outer tracker. Electrons were also used in this study because they are also a charged particle, but of smaller mass, and therefore will have more interaction with the detector's material. The effects of these interactions on the detector's ability to group hits into stubs and stubs into tracklets were analyzed. Since electrons can produce photons when interacting with other material, photons were also placed through the simulated detector in order to determine whether there was a correlation between tracking information involving electrons and that of photons. An ideal event should produce six stubs and form a tracklet between the stacks of layer 1, 2, or 3. A tracklet can also be formed from the outer stack of layer 1 and inner stack of layer 2. If all possible tracklets for a given track are successfully reconstructed, there should be four tracklets.

Using CMS software, each particle, with a specific amount of energy, was placed through a simulated CMS detector with long barrel geometry. From this simulation, the particle produced several hits in the tracker, which were grouped into stubs and tracklets by the program. This information was analyzed in order to determine whether the software correctly classified hits to form stubs and that the stubs were correctly grouped to form tracklets. In addition, the transverse momenta of the tracklets were plotted to further determine the particle's interaction with the detector. Each simulation involved 1000 events, where an event is a single muon radiating through the simulated detector using long barrel geometry.

The study revealed that most of the muons, with  $P_T = 50$  GeV, formed tracklets of about the same energy and produced around 4 to 6 stubs in each event (fig. 3). However, when electrons of  $P_T = 50$  GeV were put through the detector, there was a production of low  $P_T$  ( $\sim 2$

GeV) and high  $P_T$  ( $\sim 50$  GeV) tracklets (fig. 4). It is highly probable that this is the result of electrons radiating photons after interacting with the material of the detector. The photons can then convert to electron positron pairs, which register additional, lower momentum stubs and tracklets. A histogram of tracklet  $P_T$ , using photons, shows a high production of low  $P_T$  tracklets, which correlates to that of electrons (fig. 5). In addition, the number of stubs produced varied from 3 to over 6 and there were tracklets with stubs of both high and low  $P_T$ .

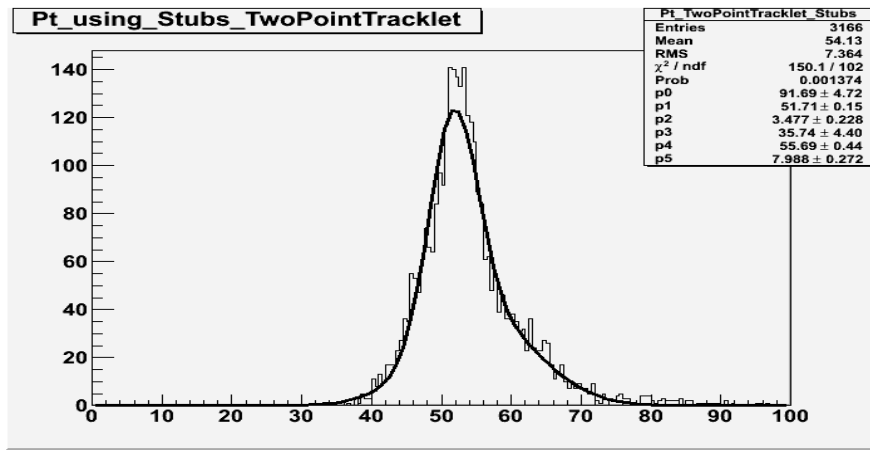


Figure 3:  $P_T$  of tracklets produced by a muon.

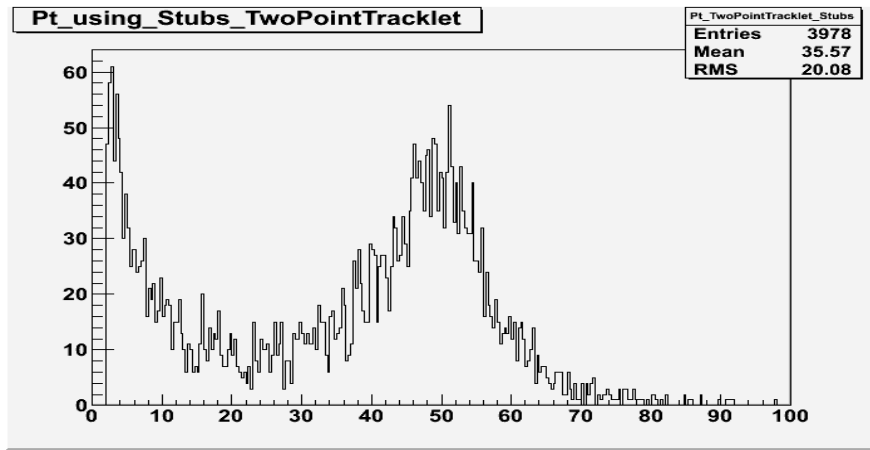


Figure 4:  $P_T$  of tracklets produced by an electron.

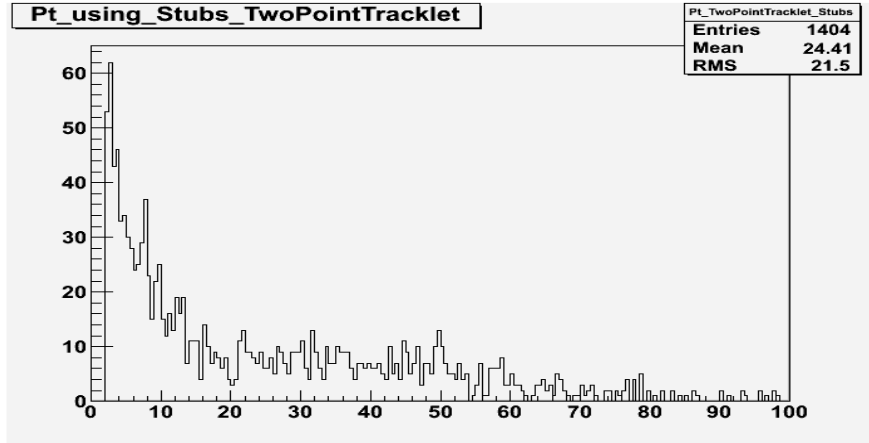


Figure 5:  $P_T$  of tracklets produced by a photon.

## Conclusion and Future Work

The luminosity upgrade to LHC will make it necessary to upgrade the tracking system of CMS. Implementing a track triggering system, where tracking information would be used in the L-1 Trigger, would allow CMS to filter through and record more data. The long barrel and Hybrid designs are alternatives to the current tracking system. In this study, the long barrel design has been tested using muons, electrons, and photons, in order to determine how effectively tracks from each particle can be reconstructed. It was found that the simulated tracker performed as expected when a muon was sent through it. However, placing an electron through the detector has shown that it will be more difficult to determine its trajectory. Due to Bremsstrahlung photon radiation, there is an increase in the number of stubs formed, which is affecting the tracker's ability to form the appropriate tracklets.

Further study of the electron trajectory using the long barrel design is necessary in order to ascertain the effectiveness of this track triggering system. Since the LHC produces about 1000 particles per bunch crossing [2], it will be essential to test the system using more than one particle per event. In addition, other particles, such as pions, kaons, and neutrons, should be

studied with this tracker. As a possible alternative to the long barrel geometry, the hybrid design of CMS will also need to be tested.

## References

- [1] *A First-Level Track Trigger Architecture for Super-CMS*. Proc. of Topical Workshop on Electronics for Particle Physics, Czech Republic, Prague. Geneva: CERN, 2007. 269-73. Print.
- [2] Amsler, C. "Mechanical Design and Material Budget of the CMS Barrel Pixel Detector." *Journal of Instrumentation* 4 (2009). <Http://iopscience.iop.org>. 12 May 2009. Web. 6 Aug. 2010. <<http://iopscience.iop.org/1748-0221/4/05/P05003>>.
- [3] Breskin, Amos, and Rudiger Voss. "The CMS Experiment at the CERN LHC." *The CERN Large Hadron Collider: Accelerator and Experiments* 2 (2009): 1-334. Print.
- [4] C. Amsler *et al.* (Particle Data Group), Physics Letters **B667**, 1 (2008) and 2009 partial update for the 2010 edition  
Cut-off date for this update was January 15, 2009.
- [5] "CERN Authentication." *Welcome to TWiki - A Web-based Collaboration Platform*. Web. 05 Aug. 2010. <<https://twiki.cern.ch/twiki/bin/view/CMS/SLHCTrackerSimuSoftTools>>.
- [6] "CMS - Detector." *CMS Experiment*. Web. 05 Aug. 2010.  
<<http://cms.web.cern.ch/cms/Detector/WhatCMS/index.html>>.
- [7] Tricomi, Alessia. "SLHC: The LHC Luminosity Upgrade." *Nuclear Instruments and Methods in Physics Research Section A: Accelerators, Spectrometers, Detectors and Associated Equipment* 596.1 (2008): 43-47. <Http://www.sciencedirect.com>. ScienceDirect, 21 Oct. 2008. Web. 5 Aug. 2010.

# **Measurement of W + Charm Production in CDF II Data**

By

Kathryn Gerbich  
2010 NSF/REU Program  
Physics Department, University of Notre Dame

Advisor: Professor Kevin Lannon  
August 6<sup>th</sup>, 2010

**Abstract::**

The Higgs boson is a theoretical force-carrying particle that physicists are currently looking for in experimental data. One setback to this search is that the Higgs signal is relatively small and can overlap with the uncertainty in the background. Describing the background is an important step in the search for the Higgs boson. The CDF experiment causes protons and antiprotons to collide at center of mass energy of 1.96 TeV using the Tevatron accelerator located at Fermi National Accelerator Lab. The background can be analyzed using data collected in run II of the CDF experiment. One interaction that produces a background signal is when a  $W$  boson and a charm quark are created.  $W +$  charm events can be found by the reconstruction of a  $W + D^0$ . The  $D^0$  is formed when the charm quark hadronizes and can be reconstructed from two charged particles that are consistent with  $K^\pm$  and  $\pi^\pm$  and which have a combined mass close to that of a  $D^0$ .  $W$  bosons can be reconstructed from an electron or muon and missing energy that comes from the respective neutrino. One important aspect of the standard model is that it is not only a descriptive model, but also a predictive one. Successful measurement of the  $D^0$  cross section will not only be useful in the search for the Higgs boson, but it will also test our theoretical calculations of how the strong and weak force work and test our current understanding of the standard model.

## **Introduction::**

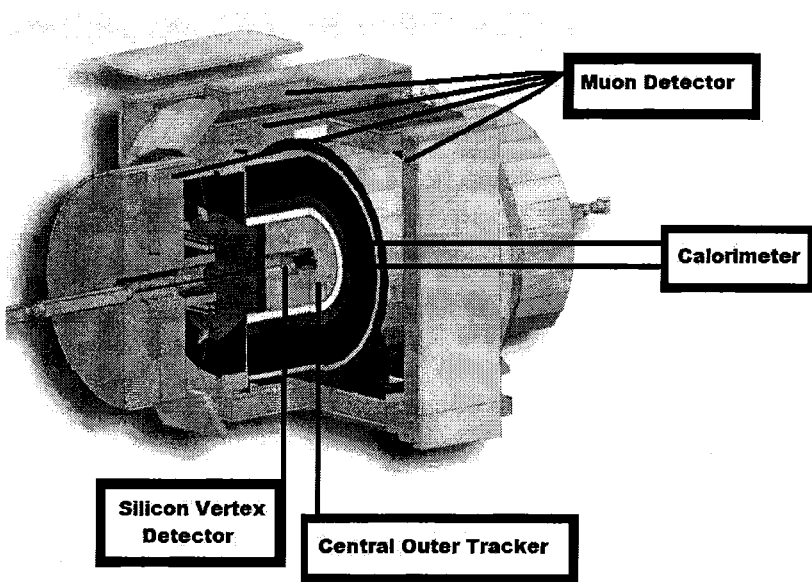
The standard model of particle physics is a description of the basic forces and elementary particles that make up our world. The standard model has not been contradicted by experimental evidence to this day. The standard model describes three forces with four force-carrying particles called bosons: photons which mediate the electromagnetic force, gluons which mediate the strong force, and  $W$  and  $Z$  bosons which mediate the weak force. The particles that make up matter are called fermions. There are two types of fermions; quarks and leptons. There are three generations of quarks. Each member of a generation has greater mass than the corresponding particles of lower generations. They are divided by their electrical charge with up, charm, and top quarks having a charge of  $+2e/3$  and down, strange, and bottom quarks having a charge of  $-e/3$ . There are also three generations of leptons; electron, muon, and tau, each with an electric charge of  $-e$ . Each of these particles has a respective neutral neutrino. Quarks interact with all of the forces while leptons do not interact with the strong force.

There is one major aspect of the standard model that has not been verified experimentally: the Higgs boson. The Higgs boson is a hypothetical force-carrying particle. One reason that the Higgs is so interesting is that it would explain the origin of mass without violating gauge invariance. However, the uncertainty in the background to Higgs production is currently too large to see the Higgs signal above it. Three of major backgrounds to the Higgs are  $W$ +bottom production,  $W$ +charm production, and  $W$ +jets production [1]. Here we focus on the interaction in which a  $W$  boson and a charm quark are created. Quarks cannot be alone, therefore when a charm quark is created, it forms a hadron made up of two or three quarks. In the case of the  $W+c$  interaction, one hadron the charm quark can form is a  $D^0$  meson. By

directly reconstructing the  $D^0$  decay, we can understand more about this interaction, which should lead to a reduction in the uncertainty on the Higgs background.

### The collider detector at Fermilab::

The Collider Detector at Fermilab (CDF) is the source of the data that we will be using to locate a signal from W+charm interactions. The CDF experiment studies protons and antiprotons collided at a center of mass energy of 1.96 TeV using the Tevatron accelerator located at Fermi National Accelerator Lab. The detector is made up of many layers that are used for particle tracking and energy measurements.



On the innermost layer is the Silicon Vertex Detector (SVX). The SVX detects charged particles with great precision for a very small radius. The next layer is the central outer tracker (COT). The COT also detects charged particles, but at a much larger distance from the primary vertex. Outside of this layer are the calorimeters. The calorimeter layer measures the energy of

particles and it can interact with both charged and neutral particles. Lastly the outside layer is a muon detector which detects the muons which are able to get through all of the other layers of the detector.

The two detectors that are the most important to the analysis of W+c interactions are the charged particle trackers. The first is the silicon vertex detector. It contains two components, the SVX II and the Intermediate Silicon Layers (ISL). It is made up of three cylindrical barrels which support 5 double sided silicon microscript detectors. As the particles pass through the detector they ionize the layers of silicon, which then sends a signal about the location of the particle. . The other tracking detector, the COT, is a gas filled chamber containing wires at high voltage. When charged particles pass by the wires that fill the chamber, they ionize the gas, and electrons from the ionization drift to the wires, causing signals that indicate the location of the particle. Both the SVX and the COT are contained in a magnetic field which allows information to be gathered about the momentum of a particle. The curvature of the trajectory of the particles in the magnet field allows physicists to calculate the momentum of each of the particles. There are two types of wires; axial and stereo. The stereo wires are positioned at an angle compared to the axial wires, allowing a measurement of the  $z$  location of the particle as well as the  $r$  and  $\phi$  direction. The silicon vertex tracker and the central outer tracker are very important in gathering information about the tracks that we will use to reconstruct the particles that we are interested in finding.

### **Analysis::**

W+c events can be found by the reconstruction of the W boson and the D<sup>0</sup> meson that is formed when the charm quark hadronizes. In order to reconstruct events that contain a W boson

we needed to look for the lepton and neutrino that result from the decay of the  $W$ . This can take the form of an electron or a muon and missing transverse energy (MET) that is used by the neutrino. The trigger consists of dedicated electronics and computer software that sorts the data, saving only a small portion of the collisions. This is beneficial because there is not enough time or space to save every event so the trigger uses a basic analysis to pick out the interesting events. This allows researchers to focus on events that have the potential to contain interesting particles or attributes. The transverse momentum ( $p_T$ ) of a particle is the momentum in the  $xy$  plane, perpendicular to the beam axis. In the case of  $W+c$  interactions the main trigger is an electron or a muon with a large transverse momentum.

Here, we use a selection identical to the one most commonly used in top quark and  $W$  analyses, as well as Higgs searching involving  $W$  bosons. We start by requiring an electron or muon trigger. This trigger looks for leptons with a  $p_T > 20\text{GeV}$  as well as a  $\text{MET} > 20\text{GeV}$ . For more information on the high momentum trigger see T. Aaltonen [2]. When looking at a plot of the missing transverse energy (MET), we saw there was a large peak at a value that was not consistent with a real  $W$  boson. We put the restriction  $\text{MET} > 20\text{ GeV}$ . This restriction was put in place in order to eliminate most of the fake  $W$ s that can be mistaken for real bosons in the trigger.

Once you have isolated events that contain  $W$  bosons you can select the events from that group that also contain  $D^0$  mesons. The  $D^0$  mesons can be identified by the reconstructing two charged particles, one of which is consistent with a  $K^\pm$  and the other with a  $\pi^\pm$ . One of the major benefits of looking at the  $D^0$  particle in this manner is that since, for this mode, the  $D^0$  decays into only two particles, which we both reconstruct, we get a full picture by looking at the kaon and pion only.

In order to see a signal at the mass of the  $D^0$ , restrictions can be placed on the kaon and pion track candidates to remove some of the background tracks. The optimal cut would be the one that makes the biggest reduction on particles that not coming from  $D^0$  decay while making only a small reduction in the real  $D^0$  decay products. There are many different track characteristics that can be used when selecting tracks that are consistent with a  $D^0$ . The track-level cuts that I placed on the data were:

- The number of axial segments > 2
- The number of stereo segments > 1
- The number of SIHits > 1

Numbers of axial and stereo segments are used in order to determine that you have enough data to analyze the track in the central outer tracker. The number of SIHits is in order to determine that you have enough data to analyze the track in the silicon vertex tracker.

- The impact parameter of the track, or the perpendicular distance of the track with respect to the reconstructed primary vertex  $D0c < 2$  cm

The  $D0c$  cut was put in place to eliminate particles that decayed very far from the primary vertex. Although the  $D^0$  has a significant lifetime, it will decay before it gets extremely far from the primary vertex. This cut will eliminate tracks that look like they could have come from a decay but do not actually come from a  $D^0$ .

- The transverse momentum  $> 1$  GeV/c.

The  $D^0$  particle moves a distance away from the primary vertex before decaying so it has a  $p_T$ . Looking at simulated data we found that most of the real  $D^0$ 's had a  $p_T$  greater than or equal to one. Therefore, by cutting the transverse momentum here you are able to get rid of a lot of background and not a lot of signal.

There are also characteristics of the pairs of tracks that can help to distinguish which pairs are more likely to have come from a real  $D^0$ .

- Opposite charge requirement

Since the  $D^0$  is a neutral particle, the sum of the charges of the decay products has to be zero. Since we know there are only two decay products we know they have to be either  $K^+$  and  $\pi^-$  or  $K^-$  and  $\pi^+$ . This will create a background signal that should resemble a low and wide Gaussian. Placing this opposite charge requirement on the tracks will help to prevent seeing tracks that are similar to but that do not actually come from a  $D^0$ .

- $\Delta R < 1.2$

$\Delta R$  is a measurement of the angle between the two tracks. You can calculate  $\Delta R$  with the equation  $\Delta R = \sqrt{\Delta\eta^2 + \Delta\varphi^2}$ . When the two tracks come from the same original particle, they are very unlikely to have a huge  $\Delta R$ . The  $D^0$  has momentum of its own; therefore it is unlikely that it will decay into two particles that are 180 degrees apart because you must conserve the original momentum of the  $D^0$ . Therefore by restricting the  $\Delta R$  to less than 1.2 in the simulated data we were able to eliminate many of the tracks that have similar characteristics to a kaon or pion track which did not come from the same particle as the other

- $\Delta z_0 < 1.0$  cm

If there was more than one collision that overlapped it is more likely that the particles could have been coming from different collisions rather than from the same particle. The intensity of the Tevatron beams means there is usually more than one p-pbar collision. The region in which the collisions can occur is a  $\pm 60$  cm window around the center of the detector in  $z$  (along beam direction). Multiple collisions are often separated in  $z$ . Tracks from the same collision should all have the same  $z_0$ , but tracks from different collisions won't. Looking at simulated D0, 1cm is a save cut.

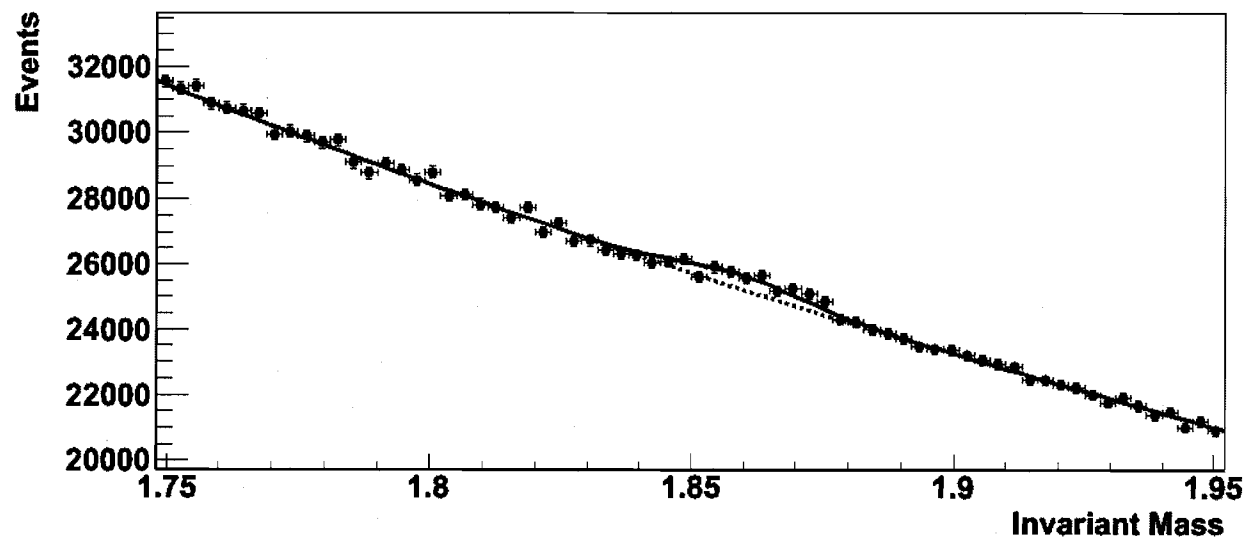
- Invariant Mass  $> 1.75 \text{ GeV}/c^2$  and invariant mass  $< 1.95 \text{ GeV}/c^2$ .

The invariant mass is the rest energy of a particle. It is calculated from the reconstructed four-momentum of the  $K$  and  $\pi$ . If the invariant mass of the  $D^0$  is consistent with the known

value for the  $D^0$  mass then we will know that we have observed real  $D^0$ 's in the data. Tracks which have a pair mass far from the known value of the  $D^0$  most likely do not come from a  $D^0$  decay. By placing a restriction on the invariant mass window we can get rid of some of the pairs of tracks that are definitely not  $D^0$  tracks. However, since we have no way to know which track is a kaon and which track is a pion we must loop over every pair of tracks twice, swapping the masses of the particles the second time through. The invariant mass window we choose was 1.7 GeV/c<sup>2</sup> to 2.0 GeV/c<sup>2</sup>. This allows the whole peak as well as background on both sides of the peak.

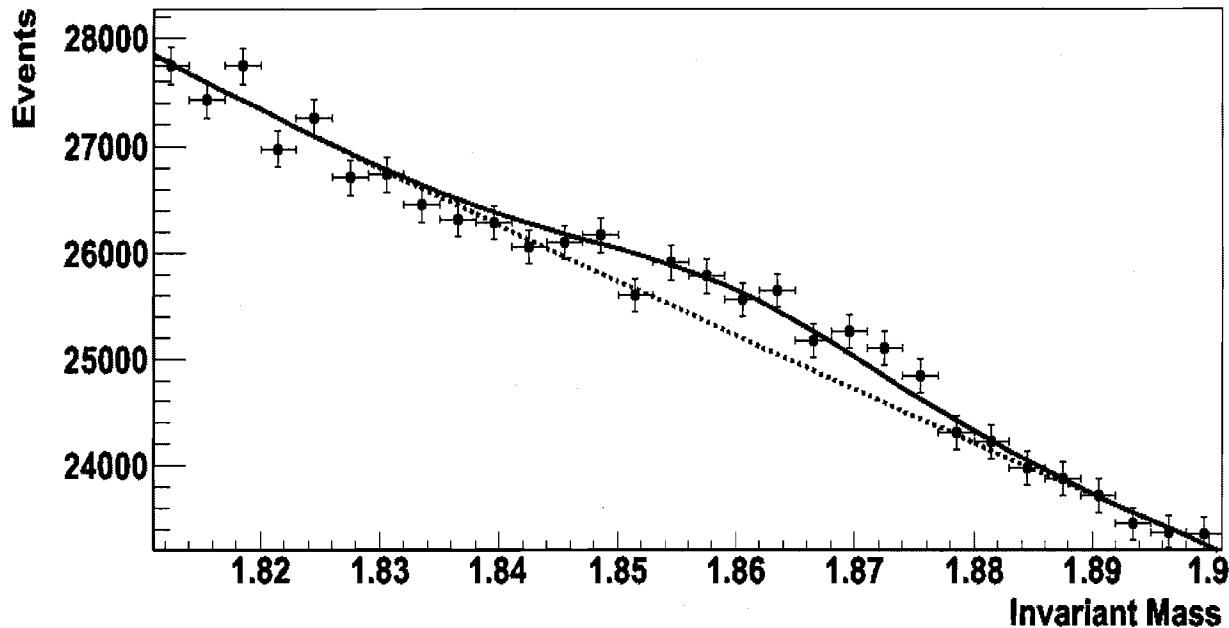
### **Conclusions::**

After making the above cuts on 5.9 fb<sup>-1</sup> of the data from the CDF run II we found that there was an indication that there might be a signal at the mass of the  $D^0$ .



This is a plot of the number of events that come from a particle of a certain invariant mass. This graph shows a slight peak around the expected value of 1.86GeV, the accepted value or the invariant mass of the  $D^0$ . The signal is not

significant enough to tell much about the D<sup>0</sup>'s except that we were able to find a peak at the right invariant mass.



This is an enlarged view of the invariant mass vs. the number of events.

In order to make a fit for this data we used a second order polynomial to describe the background curve. We added a Gaussian term to the polynomial to describe the part of the curve that is the signal. We set the mean of the Gaussian to 1.86 GeV/c<sup>2</sup>, the mass of the D<sup>0</sup> meson. We set the width of the Gaussian to  $1.2 \times 10^{-2}$ , a value that we found from looking at simulated data. Only the normalization of the Gaussian was allowed to flow.

We evaluate the quality of the fit by calculating the  $X^2$  value between the fit function and the data, where  $X^2 = \sum_{i=1}^k \left( \frac{x_i - \mu_i}{\sigma_i} \right)^2$ . In order to judge how significant the signal peak is, we compare a fit using only a polynomial function compared to the full fit with both the polynomial and the Gaussian term. We find a  $X^2$  value of 142.0 for the fit with just the polynomial and a  $X^2$  value of 102.1 with the Gaussian term included. Our  $X^2$  value should be distributed according to

a  $\chi^2$  distribution with a number of degrees of freedom equal to the number of data points (100) minus the number of fit parameters (3 for the polynomial only case and 4 for the polynomial plus Gaussian fit). We can use the appropriate  $\chi^2$  distribution to calculate the probability that, assuming the fit function is a true description of the data, that random fluctuations would generate a  $\chi^2$  value as large as or larger than what we see in our data. The probability for the polynomial only fit is 0.2% while the polynomial plus Gaussian fit has a probability of 31.6%. The higher probability for the polynomial plus Gaussian indicates that fit agrees significantly better with the data.

### **Future Plans::**

The graph of invariant mass versus the number of events suggests strongly suggests a  $D^0$  signal. However, at the current stage there is still too much background for the signal to show us any interesting characteristics about the  $D^0$ . In the future we hope to make some more requirements on the track and to isolate the signal even further. There are still several cuts that we would like to try in order to reduce the background on the signal, such as cuts on the vertex fit quality, the decay distance in the transverse plane, and angle between the  $D^0$  direction and the direction of the kaon and pion. We hope that with these cuts we can find an indisputable signal from the  $D^0$  mesons. We plan to take the observed  $D^0$  signal and calculate a production cross section for  $W+D^0$ , using simulated  $D^0$  decays to help calculate the acceptance and efficiency for  $D^0$  reconstruction.

We hope to explore is how many of the  $D^0$  mesons came from bottom quarks rather than directly from charm quarks.

Another major area of exploration would be to look at the data that we know contains a large number of real  $D^0$ 's and to flag each pair as one of the following; a real  $D^0$ , a  $D^0$  with the track masses wrong, one track from a  $D^0$  and one wrong track, or not a  $D^0$  at all. When we have this we can look at the data to see what functions would best fit the data and what cuts would work best.

### **References::**

- [1] M.Soderberg, Ph.D. Thesis, UniversityofMichigan(2006)
- [2]T. Aaltonen et al., The CDF Collaboration, Phys. Rev. Lett. 105, 012001 (2010). arXiv: 1004.3224.

# Progress toward a Monte Carlo Simulation of the Ice VI-VII Phase Transition

Christina Gower  
2010 NSF/REU PROJECT  
Physics Department  
University of Notre Dame  
Advisor: Dr. Kathie E. Newman

August 6, 2010

## **Abstract**

We study the phase transition between the self-clathrate forms of ice: Ice VI and Ice VII. This continues a project started the previous summer by REU student, Dawn King, who studied the geometry of the structural phase transition and developed a common coordinate system for the two structures. We are working to develop a phenomenological Ising-like spin model of the system to capture the energetics of the transition. The ultimate goal is to study the ice phase transition using Monte Carlo simulation methods. We have created a FORTRAN 95 program implementing the Metropolis algorithm and have tested it on the two-dimensional Ising model. We present results which show the nature of the Ising phase transition. The next step will be to extend the Ising model into an Ising-like model for describing the three-dimensional interpenetrating lattices of ice.

## 0.1 Introduction

This project is a continuation from the summer 2009, where Dawn King studied the geometrical structure of the phase transition between Ice VI and Ice VII. Ice VI and VII are known as the self-clathrate forms because their structure is composed of interpenetrating sublattices with tetrahedral bonds. Our goal is to understand the mechanism that causes Ice VI to transform into Ice VII. When the phase transition occurs, hydrogen bonds are broken and the structure is distorted. We want to model the system through Monte Carlo simulations.

## 0.2 Monte Carlo Simulations

Monte Carlo simulation was originally termed "statistical sampling" and was used to solve integrals of complicated functions Ref. [1]. This technique was particularly useful for functions of higher than three dimensions. Statistical sampling was not implemented in the field of physics until the 1930's when Fermi used it on his work in neutron diffusion. Fermi did not publish his method of statistical sampling, so the Monte Carlo simulation was not acknowledged in the physics community until Nicolas Metropolis introduced it in his paper on hard-sphere gases in 1953. It is now a widely used numerical method for calculating the partition function of systems in statistical mechanics Ref. [3]. The partition function is the sum of all of the states in a system, denoted by  $Z = \sum_{\nu} e^{-\beta E_{\nu}}$

### 0.2.1 Ising Model

The Ising Model is used in statistical mechanics as a way to mathematically explore the properties of a ferromagnet Ref. [1]. A ferromagnet is a substance that has a high level of magnetization. The model consists of two-state values, called spins, that are arranged on a

lattice or a graph. The spins represent dipoles in a ferromagnet. The Ising model is generally

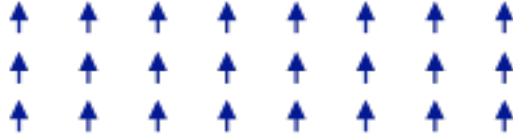


Figure 1: **The Ising Model**

arranged in one of two initial states: The  $T = 0$  state and the  $T = \infty$  state. When the temperature is zero, we know that all of the spins are oriented in the same direction. This is termed an ordered state, and is illustrated in the figure above. The initial condition of  $T = \infty$  specifies that the spins are randomly oriented. A disordered, or randomly ordered, system would consist of an equally likely chance for a given state to be either spin-up or spin-down.

The Hamiltonian for the Ising Model is given by;

$$H = -J \sum_{\langle ij \rangle} s_i s_j - B \sum_i s_i \quad (1)$$

Where  $s_i$  are the spins on the lattice, and  $J$  is the interacting energy, or coupling constant, between nearest neighbor spins. Nearest neighbors are sites on the lattice that are directly touching the selected site. The first term is the sum of the selected spin multiplied by it's nearest neighbors, and is scaled by  $-J$ . The second term in the Hamiltonian takes into account an external magnetic field, denoted by  $B$ .

For the two-dimensional Ising model, the phase transition occurs at a temperature of  $T_c \simeq 2.269J$ . Below this point, called the Critical Temperature, the orientation of the spins are completely random. Above the Critical Temperature most of the spins spontaneously align in one direction without the aid of an external magnetic field. Ref. [3]

### 0.2.2 Metropolis Algorithm

The Metropolis algorithm was the very first Monte Carlo simulation done through a computer. This algorithm simulates the random fluctuations of a dynamic system as it reaches equilibrium. This is done through the following steps:

- Create a lattice.
- Select a site on the lattice.
- Calculate the change in energy of the system.
- Generate a random number  $r$  strictly between 0 and 1
- If the random number  $r$  is less than  $e^{-\Delta E}$ , then flip the sign of the spin
- Otherwise, randomly choose the next site from nearest neighbors and repeat process

## 0.3 Our Project

Ice VI and VII are complex structures composed of interpenetrating sublattices and are further complicated by the order-disorder of the hydrogen bonds between the molecules. Before we could intelligently study the Ice VI-VII transition, we had to first explore a simpler model to understand the nuances of such a process. Our solution was to devote this summer to simplifying our model of Ice into a two-dimensional Ising Model. With this, we were able to explore the logic behind writing a program for a phase transition. We discovered that if we divided the coupling constant by  $k_b T$ , our Hamiltonian would be dimensionless and we wouldn't have to worry about the units we were working in. We plotted the energy of each state against the number of iterations. By changing the energy constant,  $J$ , we can see that

our state comes to equilibrium at specific energies. This is what we expect to happen, which tells us that our program is consistent and follows the correct logical steps.

### 0.3.1 Computer Simulation

We created the Monte Carlo simulation using FORTRAN 95. Our code was based primarily on the Metropolis algorithm. We declared a two-dimensional array, assigned the value 1 to each site in the array, then randomly chose a nearest neighbor to alter. The FORTRAN code contains an IF statement that applies periodic boundary conditions to the array. Periodic boundary conditions allow us to model an infinite square lattice, because the lattice repeats itself infinitely in all directions. Once our array is made, we call a random number  $r$  and run through iterations of the Metropolis algorithm.

### 0.3.2 Results

From our FORTRAN code, we were able to graph the energy changes in the system against the number of iterations the program went through in GNUploat. We varied our coupling constant and the number of iterations in our code in order to see the effects on the coupling constant, as well as determine the point of equilibrium of the system. We can see from the following charts that we accurately modeled a two-dimensional Ising model. By developing an Ising-like model of ice, we will be able to study the phase transition between Ice VI-VII both geometrically and through statistical mechanics. These methods will allow us to study the energetics of the transition as well as to gain a better understanding of the properties of Ice. We can see from Figure 2 that our system comes to equilibrium within the first five thousand iterations. Figure 3 shows us a more detailed description of the system coming to equilibrium.

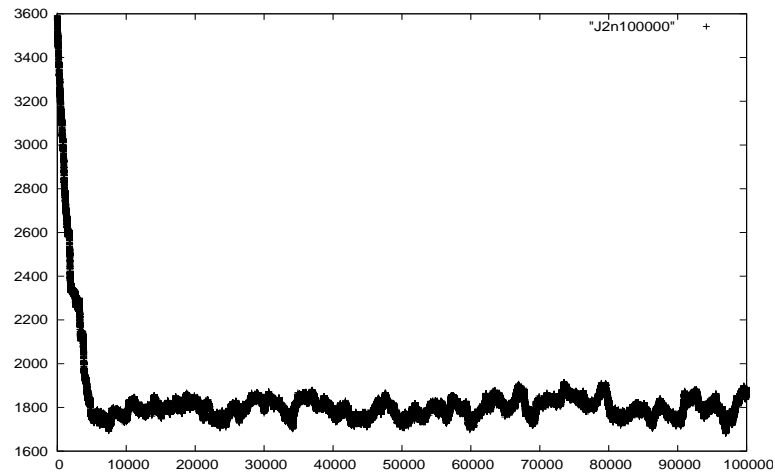


Figure 2: Energy vs. Iterations on a 30x30 Lattice where J is set at 2 with 100000 iterations.

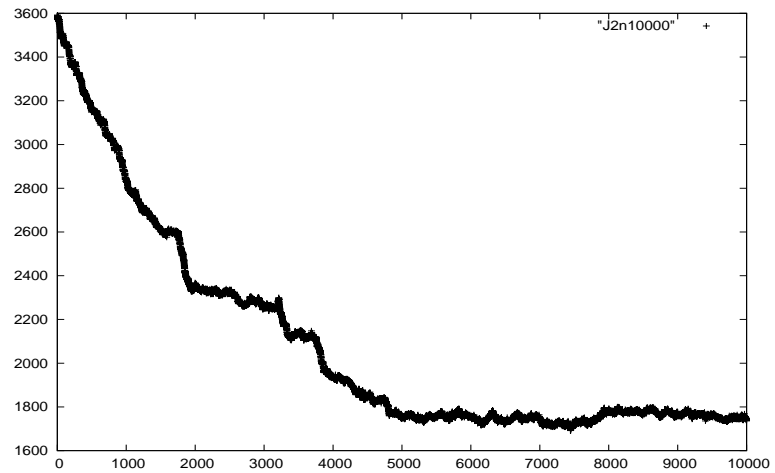


Figure 3: Energy vs. Iterations on a 30x30 Lattice where J is set at 2 with 10000 iterations.

## **0.4 Future**

We can see from our figures that our program is successful. Our hope is to expand our program in the future into three dimensions. We have already worked on the visualization of the Ice model, and now that we have developed a FORTRAN model for a two-dimensional Ising Model we can start developing an Ising-like model in three dimensions for the Ice VI-VII transition.

# Bibliography

- [1] Chandler, David. Introduction to Modern Statistical Mechanics. New York: Oxford UP, 1987. Print.
- [2] Allen, M. P., and D. J. Tildesley. Computer Simulation of Liquids. Oxford, England: Clarendon, 1987. Print.
- [3] Newman, M. E. J., and G. T. Barkema. Monte Carlo Methods in Statistical Physics. Oxford: Clarendon, 1999. Print.
- [4] Landau, David P., and K. Binder. A Guide to Monte Carlo Simulations in Statistical Physics. Cambridge: Cambridge UP, 2000. Print.



# Detecting and Suppressing Background Signal

Valerie Gray  
St. Norbert College

Advisors:

Dr. Michael Wiescher  
Freimann Professor Nuclear Physics  
University of Notre Dame

Dr. Ed Stech  
Associate Professional Specialist Nuclear Physics  
University of Notre Dame

August 5, 2010

# Chapter 1

## Introduction

Nuclear Astrophysics is the study that bridges astrophysics and nuclear physics. Specifically nuclear astrophysics is interested in stellar processes. Processes which happen in the stars are of interest as they are limited in the element that are involved and investigating them can lead to information about what happen after the big bang. [4] At Notre Dame the main interest is to understand the process that happen in stars to make heavy elements. [1]

In looking at these processes often high energy gamma rays are of interest. These events are often hard to see due to the cosmic ray background. Cosmic rays are particles that originate in outer space and come towards the earth. These particles come in at high speeds. These particles include muons, alphas, and neutrinos. Cosmic rays cause issues in many nuclear physics experiments as their signal, the background that needs to be taken out in order to make the results of an experiment conclusive. Getting an accurate measure of the background signals in any experiment can be very difficult. Above ground experiments are subject to cosmic rays, this can be avoided by going below ground, however this introduces its own background. Being able to count the rate in which the background is coming in is very important to make sure that the results that are accurate.

My project is to help reduce the background signal. By putting a piece of scintillator above the target at the end of beam line and counting the times that there are interactions between both the scintillator and the germanium detector at the beam line. The support structure for the scintillator was designed in AutoCAD. This can then be subtracted from the data that was gathered in the experiment. Using Geant 4 a simulation was made to get the efficiency of the veto.

# Chapter 2

## Equipment

### 2.1 Detector

The scintillator that is used in this experiment is plastic scintillator material, made mainly of carbon and hydrogen. When a cosmic ray goes through the scintillator the rays interact with the material causing it to scintillate or produce light. This light pulse is then received by a photomultiplier tube or PMT. Photomultiplier tubes convert the light pulses into an electric signal, this electric signal can then be inputted into the computer along with the signals the germanium detectors signal. This then can be subtracted out. [3]

The scintillator detector is a 1.93 m x 1.93 m x .102 m box. The scintillator is incased in plywood so that no light can reach it. There are four photomultiplier tubes (PMTs), one that goes on each of the small sides of the detector.

### 2.2 Supports

In order to get the scintillator above the beam line and the germanium detector, a brace needed to be made and designed. There are many different restraints that need to be met in order to meet the needs of the detector and the beam line. The support needs to be made out of a material that will not add background signals to the experiment. It also must be big enough to support the scintillator. This means that the top must be big enough so that the scintillator can rest on the top easily with out hanging over or being with out support outside. The stand needs to be tall enough so that the cold trap, a container that holds liquid nitrogen to help eliminate carbon build up on targets can get filled. Balancing this along with the solid angle that can be blocked out is very important. The solid angle is the angle that would be covered by the scintillator depending on where the beam line is, this value changes with height. Figure 3.1 shows this. In figure a, the solid angle covered is 180 degrees. In figure b, where the cold trap is added the solid angle covered is 106 degrees. In figure c, the solid angle covered is 96 degrees, and in figure d, the solid angle covered is 86 degrees. To maximize the solid angle and still be able to fill the cold trap the 6 inch clearance was chosen.

The initial design was made in AutoCAD. The support structure is 107 inches tall in total and 77 inches square. It was sent to an engineering firm to make sure that it could hold the scintillator, there were minor changes, including the number of supporting bars in the top. These were cut down the three and made thicker. The support was made out of aluminum. Figure 2.2 shows the

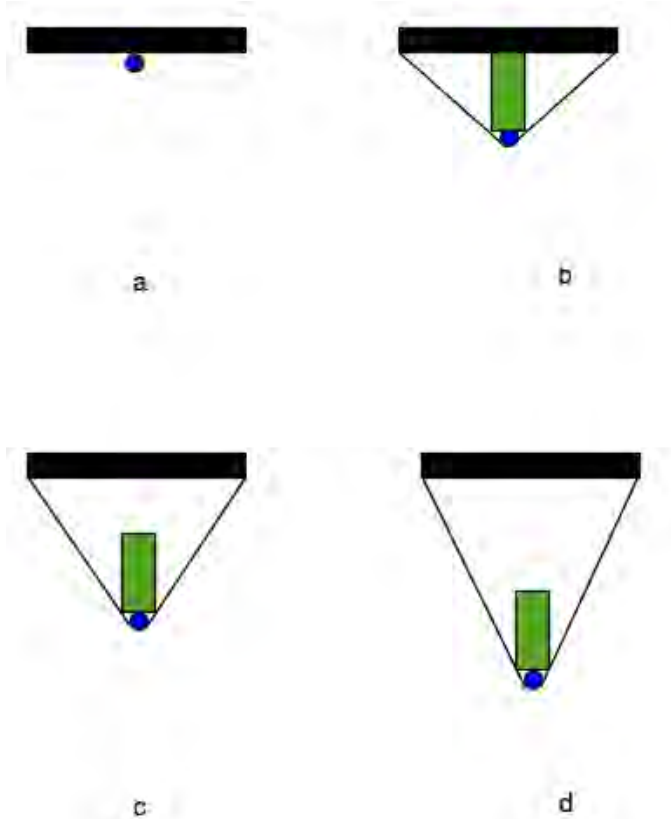


Figure 2.1: Modeling how solid angle changes with distance. In figure a, the beam line is right below the scintillator, figure b, the scintillator is right above the cold trap, figure c, the scintillator is 6 inches above the cold trap, and in figure d, the scintillator is 12 inches above the cold trap.

AutoCAD design for the stand. Figure 2.3, shows the stand with the scintillator and the germanium detector at the end of the beam line.

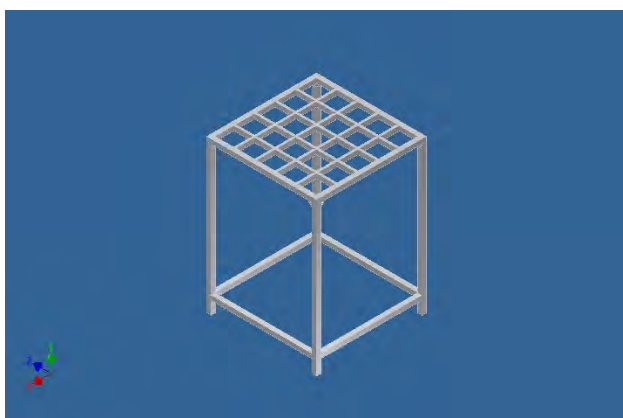


Figure 2.2: Initial design of the support structure for the scintillator.

## 2.3 Electronics

In order to set up a coincidence, the signal that comes in from a detector must be ran through electronics. The signal then is processed by a computer and is analyzed.

### 2.3.1 Scintillator Detector

For the scintillator, the four photomultiplier tubes (PMTs) signals are combined then put into a preamplifier. This takes out some of the background noise and amplifies the negative signal. This signal then goes into a timing amplifier. The timing amplifier is used put a time stamp on the signal and also to help shape the pulse. This new signal then goes to the constant fraction discrimination (CFD) where it is digitalized, this is needed so that the NIM signal that the signal is now, can be converted into a TTL signal which is what the ASPEC needs for the computer acquisition system. The now digital signal is sent to the level adaptor which has the job of converting an input signal, either NIM or TTL and outputting a signal of the opposite type. It can also invert the signal, which is what is needed here. This positive digital signal is then stretched by the Linear Gate Stretcher. Making the signal wider is needed for the ASPEC. The ASPEC requires the gated signal or the signal which is used to see if an event happens during it. The ASPEC requires the signal that is being compared to the scintillator pulse to begin  $2.0 \mu\text{s}$  after the scintillator pulse and finish  $0.5 \mu\text{s}$  before the scintillator pulse is done. This can only be achieved by lengthening the scintillator pulse with the linear gate stretcher. After the Linear Gate Stretcher the scintillator pulse goes to the ASPEC.

### 2.3.2 Germanium Detector

The germanium detector out puts a positive signal. From the detector the signal is sent to an amplifier, here the pulse is shaped and amplified. As this signal is already positive and the signal comes in very nice positive pulses. These pulses are already TTL so the ASPEC can use them, so the amplified signal can be put directly into the ASPEC. The ASPEC take the signal that comes into it from the germanium and compares it to the signal from the scintillator. The computer software then will display a spectrum of the germanium that consist of only the coincidence signals, only the anti-coincidence signals, or just the plain signal.

In order to be able to tell what has been vetoed, the computer collects two spectrum from the germanium. One of these is a plain signal, the other was set up to collect all the anti-coincidence data. Then taking the ratio of the number of events in the spectrum that show the anti-coincidence to the number of event of particle in the plain spectrum will give the percent of event that have been not been vetoed.

# Chapter 3

## Monte Carlo

The theoretical background for this set up is to make a Monte Carlo simulation. This specific simulation is made with the use of Geant 4. After the simulation is written then multiple particles from random positions moving in random directions in a range of angles are simulated so that the percentage of interactions that hit the scintillator or the germanium detector or both of the detectors. The goal being to have a count of the number of events that hit the scintillator or the germanium or both, and calculate the amount of muons vetoed, by the detector.

The simulation was written using Geant 4 is a bases for a computer program designed by the High Energy Physics community. The goal of Geant 4 is to make it easy to simulate different particle interactions that happen in high energy and nuclear physics. It has made it easy to look at particle interactions that happen and track all of the particles. [2]

Figures 3.1 and 3.2 show what the visualization is after 10 particles have been fired. The plane that the incident particles can clearly be seen in is Figure 3.4. The red lines are the tracks of the incident muons and the other color lines are the tracks for secondary particles.

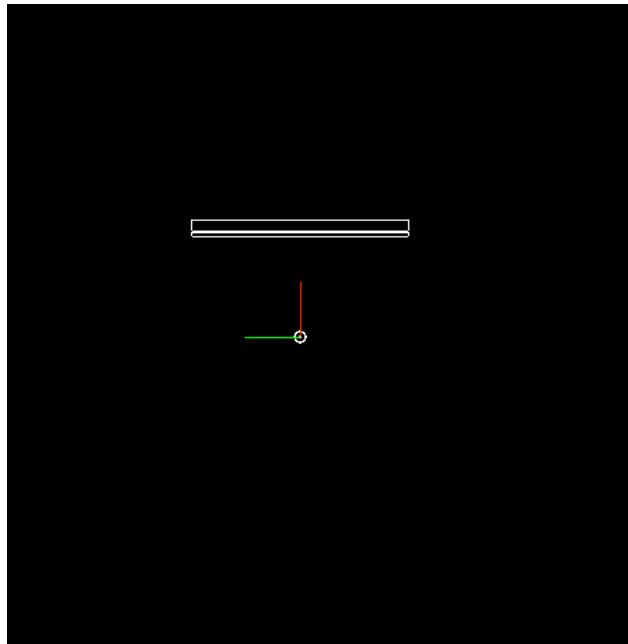


Figure 3.1: This is the visualization output for the second Monte Carlo from the side. Right below the scintillator is the conservative aluminum sheet.

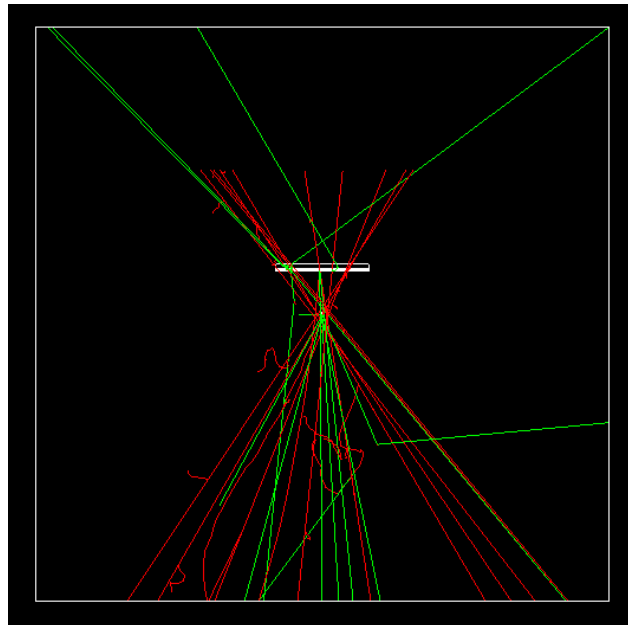


Figure 3.2: This is the visualization output from the side after 10 particles have been fired.

# Chapter 4

## Analysis

For the germanium and the sodium iodide detector, the simulation was done for multiple energies. This was because unless the energy spectrum for the muon is in the simulation there can not be a comparison between what the simulation says and what actually is seen. The table below show the percent veto for different incident muon energies.<sup>1</sup>

Incident Muon Energy	Percent Veto for Germanium	Percent Veto for Sodium Iodide
20.0 MeV	0.3%	0.1%
50.0 MeV	0.1%	0.8%
70.0 MeV	0.8%	0.8%
90.0 MeV	6.5%	6.0%
2.0 GeV	17.97%	18.81%
4.0 GeV	21.07%	19.40%
6.0 GeV	20.3%	18.9%
8.0 GeV	20.0%	19.8%
10.0 GeV	20.0%	26.9%
12.0 GeV	21.9%	19.7%
14.0 GeV	20.3%	20.6%
16.0 GeV	20.6%	19.3%
18.0 GeV	18.7%	20.5%
20.0 GeV	20.3%	20.3%
22.0 GeV	20.5%	20.8%

One can see that somewhere between 2.0 GeV and 4.0 GeV the percentage of muons vetoed is about the same for the germanium. With the sodium iodide crystal somewhere between 90.0 MeV and 2.0 GeV the percent of muons vetoed becomes approximately constant.

The veto for the whole set up was found by taking the ratio of counts in the anti-conicidence spectrum and plain spectrum of the detector, and subtracting that from one. Different regions of the energy range of the output spectrum was looked at. This allowed for a total spectrum veto, and then different areas. This shows the difference in what is vetoed at different energies. For the germanium crystal it is important to know how the position of detector changes the amount of

---

<sup>1</sup>The number of incident particle for this simulation was 100,000

muons vetoed. This was done by taking data twice, once when the detector is as close as it can be to the target and once when it is as far away from the target as it could be. For the sodium iodide detector two different set ups were also used. One of the set ups was for with the sodium iodide detector in the center of the scintillator down 1 m, and the other was with the sodium iodide detector right below the center of the scintillator. These two test showed the difference that solid angle covered makes in vetoing muons.

# Chapter 5

## Conclusion

Using the sodium iodine crystal center 1 meter below the scintillator, it was found that in the 3 to 8 MeV range of the output  $17.51 \pm 0.06\%$  of background muons were blocked. In the 8 to 19.5 MeV range of the output  $43.13 \pm 0.28\%$  of background muons are blocked. When moving the sodium iodide detector right below the middle of the scintillator, it was found that in the 3 to 8 MeV range of the output  $8.37 \pm 0.03\%$  of background muons were blocked. The drop in the percentage blocked is most likely due to more of the muons that would deposit energy into the detector are more likely to get stopped by the scintillator, and not reach the detector. As more solid angle is covered in this arrangement is greater and it is harder for the muons to reach the detector without going through the scintillator. For the 8 to 19.5 MeV range of the output  $73.14 \pm 0.68\%$  of background muons are blocked. This demonstrates the effect that the solid angle covered can effect a result.

For the germanium crystal looking at the percent veto at the two extremes of where it can be located was of interest. For the 2.3 to 17.1 MeV output range, the percent veto was  $45.3 \pm 1.2\%$  when as close to the target as the germanium detector could get, and  $48.0 \pm 0.2\%$  when as far from the target as the germanium detector could get. This was very good as knowing the veto is a good no matter where it is very useful information to have. Testing out the veto with high energy gamma rays coming into the target is a future test that will be done.

As there is no direct correlation between the muons spectrum energy and the energy spectrum that is outputted from the computer. A direct comparison between the simulation and the actual data without putting in the energy spectrum into the simulation. cannot happen. Putting the energy spectrum into the simulation, will allow this comparison to be made. This will be in the next step of the project.

# Bibliography

- [1] "Experimental Research, Institute for Structure and Nuclear Astrophysics (ISNAP), University of Notre Dame." *University of Notre Dame*. Web. 18 July 2010. <[http://www.nd.edu/~ns1/html/research\\_exp.html](http://www.nd.edu/~ns1/html/research_exp.html)>.
- [2] "Introduction to Geant4." *Geant4: A Toolkit for the Simulation of the Passage of Particles through Matter*. Web. 04 July 2010.<<http://geant4.web.cern.ch/geant4/UserDocumentation/Welcome/IntroductionToGeant4/html/introductionToGeant4.html#1>>.
- [3] Leo, William R. *Techniques for Nuclear and Particle Physics Experiments: A How-to Approach*. 2nd ed. Berlin: Springer-Verlag, 1994. Print.
- [4] "Science, JINA." *JINA, Joint Institute for Nuclear Astrophysics*. Web. 18 July 2010.<<http://www.jinaweb.org/html/science.html>>.



# Reconstruction of Semileptonic $K^0$ Decays at BaBar

Henry HINNEFELD

2010 NSF/REU Program

Physics Department, University of Notre Dame

Advisor: Dr. John LoSECCO

## Abstract

The oscillations observed in a pion composed of a superposition of energy states can provide a valuable tool with which to examine recoiling particles produced along with the pion in a two body decay. By characterizing these oscillation in the  $D^+ \rightarrow \pi^+ \bar{K}^0$  decay we develop a technique that can be applied to other similar decays. The neutral kaons produced in the  $D^+ \rightarrow \pi^+ \bar{K}^0$  decay are generated in flavor eigenstates due to their production via the weak force. Kaon flavor eigenstates differ from kaon mass eigenstates so the  $K^0$  can be equally represented as a superposition of mass eigenstates, labelled  $K_S^0$  and  $K_L^0$ . Conservation of energy and momentum require that the recoiling  $\pi$  also be in an entangled superposition of energy states. The  $K^0$  flavor can be determined by measuring the lepton charge in a  $K_L^0 \rightarrow \pi^- l^+ \nu_l$  decay. A central difficulty with this method is the accurate reconstruction of  $K_L^0$ s in experimental data without the missing information carried off by the (undetected) neutrino. Using data generated at the Stanford Linear Accelerator (SLAC) and software created as part of the BaBar experiment I developed a set of kinematic, geometric, and statistical filters that extract lists of  $K_L^0$  candidates from experimental data. The cuts were first developed by examining simulated Monte Carlo data, and were later refined by examining trends in data from the  $K_L^0 \rightarrow \pi^+ \pi^- \pi^0$  decay. In this  $3\pi$  decay the mass, momentum, and decay radius of the original  $K_L^0$  can be fully reconstructed. The distributions of these variables were compared between the  $3\pi$  and semileptonic decay modes for agreement. In the future the  $K_L^0$ s detected by these filters can be used to find  $D^+ \rightarrow \pi^+ \bar{K}^0$  decays. By measuring the oscillation of the pions associated with these decays we hope to improve the characterization of other particles involved in similar decays, such as  $B^+ \rightarrow \pi^+ \bar{D}^0$ .

## 1 Introduction

This paper presents the results of efforts to extract a usable sample of flavor-tagged kaons from experimental data collected as part of the BaBar experiment at SLAC. These flavor-tagged kaons can be used to characterize the pions in the two body decay

$$D^+ \rightarrow \pi^+ \bar{K}^0. \quad (1)$$

This pion characterization can then be applied to other similar two body decays to learn more about the recoiling particle produced along with the pion. Additionally, the kaon sample produced by the filters developed here can be used to check other kaon analyses performed at BaBar.

In this analysis the semileptonic decay mode of the long lived kaon mass eigenstate was examined along with its charge conjugate:

$$\begin{aligned} K_L^0 &\rightarrow \pi^- l^+ \bar{\nu}_l \\ K_L^0 &\rightarrow \pi^+ l^- \nu_l. \end{aligned} \quad (2)$$

This decay mode was chosen because the charge of the pion identifies the flavor of the decaying kaon.

The information carried by the undetected neutrino makes accurate reconstruction of the original kaon difficult, so several filters were developed to refine the sample of kaons extracted from data. These filters were based on geometric, kinematic, and statistical constraints on the decaying kaon and were developed by examining Monte Carlo simulations.

## 2 Theory

The decay in Equation 1 proceeds via the weak force which causes the resulting  $\overline{K^0}$  to be produced in a flavor eigenstate. Kaon mass eigenstates differ from kaon flavor eigenstates so the  $\overline{K^0}$  can equally be represented as a superposition of mass eigenstates [1]:

$$|\overline{K^0}\rangle = \frac{1}{\sqrt{2}} (|K_S^0\rangle - |K_L^0\rangle). \quad (3)$$

By conservation of energy and momentum the pion produced along with the kaon must be in an entangled superposition of energy states. The energy of the recoiling pion can be determined using relativistic kinematics and is given by [2]:

$$E_\pi = \frac{m_D^2 + m_\pi^2 - m_K^2}{2m_D} \quad (4)$$

One can therefore write the final pion-kaon state as [2]:

$$|\pi(t)\overline{K^0}\rangle = \frac{1}{\sqrt{2}} e^{-(\Gamma/2+iE_1)t} |\pi(0)\rangle |K_S^0\rangle - \frac{1}{\sqrt{2}} e^{-(\Gamma/2+iE_2)t} |\pi(0)\rangle |K_L^0\rangle \quad (5)$$

where  $\Gamma$  is the pion width and  $E_1$  and  $E_2$  are the pion energies associated with the two mass eigenstates. The mass eigenstates can also be expressed as a superposition of the flavor eigenstates. In this case the final pion-kaon state takes the form:

$$\begin{aligned} |\pi(t)\overline{K^0}\rangle &= \frac{1}{2} \left( e^{-(\Gamma/2+iE_1)t} - e^{-(\Gamma/2+iE_2)t} \right) |\pi(0)\rangle |K^0\rangle \\ &\quad + \frac{1}{2} \left( e^{-(\Gamma/2+iE_1)t} + e^{-(\Gamma/2+iE_2)t} \right) |\pi(0)\rangle |\overline{K^0}\rangle \end{aligned} \quad (6)$$

By performing a measurement that determines the flavor of the kaon one can project out a pion in a superposition of energy states:

$$|\pi(t)\rangle = e^{-\Gamma t/2} \frac{1}{2} (e^{-iE_1 t} \pm e^{-iE_2 t}) |\pi(0)\rangle \quad (7)$$

In this case the pion's decay will be modulated by  $1 \pm \cos\left(\frac{\Delta m_K^2}{2m_D} t\right)$  [2]. Since this oscillation is dependent on the mass difference of the two mass eigenstates it can be used to determine this quantity for other similar decays.

### 3 Methods

The extraction of kaon particle candidates was a two step process. First, pre-existing lists of pion and lepton candidates were passed through a reconstruction program developed as part of BaBar. This program took as input a desired decay mode, lists of possible daughter particle candidates, a fitting algorithm, and any constraints that the fitting algorithm could apply to the reconstruction of the parent particle candidate. It returned a set of parent particle candidates that passed the constraints. In this analysis it was only possible to constrain the fitting geometrically; the tracks of the two daughter particle candidates were required to pass near each other. Constraining the fit by the mass of the reconstructed candidate was impossible because of the missing neutrino. This first list of possible kaon candidates contained many falsely identified kaons due to falsely identified daughter particle candidates and the weak constraint imposed by the fitting algorithm.

In the second step the list of reconstructed particle candidates from the fitting algorithm was passed through a series of cuts to filter out candidates that were unlikely to have come from the desired decay mode. These cuts were developed by examining trends in simulated Monte Carlo data. In the case of Monte Carlo data it was possible to test whether a reconstructed particle candidate corresponded to an actual particle track in the simulation. By comparing the unfiltered candidates to those candidates that agreed with the simulated data it was possible to determine which variables were effective in selecting actual kaon candidates and over what range those variables should be filtered. Two variables proved effective in filtering out false candidates: the  $\chi^2$  value of the fit and the radius at which the kaon decay occurred. A third cut based on relativistic kinematics was also developed.

### 3.1 $\chi^2$ Probability Cut

The  $\chi^2$  test is a statistical tool commonly used to evaluate hypotheses. It is calculated according to [3]:

$$\chi^2 = \sum_{i=1}^k \frac{(x_i - \mu)^2}{\sigma^2} \quad (8)$$

where  $x_i$  are the measured values,  $\mu$  is the expected mean of the quantity being measured, and  $\sigma$  is the standard deviation about that mean. For a given number of degrees of freedom the  $\chi^2$  value can be used to determine the probability, called the P-value, of observing a test statistic at least as extreme as the measured value.

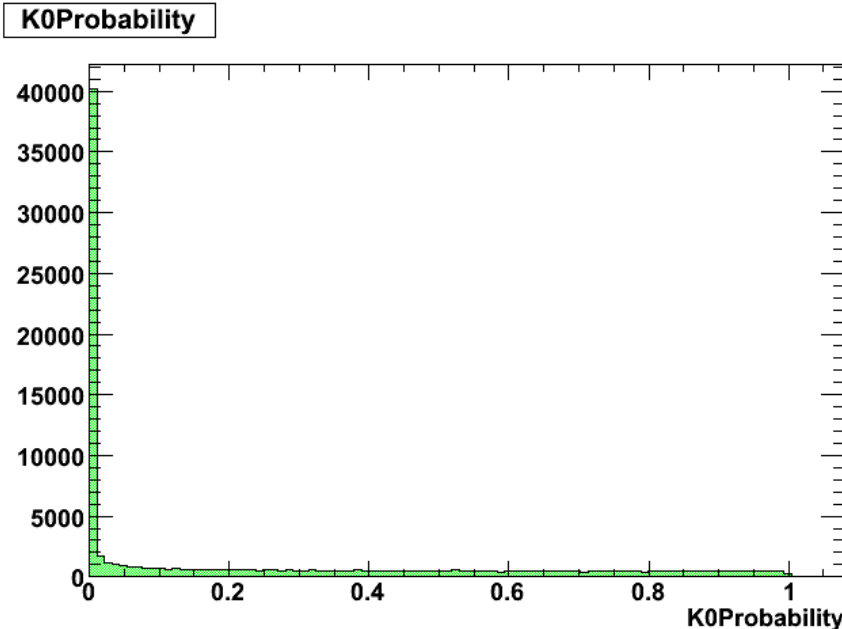


Figure 1:  $\chi^2$  probability of the kaon reconstruction

The reconstruction program that created the first, rough list of kaon particle candidates calculated a  $\chi^2$  value for the vertexing of the two daughter candidates. This value describes the errors related to the observed tracks of the particle candidates and the tracks they would have followed if they had come from the same vertex. The reconstruction program also provided the degrees of freedom associated with the  $\chi^2$  value. Combining these two values produced the  $\chi^2$  probability for each particle candidate. The distribution is plotted in Figure 1. For a sample of particle candidates containing only valid kaon candidates with a normal distribution of errors the probability distribution would be perfectly flat [4].

By accepting only particle candidates with  $\chi^2$  probabilities greater than 0.03 a large percentage of the specious candidates were removed.

### 3.2 Decay Radius Cut

The second filter applied to the reconstructed particle candidates made a cut based on particle lifetime as measured by the distance from the decay vertex to the origin of the detector. The long lived kaon mass eigenstate ( $K_L^0$ ) has a mean lifetime of  $5.116 \pm 0.020 \times 10^{-8}s$ . This is significantly longer than the  $8.953 \pm 0.0005 \times 10^{-11}s$  lifetime of the short lived kaon mass eigenstate ( $K_S^0$ ), as well as the lifetimes of several other particles that contributed to the background in the reconstruction kaon candidate list.

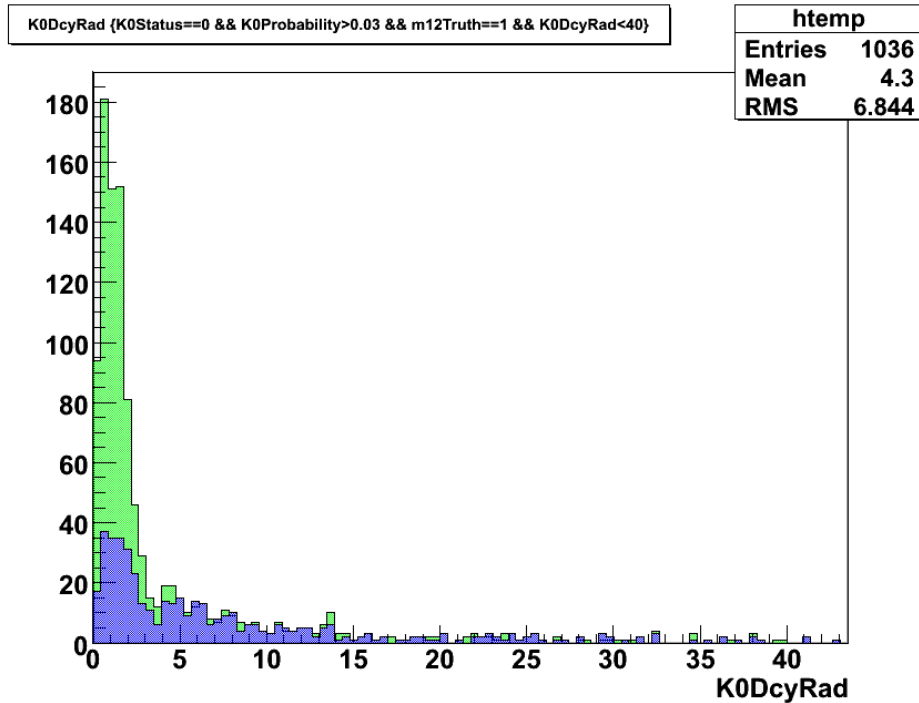


Figure 2: Decay radii of reconstructed particle candidates. Candidates matching Monte Carlo simulated tracks are shown in blue.

Figure 2 shows the distribution of decay radii. Reconstructed particle candidates that matched tracks in the Monte Carlo simulated data are shown in blue, while all of the reconstructed candidates that passed the  $\chi^2$  cut as well as the constraints imposed by the fitter are shown in Green. From the figure it is apparent that considering only candidates that decay beyond 4cm greatly improves the

purity of the list of particle candidates. Note that the short lived  $K_S^0$ s would decay too quickly to leave a track in the detector, and would therefore fail the Monte Carlo matching test. However this is not a problem because it is only the long lived  $K_L^0$ s that decay semileptonically. Also of interest in Figure 2 is the overall distribution which closely resembles the sum of two exponential decays with differing decay constants. A sample composed of a combination of two particles with different lifetimes would display the same distribution, lending credibility to the identification of the reconstructed particle candidates as a combination of  $K_L^0$ s and  $K_S^0$ s.

### 3.3 Relativistic Mass Cut

The final cut applied to the reconstructed particle candidates was based on the mass of the kaon. While it is impossible to fully determine the mass of a kaon reconstructed from a semileptonic decay because of the missing neutrino, it is possible to impose limits using relativistic kinematics. By conservation of four-momentum:

$$\begin{aligned} (\mathbf{p}_K - \mathbf{p}_\nu)^2 &= (\mathbf{p}_\pi + \mathbf{p}_l)^2 \\ M_K^2 - 2M_K E_\nu &= (\mathbf{p}_\pi + \mathbf{p}_l)^2 \\ E_\nu &= \frac{M_K^2 - (\mathbf{p}_\pi + \mathbf{p}_l)^2}{2M_K}. \end{aligned} \tag{9}$$

The four-momenta of the pion and lepton are measured by the detector so the energy of the neutrino can be determined. The complete four-momentum of the neutrino is unknown because the direction of travel is not measured and cannot be determined from measured quantities. However knowing the neutrino energy is sufficient to calculate the invariant mass of the pion and lepton:

$$\begin{aligned} m_{\pi l}^2 &= (\mathbf{P}_{total} - \mathbf{p}_\nu)^2 \\ &= M_K^2 + m_\nu^2 - 2M_K E_\nu. \end{aligned} \tag{10}$$

The mass of the kaon provides an upper bound at 497.614 MeV and the sum of the rest masses of the daughter particles provides a lower bound at 140.081 MeV for an electron and 245.228 MeV for a muon.

Figure 3 shows the mass distribution of candidates that pass this relativistic mass cut as well as the

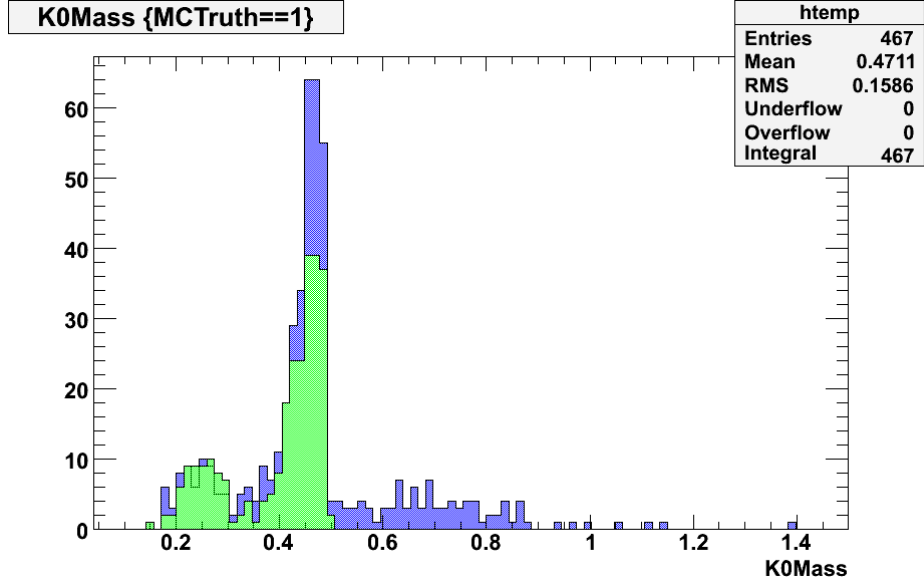


Figure 3: Masses of reconstructed particle candidates. Candidates matching Monte Carlo simulated tracks are shown in blue. Candidates passing all 3 filters are shown in green.

two previous cuts. The peak spread below 500 MeV corresponds to the kaon rest mass. The smaller peak near 250 MeV could be the result of a pion from a multi-pion decay misidentified as a muon.

## 4 Discussion

To test the efficacy of these filters a list of  $K_L^0$  particle candidates was prepared using the filters. A second list of particle candidates was created consisting of  $K_L^0$ s reconstructed from the  $3\pi$  decay mode. The  $3\pi$  mode is fully reconstructable, allowing the fitting algorithm of the original reconstruction program to impose much more strenuous constraints. Figure 4 shows a comparison of the decay radii of the particles in each list. The close agreement strongly implies that the filters are effectively extracting the  $K_L^0$ s from the data.

These filters can also be adapted to specific needs. Note that in Figure 3 some particle candidates matched tracks in the Monte Carlo simulated data but failed the cuts imposed by the three filters described above. This is a result of the inevitable tradeoff between selection efficiency and sample purity. The  $\chi^2$  probability and decay radius cuts both filter out a small number of valid candidates, but the far greater number of false candidates removed by these cuts makes them worthwhile. In the

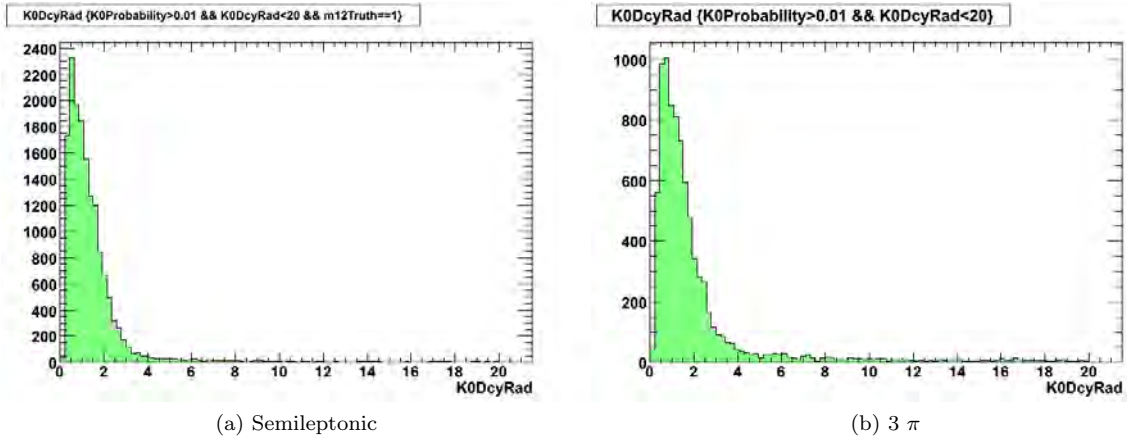


Figure 4: Comparison of decay radii for the semileptonic and  $3\pi$  decay modes

future the levels at which the filters are applied could be modified to suit the needs of any particular analysis.

## 5 Conclusion

During the course of this project three filters were developed that extracted lists of  $K_L^0$  candidates reconstructed from semileptonic decays when applied to simulated Monte Carlo data. The filters removed particle candidates that had a  $\chi^2$  probability less than 0.03, candidates that decayed within 4cm of the origin, and candidates whose observed invariant masses were greater than the mass of the  $K_L^0$  or less than the sum of the pion and lepton masses. When compared to candidates from fully reconstructable  $3\pi$  decays the semileptonic  $K_L^0$  candidates showed excellent agreement. In the future these semileptonic  $K_L^0$ s can be used to study the oscillation of entangled pions produced in two body decays.

## References

- [1] David Griffiths. *Introduction to Elementary Particle Physics*. New York: John Wiley & Sons, Inc., 1987
- [2] John M. LoSecco, *Pion Oscillations*, arXiv:0912.0900v1

[3] D. Montgomery, G. Runger. Applied Statistics & Probability for Engineers 3rd ed. New York: John Wiley & Sons, Inc., 2003

[4] John M LoSecco, *Private communication.*

# Determining the Existence of a Radiation Amplitude Zero in $W\gamma$ Events

Alexander W. Kocurek

2010 NSF/REU Program  
Physics Department, University of Notre Dame

Advisor: Professor Michael D. Hildreth

## Abstract

The Standard Model of Particle Physics currently makes very specific predictions regarding the behavior of Wy-coupling events. In particular,  $q\bar{q}' \rightarrow W\gamma$  processes are expected to produce a Radiation Amplitude Zero between the W boson and the incoming quarks due to interference patterns between the particles. This means that a zero in the angular distribution of the W boson is expected to occur, and current Wy theory tells us that the precise angle that this zero occurs can be found based on the charge of the quark as well as the sign of the W boson that is originally produced. Determining if these results are consistent with the experimental data is a good way check the accuracy of the Standard Model and a good test to see if the Standard Model needs to be revised or not. Such results can be tested using data regarding these kinds of processes that was collected from the Tevatron at Fermilab. A crucial part of this analysis is the transverse energy distributions of the particles in this event, which can be skewed by background events that might ostensibly appear similar to the events that are trying to measured and analyzed. Although this analysis was carried out by the DØ project in the past, technology has improved since the last measurements were taken, so it is necessary to reexamine this analysis to have a more accurate, up-to-date description of  $q\bar{q}' \rightarrow W\gamma$  processes. Current Wy theory is mentioned as well as some further complications that arise when attempting to carry out this analysis more thoroughly.

## The Standard Model

The Standard Model of particle physics is a misfit in the history of physics; it is quite a handy tool, but physicists want nothing more than to replace it. Although the Standard Model is logically consistent, and is capable of making very accurate experimental predictions in the field of high-energy particle physics, it carries with it a number of oddities that make some physicists

shiver. I do not wish to go into great detail on this matter, but some of the anomalous features of the Standard Model include an exclusion of gravity in the theoretical structure, an inability to properly explain neutrino oscillations, several abstract puzzles (e.g. the hierarchy problem, the strong CP problem, etc.), and most importantly the unaesthetic nature of model itself [1]. For this reason, particle physicists have been searching long and hard for clues as to how, where, and why the Standard Model might collapse, as well as what alternatives might supersede the Standard Model in the future.

Currently, the Standard Model has two kinds of particles: fermions (half-integral spin particles) and bosons (integral spin particles). Of the fermions, there are six quarks (up, down, charm, strange, top, bottom), and six leptons (electron, muon, tau, and their corresponding neutrinos). Of the bosons, there are photons (electromagnetic interactions), gluons (strong interactions),  $W^+$ ,  $W^-$ , and Z bosons (weak interactions). The topic of this paper will mainly concern W bosons, and their production from collisions produced at the Tevatron at Fermilab.

### Wy Theory

When a proton and antiproton collide with each other, there are a variety of things that could happen. Among them, we are interested in processes where a W boson and a photon are produced, i.e. processes of the form  $q\bar{q}' \rightarrow W\gamma$ . This process mainly occurs when either an up quark collides with a down antiquark or when a down quark collides with an up antiquark. The three most important processes where this occurs are represented by the Feynman diagrams in Figure 1. These three different processes can destructively interfere with one another, creating a zero in the angular distribution of the W boson relative to the initial beam line [2]. This zero is called the Radiation Amplitude Zero (RAZ). According to the Standard Model, the RAZ should occur at an angle  $\theta^*$ , such that:

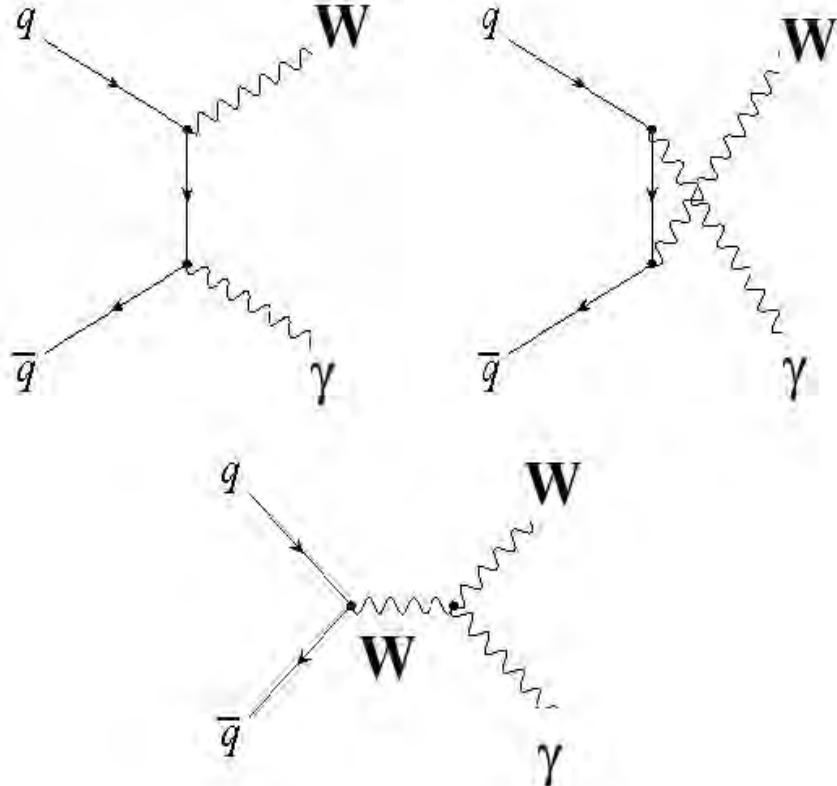


**Figure 1:** Feynman diagrams for  $W\gamma$  Coupling. See [4].

$$(1) \quad \cos(\theta^*) = (1 \mp 2q_i)$$

where  $q_i$  is the charge of the incoming quark (as opposed to that of the antiquark) in units of  $e$ , the fundamental unit of charge [3]. The sign of the  $\mp$  is (inversely) determined by the sign of the  $W$  boson produced (plus for  $W^-$  and minus for  $W^+$ ) [4]. From this, it can be readily verified<sup>1</sup> that (1) becomes  $\cos(\theta^*) = \mp 1/3$ , where again the minus sign denotes the  $W^+$  boson and the plus sign denotes the  $W^-$  boson.

As it turns out, the RAZ is not the easiest thing to measure directly. Shortly after the  $W$  boson is produced, it decays into a lepton (often either an electron or a muon) and its corresponding neutrino. These will then scatter off at their own angle, so it's not immediately

---

<sup>1</sup> A  $W^+$  boson can only be made from a up quark ( $+2/3 e$ ) and a  $W^-$  boson can only be made from a down quark ( $-1/3 e$ ), so with the sign conventions provided, both values should have a magnitude of  $1/3$ .

clear that one can deduce the angular distribution of the W boson (and thus the existence of a RAZ) from the angular distribution of the lepton produced. Thankfully, the existence of a RAZ in this process will make itself apparent in the charge-signed rapidity difference (CSRD) between the generated lepton and the photon, which is a quantity that can be measured at hadron colliders like the Tevatron at Fermilab. Thus, even though we cannot measure the angle at which the W boson scatters directly, we can measure it indirectly through a concomitant process.

It might be beneficial to briefly describe what rapidity is in greater detail. Rapidity is defined like a kind of relativistically corrected velocity. It is not quite the same as velocity (since it is unitless), but it is a quantity related to a particle's velocity that is mathematically designed so that it can add like classical velocities normally do without bound. More formally, rapidity is defined as follows:

$$(2) \quad y \equiv \tanh^{-1}(\beta) = \frac{1}{2} \ln \left( \frac{1 + \beta}{1 - \beta} \right)$$

where  $\beta = v/c$ , which is the beta-factor in special relativity [5, 6]. It turns out that the sign of the rapidity will depend on the W boson that is produced amongst the colliding quarks (i.e. on whether the W boson is a  $W^+$  or a  $W^-$ ), hence the “signed” part of CSRD. The “charge” part comes from the dependence upon the charge of the incoming quark that produces the W boson.<sup>2</sup>

Rapidity is an interesting quantity because, though it adds like classical velocities would add, it only does so for the parallel components of the velocity (relative to a given direction). Thus, one can (and actually, more often does) use rapidity as a kind of measurement of the angle

<sup>2</sup> This is, of course, slightly redundant for this process since the charge of the colliding quarks would determine the sign of the W boson anyway.

from the beam line produced in a hadron collider. Measuring such a quantity isn't technically straightforward, but often particle physicists will substitute rapidity for a similar, approximate notion of pseudorapidity. If one ignores masses, then the pseudorapidity turns out to be equivalent to the rapidity [7]. So measuring (or at least approximating) the photon-lepton CSRD can be done at the Tevatron, and this makes it possible to search for a RAZ in  $q\bar{q}' \rightarrow W\gamma$  processes.

How exactly can one detect the existence of a RAZ in  $q\bar{q}' \rightarrow W\gamma$  processes from the photon-lepton CSRD? It turns out that a RAZ would cause a dip in the observed photon-lepton CSRD distribution for  $q\bar{q}' \rightarrow W\gamma$  processes. Thus, because the Standard Model predicts that  $q\bar{q}' \rightarrow W\gamma$  processes should have a RAZ, it follows that we should observe such a dip in the photon-lepton CSRD if the Standard Model is consistent with the experimental data. Figure 2 shows a plot of what is expected according to the Standard Model and what is expected according to an alternative hypothesis, which suggests that there will be no RAZ in this process. This dip is expected to occur at a photon-lepton CSRD of:

$$(3) \quad y(\gamma) - y(\ell) = \Delta y(\gamma, \ell) \approx \mp 0.3$$

Once again, the final sign is inversely correlated with the sign of the W boson [7]. Thus our goal is clear: to determine if there is a significant dip like that of Figure 2. Yet there are further problems that we must engage ourselves in to truly determine what the experimental data is consistent with.

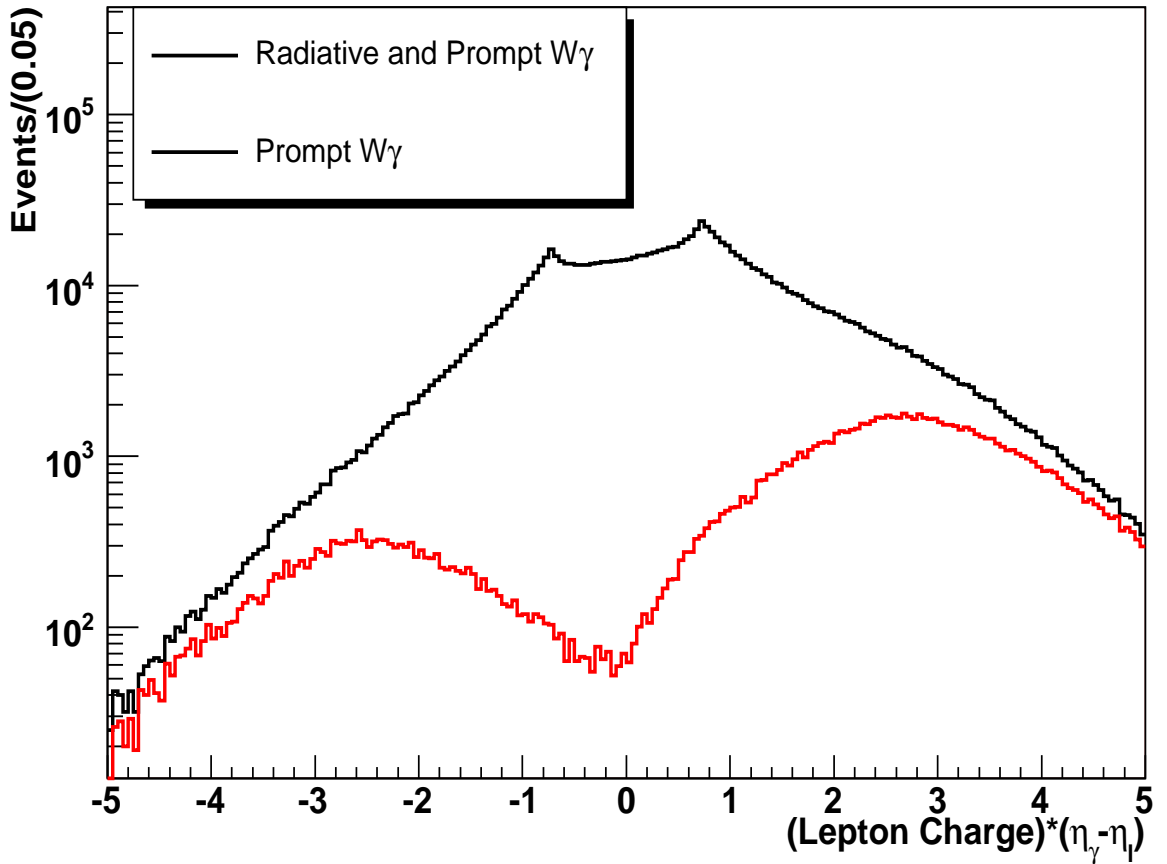


**Figure 2:** The number of events that produce a lepton and a photon with the indicated CSR. The red (bottom curve) indicates the Standard Model prediction and the black (top curve) indicates an alternative hypothesis. Note that the x-axis is actually *pseudorapidity*,  $\eta$ . See [4, 7].

### Complications

Bigger is not always better. It is well known that making a larger and larger cyclotron, for instance, is futile for some collisions due to synchrotron radiation, where a particle radiates as much energy as it gains from the accelerator itself. An analogous situation appears in the analysis of  $q\bar{q}' \rightarrow W\gamma$  processes. It turns out that Next-to-Leading Order QCD Effects will blur the resolution of the photon-lepton CSR, and that the effect becomes more severe as the energy of the W boson increases [4]. This makes analysis of  $q\bar{q}' \rightarrow W\gamma$  processes for the sake of observation of a RAZ unfit for hadron colliders the size of the LHC. The Tevatron, however,

happens to be suitable for this analysis because of the energy ranges it provides to collisions, and though Next-to-Leading Order QCD Effects are still prevalent in the Tevatron, they are not as detrimental as they would be at the LHC.

But despite this advantage, there are a number of complications with this analysis that still make it difficult to see this kind of dip. In particular, there are a number of other events that may look like a  $q\bar{q}' \rightarrow W\gamma$  event that could skew the measurements on  $q\bar{q}' \rightarrow W\gamma$  events. As a result, particle physicists have to estimate what properties these background events have that  $q\bar{q}' \rightarrow W\gamma$  events do not have, and must attempt to cut them out as they process the data. This is known as the acceptances of  $q\bar{q}' \rightarrow W\gamma$  analysis. Of course, given the probabilistic nature of contemporary physics (as well as simple practical considerations regarding the technical equipment of the experiment), this method will not eliminate all the background events from the selection, and so particle physicists must also estimate the ratio of background events to that of bona fide  $q\bar{q}' \rightarrow W\gamma$  events. This is known as the efficiencies of  $q\bar{q}' \rightarrow W\gamma$  analysis. I cannot delve into the technicalities of calculating the acceptances and efficiencies of this process here, but I will mention that a large part of the work I performed over the summer involved testing and coding these constraints so as to improve the analysis of  $q\bar{q}' \rightarrow W\gamma$  processes.

There are four main background events to consider. First, it is possible for a jet to be mistaken for a photon (denoted as W+jet events). This is the most significant background that needs to be considered, as it is the most abundantly produced. Second, it is possible for a Z boson to look like a W boson (denoted as Zy events). This might happen if a generated lepton is

not detected<sup>3</sup>, or if a jet is mismeasured. Third, events that produce a lepton, an electron, and have missing transverse energy (denoted as  $\ell e X$  events) can skew the resolution of  $q\bar{q}' \rightarrow W\gamma$  events. Finally, a small portion of the background events can come from events where the  $W$  decays into a tau and its neutrino (denoted as  $\tau\nu\nu$  events).<sup>4</sup> Although there are other background events that could skew this analysis, their effect is so small that they are considered negligible [4].

There is one other complications I will briefly mention. This analysis has been performed at Fermilab before, but the previous analysis was not able to conclusively rule out either the Standard Model or other alternative hypotheses. The data resolution and error analysis made the data consistent with the Standard Model, but not inconsistent with alternative hypotheses. Technology has improved, of course, and now the data resolution should hopefully be a little tighter. It turns out that a statistical analysis of a dip is very difficult (much more difficult than, say, a bump in the data, which is more commonly analyzed in particle physics nowadays), and the statistical analysis used on previous runs was complex. So one major challenge that must be confronted later is finding a suitable statistical analysis for the data collected.

## Data

Although a complete analysis of the photon-lepton CSRD of  $q\bar{q}' \rightarrow W\gamma$  processes was not possible for the time span given this summer, I provided a preliminary measurement that will prove to be useful for calculating the photon-lepton CSRD distribution of  $q\bar{q}' \rightarrow W\gamma$  events.

---

<sup>3</sup>  $Z$  bosons decay into a fermion-antifermion pair, so if a lepton-antilepton pair is produced and one is not found, then it might look like a  $W$  boson decaying into a single lepton.

<sup>4</sup> Although it was previously mentioned that the  $W$  boson can decay into any kind of lepton, the main focus of this analysis is when the  $W$  boson decays into either an electron or a muon, since the event where the  $W$  decays into a tau occurs so infrequently. Thus, it is considered a background event in this analysis.

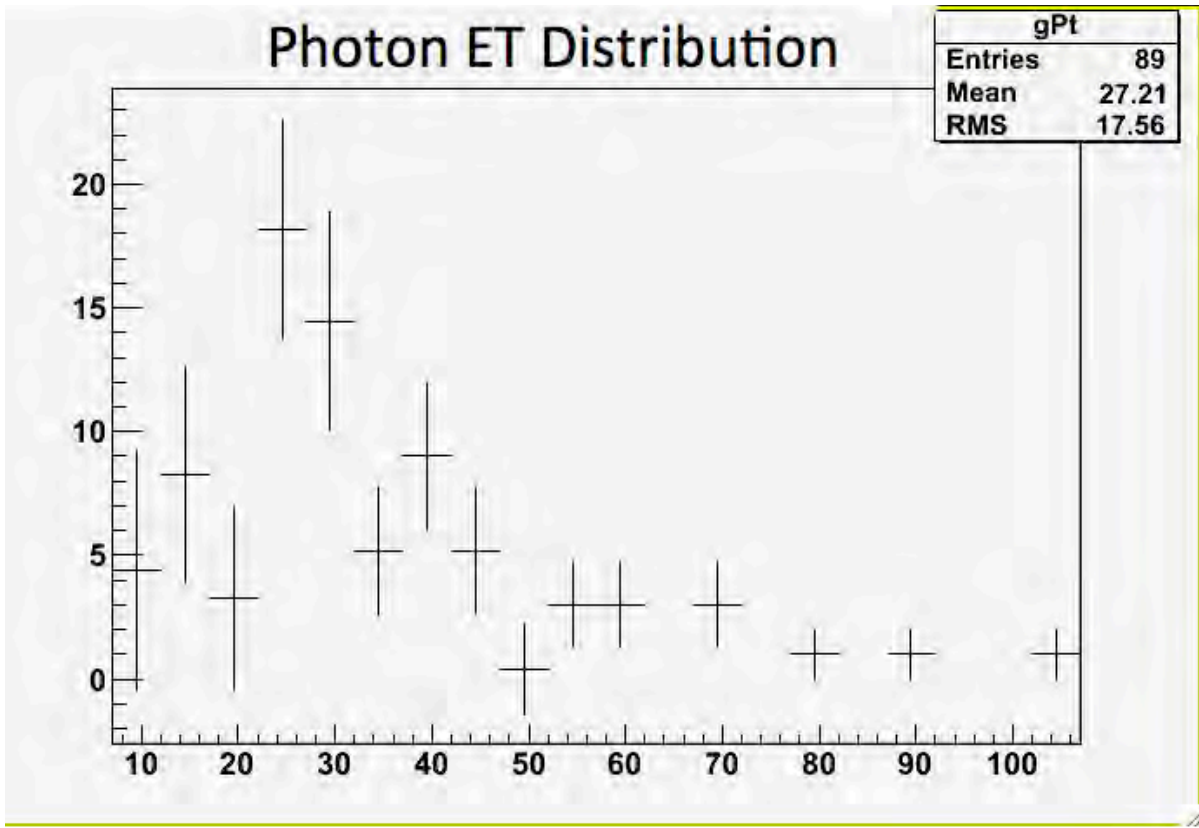


**Figure 3:** The background-subtracted transverse energy distribution for the photon in  $W\gamma$  events.

Often in high-energy particle physics, it is helpful to determine the transverse energy distribution of the various particles you are observing. Such a distribution could be used in calculating the CSRD for  $q\bar{q}' \rightarrow W\gamma$  events [3,4]. However, this distribution is only useful if the background is subtracted from the original data. Figure 3 displays a transverse energy distribution for the photon in  $q\bar{q}' \rightarrow W\gamma$  events. This distribution has the background events subtracted out so that it is (as far as we are concerned) representative of the photons in  $q\bar{q}' \rightarrow W\gamma$  events. Of course, more analysis needs to be performed before this distribution can be put to work to calculate the photon-lepton CSRД. But it's a start.

### Conclusion

Although  $q\bar{q}' \rightarrow W\gamma$  events have been observed by Fermilab in the past, it is important to be sure that the experimental data from this analysis is consistent with the Standard Model.

Since the experimental data was not conclusively shown to be either consistent or inconsistent with either the Standard Model or alternative hypotheses, and since technology has improved since the last analysis of  $q\bar{q}' \rightarrow W\gamma$  events, it is fruitful and important to update this analysis to see if any headway can be made regarding the photon-lepton CSRD distribution. Given the limited time span, this summer was fruitful in producing some progress towards this analysis. But clearly more time and work needs to be done before a full conclusion can be reached.

## References

- [1] Wikipedia contributors. "Standard Model." *Wikipedia, The Free Encyclopedia*. Wikipedia, The Free Encyclopedia, 29 Jun. 2010. Web. 25 Jul. 2010.
- [2] V. M. Abazov, et al. "First Study of the Radiation-Amplitude Zero in  $W\gamma$  Production and Limits of Anomalous  $WW\gamma$  Couplings at  $\sqrt{s} = 1.96$  TeV ." *Physical Review Letters*. The American Physical Society. 20 June 2008.
- [3] F. Mamedov. "Radiation Zeros in Weak Boson Production Processes at Hadron Colliders." AIP Conf. Proc. 541, 202–212. 31 Jul. 2001. <<http://arxiv.org/abs/hep-ph/0107326v1>>.
- [4] A. Askew, A. Lyon, G. Pawloski. "Measurement of the Charge Signed Photon-Lepton Rapidity Difference in  $W\gamma$  Events." DZero note 5256 Version 0.1.
- [5] Weisstein, Eric W. "Rapidity." *Eric Weisstein's World of Physics*. Wolfram Research, 2007. <<http://scienceworld.wolfram.com/physics/Rapidity.html>>.
- [6] Wikipedia contributors. "Hyperbolic function." *Wikipedia, The Free Encyclopedia*. Wikipedia, The Free Encyclopedia, 24 Jul. 2010. Web. 25 Jul. 2010.
- [7] U. Baur, S. Errede, G. Landsberg. "Rapidity Correlations in  $W\gamma$  Production at Hadron Colliders." Physics Review D, Vol. 50, Num. 3. 1 Aug. 1994.

## Additional Resources

- V. M. Abazov, et al. "Measurement of the  $p\bar{p} \rightarrow W\gamma + X$  Cross Section at  $\sqrt{s} = 1.96$  TeV and  $WW\gamma$  Anomalous Coupling Limits."
- B. Abbott, et al. "Studies of WW and WZ Production and Limits on Anomalous  $WW\gamma$  and  $WWZ$  Couplings." Physical Review D. 4 May 1999.
- J. Cortés, K. Hagiwara, F. Herzog. "Testing the  $WW\gamma$  Coupling of the Standard Model at  $p\bar{p}$  Colliders." Nuclear Physics B278. 21 May 1986.

Perkins, Donald H. *Introduction to High Energy Physics*. Cambridge: Cambridge UP, 2000. Print.

C. J. Goebel, F. Halzen, J.P. Leveille. "Angular Zeros of Brown, Mikaelian, Sahdev, and Samuel and the Factorization of Tree Amplitudes in Guage Theories." Physical Review D, Vol 23, Num. 11. The American Physical Society, 1 June 1981.



# Development of a Low-Level Counting Station

Omar Magaña

2010 Notre Dame Physics REU

Physics Department, University of Notre Dame

Advisor: Dr. Philippe Collon

Mentors: Mathew Bowers, Karen Chamberlin, Wenting Lu, Daniel  
Robertson, Christopher Schmitt

## *ABSTRACT*

A low-level counting station was developed to determine the half-life of  $^{60}\text{Fe}$ . The iron source was selected among other products during the process of nuclear collision. Utilizing a *K1900* fragment separator from the NSCL facility at MSU, the  $^{60}\text{Fe}$  was produced and implanted into Al Foils. The iron was later extracted by a chemical process and precipitated nucleus as  $\text{Fe}_2\text{O}_3$  at the Argon National Laboratory. Since, the  $^{60}\text{Co}$  serves as a contaminant; the Cobalt was removed in chemistry, to insure all measure  $^{60}\text{Co}$  is from the decay of  $^{60}\text{Fe}$ . In order to achieve successful results, a low-level counting station was developed to maximize the background suppression using lead bricks. The lead castle was engineered to reduce background radiation that interferes with the detector. By doing so, various calibrations and arrangement of lead bricks were done to add suppression into the counting station. Once the detector shielding was ready, a background run was made in order to compare the difference between the previous shielding that was built last year by other colleagues. In future experiments, the  $^{60}\text{Fe}$  sample will be inserted into the detector. The  $^{60}\text{Co}$  activity will be measured to determine the half-life of  $^{60}\text{Fe}$ .

## INTRODUCTION

$^{60}\text{Fe}$  has played a predominant role in the knowledge of the processes in the Universe. By understanding the half-life of  $^{60}\text{Fe}$ , it can serve as a chronometer for the history of the Solar System.  $^{60}\text{Fe}$  is produced during *nucleosynthesis* in massive stars and was observed in type II supernova, which is thought to be collapsing massive stars. In addition, the isotope's half-life also played an essential role during the observation of meteoritic inclusions. Since  $^{60}\text{Fe}$  decays to  $^{60}\text{Co}$  which decays to the stable nuclide  $^{60}\text{Ni}$ , various amounts of condensed solids were observed on a stellar cloud formed by the Solar System. It was determined that  $^{60}\text{Fe}$  was a heating source in the stage in which planetesimals was formed. However, discrepancies arose due to the fact that planetary disks are formed 1 million years after the time of collapse of the interstellar cloud. As the half-life of  $^{60}\text{Fe}$  was first given to be 1.4 million years, a timing constraint became apparent between the formation of the disks and the condensed solid  $^{60}\text{Fe}$ . Though, the evolution of the protoplanetary disk could be determined by the abundances of  $^{60}\text{Fe}$  and the distribution on the disks, a more precise half-life is needed to resolve and clarify data.

Another course of action in which the half-life of  $^{60}\text{Fe}$  plays a crucial role is during the ejection of a supernova.  $^{60}\text{Fe}$  was found on Earth's ocean crust due to a nearby supernova that occurred many million years ago. Numerous constraints in the distance of  $^{60}\text{Fe}$  ejection by the supernova and the amount of material decayed before measurement were present. Thus, a more precise determination, or measurement, of the half-life of  $^{60}\text{Fe}$  is needed since the other two previous measurements of  $(1.49 \pm 0.27) \cdot 10^6$  and  $(2.62 \pm 0.04) \cdot 10^6$  years are inconsistent.

## THEORY

In order to measure the accurate half-life of  $^{60}\text{Fe}$ , two different procedures will be followed, which are implantation and accelerator mass spectrometry (AMS). In implantation, the  $^{60}\text{Fe}$  is extracted from an aluminum plate and is placed into a plastic vial. The vial holder can then be set into a low-level counting station to measure the activity of  $^{60}\text{Co}$ . The activity of  $^{60}\text{Co}$  is important because it has a known half-life and it is the daughter nucleus of  $^{60}\text{Fe}$ , so it can be used to determine the activity of  $^{60}\text{Fe}$  using the following formula.

$$A_{\text{Co}}(t) = A_{\text{Fe}}[1 - e^{-\lambda_{\text{Co}}(t)}] \quad (1)$$

where  $A_{\text{Co}}(t)$  is the activity of  $^{60}\text{Co}$ ,  $t$  is time,  $\lambda_{\text{Co}}$  is the decay constant of  $^{60}\text{Co}$ , and  $A_{\text{Fe}}$  is the amount of  $^{60}\text{Fe}$  activity of our unknown. The decay constant of cobalt is calculated utilizing the equation below, where  $T_{1/2\text{Co}}$  is the half-life of  $^{60}\text{Co}$ , which is 5.27 years.

$$\lambda_{\text{Co}} = \frac{\ln(2)}{T_{1/2\text{Co}}} \quad (2)$$

Using the activity and decay constant of  $^{60}\text{Co}$ , we can now calculate the activity of  $^{60}\text{Fe}$  using Equation 1. We can then further implement the calculated activity into Equation 3 to determine the decay constant of  $^{60}\text{Fe}$ .

$$A_{\text{Fe}} = \lambda_{\text{Fe}} \cdot N_{60\text{Fe}}, \quad (3)$$

where  $\lambda_{\text{Fe}}$  is the decay constant of  $^{60}\text{Fe}$  and  $N_{60\text{Fe}}$  is the amount of  $^{60}\text{Fe}$  nuclei in the source. The  $N_{60\text{Fe}}$  is determined during the process of AMS, which is a method for detecting specific nuclides and measuring their concentration to extremely low levels. With these two values we can now calculate the decay constant of  $^{60}\text{Fe}$  and implement into,

$$\lambda_{\text{Fe}} = \frac{\ln(2)}{T_{1/2}} \quad (4)$$

The half-life of  $^{60}\text{Fe}$   $T_{1/2}$  can now be obtained and compared to the previous measurements of the value.

Our main concentration is on  $^{60}\text{Co}$  due to the fact that it is easier to measure the activity because of its gamma-ray ejection. The gamma-ray ejection can be measured using a low-level counting station, or a Germanium detector. A Germanium detector is a solid state detector, also known as HPGe, that detects  $\gamma$ -rays from an isotope. Due to the uniqueness of the detector, the HPGe must be cooled to eliminate the leakage current. This is done by filling a dewar with liquid nitrogen ( $LN_2$ ) at a temperature of 77K. However, the detector cannot eliminate external or background radiation found in our surrounding. For that reason, a lead shielding is needed to aid to result for more accurate results.

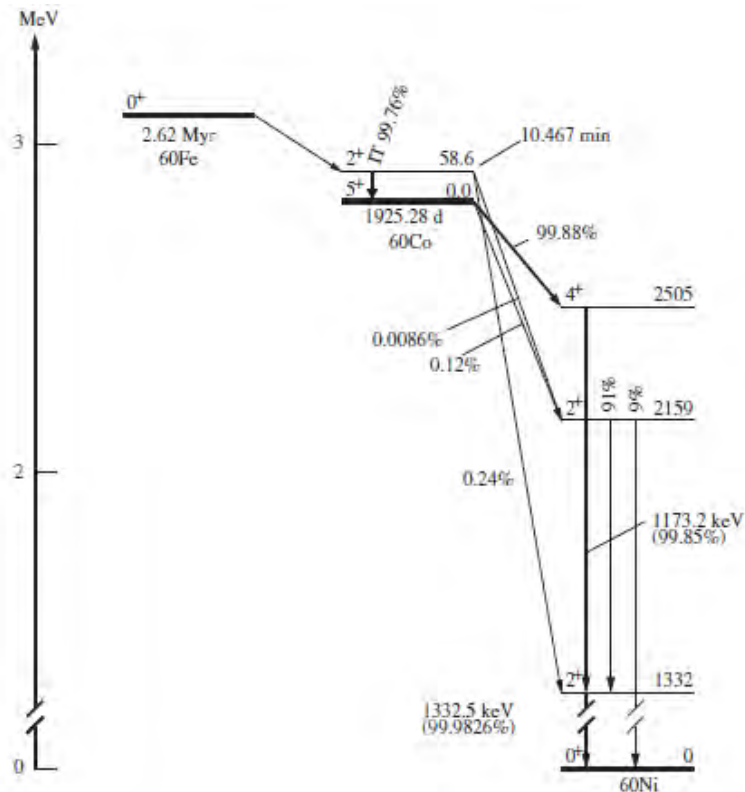


Fig. 1. Decay Scheme of  $^{60}\text{Fe}$  that shows the father decay of  $^{60}\text{Fe}$  to  $^{60}\text{Co}$ , and the stabilized nuclide  $^{60}\text{Ni}$ .

## *RESULTS AND DISCUSSIONS*

To determine the amount of activity in the  $^{60}\text{Co}$  source, we utilized a 55% High-Purity Germanium detector (HPGe). After the detector was set up and the Bias was set to 4000 volts, we began to run the detector with no radioactive source. The detector was run using software named Maestro in which we could view the data and the background radiation in the testing room. Based on our run, various quantities of K-40, Cs-137, Tl-208, and U-238 were present because of the bricks and concrete of the building and room. Therefore, we then developed a new lead shielding castle that will reduce the amount of background. The castle was built with lead due to the fact of its high density and atomic mass. Although lead can attenuate many kinds of radiation, it was important to not exceed the surrounding thickness of 6 to 8 inches. Lead shielding does in fact improve results, but lead may also create Bremsstrahlung Effects, which is worse than background radiation.

The lead castle was engineered with lead bricks with dimensions of 2in. x 4in. x 8in. During the development of the castle, the lead bricks were altered in a formation where one brick covers another gap opening between two bricks. See Figure 2 and 3.

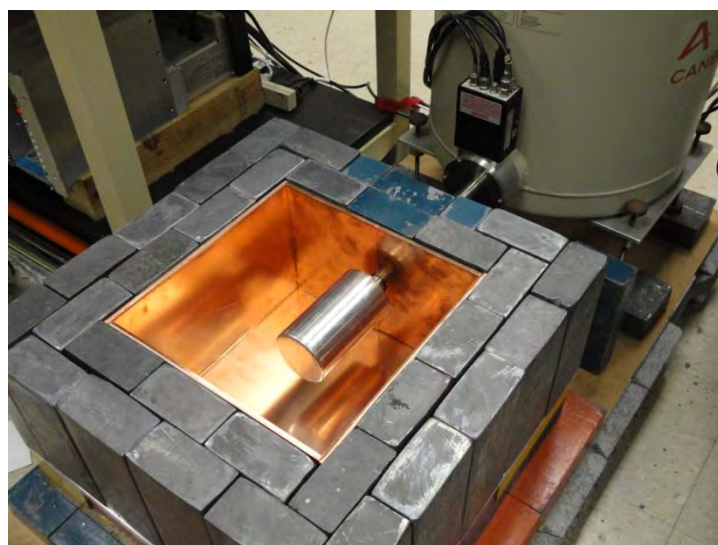


Fig. 2. Top view of Germanium detector with lead shielding and copper box.



Fig. 3. Front view of the Germanium detector with shielding and ready to run.

Once the bottom layer and walls were built, a  $\frac{1}{4}$ " copper sheet was then placed against the inner box, where the detector was located. The Copper material was used as an absorber to filter out any gamma-rays that undergo interactions such as the Compton Effect and Photoelectric Effect. Based on the interactions, low-energy or low-intensity gamma-rays will then be transmitted through the detector. To finish the building of the castle, we then placed an aluminum plate to suffice the efficiency of the detector. The plate allowed for stability and for a flat surface to place the bricks on top.

When the development of the lead castle was finished, we then ran the detector to view the amount of radiation reduced. Due to lack of time, the activity of  $^{60}\text{Co}$  was unable to be measured. However, preliminary results of the shielding took place. We compared the total sum of the counts of radioactive material with the time run or the total live time the detector was run. The number of counts of no shielding, bottom and side layers, and the complete shielding are shown below (See Table 1).

	<b>Total Counts</b>	<b>Time Run (Live time)</b>	<b>Counts per second [cts/sec.]</b>
		[sec.]	
<b>No Shielding</b>	22,085,600	172,013	128.395
<b>Bottom and Side Layers</b>	2,953,160	86,288	34.22
<b>Complete Shielding</b>	309,744	164,943	1.87

Table 1. Total count measurements of different steps during the building of lead castle.

Utilizing the data above, the total reduction count rate of the no shielding vs. the complete shielding was reduced by a factor of 68.6.

## *CONCLUSION*

It was concluded that every layer did make a significant difference on the total number of counts. In future experiments, the  $^{60}\text{Fe}$  source will be placed inside the lead shielding to obtain the measurement of  $^{60}\text{Co}$ . Using Maestro, we will analyzed the decay peaks at energies of 1173.2 keV and 1332.5 keV, which are the energy levels of  $^{60}\text{Co}$  (See Figure 1), and the activity of  $^{60}\text{Co}$  will then be measured. Next, we would then determine the number of  $^{60}\text{Fe}$  nuclei in the process of AMS. Based on Equation 3, we will then be able to determine the decay constant of  $^{60}\text{Fe}$ , which will lead us to the half-life of  $^{60}\text{Fe}$ .

## *REFERENCES*

- [1] Knoll, Glenn. *Radiation Detection and Measurement*. 3rd ed. New York, NY: John Wiley & Sons, Inc., 1999. 387-397.
- [2] Walter Kutschera, Michael Paul. "Accelerator Mass Spectrometry in Nuclear Physics and Astrophysics." *Annual Reviews of Nuclear Particle Science*. 40. (1990): 411-438.
- [3] Rugel, G. *et al.*, "New Measurement of the  $^{60}\text{Fe}$  Half-Life." *Physical Review Letters*. (2009): 1-4.
- [4] Kutschera, Walter *et al.*, "Half-Life of  $^{60}\text{Fe}$ ." *Elsevier Science Publishers B.V.*. (1984): 430-435.



The Segmented Universe:  
Identifying Cosmic Voids with a Multi-Scale Geometric Flow

Andrew Miller

2010 NSF/REU Program  
Physics Department, University of Notre Dame

Advisor: Dr. Lara Arielle Phillips

## Abstract

The complex, filamentary nature of large-scale dark matter and density structure in the universe is a prominent feature of both redshift surveys and large N-body simulations of cosmic evolution. Here, we present a quantitative method for the analysis of such structure though the application of a medical imaging algorithm to dark matter and semi-analytical model galaxy data from the Virgo Consortium's 2005 Millennium Simulation (MS). The algorithm, a multi-scale geometric flow for segmenting vasculature in proton density images of the human brain, originally identified regions of vessel-like structure in an intensity field using level set methods. Due to the striking similarity between the types of structure observed in the universe on cosmic scales and the type of organization exhibited by the vasculature of the brain, we theorized that this method of structure analysis would prove an accurate means of classification for formations of cosmic dark matter overdensity and the accompanying density voids. We have modified the algorithm to identify sheet-like, clump-like, and void-like structure in addition to filament-like features in a density field. We focus on regions of cosmic void to determine the robustness of this segmentation method from a systematic comparison of its results with those of previously published void-finding algorithms. To this end, we extract the dark matter halo distribution from a subvolume of the MS and convert it to a three-dimensional image of variable cell resolution. We distribute the mass of each halo according to the Navarro, Frenk, & White (NFW) mass-density profile and write the data set to a Medical Image NetCDF (MINC) volume. We apply the segmentation algorithm to this MINC volume and analyze the initial results.

## Introduction

The existence of structure in our universe has been known almost since the discovery of galaxies remote from our own Milky Way.<sup>1</sup> Abell presented the first evidence of large associations of galaxy clusters, providing an effective means for a systematic phenomenological investigation of the large-scale distribution of matter in the universe.<sup>2</sup> Since then, large redshift surveys, such as the Sloan Digital Sky Survey (SDSS) have revealed in great detail the nature of this large-scale distribution of galaxies: the clusters connected by filaments and sheets, and the great regions of void in between.

Voids in cosmic structure are generally defined as underdense regions in the current mass distribution of the universe, often with very steep edges.<sup>3</sup> Readily apparent as the counterpart to the overdense filaments observed both in redshift surveys and in theoretical cold dark matter (CDM) numerical simulations<sup>4,5,6,7</sup>, voids have become a prominent means of large-scale structure (LSS) analysis. The current CDM cosmological model (augmented with the cosmological constant  $\Lambda$ , representing the dark energy density which governs the rate of expansion of the universe) holds that such observed cosmic structure has its origins in weak density fluctuations in the early ages of the otherwise homogenous universe (observable today in the cosmic microwave background radiation) which were exacerbated through gravitational clustering.<sup>8,1,7</sup> Voids themselves grow around regions of underdensity as a result of the gravitational collapse of dark matter particles in the initially nearly homogenous CDM distribution of the early universe into filaments and clusters around regions of original weak overdensity. These overdense areas develop into interstitial nodes<sup>9</sup> between a packing of roughly spherical voids, towards which matter continues to condensate, causing the fluctuations of large-scale mass distribution of the universe to become more pronounced with time. Within

regions both of void and of populated space, matter density is not homogenous, being collected into local regions of underdensity and overdensity analogous to the larger-scale structure.

Although it is possible to model the initial growth of density perturbations analytically, the nonlinear nature of gravitational collapse and hierarchical structure development necessitates direct numerical simulation.<sup>7</sup> Due to the dominance of CDM, which subject only to the forces of gravitational attraction, over regular matter the mass distribution of the universe may be modeled as a hydrodynamic-free set of discrete point particles.<sup>7</sup> We use the Millennium Simulation<sup>7</sup> (MS) and Millennium-II Simulation<sup>10</sup>, which were carried out by the Virgo Consortium in the years 2005 and 2009 respectively, and follow approximately  $1.0078 \times 10^{10}$  simulation particles from redshift  $z = 127$  to the present.<sup>7</sup> This most recent family of high-resolution N-body  $\Lambda$ CDM simulation represents the largest pure dark matter efforts to date.

Attempts have been made to systematically quantify the LSS of the universe seen in redshift surveys and numerical simulation, notably Regős and Geller,<sup>11</sup> Babul and Starkman,<sup>12</sup> and Mecke, Buchert, and Wagner.<sup>13</sup> A wide variety of void-finding algorithms have sprung from these early efforts, motivated by the importance of cosmic voids to a full understanding of cosmic structure, a greater knowledge of cosmological information and galaxy formation. The *Aspen-Amsterdam Void-finder Comparison Project*, described as the first such systematic study in this area, evaluates thirteen void-finding algorithms from different groups on a small subvolume of the MS, and gives a qualitative and quantitative analysis of the differences of each.

We present a novel void-finding algorithm which is an adaptation of a computer vision algorithm designed to detect blood vessels in proton density images of the human brain and apply it to the MS dark matter distribution.

## Simulation and Extraction Procedure

We obtain the simulation outputs from the MS, which comprises a  $500h^{-1} Mpc$  per side cubic region with periodic boundary conditions, where the total matter density is given  $\Omega_m = 0.25$ , the baryonic matter density  $\Omega_b = 0.045$ , the dark energy density  $\Omega_\Lambda = 0.75$ , the Hubble constant  $h = 0.73$ , and the normalization of the power spectrum  $\sigma_8 = 0.9$ .<sup>7</sup> Two separate semi-analytic galaxy formation models were implemented in the MS to populate the CDM substructure.<sup>14,15</sup>

For this work, we use the CDM halo distribution and the L-Galaxies  $z = 0$  semi-analytic galaxy catalogue<sup>14</sup>. From the SUBFIND<sup>16,17</sup> halo table we extract the spatial coordinates and the mass within the radius where the halo has an overdensity 200 times the critical density of the simulation of all halos at  $z = 0$  in a  $60h^{-1} Mpc$  per side subvolume of the MS. We extract a total of 4277 halos with  $M_{200} > 10^{11} h^{-1} Mpc$ , comprising 7655905 simulation particles, giving our subsample an underdensity  $\delta = \rho/\bar{\rho} - 1 = -0.56$  (where  $\rho$  is the density of our MS subvolume and  $\bar{\rho}$  is the density of the entire MS). In this subvolume we extract the spatial coordinates, stellar and cold gas mass, and BVRIK dust-corrected magnitudes of the 39753 galaxies with  $B < -10$  present at  $z = 0$  in the semi-analytical L-Galaxies catalogue.

### NFW Profiling

Since the MS gives as the position of each halo only the coordinates of the constituent particle with the least potential energy, we distribute the mass of each halo into a volume to reconstruct the spatial extend of the halo. We use the Navarro, Frenk, & White<sup>18</sup> (NFW) mass-density profile, a simple formula with two free parameters:

$$\rho(r)/\rho_{crit} = \delta_c / \left[ (r/r_s)(1 + r/r_s)^2 \right]. \quad (1)$$

The critical density to collapse is given in the MS:  $\rho_{crit} = 3H_o^2/(8\pi G)$ , where  $G$  is the gravitational constant,  $H_o$  is Hubble's constant, and  $r$  is the radial distance from the center of the halo's mass.  $r_s$  is a scaled, characteristic radius,  $r_s = r_{200}/c$ , defined in terms of the dimensionless halo concentration parameter,  $c$ , and  $r_{200}$ , the radius inside which the halo has an overdensity 200 times  $\rho_{crit}$ , such that the mass inside that radius  $M_{200} = 200\rho_{crit}(4\pi/3)M_{200}$ .  $\delta_c$  is a “characteristic density contrast”, a dimensionless parameter:

$$\delta_c = (200/3)c^3/\left[\ln(1+c) - c/(1+c)\right] . \quad (2)$$

The halo concentration parameter  $c$  is specific to each halo. It has a well-defined, though weak, correlation to mass, generally decreasing with increasing mass.<sup>19</sup> We use the power law derived by Neto<sup>19</sup> from a sample of MS halos:

$$c_{200} = 4.67 \left( \frac{M_{200}}{10^{14} h^{-1} M_{sun}} \right)^{-0.11}, \quad (3)$$

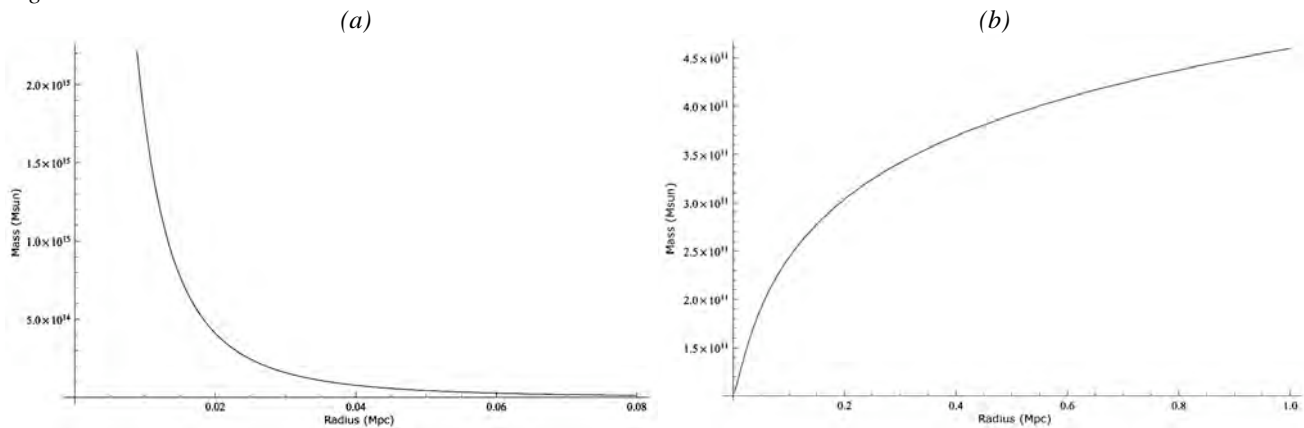
where  $M_{sun}$  is the mass of the Sun. Using eqs. (1) – (6), a radial density profile only dependent upon  $M_{200}$  is found, and by integrating over a spherical volume we obtain the spatial dependence of the of the halo mass function

$$M(r) = \int 4\pi\rho(r)r^2 dr = 4\pi\delta_c\rho_{crit}r_s^3 \left( \frac{r_s}{r_s + r} + \ln(r_s + r) \right), \quad (4)$$

whereby the mass of the halo may be distributed over a number of voxels in the MINC volume.

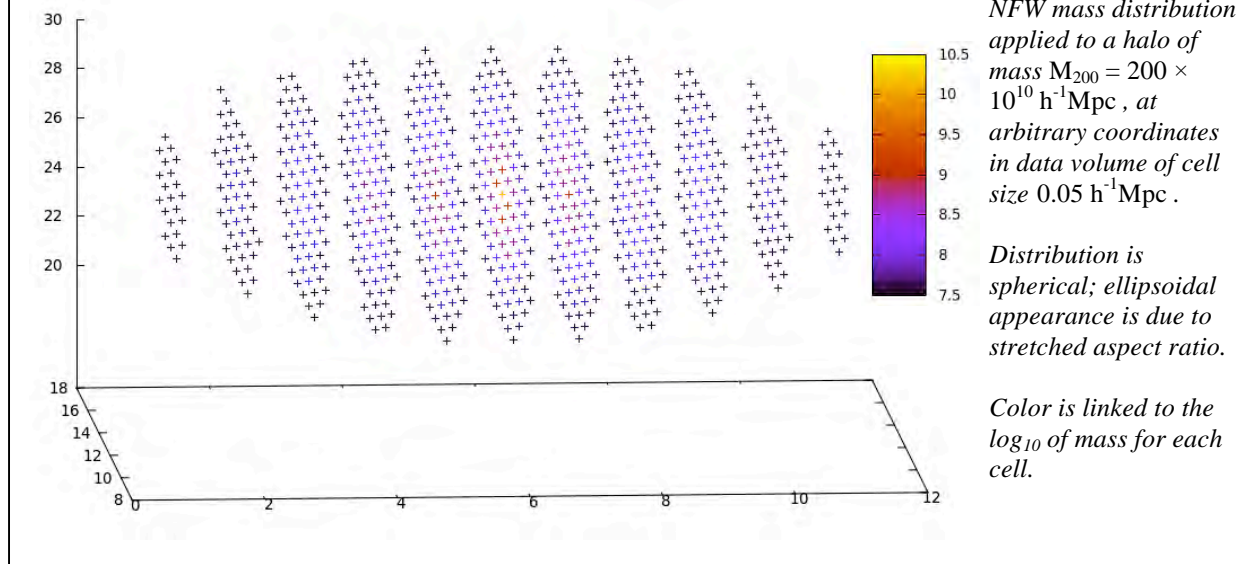
*Figure 1* displays the radial density profile, mass distribution, and volume distribution of a moderately-sized halo of  $M_{200} = 200 \times 10^{10} h^{-1} M_{sun}$ . *Figure 2* shows the halo, at an arbitrary position in an array with cell size  $(0.05 h^{-1} Mpc)^3$ , distributed over a volume.

Figure 1



(a) NFW Spherically-averaged radial density profile for halo of  $M_{200} = 200 \times 10^{10} h^{-1}\text{Mpc}$   
 (b) NFW Spherically-averaged radial mass profile for halo of  $M_{200} = 200 \times 10^{10} h^{-1}\text{Mpc}$

Figure 2

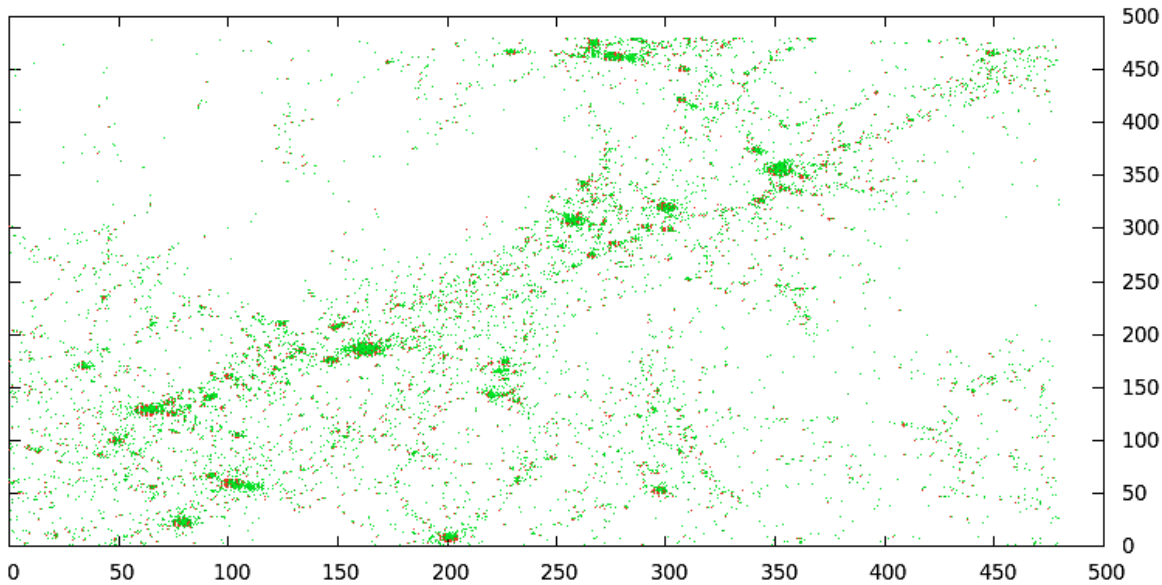


## Implementation

The MS data are obtained in comma-separated variable (CSV) format, and a C program was written to convert the data into a three-dimensional Medical Image NetCDF (MINC) volume of variable cell resolution. The NFW profile is applied to each halo. The segmentation program is applied to the MINC volume in three separate stages filtering for filaments, sheets, and clumps,

respectively, each producing a new MINC volume holding the corresponding structure measure for each cell. The “ncdump” shell command in the NetCDF library allows extraction of MINC data in common data language format (CDL). A C program was written to read CDL data and extract it for analysis. We use existing tools to visualize the resulting volumes. *Figure 3* displays a  $15h^{-1}Mpc$  slice of a MINC data volume of  $480^3$  cells after the NFW profile has been applied.

*Figure 3*



A slice of thickness  $15h^{-1}Mpc$  in the  $z$  dimension through the center of the subvolume extracted from the MS. The image shows all galaxies in slice plotted in green (light) over dark matter, distributed according to NFW profile, plotted in red (dark).according to the NFW profile. Axes give voxel coordinate in the MINC volume. Vertical lines through plot are artifacts of graphing program.

### Segmentation Algorithm

The multi-scale geometric flow, employed here as the basis for a void-finding algorithm, was developed by Descoteaux, Collins, and Siddiqi at the McConnell Brain Imaging Centre of the Montreal Neurological Institute.<sup>20</sup> The algorithm uses the eigenvalues of the Hessian matrix with

Frangi's vesselness measure<sup>21</sup> to identify tubular structure in a density or intensity field.<sup>20</sup>

Descoteaux's algorithm was modified to also identify sheet-like and clump-like structures in addition to filaments in baryonic density data.<sup>22</sup>

The full, modified algorithm may be described as three processes: structure filtering, measure propagation, and structure bounding. The structure filtering process, which is our focus here, first convolves the density distribution in the MINC volume with a Gaussian,  $G(\sigma)$ , at multiple scales. Then, using the first and second order information in the Taylor expansion of the vector field around each point

$$\rho(x_0 + \delta x_0, \sigma) \approx \rho(x_0, \sigma) + \nabla \rho_i \delta x_0^i + H_{ij} \delta x_0^i \delta x_0^j + \dots \quad (5)$$

and curvature is measured at each scale level.  $H$  is the Hessian matrix, defined for a

function  $f(x_1, x_2, x_3)$  in three dimensions as

$$H = \begin{bmatrix} \frac{\partial^2 f}{\partial x_1^2} & \frac{\partial^2 f}{\partial x_1 \partial x_2} & \frac{\partial^2 f}{\partial x_1 \partial x_3} \\ \frac{\partial^2 f}{\partial x_2 \partial x_1} & \frac{\partial^2 f}{\partial x_2^2} & \frac{\partial^2 f}{\partial x_2 \partial x_3} \\ \frac{\partial^2 f}{\partial x_3 \partial x_1} & \frac{\partial^2 f}{\partial x_3 \partial x_2} & \frac{\partial^2 f}{\partial x_3^2} \end{bmatrix}. \quad (6)$$

The eigenvalues of  $H$  provide information about the level and type of local structure at each point.

Setting the eigenvalues  $|\lambda_1| \leq |\lambda_2| \leq |\lambda_3|$ , four possible conditions arise: (1) Filament-like structure if

$|\lambda_1| \approx 0, |\lambda_2| \approx |\lambda_3| \gg 0$ , (2) Sheet-like structure:  $|\lambda_1| \approx |\lambda_2| \approx 0, |\lambda_3| \gg 0$ , (3) Clump-like structure:

$|\lambda_1| \approx |\lambda_2| \approx |\lambda_3| \gg 0$ , and (4) Noise-like structure:  $|\lambda_1| \approx |\lambda_2| \approx |\lambda_3| \approx 0$ . Four corresponding

parameters may thus be defined

$$R_A = |\lambda_2 / \lambda_3|, \quad (7)$$

$$R_C = |\lambda_1 / \lambda_2|, \quad (8)$$

$$R_D = |\lambda_1 / \lambda_3|, \quad (9)$$

$$S = (\lambda_1^2 + \lambda_2^2 + \lambda_3^2)^{\frac{1}{2}} / S_{\max}. \quad (10)$$

A low  $R_A$  indicates the presence of sheet-like structure, a low  $R_C$ , the presence of filament-like structure, and a high  $R_D$ , the presence of clump-like structure. The fourth parameter, the Frobenius norm, is used to eliminate random noise effects.<sup>20</sup> Three measures of local structure are calculated for each point from the above values:

$$\text{Sheetness measure: } M_1(\sigma) = (e^{-\alpha_1 R_A^2} - e^{-\alpha_1}) (1 - e^{-\beta S^2}), \quad (11)$$

$$\text{Filament measure: } M_2(\sigma) = (e^{-\alpha_2 R_C^2} - e^{-\alpha_2}) (1 - e^{-\beta S^2}), \quad (12)$$

$$\text{Clumpiness measure: } M_3(\sigma) = (e^{-\alpha_3 R_C^2}) (1 - e^{-\beta S^2}). \quad (13)$$

We adapt the algorithm to identify void-like structures in the CDM distribution and semi-analytic galaxy catalogue of the MS through three separate methods. In the first method, we identify voids as absences of positive structure. Those cells in the MINC data volume assigned by the filtering process with high sheetness, filament, or clumpiness measures, are identified, and all other cells are designated as being void-like. In the second method, we identify voids as regions of positive clump-like or group-like shape. The density distribution of the data volume is first inverted, and then the segmentation filter run as normal. The cells assigned by the filter with high clumpiness measures are designated as belonging to a void. In the third method, yet untried, we will create a new voidness measure, based on the Eigen values of the Hessian in a manner analogous to the existing sheetness, filament, and clumpiness measures.

## Conclusions

We have successfully applied a novel multi-scale geometric flow void-finding algorithm to the CDM halo distribution of the MS. We have completed a full pipeline to implement the segmentation program on MS data. In addition, a set of supplementary plotting and sorting programs have been written to provide information about and visualization of data at the various stages of the process. Analysis of the MS data using the filament, sheetness, and clumpiness structure measures to identify void structure, must follow. The three methods of adapting the segmentation program should be thoroughly tested and the robustness of our void-finding methods be measured against contemporary void-finding efforts. The implementation process has been designed with such testing in mind. To evaluate our algorithm by the current standard, we seek to apply the segmentation algorithm to the same MS subvolume and accord it the same analysis as that of the *Aspen-Amsterdam Void-finding Project*. In the future, the segmentation algorithm may be extended to include the final two stages of structure identification: measure propagation, and structure bounding. Although not discussed here, these two processes have the potential to improve the ability and accuracy of the void-finding capabilities of the segmentation program.

## References

- 
- <sup>1</sup> Oort J. H. 1983, *Ann. Rev. Ast. Ap.*, **21**: 373.
  - <sup>2</sup> Abell, G. O., 1958, *Ap. J. Suppl.*, **3**: 211.
  - <sup>3</sup> Colberg, J. M. *et al.* 2008, *MNRAS*, **387**: 933.
  - <sup>4</sup> Centrella, J. and Melott, A. L., 1983, *Nature*, **305**: 196.
  - <sup>5</sup> Davis, M., Efstathiou, G., Frenk, C. S., and White, S. D. M. 1985, *Ap. J.*, **292**: 371.
  - <sup>6</sup> Bond, J. R., Kofman, L., and Pogosyan, D. 1996, *Nature*, **380**: 603.
  - <sup>7</sup> Springel, V. *et al.*, 2005, *Nature*, **435**: 629.
  - <sup>8</sup> Rood, H. J. 1988, *Ann. Rev. Ast. Ap.*, **26**: 245.
  - <sup>9</sup> Icke, V. 1984, *MNRAS*, **206**: 1.
  - <sup>10</sup> Boylan-Kolchin, M. *et al.*, 2009, *MNRAS*, **398**: 1150.
  - <sup>11</sup> Regős, E. and Geller, M. J. 1991, *Ap. J.*, **377**: 14.
  - <sup>12</sup> Babul, A. and Starkman, G. D. 1992, *Ap. J.*, **401**: 28.
  - <sup>13</sup> Mecke, K. R., Buchert, T., and Wagner, H. 1994, *Ast. Ap.*, **288**: 697.
  - <sup>14</sup> Croton, D. J. *et al.* 2006, *MNRAS*, **365**: 11.

- 
- <sup>15</sup> Bower, R. G. *et al.* 2006, *MNRAS*, **370**: 645
- <sup>16</sup> Springel, V., White, S. D. M., Tormen, G., Kauffmann, G. 2001, *MNRAS*, **328**: 726.
- <sup>17</sup> cf. Springel, V. *et al.*, 2005, *Nature*, **435**: 629. Supplementary Methods.
- <sup>18</sup> Navarro, J. F., Frenk, C. S., White, S. D. M. 1996, *Ap. J.*, **462**:563.
- <sup>19</sup> Neto, A. F. *et al.* 2007, *MNRAS*, **381**:1450.
- <sup>20</sup> Descoteaux, M., Collins, L., and Siddiqi, K. A Multi-Scale Geometric Flow for Segmenting Vasculature in MRI. 2004, *Computer Vision and Mathematical Methods in Medical and Biomedical Image Analysis*, 168-180.
- <sup>21</sup> Frangi, A., Niessen, W., Vincken, K. L., and Viergever, M. A. Multiscale Vessel Enhancement Filtering. 1998, in *MICCAI'98*, 130-137.
- <sup>22</sup> Phillips, L. A. Parsing the WHIM. 2005, *AAS 205<sup>th</sup> Meeting*, **129**.07.

# Measurement of the $^{12}\text{C} + ^{12}\text{C}$ Fusion Cross Section at Sub-Barrier Energies

Alexander Moncion

2010 NSF/REU Program

Physics Department, University of Notre Dame

Advisor: Xiao-Dong Tang

## Abstract

The goal of nuclear astrophysics is to understand the nuclear processes which power the stars and synthesize heavier elements. One important nuclear process is the  $^{12}\text{C} + ^{12}\text{C}$  fusion occurring in massive stars. The  $^{12}\text{C} + ^{12}\text{C}$  fusion produces  $^{24}\text{Mg}$  which can decay to  $^{20}\text{Ne}$  or  $^{23}\text{Na}$  via particle evaporation. Most of the residues may emit gamma radiation that can be detected using a gamma detector. We have studied the  $^{12}\text{C} + ^{12}\text{C}$  fusion reaction within the center of mass energy range of 4.1 MeV to 6.5 MeV by detecting the 440 keV and 1634 keV gamma lines using a germanium detector. The total fusion reaction cross section is determined after correcting decay branching ratios and summing effect.

## 1 Introduction

The  $^{12}\text{C} + ^{12}\text{C}$  fusion reaction occurs in massive stars several times the size of the Sun. It is one of the nuclear reactions that leads to the synthesis of a variety of heavier elements, and occur at sufficiently low energies to be able to be reproduced here on Earth. The main products of the carbon fusion reaction are  $^{20}\text{Ne}$  through the alpha channel  $^{12}\text{C}(^{12}\text{C},\alpha)^{20}\text{Ne}$  reaction,  $^{23}\text{Na}$  through the proton channel  $^{12}\text{C}(^{12}\text{C},p)^{23}\text{Na}$  reaction, and  $^{23}\text{Mg}$  through the neutron channel  $^{12}\text{C}(^{12}\text{C},n)^{23}\text{Mg}$  reaction[2]. However, limited by time, in this report, our studies focus solely on the proton channel. In order to determine the reaction probability at a given energy, we detect the gamma radiation, emitted as a byproduct of the alpha, proton, and neutron channels, with a germanium gamma particle detector. Each channel emit gamma particles of particular energies, and depending on the excitation energy of the produced fusion residue we can deduce the identity of the reaction product and

predict the likelihood (cross section) of the  $^{12}\text{C} + ^{12}\text{C}$  reaction occurring.

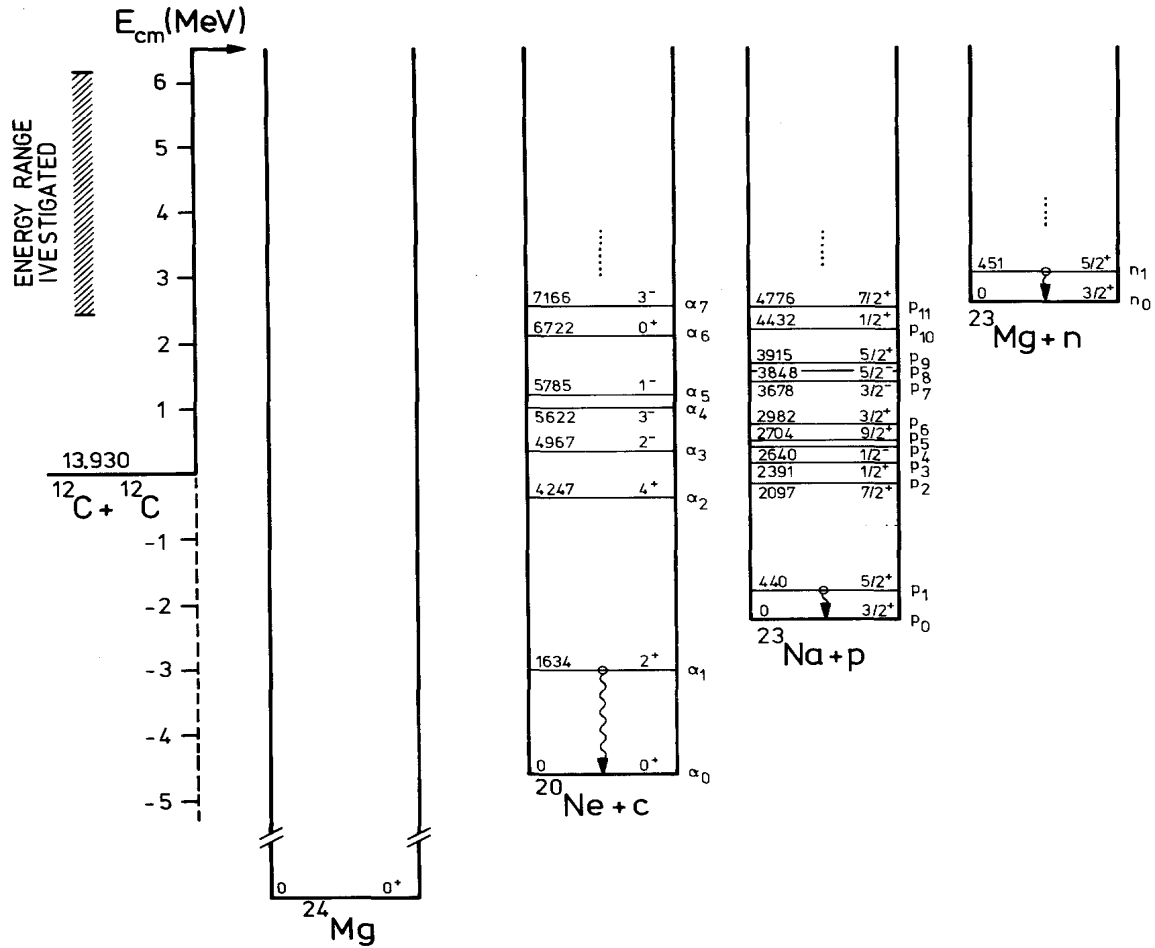


**Figure 1:** [1]Alpha, proton, and neutron channels of the  $^{12}\text{C} + ^{12}\text{C}$  reaction.

Initially,  $^{24}\text{Mg}$  is produced from the  $^{12}\text{C} + ^{12}\text{C}$  reaction, and that further decays via alpha, proton, or neutron channels. There are various excited states that the fusion residues may decay to, and some of those excited states may branch into several gamma channels as displayed in Figure 1. Each with their own probability of gamma emission. A example decay scheme for  $^{20}\text{Ne}$  is also shown in Figure 1. Aside from that, cascading decays may sum together, while being detected, and interfere the detection of certain gamma rays. With our current equipment we focus on the two gamma rays, 440 keV and

1634 keV gammas, which are emitted from the first excited states of the fusion residues,  $^{23}\text{Na}$  and  $^{20}\text{Ne}$ , respectively. Therefore, in order to accurately calculate the cross section of the  $^{12}\text{C} + ^{12}\text{C}$  reaction we must correct for decay branching and the summing effect that occurs from the timespan of the decay of the parent nuclei to the detection of the gamma particle.

## 2 Experimental Method

### 2.1 Efficiency Calibration

We initially determined the relative efficiency of our germanium detector using a  $^{56}\text{Co}$  source. This source was used due to its wide range of detectable energy decays ranging from 846 keV to 2598 keV. The relative efficiency provides a method of comparing the detector's efficiency at various energies. The absolute peak efficiency was acquired using three radioactive sources with high decay intensity and known radioactive activity,  $^{60}\text{Co}$ ,  $^{22}\text{Na}$ , and  $^{137}\text{Cs}$ . The total number of counts for the major peaks produced by the decay of these sources was acquired and compared to the source's current decay rate. We then fit the relative efficiency to these points and acquired equation 1, where  $x$  represents  $\ln(Energy)$  in keV.

$$\epsilon_{Peak} = -0.00174x^2 - 0.87195x + 4.224 \quad (1)$$

### 2.2 Branching and Summing Effect Correction

When correcting for branching we must account for the probability of the nuclei decaying at a particular proton channel, ranging from p0 to p10. Once the nuclei has decayed to

a certain proton channel, that channel may contain further branching that must also be accounted for. For example, the p0 branch populates the ground state of  $^{23}\text{Na}$  without emitting any gamma ray. Some excited states may have a cascading decay, a decay mode that emits more than one gamma before reaching the ground state. Summing may occur in which two separate gamma particles interact with the detector simultaneously. The detector may record these two separate interactions as a single entity, which leads to error in counting the number of peak and total counts. In order to detect 440 keV gamma rays, we must miss every single gamma particle emitted by the source while the 440 keV gamma is being detected. We can correct for summing by subtracting the gamma particles emitted by the source that are not 440 keV and implementing this into the same equation used to correct for branching. This is expressed in the following set of equations.

$$\begin{aligned}
 \sigma_{1,440} &= \sigma_1 B_{440} \eta_{440}^P \\
 \sigma_{2,440} &= \sigma_2 B_{1636} \eta_{440}^P (1 - \eta_{1636}^T) \\
 \sigma_{3,440} &= \sigma_3 B_{1951} \eta_{440}^P (1 - \eta_{1951}^T) \\
 \sigma_{4,440} &= \sigma_4 B_{2200} \eta_{440}^P (1 - \eta_{2200}^T) \\
 &\quad + \sigma_4 B_{564} \eta_{440}^P (1 - \eta_{564}^T - \eta_{1636}^T + \eta_{564}^T \eta_{1636}^T) \\
 \sigma_{5,440} &= \dots
 \end{aligned} \tag{2}$$

where  $\sigma_i$  is the partial cross section of the parent nuclei,  $^{24}\text{Mg}$ , decaying to a specific excited state of  $^{23}\text{Na}$  after evaporating a proton,  $B_i$  represents the branching ratio of the gamma that cascades to the 440 keV gamma,  $\eta_{440}^P$  is the peak efficiency of the 440 keV gamma, and  $\eta_\gamma^T$  is the total efficiency of a specified gamma. The sum of the 440 keV

gammas is acquired for each proton channel using each channel's specified equation. This yields the actual observable cross section of 440 keV gamma emitted from a particular proton channel and then detected by a Ge detector,  $\sigma_{i,440}$ .

## 2.3 Calculating Cross Section

The  $^{12}\text{C} + ^{12}\text{C}$  fusion reaction has been measured in a energy range of 4.1 MeV to 6.5 MeV in the center of mass frame using the  $^{12}\text{C}^{2+}$  beam from the FN tandem accelerator at University of Notre Dame. The beam intensity is below 500  $\mu\text{A}$ . A 20  $\mu\text{g}/\text{cm}^2$  C foil is used as a target. Two Faraday cups are placed before and after the target to measure the change of the charge state. The gamma rays from the reaction is detected by a Ge detector placed at  $90^\circ$  with respect to the beam direction to minimize the Doppler shift effect. A sample gamma ray spectrum is shown in Figure 2. The fusion cross section for

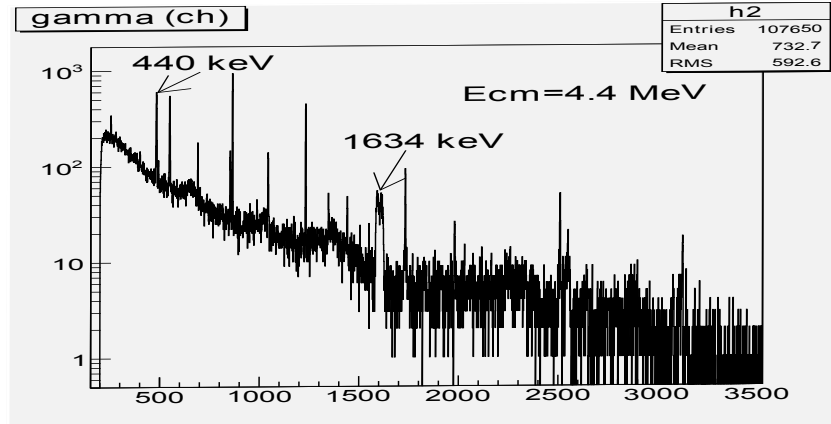


**Figure 2:** Sample gamma ray spectrum at 4.4 MeV center of mass.

the proton channel can be determined using Equation 3,

$$\sigma_p = \frac{N_{440}}{\epsilon_{440} C_{440}} \frac{1}{N_{beam} N_s} \quad (3)$$

where  $N_{440}$  depicts the number of 440 keV gamma recorded by our detector,  $\epsilon_{440}$  is the absolute efficiency at the 440 keV peak,  $C_{440}$  is the correction factor which is ratio of the observed 440keV cross section and the actual fusion cross section for the proton channel as shown in Eq. 2. The particle fusion cross section used in the calculation is taken from ???. In Equation 3,  $N_{beam}$  is the total number of incident  $^{12}\text{C}$  beam particle, and  $N_s$  is the aerial density of the target in particles per millibarn. For thin target measurement (beam particle loses little energy inside of target), the greater the density of the target, the higher the probability of an impinging  $^{12}\text{C}$  ion to react with a stationary target. The same principle works with increasing the number of moving ions.

### 3 Results and Discussion

Our results, labeled "REU", are compared with those of Aguilera[4], High[5], Patterson[6], Becker[3], and Mazaraki[7] in Figure 3. As you can see the data converges from about 5.3 to 6.5 MeV<sub>c.m</sub>, however there is discrepancy from 5.3 MeV<sub>c.m</sub> to lower energies. This may be due to different target thickness and large energy shifts between the different experimenters as depicted by Barnes, Trentalange, and Wu[8]. The error of the beam particle is estimated as 5%. However, the target density is based on the number provided by the supplier. It needs to be checked with an independent measurement, such as measuring alpha energy loss in the carbon foil. Branching and summing effects must always be corrected since it is dependent on the detector used. It is widely known that larger detectors seem to have a greater summing effect due to their greater exposure area. The dependence of the correction factor on the Ge detection efficiency is investigated using a Geant4 simulation. We noticed an inverse relation between the detector efficiency and

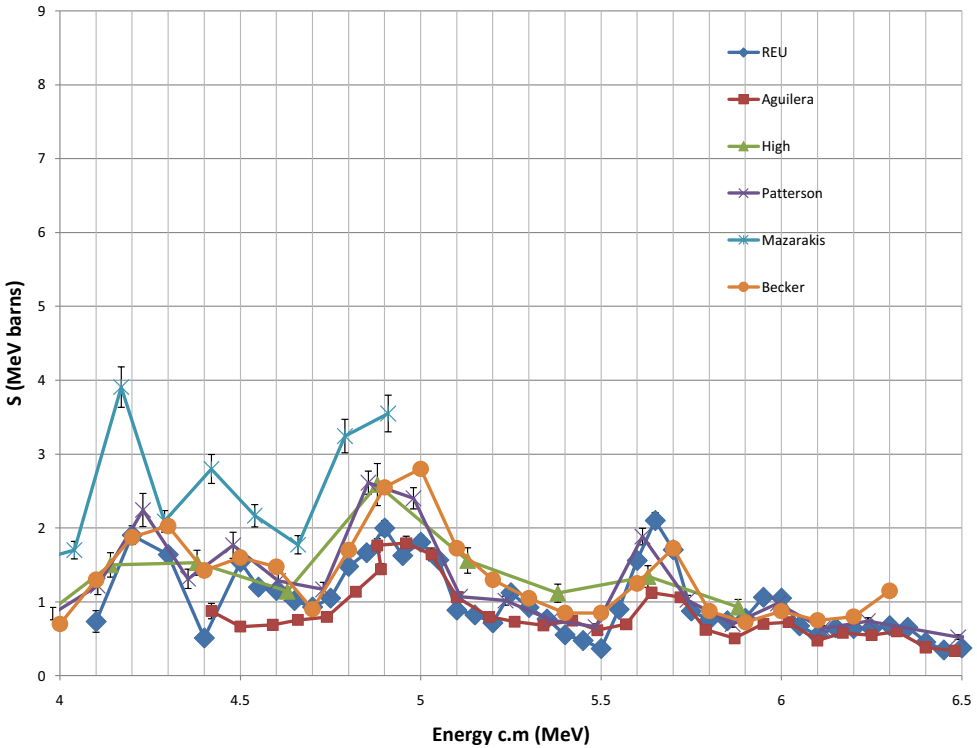


**Figure 3:** Modified S factor (see 1 for definition) for the proton channel from various experimenters between 4 and 6.5 MeV in the center of mass frame.

corrected partial cross section. This is shown in Figure 4.

One may think that using the same detector in every experiment would lead to the same branching and summing effect contribution, but then beam intensity, target thickness, accelerator settings, and the detector's distance from the collision point, amongst other things, must also remain unchanged. These are conditions that, even under the most favorable conditions, will not remain intact. For future experiments, an experimental standard should be placed. For the sub-barrier fusion reaction, because the cross section is very sensitive to energy, a careful beam energy calibration is required. The target thickness is also crucial for the yield determination as well as the effective beam

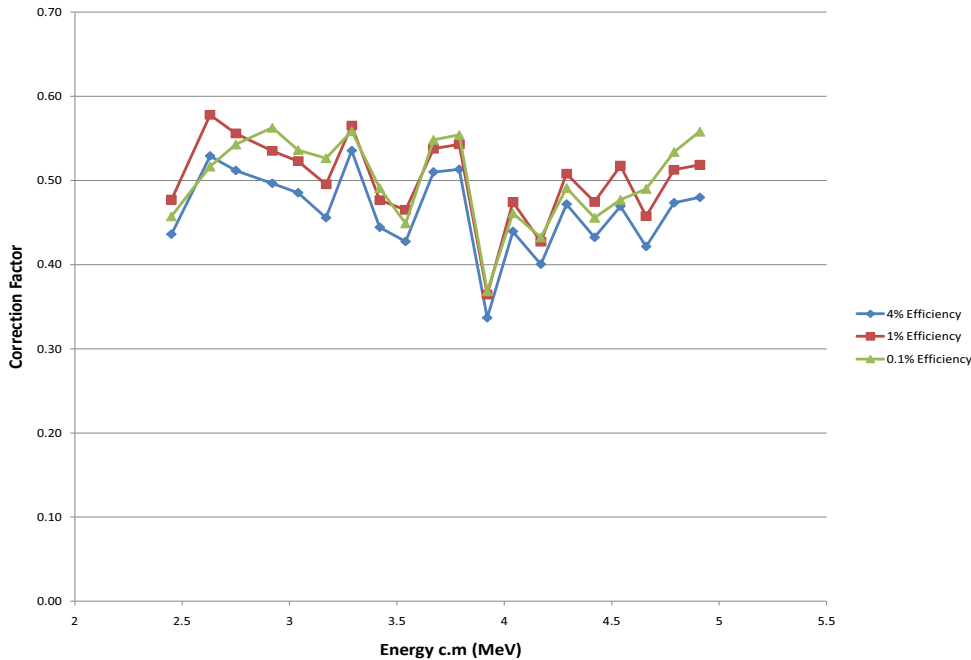


**Figure 4:** Correction factor based on simulations of three different Ge detectors with 0.1%, 1% and 4% peak efficiency at 440 keV respectively.

energy. Because of carbon build up problems, the target thickness is a function of integrated dose of the beam particle. In the future experiment, the target thickness needs to be monitored with elastically scattered beam particle. A complimentary thick target measurement is useful.

## Acknowledgements

I'd like to thanks the NSF for funding my research experience at the University of Notre Dame. My gratitude is also extended to Dr. Umesh Garg for giving me the opportunity to be part of the REU program. Many thanks to Ms. Shari Herman and Ms. Susan Baxmeyer for their kindness and concern. I am extremely grateful to Dr. Xiao-Dong Tang, Brian Bucher, and Xiao Fang for their help, support, advice, and endless patience.

## References

- [1] Kettner, K.U., "The  $^{12}\text{C} + ^{12}\text{C}$  Reaction at Subcoulomb Energies." In *Zeitschrift fr Physik A Hadrons and Nuclei*, 65-75. Springer Berlin / Heidelberg, 1980.
- [2] Fowler, W. A., 1983, Experimental and Theoretical Nuclear Astrophysics; the Quest for the Origin of the Elements, in Ekspang, G., ed., *Nobel Lectures, Physics 1981-1990*, World Scientific Publishing Co., Singapore, 172-229.
- [3] Becker, Hans-Werner. "Teilchenspektroskopische Untersuchungen Zur Absorption Unter Der Barbiere Bei Der  $^{12}\text{C} + ^{12}\text{C}$  Reaktion." Ph.D. diss., Institut fur Kernphysik Munster
- [4] E. F. Aguilera, P. Rosales, E. Martinez-Quiroz, G. Murillo, M. Fernndez, H. Berdejo, D. Lizcano, A. Gmez-Camacho, R. Policroniades, A. Varela, E. Moreno, E. Chvez, M. E. Ortz, A. Huerta, T. Belyaeva, and M. Wiescher. "New  $\gamma$ -ray measurements for  $^{12}\text{C} + ^{12}\text{C}$  sub-Coulomb fusion: Toward data unification" *Physical Review C*, 2006.
- [5] High, M.D., Cujec, B. "THE  $^{12}\text{C} + ^{12}\text{C}$  SUB-COULOMB FUSION CROSS SECTION" In *Nuclear Physics A282*, 181-188. North-Holland Publishing Co., Amsterdam.
- [6] Patterson, J.R., Winkler, H., Zaidins, C.S. "Experimental Investigation of the Stellar Nuclear Reaction  $^{12}\text{C} + ^{12}\text{C}$  at Low Energies" In *The Astrophysical Journal, Vol. 157*, 367-373. University of Chicago, 1969.
- [7] Mazaraki, M.G., Stephens, W.E. "Experimetal Measurements of the  $^{12}\text{C} + ^{12}\text{C}$  Nuclear Reactions at Low Energies" In *Physical Review C, Vol. 7 #4*, 1280-1287. 1973.
- [8] "Heavy ion reactions in Nuclear Astrophysics," C.A. Barnes, S. Trentalange, and S.C. Wu, Treatise on Heavy-ion Science, edited by D. A. Bromley, Vol. 6, p. 3 (Plenum, New York, 1985).

# MBE Growth and Characterization of ZnTe and Nitrogen-doped ZnTe on GaAs(100) Substrates

Dakota O'Dell

2010 NSF/REU Program  
Department of Physics, University of Notre Dame

*Advisors:*  
Jacek K. Furdyna, Xinyu Liu

## 0 Abstract

In this paper, we investigate the interfacial, electrical, and optical characteristics of ZnTe and p-type ZnTe:N thin films grown on lattice-mismatched GaAs(100) substrates by molecular beam epitaxy (MBE) to determine the suitability of GaAs as a substrate for a proposed integrated 6.1 $\text{\AA}$  III-V/II-VI semiconductor solar cell. The interface between GaAs and ZnTe was examined with transmission electron microscopy (TEM) and high-resolution transmission electron microscopy (HRTEM). In addition, the hole concentrations and mobilities of the samples were determined with magneto-transport measurements, and the band structure was determined by photoluminescence (PL) spectroscopy. Despite a high lattice mismatch, the TEM images revealed a low density of defects, indicating that high quality ZnTe can be grown on GaAs, and the magneto-transport and photoluminescence data are generally consistent with heavily-doped ZnTe. We conclude that GaAs can be used as a substrate for the 6.1 $\text{\AA}$  lattice solar cell project, instead of the more costly, lattice-matched GaSb, and that the nitrogen plasma used in the MBE can effectively dope ZnTe to sufficiently high concentrations. Further work on the solar cell project can now continue, with the next immediate goal being the n-type doping of ZnTe with Al donors.

## 1 Introduction

While high-efficiency solar cells are very desirable for both space and terrestrial applications, the current photovoltaic market is dominated by single-junction Si-based cells which have a maximum theoretical efficiency of just 31% under 1 sun. [1] Multi-junction solar cells can cover a much larger range of the solar spectrum, and can thus convert a much higher percentage of the incoming solar energy. The current record for solar cell efficiency is held by a

triple-junction GaInP/GaInAs/Ge cell at 40.7% achievable energy conversion efficiency under 240 suns. [2]

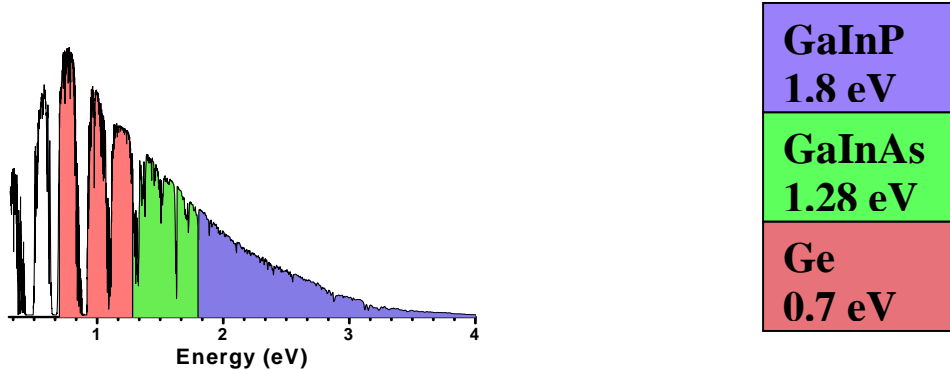


Figure 1: The energy spectrum of a 40.7% efficiency triple-junction solar cell.

For this cell, seen in Figure 1, the efficiency could be further increased by adding additional junctions with band gaps in the infrared part of the solar spectrum, but such an endeavor is complicated by the lack of appropriate lattice-matched materials. We propose that the ideal material system for a high- efficiency multi-junction solar cell is a series of monolithically integrated III-V and II-VI semiconductors with lattice constant around  $6.1\text{\AA}$ , as shown in Figure 2 below.

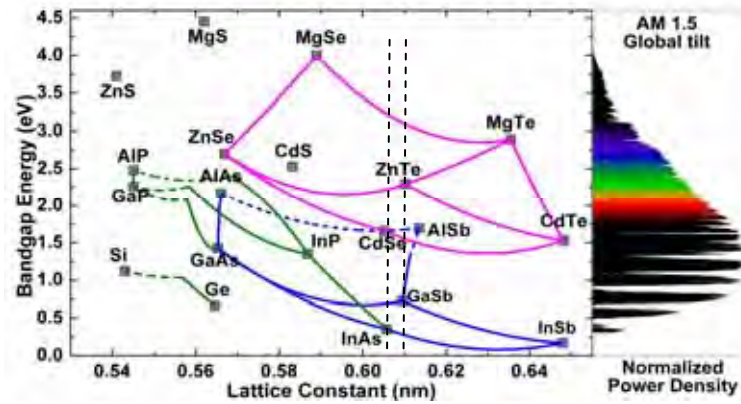


Figure 2: A comparison of band gap energy for the  $6.1\text{\AA}$  materials to the normalized solar spectrum.

Because there are more lattice-matched materials to use, integrated III-V and II-VI

semiconductor solar cells have the potential to have many junctions. Moreover, the 6.1Å lattice constant materials have band gap energies which are more optimized to the solar spectrum. The result is that a III-V/II-VI cell can be made far more efficient than current solar cell technology.

A four-junction model of such a solar cell, with an achievable energy conversion efficiency of 40% under 1 sun and 48% under 1000 suns, is currently being developed at the University of Notre Dame in collaboration with Arizona State University. The cell was originally designed to be grown on lattice-matched GaSb substrates, but preliminary results indicated that far cheaper, but lattice-mismatched GaAs might be a suitable alternative. This paper concerns the growth and characterization of ZnTe and p-type ZnTe:N on GaAs(100) substrates to investigate that hypothesis.

## 2 Sample Growth

The samples for characterization were grown in the University of Notre Dame dual-chamber molecular beam epitaxy (MBE) laboratory. Epilayers of ZnTe were deposited onto GaAs(100) substrates, followed by epilayers of ZnTe:N, which were doped p-type by means of a nitrogen plasma, in the proportions shown in Figure 3.

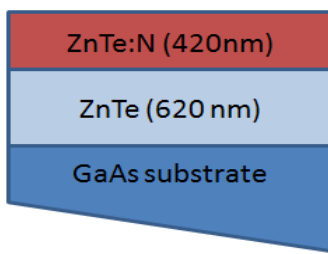


Figure 3: The dimensions of the GaAs/ZnTe/ZnTe:N samples

The flux of the nitrogen plasma during growth was varied to create a distribution of doping

concentrations in the samples.

### 3 Methods of Characterization

#### 3.1 Transmission Electron Microscopy

To investigate the effects of the 8% lattice mismatch between GaAs and ZnTe, the interface between the two materials was imaged via transmission electron microscopy (TEM) and high-resolution transmission electron microscopy (HRTEM) by the group at Arizona State University led by D.J.Smith. For TEM, beams of electrons are transmitted through an ultra-thin sheet of a material and focused, forming a magnified image of the sample being observed, much like in a conventional light microscope. Because the de Broglie wavelength of the electron is significantly smaller than the wavelength of visible light, the transmission electron microscope can resolve single atoms, providing a way to analyze the lattice structure and interfacial defects of the material directly.

#### 3.2 Magneto-transport

The electrical characteristics of the samples -- in particular, the hole concentrations and mobilities of the ZnTe:N layers -- were determined with magneto-transport measurements, which are dependent on the Hall effect. Five gold wires were soldered to each sample in the configuration shown in Figure 4.

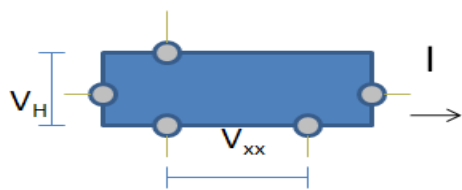


Figure 4: A sample with Ohmic contacts for magneto-transport measurements. The longitudinal and Hall voltages are marked.

The sample was mounted in a sample holder and wired into a current source and a series of

voltmeters. The sample assembly was then placed in a cryostat which allowed temperature control and application of an external magnetic field to the sample. A current was passed through the sample, and the magnetic field was swept from -0.75 T to 0.75 T. A voltage  $V_{xx}$  was applied across the longitudinal dimension of the sample (i.e., the direction of the current), and the motion of the charges due to  $V_{xx}$  in turn produced a voltage  $V_H$  along the transverse direction of the sample -- the phenomenon caused by the Lorentz force, known as the Hall effect. Using the voltmeters, we measured both  $V_{xx}$  and  $V_H$ , from which Ohm's Law yields the resistivities  $\rho_{xx}$  and  $\rho_H$ . These quantities allow us to calculate the hole concentration  $p$  and the hole mobility  $\mu$  using equations (1) and (2) below:

$$\rho_{xx} \approx \frac{1}{peB} \quad (1)$$

$$\rho_H \approx \frac{1}{peB} \quad (2)$$

After determining the hole concentrations and mobilities at room temperature, the temperature of the cryostat was lowered, and these measurements were taken again at 250, 200, 150, 100, 50, and 25 K.

## Photoluminescence

The optical characteristics of the samples -- and the band gap energy in particular -- were investigated by photoluminescence (PL) spectroscopy. For the PL measurements, light from a 45mW laser was directed onto the sample to excite electrons within the material from the valence band to the conduction band. The electrons are unstable in the conduction band states, and fall back to their equilibrium valence band state, releasing their excess energy by emitting photons equal to the energy difference between the bottom of the conduction band and the top of the

valence band. By detecting and analyzing the photons emitted from the sample, the band gap energy of the material can be determined.

## 4 Results,

### 4.1 TEM

The results of the transmission microscopy are shown in Figure 5 below.

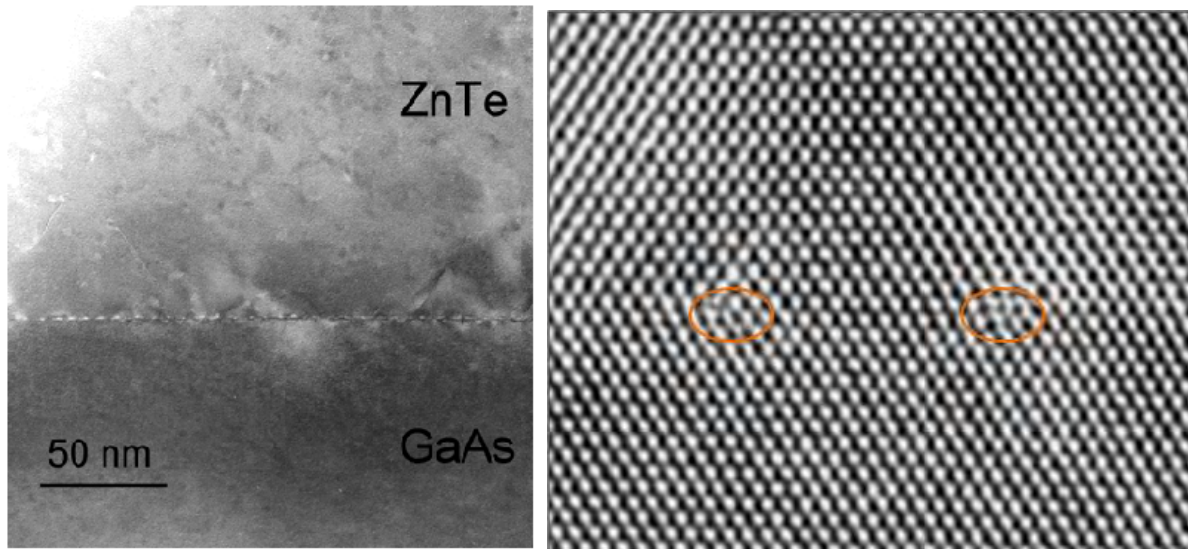


Figure 5: TEM images of the interface between GaAs and ZnTe

Despite the 8% lattice mismatch, the TEM images reveal a high-quality crystal growth with an unexpectedly low density of defects. In the lower resolution TEM, the defects which are present in the crystal appear in a nearly regular pattern — an analysis of the HRTEM reveals that they occur as nucleation centers on the interface with a period of about 13 times the ZnTe lattice constant, or 14 times the GaAs lattice constant. The following calculation shows the effective reduction of the original 8% lattice mismatch:  $13a_{\text{ZnTe}} = 79.348 \text{\AA}$ ,  $14a_{\text{GaAs}} = 79.146 \text{\AA}$ , resulting in a lattice mismatch of 0.255% (!) between the two crystalline layers.

## Magneto-transport

The magneto-transport data for one sample are presented below.

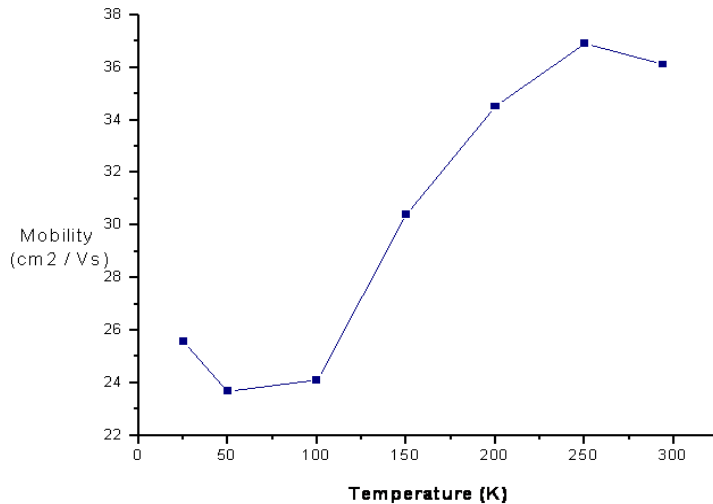


Figure 6: Hole mobility as a function of temperature

Hole mobility is related to scattering; as the amount of scattering within the lattice increases, the mean free path decreases, and the hole mobility similarly decreases. At low temperatures, the dominant form of scattering is ionized impurity scattering, which scales as  $T^{-3/2}$ . As the temperature increase, therefore, one would expect that the mobility would increase. The data shown in Figure 6 agree with this prediction.

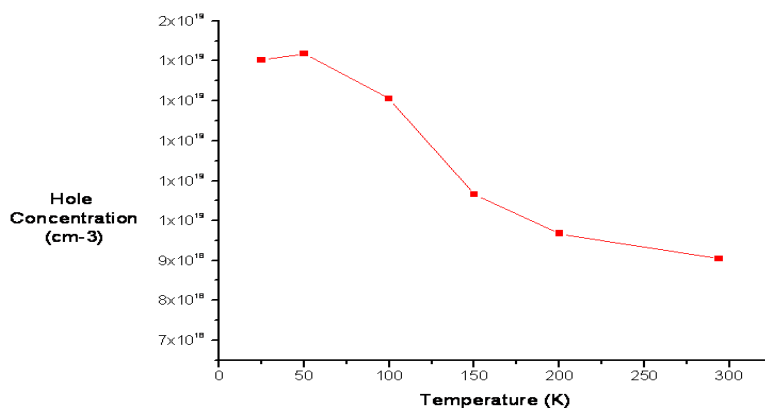


Figure 7: The hole concentration for one sample as a function of temperature

By contrast, the temperature dependence of the hole concentration, shown in Figure 7, does not agree with predictions. It takes very little energy for an electron to be trapped by an acceptor site, and thus as the temperature increases, more electrons will be thermally promoted to the impurity band. The exodus of electrons will leave more holes in its wake, and thus the hole concentration should increase with increasing temperature; however, the data suggest the opposite trend. The reason for this behavior is as yet a matter of speculation, and further investigation will be necessary to gain understanding of the physical process responsible for this unexpected behavior.

## Photoluminescence

The photoluminescence data agrees well with prediction. The PL spectrum, seen in Figure 8, shows a maximum intensity at 2.32 eV, which is consistent with prior measurements of the ZnTe band gap energy.

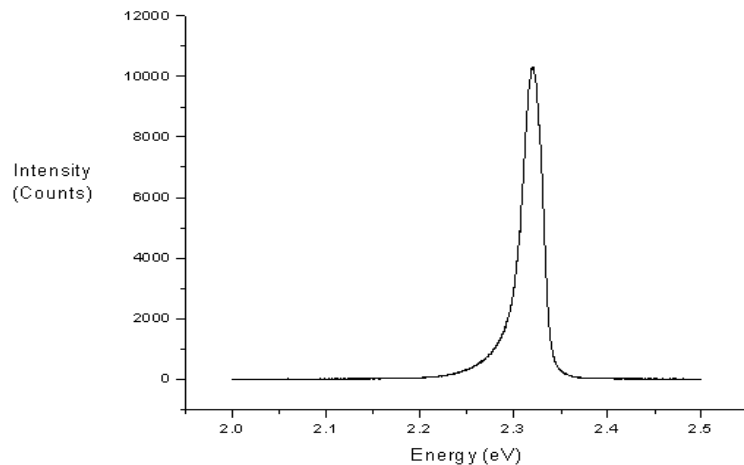


Figure 8: The photoluminescence spectrum for GaAs/ZnTe/ZnTe:N. The maximum intensity occurs at 2.32 eV.

The intensity of the ZnTe peaks is also rather high, with counts of over 100,000 in some samples. This is indicative of heavy doping, as interband transitions in intrinsic ZnTe are very difficult to detect via photoluminescence.

## 5 Conclusions

Although the full characterization of GaAs/ZnTe/ZnTe:N is not yet complete, the preliminary results are promising. Our results have demonstrated that – while a lattice mismatch of 8% should make high-quality growth of ZnTe on GaAs substrates infeasible – the 0.255% “effective lattice mismatch” existing between the two materials is small enough to make the use of GaAs substrates a definite possibility. Moreover, the TEM imaging indicates that lattice relaxation occurs within a few monolayers of the interface, indicating that the rest of the ZnTe crystal has a very small density of defects. The use of GaAs as a substrate as opposed to GaSb would then very significantly reduce production costs of integrated multijunction solar cells, thus increasing the range of potential applications.

In addition to the question of substrates, the results for characterizing the doping in the ZnTe:N layer are also interesting. The photoluminescence and mobility data are suggestive of a heavy p-type doping, and thus an encouraging indication of the efficacy of the nitrogen plasma doping in the MBE. The hole concentration data, however, display a trend opposite to what would be expected for either an intrinsic or extrinsic semiconductor. While this last result merits further investigation, the rest of the data -- interfacial, electrical, structural, and optical -- supports the potential use of a GaAs/ZnTe junction in the proposed 6.1 Å III-V/II-VI solar cell project.

## **6 Future Work**

Future work on this project will consist of two parts: further research on GaAs/ZnTe/ZnTe:N, and research for the next phase of solar cell design. With regards to the former, the focus will be on further magneto-transport data collection and electrical characterization. For the latter, the next materials development goals will be to achieve good n-type doping in ZnTe with Al donors, and the optimization of n- and p-type dopings in ternary II-VI materials.

## **7 Acknowledgments**

I would like to thank R. Pimpinella and K. Tivakornsasithorn for laboratory assistance and training, my advisors X. Liu and J.K. Furdyna for their continued support and guidance, M. Dobrowolska for the use of her laboratory equipment, and NDnano for generously providing the funding which made this research possible.

## **8 References**

- [1] W. Shockley and H. J. Queisser, JAP **32**, 510 (1961)
- [2] R. R. King et al., Appl. Phys. Lett. **90**, 183516 (2007)



# A Study of Gold Nanoparticles Using Laser Transmission Spectroscopy

Robert H. Schafer

2010 NSF/REU Program

Physics Department, University of Notre Dame

Advisors: Professors Steven Ruggiero and Carol Tanner

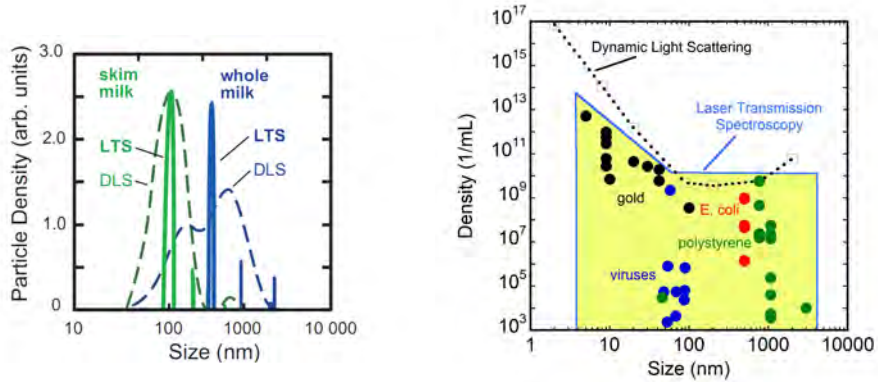
## **Abstract**

Gold nanoparticles are an important widely used material, with applications ranging from pharmaceutical delivery to tumor destruction to electron microscopy. I utilized a novel measuring system, Later Transmission Spectroscopy (LTS), to quickly and accurately size these particles. The properties of gold nanoparticles vary widely based on the geometry and size, so an accurate measurement of these characteristics is essential. I studied several different sizes of gold nanoparticles, from 100 nanometers all the way down to 5 nanometers. To obtain accurate results, the plasmon resonances were compensated for in the data reduction. Results indicated that LTS is a useful tool for future gold nanoparticle work. The system was able to accurately detect and measure all of the different sizes of particle. LTS will prove a useful tool for the characterization of gold nanoparticles.

# 1 Introduction

## 1.1 Laser Transmission Spectroscopy

Laser Transmission Spectroscopy (LTS) is a new approach for the characterization of colloidal suspensions of nanoparticles. Using a laser that is tunable over a large range of wavelengths, LTS offers remarkable increases in sensitivity and precision. Developed recently by Professors Steven Ruggiero and Carol Tanner and Dr. Frank Li, this technology is promising for many reasons. The enhanced sensitivity allows a very accurate particle sizing. Previous techniques, such as Dynamic Light Scattering, could only give broad size distributions over tens or even hundreds of nanometers. LTS has achieved sharp size distributions, down to a resolution of 1 nanometer. LTS also has the capability to ascertain the geometry of particles. Rod shaped objects will show up as two peaks, one for the length and one for the width. Another quantity that LTS is able to measure is the density of particles in solution. With these three main capabilities, you can do any number of experiments. Previous work has included the tracking of live organism growth, the study of DNA folding in solution, liposome aggregation and fusion, and Aluminum Oxide sizing. [1]



A comparison of DLS and LTS results for milk. LTS produces sharper, more accurate peaks.

The sensitivity of LTS over many different materials, sizes, and densities.

DLS is displayed as well.

Biological systems are ideal for LTS because it allows accurate measurements of particles in solution. Previous measuring techniques just would not cut it with biological systems. Traditionally, microscopy was accepted as the most accurate technique for sizing. But it presents several difficulties. The number of particles could not be determined without hand-counting of all of the particles on the substrate. the main issue was that the particles needed to be dried out onto a substrate. For biological systems, this could alter their physical characteristics in many ways. The natural state of biological particles is to be in solution, and this drives much of their function. Diffraction and DLS were able to work with particles in solution, but left much to be desired with their sensitivity and precision when it came to sizing. They also were unable to derive the geometry. LTS allows you to deal with the particles in solution, to determine the absolute density, the geometry, and the size at remarkable precision.

## 1.2 Colloidal Gold

This work will focus on the sizing of gold nanoparticles. Gold nanoparticles have recently become important in widely varying fields. But the use of colloidal gold goes back hundreds of years. Colloidal gold suspensions below 100 nm have a red color to them; at larger sizes they are more yellow. To achieve red or yellow stained glass, gold impurities were mixed in with the silica.

### 1.2.1 Production

The most common method for attaining colloidal gold suspensions is by chemical means. Reduction of chloroauric acid, ( $\text{H}[\text{Au Cl}_4]$ ), allows one to create monodispersed particles across a range of sizes. The acid is dissolved in water and stirred at a constant, fast rate. Sodium citrate,  $\text{Na}_3\text{C}_6\text{H}_5\text{O}_7$ , or another reducing agent is then added to the solution. This reducing agent will donate electrons to the  $\text{Au}^{3+}$  ions, neutralizing them. eventually, the solution becomes supersaturated with neutral gold atoms, and they begin to precipitate. The first particles to form are very small, less than a nanometer in diameter. These act as seeds for the precipitation of more gold atoms. The constant mixing ensures that the rate of deposition onto the seeds is consistent in the solution. To prevent aggregation between these newly formed particles, a surfactant or other stabilizing agent is used. The sodium citrate can perform this task, as the negative citrate ions will surround the gold nanoparticles, creating an electrostatic repulsion between particles. To manufacture different sizes of gold nanoparticles, from 5 to 100 nm, the initial concentration of chloroauric acid can be adjusted.<sup>[1]</sup>

### 1.2.2 Uses

Gold nanoparticles are being used widely in biological fields. One of the

most common uses is in immunogold labeling. This method attaches secondary antibodies to the gold nanoparticles. These functionalized nanoparticles are then used to bind to specific targets within a cell. These gold-target systems are then imaged with electron microscopy. The gold will show up highly contrasted to the rest of the cell, allowing a precise determination of location. LTS would be extremely useful in multi-target staining. To attach to multiple targets, more than one size of nanoparticle is used, with different antibody or protein attachments. The resultant image will show multiple sites with different gold particles connected. LTS will be able to differentiate between differently sized gold nanoparticles, and sometimes even between non-connected particles and connected ones. This could be used as a quick test for the presence of a specific protein in a sample.

Other uses for gold nanoparticles in the biological fields are as treatment for arthritis, Alzheimer's, drug carriers, and tumor detection.<sup>[2][3][4][5]</sup> To properly understand the effect the gold nanoparticles will have on the inner workings of the human body, it is crucial to understand the exact size and shape of these particles. LTS provides a fast, easy way to do that in solution.

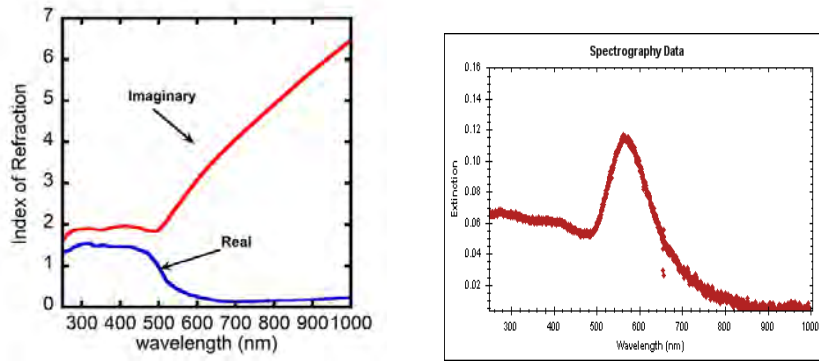
### **1.2.3 Electromagnetic Properties**

Gold has interesting electromagnetic properties as well. The gold nanoparticles scatter electromagnetic radiation according to the Mie solutions to Maxwell's equations. The extinction cross section over the range of wavelengths and the transmission are factors in the Beer-Lambert law; with these known, it is possible to solve for the density distribution. Mie theory provides this cross section.

In previous experiments with LTS, the real part of the index of refraction has been the only part used. The imaginary part was disregarded. But with gold nanoparticles, the imaginary part of the index of refraction begins to dominate

within the region we are working in. This is because of the surface plasmon resonance. The electrons gathered on the surface of the particle begin to oscillate due to the excitation from the external electromagnetic field. They achieve a resonant frequency that depends on the geometry and size of the particle, as well as the medium the gold is in. This resonance shows up clearly in the extinction spectrum of the sample, so it must be factored into the data reduction. The below extinction spectrum shows a peak where the plasmon resonance starts.

[1]



The extinction spectrum of 100 nm gold.

The index of refraction for gold. The plasmon resonance begins where the imaginary part rises sharply.

## 2 Methods

### 2.1 Data Reduction

Once I had properly diluted the sample, I measured its transmission as a function of wavelength using a cuvette of pure water as a reference spectrum. This transmission function was then modified into the extinction by taking its negative natural logarithm. This extinction function was loaded into an

inversion program. Through several matrix decompositions, the inversion code finds the most accurate fit for the density distribution.

The density distribution file had a specific density associated with each size. I ran my experiments from 0-200 nm, with a 1 nm resolution. Only the data points past 270 nm were considered; before that, noise dominated the experimental data.

The plasmon resonance was compensated for within the inversion code, using the index of refraction information. The program was able to compensate for the different onsets of the resonance between different sizes of colloidal gold. The results show that the plasmon resonance was accurately canceled out.

## 3 Discussion

### 3.1 Results

I ran six different sizes of gold nanoparticles, 5, 9, 20, 30, 50, and 100 nanometers. The results came out cleanly. In some instances, peaks were off by 1-2 nanometers. Given the resolution of the apparatus, this is acceptable error. The next page has a table with all of the resultant images.

### 3.2 Future

#### 3.2.1 Experiments

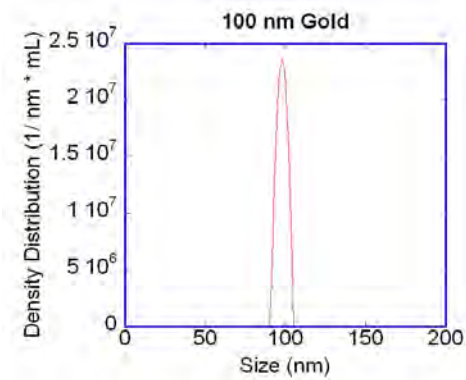
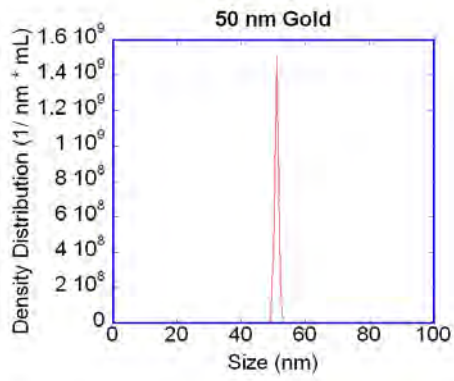
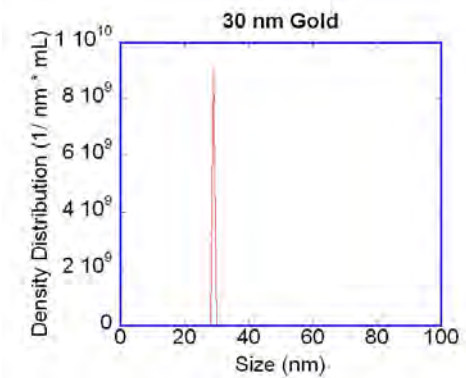
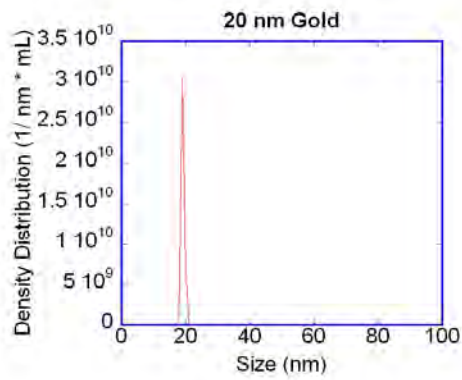
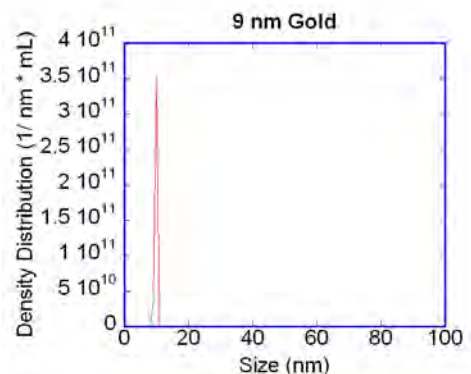
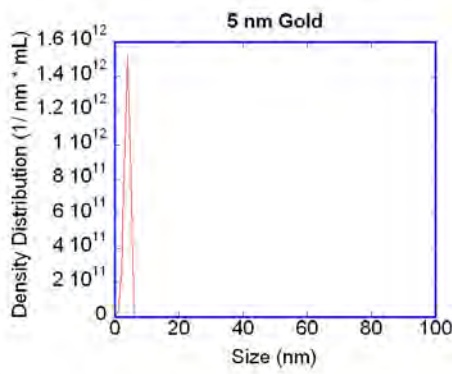
In this experiment, I did not focus on the density of the solutions. I instead investigated the sizing of the particles. Future experiments could vary the level of dilution instead of the size of particle. LTS has already proven that it can distinguish between different densities of solution, but verification could be achieved with gold.

Given the nature of multi-target immunogold labeling, a mixture of sizes would be an interesting experiment. LTS should be able to detect multiple sizes of gold particles within the same sample, and return that information as multiple peaks on a density distribution.

### **3.2.2 Applications**

Accurate sizing of gold nanoparticles would be useful wherever they are used. The medical field could definitely benefit from being able to gain this information quickly. LTS can obtain this information in a matter of minutes, whereas other techniques could take hours.

Modeling of biological systems has become more commonplace as computer power has increased. This modeling could greatly benefit from accurate size distributions. The programs that do this modeling would return better results, and more uses of gold nanoparticles could be discovered.



## 4 Acknowledgments

I would like to thank Professors Ruggiero and Tanner, my advisors, for giving me the opportunity to work with them. I would especially like to thank Dr. Frank Li for his immense help on this project and on all of my other endeavors. I am grateful for Dr. Garg and Mrs. Shari Herman for their work and patience in organizing this REU. Most of all, I would like to thank all of the other REU participants for giving me such a memorable summer.

## 5 References

1. Li, Frank F. "Laser Transmission Spectroscopy: A Discussion of Technique and Studies of Biological Systems." Diss. University of Notre Dame, 2010. Print.
2. Qian, Ximei. "In vivo tumor targeting and spectroscopic detection with surface-enhanced Raman nanoparticle tags." *Nature Biotechnology*. 2008. Vol 26 No 1.
3. Paclitaxel-Functionalized Gold Nanoparticles Jacob D. Gibson, Bishnu P. Khanal, and Eugene R. Zubarev *J. Am. Chem. Soc.* 2007, 129, 11653-11661
4. CY, Tsai. *et al.* "Amelioration of Collagen-induced Arthritis in Rats by Nanogold." *Arthritis and Rheumatism* 56.2 (2007): 544-54. PubMed.gov. Web. 5 Aug. 2010.
5. Pissuwan, D., SM Valenzuela, and MB Cortie. "Therapeutic Possibilities of Plasmonically Heated Gold Nanoparticles." *Trends in Biotechnology* 2nd ser. Feb.24 (2006): 62-67. PubMed.gov. Web. 5 Aug. 2010.



# **Critical Current and Vortex Lattice Properties in Superconducting MgB<sub>2</sub>**

**KIMBERLY SCHLESINGER**

**2010 NSF/REU Program**

**Physics Department, University of Notre Dame**

**ADVISOR: Prof. Morten Eskildsen**

**GRADUATE STUDENT COLLABORATORS:**

**Catherine Rastovski and Pinaki Das**

**ABSTRACT:** Magnesium diboride ( $MgB_2$ ) is a type-II superconductor, with a mixed state characterized by the presence of discrete vortices of magnetic flux passing through the material, arranged in an orderly vortex lattice (VL). Several experiments were performed to determine the characteristics and behavior of superconducting  $MgB_2$  and its VL under various conditions. Using a SQUID magnetometer, magnetization hysteresis loops were measured at various temperatures for three single-crystal  $MgB_2$  samples. The results were used to estimate the value and the field and temperature dependence of the critical current density ( $J_c$ ) in  $MgB_2$ , according to the Bean model. The configuration of the VL in  $MgB_2$  was studied with small angle neutron scattering (SANS), in order to both map out the phase diagram of VL phase transitions within the mixed state, and explore the behavior of previously observed metastable configurations.

## SUPERCONDUCTIVITY AND VORTICES

Superconductors have an electrical resistance of zero below a certain material-specific critical temperature ( $T_c$ ), which falls anywhere between a few mK and over 100 K in currently known superconductors. This makes them invaluable in numerous technological applications, due to their ability to carry a current of any magnitude without heat dissipation when cooled sufficiently. There has been active research interest both in discovering and fabricating new superconducting materials with higher critical temperatures, and in deepening understanding of this phenomenon by exploring the properties of known superconductors. This paper will focus on experiments conducted on  $MgB_2$ , a known two-band, two-gap superconductor [2].

Superconductors are generally divided into two classes. In type I superconductors, the Meissner state, in which all magnetic field is expelled from the material, occurs below  $T_c$  and a very low critical applied magnetic field  $H_{c1}$ ; otherwise, superconductivity vanishes completely. However, type II superconductors such as  $MgB_2$  have two distinct superconducting states: the Meissner state below  $H_{c1}$ , and a "mixed state" between upper and lower critical fields  $H_{c1}$  and  $H_{c2}$  (Fig. 1 [2]), where some magnetic induction does exist, although the surrounding material remains superconducting. The mixed state is characterized by the presence of discrete lines of

magnetic flux, or “vortices,” passing through the material, which arrange themselves in an orderly vortex lattice (VL) (Fig. 2 [4]). These vortices of magnetic flux are screened from the surrounding Meissner state by circling supercurrents; the supercurrent density in a given material required to cause the vortices to move is known as the critical current density ( $J_c$ ).

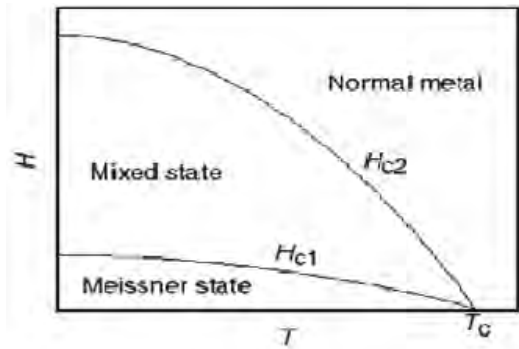


**Figure 1:** Temperature-field phase diagram for a type-II superconductor, including the Meissner, mixed, and normal states. [2]

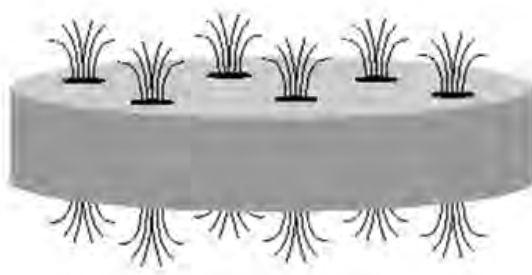


**Figure 2:** Illustration of discrete flux lines passing through a type-II superconductor. Superconductivity is destroyed in the black cores, while the gray remains superconducting. [4]

$\text{MgB}_2$  has a  $T_c$  of approximately 39 K, and a hexagonal VL below  $H_{c2}=3.1$  T. Three distinct phases of lattice orientation have been observed in the mixed state of  $\text{MgB}_2$ , as shown in figures 3 and 4. In the  $\alpha$ -phase, opposite peaks are aligned with the crystalline a-axis; in the  $\gamma$ -phase, they are rotated so that the a-axis lies directly between them [4]. The  $\beta$ -phase is characterized by split peaks as the lattice goes through the continuous 30-degree transition between  $\alpha$  and  $\gamma$  (Fig. 4 [2]). This paper will describe SANS study of transition lines between and within these phases.

## MAGNETIZATION HYSTERESIS LOOPS AND CRITICAL CURRENT

Using a SQUID magnetometer, several measurements were taken of the magnetization in two single-crystalline samples of  $\text{MgB}_2$  and one enriched sample of  $\text{Mg}^{11}\text{B}_2$ . Considerable magnetic hysteresis is observed in these materials when an external magnetic field is

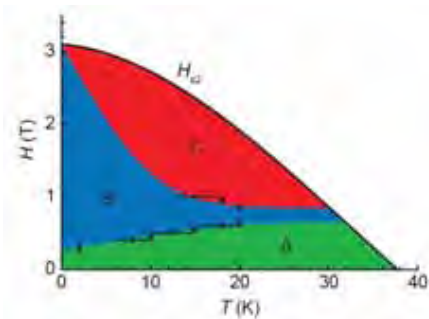


**Figure 3:** Phase diagram for  $\text{MgB}_2$ , showing the  $\alpha$ -,  $\beta$ -, and  $\gamma$ -phases (here marked as A, B, and C respectively).

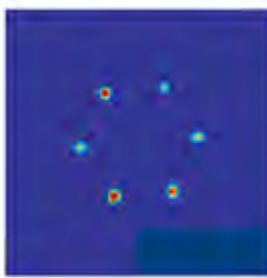


**Fig. 4a:**  $\alpha$ -phase [2]

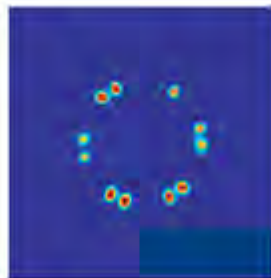


**Fig. 4b:**  $\beta$ -phase [2]

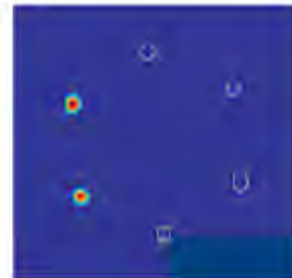


**Fig. 4c:**  $\gamma$ -phase [2]

applied. To obtain hysteresis loops, consecutive magnetization measurements were made over a wide range of fields, first while ramping the field up in steps, and then while ramping down. For all measurements, the sample was aligned with the crystalline c-axis parallel to the applied field and cooled with zero field applied (known as a zero field cool, or ZFC), with the initial temperature at or above 40 K, exceeding  $T_c$ . Hysteresis loops running from -1.5 T to 1.5 T in intervals of approximately .03 T were measured on the first oriented sample. For better resolution of the drastic change in magnetization seen at very low fields, these measurements were repeated over a narrower range of -0.4 T to 0.4 T, with a finer step size of .019 T. Similar high-resolution measurements were made on the samples at temperatures of 2.5, 5, 10, and 15 K. An example of hysteresis loops obtained in this manner, with the magnetization values normalized to the area of the sample, can be seen in figure 5.

These results were analyzed with the goals of estimating a maximum critical current for

$\text{MgB}_2$  and  $\text{Mg}^{11}\text{B}_2$  and determining the dependence of critical current on applied field.

According to the Bean model [1], the relation of the magnetic hysteresis to the critical current density in a type II superconductor at a given applied field  $H$  is given by

$$J_c(H) = 20 \frac{\Delta M(H)}{d}, \quad (1)$$

where  $d$  is the sample thickness in cm,  $\Delta M(H)$  is the difference between the magnetization values for increasing field and decreasing field at a particular applied field value, measured in emu/cm<sup>3</sup>, and  $J_c(H)$  is the critical current in A/cm<sup>2</sup> [3]. Applying this analysis to the measured hysteresis loops, it is seen that the critical current decreases drastically with applied field, and that the maximum value of  $J_c$  increases with decreasing temperature (fig. 6).

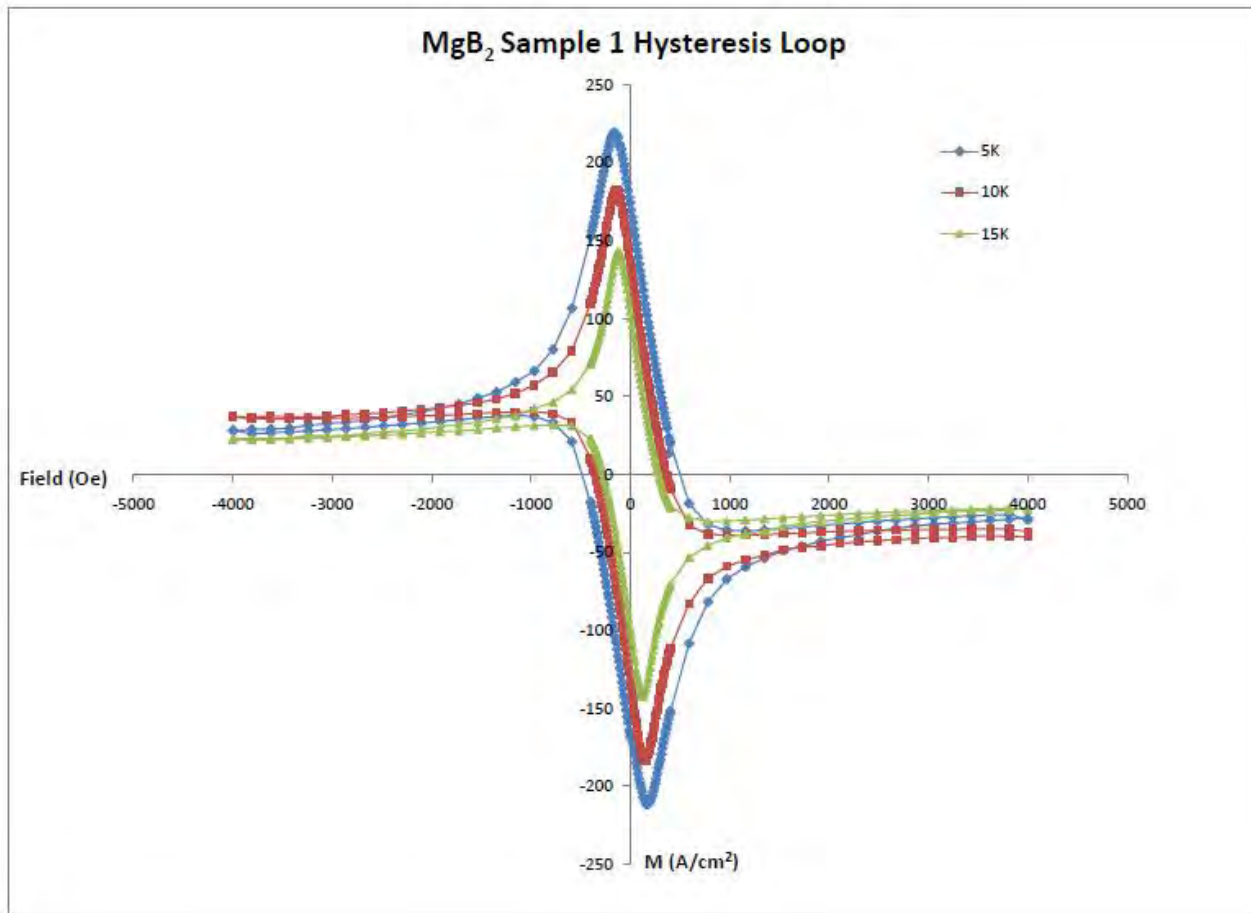


**Fig. 5:** Magnetic hysteresis loops obtained for an  $\text{MgB}_2$  sample at 5 K, 10 K, and 15 K.

The loop's height,  $\Delta M(H)$ , is used to determine  $J_c$ .

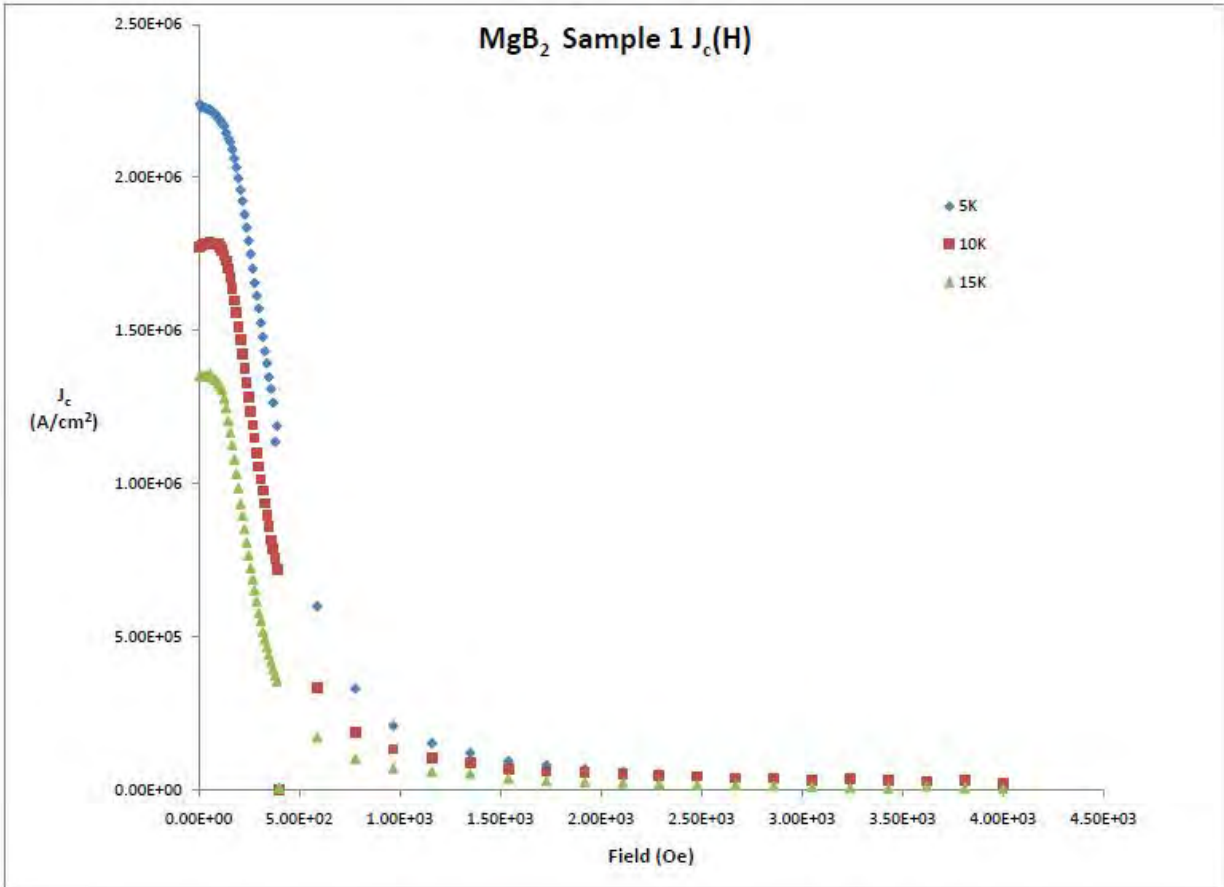


**Fig. 6:** Plot of  $J_c$  versus the applied field  $H$  for the same  $MgB_2$  sample at 5 K, 10 K, and 15 K.  $J_c$  decreases sharply as  $H$  increases, and maximum  $J_c$  is higher at lower temperatures.

### SMALL ANGLE NEUTRON SCATTERING (SANS)

SANS was the primary tool used for studying VL orientation in this experiment. Since neutrons have no charge, they will pass through matter without interacting; however, their magnetic moment ensures that they will scatter off the lines of magnetic flux which form the vortex lattice. Considered quantum mechanically, neutrons have a definite wavelength related to their momentum, so they scatter off the vortices and onto a neutron detector in a manner analogous to the scattering of photons when passed through small slits and projected on a screen. Distinct peaks are formed at scattering angles that satisfy Bragg's law of scattering, which is given by

$$\lambda = 2 \delta \sin\theta , \quad (2)$$

where  $\lambda$  is the neutron wavelength,  $\delta$  is the VL spacing, and  $\theta$  is half the total scattering angle.

The SANS experiment setup requires the neutron beam to pass through several stages (fig. 7).

First, it meets the velocity selector, a drum with slots in it through which neutrons can pass.

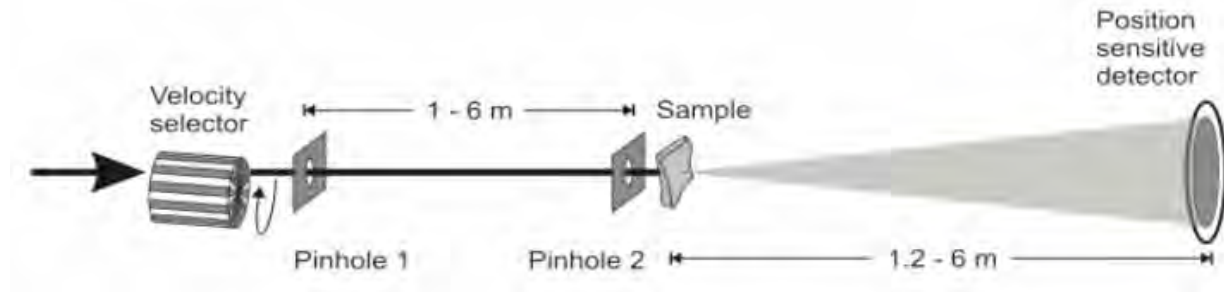


**Figure 7:** Diagram of SANS experimental setup [4]

When the drum is set to rotate at a constant frequency, only neutrons of one particular velocity and wavelength can pass through. In this experiment, wavelengths of 5 and 7 Å were used. Next, the beam passes through two apertures, the source aperture and the sample aperture, in the collimation section controlling its width [4]. Source apertures of 40 mm and 20 mm and sample apertures of 2 mm and 0.5 mm were used for a very tight collimation. The beam then interacts with the sample, which is placed in a cryomagnet whose temperature and field can be controlled, and the diffracted neutrons enter a large vacuum tank, where they fly for 19.3 m before hitting the neutron detector. The diffraction pattern on the detector can be viewed and analyzed using a piece of software called GRASP [4]. Figure 3 contains examples of GRASP images for the MgB<sub>2</sub> hexagonal VL.

#### SANS STUDY OF MgB<sub>2</sub> AT OAK RIDGE NATIONAL LABORATORY (ORNL)

From July 30 to August 3, 2010, a SANS study of MgB<sub>2</sub> and its VL was conducted at ORNL.

One purpose of this study was to complete the phase diagram for MgB<sub>2</sub> (fig. 8 [2]), since the

transition lines drawn here are largely extrapolations. Although results of the experiment have not yet undergone final analysis, preliminary analysis indicates a confirmation of the location of the  $\alpha$ - $\beta$  transition line at 5, 10, and 20 K. Higher-field measurements were also made at both 1.7 T and 1.4 T to look for the  $\beta$ - $\gamma$  transition line. At 1.7 T, the transition occurred approximately between 8 and 9 K; at 1.4 T, approximately between 9 and 10 K. Another measurement suggested that the 1.2 T transition occurred at about 10 K. These results indicate that the  $\beta$ - $\gamma$  transition line ascends much more steeply than was previously conjectured.

Measurements were also made of the splitting angle between  $\beta$ -phase peaks at several fields and temperatures, which will eventually be used to create contours within the  $\beta$  region of the phase diagram showing the rate of the transition from  $\alpha$  to  $\gamma$  in more detail.

### SANS STUDY OF METASTABLE STATES

Another goal of this experiment was to explore the behavior of previously observed metastable states in MgB<sub>2</sub>. Metastable states occur when one VL phase is “frozen in” to the sample, so that even when a transition line is crossed, the VL does not change orientation as expected, but remains in the frozen-in state, although it is less energetically favorable. These metastable states can be obtained by “field cooling,” or setting the field while above T<sub>c</sub> and cooling the sample through the  $\alpha$ - or  $\gamma$ - phase while the field remains in place. The result is a frozen-in  $\alpha$  or  $\gamma$  orientation observed even in the  $\beta$  region. Once the metastable state is obtained, a field wiggle with an amplitude of several mT will cause a transition to the ground state ( $\beta$ ).

At ORNL, a systematic study was done of the amplitude required to cause this transition. Because of concerns about uncontrollable fluctuations in the magnetic field during a wiggle, simple 2 mT drops in field were used instead. Beginning with a field cool into a metastable  $\alpha$ -

phase at 0.53 T and approximately 2 K, about 10 field drops of 2 mT each, for a total field drop of approximately 20 mT, were required to fully drive the VL into the ground state  $\beta$ -phase.

The same procedure was repeated at 2 K, this time field cooling to a metastable  $\alpha$ -phase at 0.43 T. Considering the earlier result that  $J_c$  increases sharply at lower fields, we predict that at this lower field the VL will be able to withstand a larger field drop before returning to the ground state. This seemed to be confirmed, as it took somewhere between 24 mT and 30 mT of field drops to reach a stable  $\beta$ -phase.

This SANS study, informed by the results of critical current density measurements on MgB<sub>2</sub>, was mostly successful in exploring both metastability and ground state configurations in the VL of this material. Although much can be inferred from the preliminary analysis, including a possible refinement of the location of the  $\beta$ - $\gamma$  transition line and a better understanding of what is necessary to bring the VL to the ground state from a metastable state, the possible error of these measurements is substantial, and further analysis is required to fully understand exactly what has been learned in this experiment. This analysis will be completed in the near future, and further SANS research has also been planned to further investigate the VL of this unusual superconductor.

## REFERENCES

- [1] C. P. Bean, "Magnetization of high-field superconductors," *Reviews of Modern Physics*, (1964).
- [2] M. R. Eskildsen, "Small-Angle Neutron Scattering Studies of the Vortex Lattice in Type-II Superconductors," presentation given at Michigan State University CM seminar, (2010).
- [3] M. Murakami, "Melt Processed High-Temperature Superconductors," *World Scientific*, (1992).
- [4] T. O'Brien, "Magnetic Vortex Properties of the MgB<sub>2</sub> Superconductor," Notre Dame NSF/REU program, (2009).



# **Diffusion as a Rate Limiting Effect On Microtubule Dynamic Instability**

**Adam Siegel**

2010 NSF/REU Program

Physics Department, University of Notre Dame

Mark Alber

Holly Goodson

# DIFFUSION AS A RATE LIMITING EFFECT ON MICROTUBULE DYNAMIC INSTABILITY

ADAM D. SIEGEL<sup>1,3,5</sup>, MARK ALBER<sup>2,3</sup>, HOLLY GOODSON<sup>3,4</sup>, ZILIANG XU<sup>2,3</sup>

Submitted on August 7, 2010

## ABSTRACT

Microtubules play an integral part in cell organization and subcellular structure, including the transportation of organelles and separation of chromosomes during mitosis. The key aspect of microtubules behavior that makes this possible is dynamic instability, stochastic growth and shortening of these proteinaceous structures which allows for exploration of the cell. Based on a previous study (Odde 1997), it is clear that diffusion does not have a rate limiting effect on microtubule assembly. However this paper does not address the effect of diffusion on dynamic instability. We use the diffusion equation as the mathematical model for the dynamics of the molecular interactions of tubulin, coupled with a mesoscopic scale microtubule model to study whether diffusion has any effect on the behavior of the microtubules during dynamic instability. Namely, we mesh a second order accurate Crank-Nicolson finite difference scheme for solving diffusion equation with the mesoscopic microtubule Monte Carlo model to understand the conditions resulting in diffusion whaving a restrictive effect. Parallelization and code optimization techniques are implemented due to deal with long time steps, such that the effects of dynamic instability become prominent (namely, during steady state interactions of the microtubule with its environment). This research may have profound implications in many respects, as microtubules are the target for numerous anticancer drugs, and understanding their interactions are imminent for anticancer therapy.

*Subject headings:* Computational Biophysics — Computational Cellular Dynamics, Microtubules, Cellular Dynamic Instability, Microtubule Dynamic Instability

## 1. INTRODUCTION

Microtubules (MTs) are responsible for routinely carrying out many cellular tasks including the transportation of organelles from different parts of the cell by consecutively bonding down the microtubule, support the cell by forming the rigid cores in sub-cellular bodies (such as those in the mitotic spindle), and participate in mitosis by bonding to and pulling apart the chromosomes before the cell divides (Howard & Hyman 2006, Howard and Hyman 2009). Considerable interest is taken in the need understand how MTs behave and regulate the cell. The motivation to understand this comes from the necessity to understand how the cytoskeleton is regulated, because this will help facilitate the development of microtubule directed drugs for things like cancer therapy. Since MTs are responsible for the separation of the chromosomes during mitosis, cancer directed drugs target microtubular networks. It is necessary and imminent to understand the exact mechanism behind microtubule dynamic instability to determine exactly which factors effect their resultant behavior, and to what extent.

This outwards bending of protofilaments is a result of the agitation experienced by the MT when the longitudinal bonds are lost. GTP tubulin acts as a more stable environment for the MT than its GDP counterpart. Spontaneous hydrolysis can give rise to the loss of the GTP cap, causing catastrophe. The main goal of this research is to understand exactly how the

process of dynamic instability takes place; the precise mechanism of the loss of the GTP cap, and under which conditions this will occur.

### 1.1. *Microtubules*

MTs are long chains of proteins composed of  $\alpha$  and  $\beta$  tubulin dimers, and are found in the cytoskeleton of all living cells (see Figure 1 (a)). These tubulin dimers are proteins that assemble back to back by hydrolyzing Guanosine triphosphate (GTP) to Guanosine diphosphate (GDP) via a chemical reaction that occurs spontaneously in order to minimize their free energy. In doing so, these dimers form long polymer chains that can reach tens of microns in length, called protofilaments. In addition to bonding laterally, these dimers also possess the capability to bond horizontally- 13 (sometimes more, sometimes less) protofilaments bond together horizontally to comprise one microtubule. Whether or not these bonded protofilaments first form as a sheet which folds in upon itself via some chemical interruption or if it forms initially as a cylindrical structure is still an open question. At the seam of a closed MT, there is a three monomer shift between the initial and last of the protofilaments, which results in an A lattice, such that the  $\alpha$  monomers bond directly to the  $\beta$  monomers. Structural analysis of the MT configuration advocates longitudinal bonding between chains of dimers (heterodimers) is much stronger than lateral bonds (Margolin et. al. In Prep. 2010). This observation leads to belief that loss of a GTP cap promotes catastrophe (see below).

After the initial formation of these MTs, stochastic processes take over- they irregularly (but repeatedly), undergo *catastrophe* and *rescue* (Figure 1 (b)). Collectively, this unstable “dance” is referred to as microtubule dynamic instability (henceforth, DI). Diffusion in cells is NOT a fast enough process to be able to distribute all nutrients to the proper location within a cell, nor is the cell small enough that nutrients within the cell will be able to get to their desired location without be-

<sup>1</sup> Summer 2010 REU Student: Department of Physics & Applied Mathematics, The University of Notre Dame - Notre Dame, IN

<sup>2</sup> Interdisciplinary Center for the Study of Biocomplexity, University of Notre Dame - Notre Dame, IN

<sup>3</sup> Department of Applied and Computational Mathematics and Statistics, University of Notre Dame - Notre Dame, IN

<sup>4</sup> Department of Chemistry and Biochemistry University of Notre Dame - Notre Dame, IN

<sup>5</sup> Department of Physics & Astronomy, The State University of New York - Stony Brook, Stony Brook, NY

ing brought there. For instance, single nerve cells extending from the spine to fingers in humans would otherwise be unable to transport nutrients throughout the entire cell, since the diffusivity of tubulin through cytoplasm is so low in comparison to the length of cell. Therefore, the purpose of DI is to commission the cytoskeleton to seek out and explore the area inside the cell to find the nutrients for transportation, as well as do things like bond to the kinetochores of chromosomes during mitosis (Howard and Hyman 2009).

In vitro (in living cells) biologists witness the stochastic growth and shrinkage of these microtubules. These MTs are anchored at centrosomes (microtubule “growing stations” from which they nucleate). These centrosomes are composed of centrioles, which are in turn surrounded by pericentriolar proteins (Howard and Hyman 2003). They remain fixed to the centrosomes throughout the cells life growing outwards into the cytoplasm, therefore differing from microtubules observed in vitro (during experiments). In vitro, microtubules are usually grown separated from the centrosome and beginning with some concentration of tubulin dimers, they irregularly assemble and disassemble, where in the process they can lose or gain thousands of dimers in one event, which is similar to the characteristics of instability witnessed in vivo. The exact cause of the sudden change from growth to shrinkage or vice versa has still not been experimentally verified, however there is theoretical evidence that this process is caused by the gain or loss of a GTP-Tubulin cap. As stated above, it has been theorized that the horizontal bond of a GTP cap is more stable than one composed of GDP. Therefore, when this cap disappears, the protofilaments bend outwards as dimers are lost (see Figure 1 (c)).

### 1.2. Probable Effects on Microtubule Dynamics

Previous work by Odde (Odde 1997, amongst others) has led to the conclusion that diffusion does not have a rate limiting effect on MT assembly. This is due to the fact that tubulin can diffuse rapidly relative to the assembly rate of MTs. Using the diffusivity of sea urchin eggs as the average diffusivity of tubulin ( $5.9 \times 10^{-12}$ , Salmon et. al. 1984), the average elongation of a MT will be about an order of magnitude less than the average displacement of tubulin in the same time (Odde 1997). In addition, it has been shown that the rate limiting effect in association is not likely to be translational diffusion, but other factors (Northrup and Erickson 1992). Researchers in the field have thus far only specifically pointed this out with respect to MT assembly.

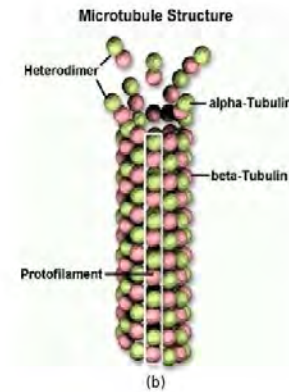
Many in the field remain convinced that diffusion *will* play a prominent role in MT dynamic instability. For one, the rates of growth and shrinkage may not be the same during dynamic instability as they are during phases of initial growth. Therefore, although the diffusivities measured by Salmon et. al. may be general, the growth rate of MTs may not be the same. As a result, if tubulin is not present, it won't be able to attach. This would result in the inability of MTs to grow. The probability of the loss of a GTP cap may be such that while the MT is not growing (or loosing tubulin), the GTP cap is lost due to hydrolysis, giving the MT no choice but to shrink. Our plan to will be to run the simulation with and without diffusion, and see whether the MTs interact differently with tubulin during dynamic instability.

### 1.3. Monte Carlo Methods

The Monte Carlo method for numerical simulation is a powerful method that relies on consecutive stochastic (ran-



(a)



(b)

### "Dynamic instability"

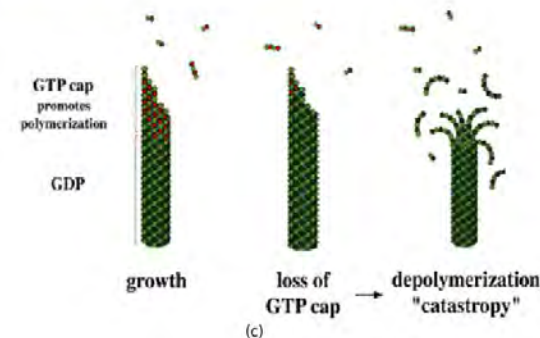


FIG. 1.— (a) Microtubules in a cell. This is an experimental image of microtubules in a cell, stained with green dye in order to ascertain their shape. (b) Depiction of a standard 13 protofilament microtubule. The microtubule is composed of long chains of  $\alpha$  and  $\beta$  tubulin dimers that bond back to back to form individual protofilaments. (c) After the loss of the GTP cap, the horizontally unstable bonds are insufficient to hold together the structure of the MT. Therefore, the MT undergoes catastrophe, as dimers fall unattach. Theoretically, the MT must wait until it obtains a stable GTP cap before it can grow again.

dom) sampling in order to emulate an event that occurs seemingly adventitiously. This method can be utilized for a variety of different things, from computing basic integrals to our case of using it for MT simulation. For instance, consider the integral

$$\int_0^1 x^2 dx. \quad (1)$$

This is easily evaluated analytically ( $\frac{1}{3}$ ). However, There are many integrals (even some trivial looking) that can not be evaluated analytically, because the antiderivatives do not exist. For simplicity, we utilize the Monte Carlo method to solve the integral in equation 1. We chose a square zone that is

1 unit length squared:  $0 \leq x, y \leq 1$  (see Figure 2 (a)). We pick some number of points to randomly put in the box (Figure 2 (b) shows the case of 10, (c) the case of 100, and (d) the case of 1000). Various random points are chosen by utilizing a random number generator on a computer. Then, the amount of points that lie below the curve is summed, as is the amount of points that lie above the curve. Taking the ratio of the amounts of points that fall under the curve to those that lie above the curve will give an approximation to the integral.

The rest of the figures (more data points) are not shown, however this can be repeated for any number of points. Figure 3 shows a study when the amount of points are increased (up to  $10k$ ). A decrease in accuracy was not observed. Although very useful for evaluating integrals with no analytic solution, we do not utilize Monte Carlo techniques for this reason. For our purposes, we are interested in Monte Carlo simulations because we can utilize random numbers to see if specific events will occur. For instance, at any given time step in the simulation, tubulin can attach to any of the protofilaments. Since we assume diffusion to be instantaneous, if the tubulin concentration is above a specific level, we randomly choose if it will attach or not. The same can be done for hydrolysis of GTP tubulin to GDP tubulin. This is what gives rise to catastrophe: the GTP tubulin cap is randomly lost and the MT falls apart. Ultimately, mathematicians would like to come up with some mathematical model to decide if events such as these will occur, and under which given conditions.

## 2. MESOSCOPIC MODEL

The current model being used is the result of work done mainly by Dr. Ivan Gregoretti for his PhD thesis in December 2007 (Gregoretti 2007). It is a mesoscopic model, meaning it does not model individual monomers or dimers, but “bricks” of previously bonded dimers. A more advanced dimer-scale model developed at the University of Notre Dame does exist, however it does not yet have the capability of simulating multiple interacting microtubules as the mesoscopic scale model does, in addition to running much slower due to the fact that it models events on much smaller scales (Margolin et. al. in Prep 2010). Therefore, the mesoscopic scale model was chosen for diffusion to be incorporated.

An important feature of this model is that it actually shows dynamic instability. Starting with first principles and a random number generator (for Monte Carlo purposes), information about MTs interacting with tubulin and the rest of the cellular environment was incorporated into the model. Multiple MTs were simulated to interact with each other to see what would happen (Gregoretti et. al. 2006). DI was readily achieved in steady state, as shown in Figure 4.

The simulation starts out with MTs of essentially zero length. Initially, every MT has just one GTP brick “cap” that will cause initial growth in a semi-stable manner (until the GTP cap is lost). At each time step, the MT can either grow, shrink, or pause at its length. The simulation picks MTs randomly (Monte Carlo) and decides what will happen. The behavior is determined by the current tubulin concentration. For each randomly chosen MT, the tubulin concentration is used to modify the MT’s activities. Based on the tubulin concentration that is returned, the simulation decides if the MT can grow, shrink, or stay at its current length. Note that the amount of tubulin available locally is the same at each node, since diffusion is not taken into account. Physically, this means that tubulin diffuses instantaneously, which may not always be a physically realizable situation (see Section

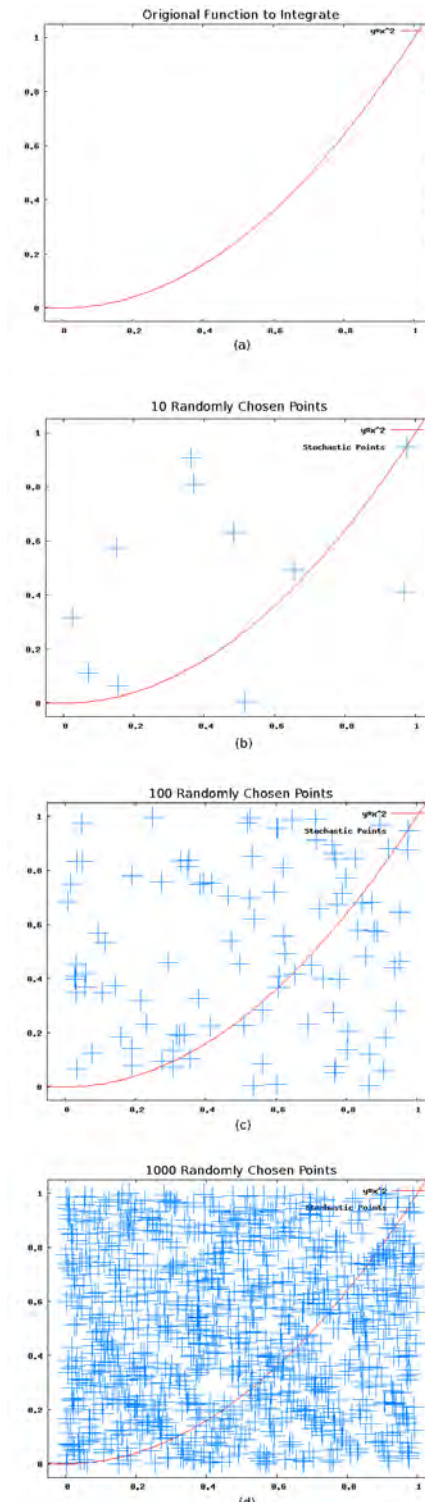


FIG. 2.— Monte Carlo method to evaluate the integral  $\int_0^1 x^2 dx$ . Each test was only run once in this case. (a) The initial set-up. The box is of length 1 on each side. The integral that must be evaluated is shown. (b) Run with 10 points. The result of the integral is 0.2. (c) Run with 100 points. The result of the integral is 0.33. (d) Run with 1000 points. The result of the integral is 0.328.

1.2). The simulation also currently utilizes physical boundary conditions (for example, the MT can now grow outside of the cell, etc.). After the length is checked, the type of tubulin is modified. MTs are picked randomly and their GTP caps have

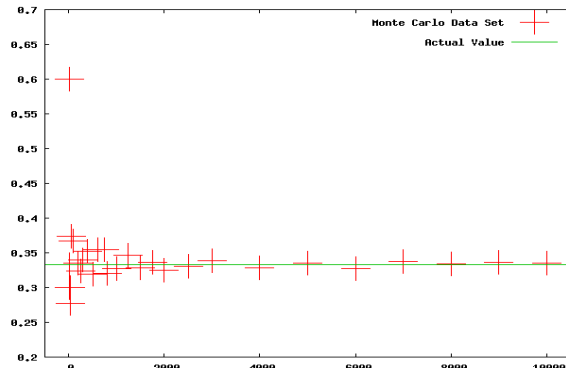


FIG. 3.—Increasing the amount of random points brings the approximation to the integral closer and closer. The green line represents the actual value and the random data points are in red. This study was done up to  $50k$  random points (data point not shown), and a decrease in accuracy was not observed. Each point represents the average of three trials.

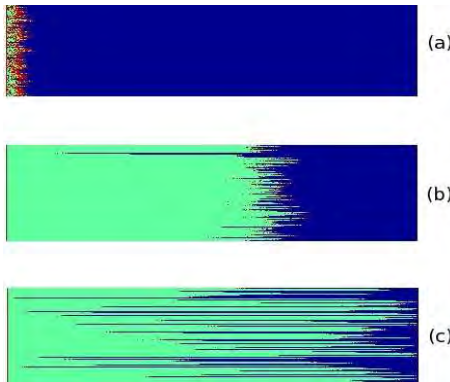


FIG. 4.—Mesoscopic Monte Carlo simulation results in arbitrary units of time. This simulation was run with 128 MTs, each with a maximum length of 512 (arbitrary units of length). (a)  $T = 70$ , this is prior to the MTs achieving steady state. (b)  $T = 1548$ , Effects of DI are just starting to occur as steady state interactions are beginning. (c)  $T = 3329$ , Effects of DI are prominent and steady state interactions of MTs are fully developed.

a chance to be hydrolyzed to GDP. As noted before, it is theorized that this causes the protofilaments of the MT to become less stable, therefore more prone to fall apart. The simulation checks this information at each remaining time step.

There are a few things that should be noted about the current model. First, it does not model individual monomers or dimers, but large “bricks” of tubulin. It runs very quickly (less than a minute on a modern processor for 128 MTs with a maximum length of 512 arbitrary units and 20k time steps. Modelling individual dimers is much more computationally expensive and does not allow uniprocessor simulations to be run in short amounts of time. Second, dynamic instability is prominent in this model (Figure 5 (a)), just as it is with the dimer scale model (Figure 5 (b)). They both show the effects of dynamic instability asserting that our theoretical understanding of instability is a correct one.

As noted before, diffusion is not taken into account in the current version of the model. Section ?? describes how diffusion may very well have a rate limiting effect on dynamic instability. We are currently working to update the most contemporary version of the mesoscopic model such that diffusion will be taken into account. Presently, tubulin can be transported to any place within the cell instantaneously. This assumption will hold if the rate of diffusion of tubulin within

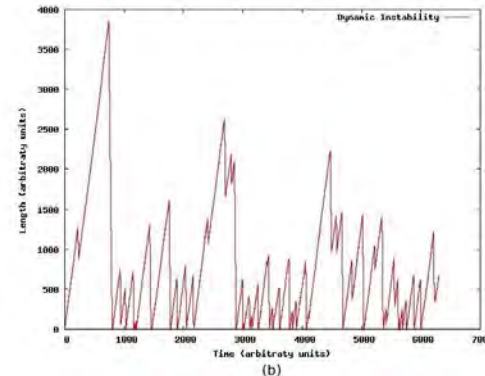
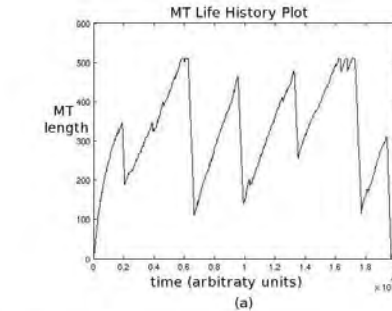


FIG. 5.—Life history plots of MTs. (a) From mesoscopic model. This plot is the life history of the first MT. (b) From dimer scale model. this plot is the life history from the first protofilament, but is almost identical to every other, since there are 13 protofilaments in each MT. Therefore, this represents the life history of one MT.

the cell under ordinary conditions is very high relative to other properties within the cell, such as distance tubulin must travel, speed at which it travels, etc. Our most current attempts to are given in section 4.

### 3. DIFFUSION

Diffusion is the random expansion of particles from an area of higher concentration to an area of lower concentration. It is a general problem that can be applied to many physical situations such as the expansion of a color dye in a glass of water or in this case, the random dispersion of tubulin within a cell. In order to create a model, diffusion is described mathematically by a parabolic partial differential equation (PDE) called the diffusion equation. The particular solution depends on the values the solution takes on the boundaries, and therefore the dependence of diffusion on dynamic instability breaks down to the solution of a boundary value problem meshed with the current mesoscopic simulation.

Diffusion of a substance in a fluid is described mathematically by the diffusion equation

$$\frac{\partial}{\partial t} C = \nabla \cdot (D \nabla C) \quad (2)$$

where  $C$  is the concentration of the substance at any point in the fluid and  $D$  is the diffusivity of the substance in the fluid. The diffusivity can be determined from Stokes-Einstein equation

$$D = \frac{k_B T}{BR\eta} \quad (3)$$

where  $k_B T$  is thermodynamic temperature,  $B$  is a constant,  $R$  is the radius of the particles, and  $\eta$  is the viscosity of the fluid in which the particles are diffusing. This equation gives the relationship between molecular movement and diffusion, since random molecular motion is responsible for diffusion through a fluid. This relationship has been experimentally verified to hold in various scenarios (Miller).

Based on a previous study, the diffusivity of tubulin was measured in sea urchin eggs to be  $5.9 \times 10^{-12} \frac{m^2}{s}$ , and is considered to be the diffusivity of tubulin in the average cell (Salmon et. al. 1984). This diffusivity was not observed to vary over a wide range of values during experimentation, and therefore the diffusivity is taken to be a constant. In addition, the inclusion or loss of a single phosphate is not enough to change the diffusion of the whole protein. Therefore, we can simplify the diffusion model by using a constant diffusivity in equation 2, which then becomes

$$\frac{\partial}{\partial t} C = D \nabla^2 C. \quad (4)$$

Here, we are interested in implementing the diffusion equation on a two dimensional Cartesian plane, since the current model (see section 2) employs MT dynamic instability on a 2-D plane. Therefore, the final version of the diffusion equation will become

$$\frac{\partial}{\partial t} C = D \left( \frac{\partial^2}{\partial x^2} C + \frac{\partial^2}{\partial y^2} C \right). \quad (5)$$

Since equation 5 is second order in two space variables and first order in time, we will need four boundary conditions and one initial condition to fully solve the problem. The most physically realizable boundary conditions in this case are Neumann boundary conditions, specifically, the zero flux boundary condition at every boundary. Therefore, we physically describe this situation of no tubulin leaking out of the cell with zero flux boundary conditions at every boundary of the mesh (see Figure 6). We mathematically describe these boundary conditions with the equations

$$\frac{\partial}{\partial x} C(x=0, y, t) = 0 \quad (6)$$

$$\frac{\partial}{\partial x} C(x=L, y, t) = 0 \quad (7)$$

$$\frac{\partial}{\partial y} C(x, y=0, t) = 0 \quad (8)$$

$$\frac{\partial}{\partial y} C(x, y=L, t) = 0 \quad (9)$$

The initial condition describes a constant amount of tubulin equally spaced through the cell, but can be changed to make the distribution whatever one pleases

$$C(x, y, t=0) = C_0, \quad (10)$$

where  $C_0$  is the initial concentration of tubulin specified at compile time.

Equations 4 and 6 through 10 completely describes the problem. The only thing left is implementing this on a grid, thereby iteratively solving the equation using numerical techniques and meshing this with the current simulation.

### 3.1. Numerical Techniques for Diffusion

This code employs a finite difference Crank-Nicolson scheme to solve the diffusion equation. The particular numerical model is utilized because it is second order accurate in time, but mainly because it is numerically stable in time steps (or at least more so than a regular explicit method). An ordinary explicit method is more easily implemented, however is extremely limited in time steps due to the numerical stability of the scheme via the Courant-Friedrichs-Lowy condition (CFL condition, or just CFL). Mathematically, this conditions states that the numerical domain of dependence of the solution must be larger than that of the physical one. Physically, this means that the propagation speed of any physical disturbance (spreading of the particles in this case) must be smaller than that of its numerical counterpart. Therefore, the physical signal is constrained to only move a certain distance in a single time step (Numerical Methods for the Solution of Partial Differential Equations).

The Crank-Nicolson scheme is an approach that weights half towards an explicit method and half towards an implicit method. The Forward Time Central Space (FTCS) method is explicit and is limited in what it can do in a single time step, however is a easy and fast to use. Therefore, it is averaged with a Backwards Time Central Space (BTCS) method in order to utilize the numerical accuracy. The reason that this method is not fully utilized is due to the fact that it requires solving a system of linear equations at each time step. The Crank-Nicolson method also requires solving a system of equations at each time step, however it is second order accurate as opposed to the first order accuracy of the BTCS method. In addition, the system of equations in matrix form will be sparse, meeting the design capabilities of modern day mathematical software packages designed for the solution of systems of equations.

In order to solve the equation numerically, we first set up the standard two dimensional coordinate grid as in Figure 6. Here, we discretize the equation in time and space using the finite difference Crank-Nicolson method. After discretizing Equation 5, it becomes

$$\begin{aligned} C_{i,j}^{n+1} = & C_{i,j}^n \\ & + \frac{D(\Delta t)}{2(\Delta x)^2} (C_{i+1,j}^{n+1} - 2C_{i,j}^{n+1} + C_{i-1,j}^{n+1} + C_{i+1,j}^n - 2C_{i,j}^n + C_{i-1,j}^n) \\ & + \frac{D(\Delta t)}{2(\Delta y)^2} (C_{i,j+1}^{n+1} - 2C_{i,j}^{n+1} + C_{i,j-1}^{n+1} + C_{i,j+1}^n - 2C_{i,j}^n + C_{i,j-1}^n), \end{aligned} \quad (11)$$

where  $\Delta x$  and  $\Delta y$  are the grid spacings in the x- and y-directions respectively, and  $C_{i,j}^n$  is the concentration at grid point  $i, j$  at time  $n$ .

It is now necessary to utilize the boundary conditions. From the zero flux boundary conditions and a Taylor expansion, we can see that we must have the ghost points equal to the values of the adjacent points. For example,

$$\frac{C_L - C_{L-1}}{\Delta x} = 0 \implies C_L = C_{L-1} \quad (12)$$

where  $C_L$  is a boundary node in the x-direction (at  $x = L$ ). We make this type of substitution at every boundary node to come up with a series of simultaneous equations to solve at every time step.

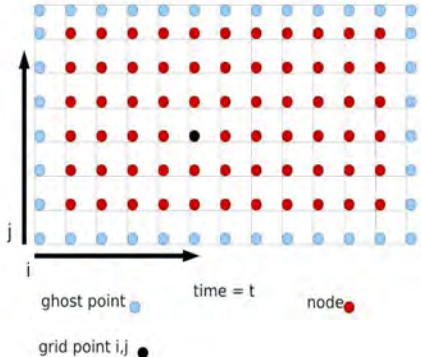


FIG. 6.— A sample two dimensional computational grid. The space coordinates (x- and y-coordinates) are discretized in space in order to use the finite difference method, while the time  $t$  is updated after the concentration at each grid point is solved for the current time step. The black point in the middle represents grid point  $i, j$ , such that the point directly to the right is point  $i + 1, j$  and directly above is  $i, j + 1$ , etc.

### 3.2. PETSc

The Portable, Extensible Toolkit for Scientific Computation (PETSc) is specifically designed to solve equations that result from partial differential equations. It contains thousands of functions and routines that can be utilized. Here, we are specifically interested in those functions that can be used to solve coupled linear equations. It exploits advanced mathematical methods as well as the Message Passing Interface (MPI) standard for parallelization. For this system of equations, we solve using the PCLU solver (direct solver), which utilizes LU decomposition to solve the system of equations. PETSc takes the system of equations in matrix form and splits it up into lower and upper tridiagonal matrices. Using an LU algorithm to solve, PETSc then finds the unknowns. This is done at every step, and offers a great advantage to other conventional methods of solution, such as row reduction (see Figure 7). PETSc is so useful in this situation because the matrix that must be solved is sparse. Therefore, most elements are zero, and row reduction is overkill in this case. It is more computationally efficient to use a different method offered by PETSc for such cases.

Therefore, solving the diffusion equation over a large grid does not pose a problem (it is much more computationally efficient than row reduction) Figure 8 shows snapshots taken at time step 0 (initial) and time step 100 for a grid 90 x 90 nodes. Therefore, there are 8100 linear equations to be solved simultaneously, and took PETSc an average of just over 100 seconds to solve this system. See presentation for full diffusion animation.

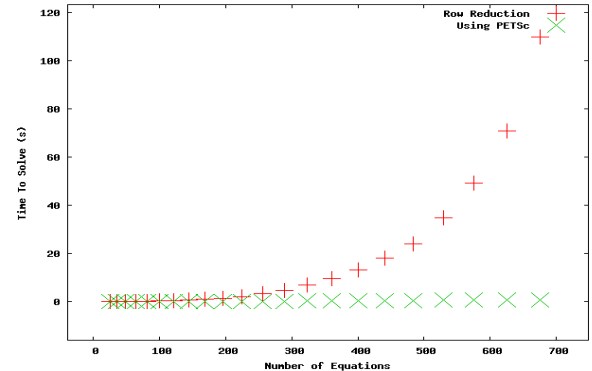


FIG. 7.— The solution times for the PETSc routines look constant, but are not. Each solution time is just extremely small (compare for 676 equations—row reduction took 109.975 seconds and PETSc LU decomposition took 0.813 seconds). These times represent the method of solution for an average of three runs at 50 time steps on a single CPU of a 3.8 GHz Intel i5 processor.

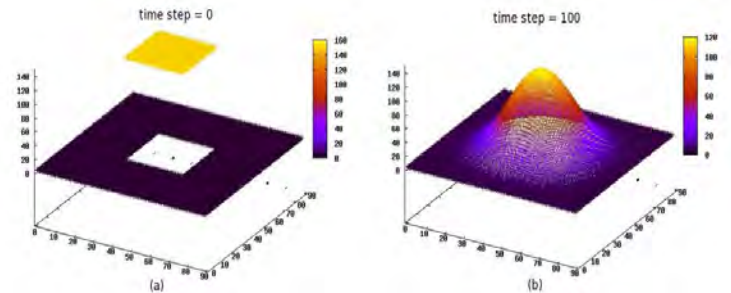


FIG. 8.— Snapshots taken from the diffusion simulation. (a) Time step 0, the concentration at a  $30 \times 30$  section of interior nodes has a high concentration ( $C_i = 150$ ), while the rest of the mesh has a concentration of  $C_0 = 5$ . (b) By time step=100 the initial concentration at the center has decreased dramatically. In this simulation, the diffusivity is  $D = 0.3$ . The entire grid is of unit length, so here  $\Delta x = \Delta y = 0.011$ .

### 4. CONCLUSIONS AND FUTURE WORK

The diffusion routine is running with PETSc as its method of solution of linear equations. It runs now on a grid of about  $95 \times 95$  nodes. With a grid this size,  $95^2 = 9025$  equations must be solved at each time step. Since they are linear equations, there must be an equal amount of unknowns per equation. Therefore, besides the three solution vectors that each contain 9025 elements, there are three matrices that must hold  $9025^2 = 81,450,625$  elements. Since these are floating point operations, precise variables are used (double precision variables, which are 8 bytes each). A quick analysis will determine that storage of doubles in the matrix and two solution vectors requires the program to have  $\approx 2$  GB of available memory to run. This is conceivable on a modern day computer with this much memory (although some clusters have many processors with only 1 GB each), however future testing might prove this to be too coarse a grid. Therefore, this program might need to be parallelized before we can proceed. PETSc is designed for quick and optimum parallelization using the MPI standard, so this is not a big deal. Splitting up the large matrices onto different computational zones and then few minor changes to the code should suffice to run this program in parallel across multiple processors. This should give an increase in computational efficiency as well as a much finer grid on which diffusion can occur.

Therefore, future work will be to mesh this diffusion routine into the mesoscopic scale simulation to see whether diffusion has a rate limiting effect on MT dynamic instability. Testing of this routine once it is integrated will determine if the grid is too coarse. If so, the routine can be run on single processors with more memory, or parallelized and run on multiple processors. Once this is done, we will be able to tell what type of effect (if any) that diffusion has on MT dynamic instability.

dation (NSF) through grant number NSF MCB 0951264. I would like to acknowledge and thank Dr. Mark Alber and Dr. Holly Goodson for their help and guidance this summer. I would also like to acknowledge the help given to me by Dr. Ziliang Xu on computer related affairs including specific library implementations and optimization. I would like to thank Dr. Umesh Garg and Ms. Shari Herman for their hard work and dedication to the Notre Dame REU program.

This work was supported by the National Science Foun-

#### REFERENCES

- Gregoretti, Ivan. Modeling Microtubule Dynamic Instability, a Dissertation (2007).
- Gregoretti, I.V., Margolin G., Alber M.S., Goodson, H.V. Journal of Cell Science 119, 4781-4788 (2006).
- Howard, Joe, Hyman, Anthony A. Nature 422, 753-758 (2003).
- Howard, Joe, Hyman, Anthony A. Nature Reviews Molecular Cell Biology 10, 569-574 (2009).
- Margolin, Gennady, Goodson, Holly V., Alber, Mark S. In prep. (2010)
- Margolin, Gennady, Gregoretti, Ivan, Goodson, Holly V., Alber, Mark S. Physical Review E 74. 041920 (2006).
- Northrup, S.H., Erickson, H.P. Proc. Natl. Acad. Sci. USA 89:3338-3342 (1992).
- Numerical Methods for the Solution of Partial Differential Equations. Lecture Notes for the COMPSTAR School on Computational Astrophysics, 8-13/02/10, Caen, France. Albert Einstein Institute, Max-Planck-Institute for Gravitational Physics, Potsdam, Germany (2010).
- Odde, David J. Biophys J. 1997 Jul;73(1):88-96.
- Salmon, E.D., Saxton, W.M., Leslie, R.J., Karow, M.L., McIntosh, J.R. J. Cell Biol. 99: 2157-2164 (1984).
- "The Stokes-Einstein Law for Diffusion in Solution". Christina Cruickshank Miller (Proceedings of the Royal Society of London). Series A, Containing Papers of a Mathematical and Physical Character, Vol. 106, No. 740 (Dec. 1, 1924), pp. 724-749. Published by The Royal Society-Stable. <http://www.jstor.org/stable/94335>

# Detectors and Data Acquisition for the St. George Recoil Mass Separator

Nathan Smith  
Indiana University South Bend  
2010 NSF/REU Program  
Physics Department, University of Notre Dame  
Advisor: Dr. Jerry Hinnefeld, Physics & Astronomy

**Abstract:** The St. George recoil mass separator, to be installed soon at the University of Notre Dame, will be used for Nuclear Astrophysics research. St. George is unique in that it has been designed with large angular and energy acceptances, so that it will be well-suited for a variety of capture reactions. Low energy ( $\alpha, \gamma$ ) reactions will be studied using inverse kinematics in order to better understand helium burning processes in stars. Reacted products will be identified using mass measurements based on energy and time-of-flight (E-TOF). In addition to a dedicated set of detectors, St. George will have a dedicated data acquisition (DAQ) system. I participated in the commissioning of the DAQ system this summer by preparing configuration files and taking two-parameter data using an existing prototype E-TOF detection system, consisting of a silicon detector and a microchannel plate detector for detecting secondary electrons produced by passage of particles through a thin foil. For this commissioning measurement, the detected particles were alpha particles. I also developed a simulation using Geant4. The purpose of the simulation is to determine whether position-sensitive detectors enhance the functionality of the St. George system and whether it is crucial to the differentiation of reacted and unreacted beam. I will present preliminary results of simulations, as well as the details of the DAQ system and results of the commissioning measurement.

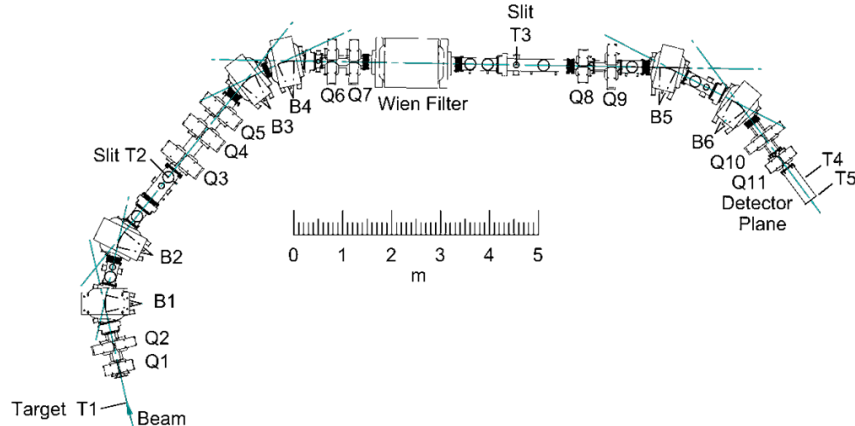
The sun is our most powerful energy generator, but there are still many questions to be answered as to how it works. The basic principles are understood. Stars form from interstellar dust and the remnants of previous stars. This dust is primarily hydrogen which, once temperature and pressure get high enough, fuse together to form helium. There is typically enough hydrogen for stars to burn for a few million years, depending on the mass. After enough of the hydrogen has been consumed, helium

burning commences. It is the helium burning process that will be primarily studied with the system I worked on this summer.

St. George is a recoil mass separator that has been optimized for low energy ( $\alpha, \gamma$ ) reactions. These reactions are studied using inverse kinematics for beam masses up to about A=40 [2]. Previous recoil separators were primarily designed for single specific reactions. St. George has been designed to identify a number of ( $\alpha, \gamma$ ) and possibly, at a later time, ( $p, \gamma$ ) reactions. These reactions are of astrophysical interest and are important to the understanding of stellar energy production and nucleosynthesis. They will also contribute to the understanding of explosive helium burning.

Since the St. George system will accommodate such a wide range of reactions, it is important to be able to efficiently and definitively differentiate between reacted and unreacted beam. According to M. Couder et al. [2], several criteria were put forth for the concept development of the separator. These included separation of a single charge state by magnetic analysis after the target, capability of handling high beam intensities, effective separation of reaction products and beam with nearly identical magnetic rigidity, ion optics for a helium jet gas target, ion optics that allows reaction products to be focused into a detector system with a diameter of 50mm, a vacuum of  $10^{-7}$  mbar in the separator, and optimal use of the physical layout of the Nuclear Science Laboratory.

In the figure to the left there are six dipole magnets (B1-B6), 11 quadrupole magnets (Q1-Q11)



and one Wien filter. The entire apparatus is under vacuum at about  $10^{-6}$  torr pressure. T1 is the target where the nuclear reactions will take place. Below are a

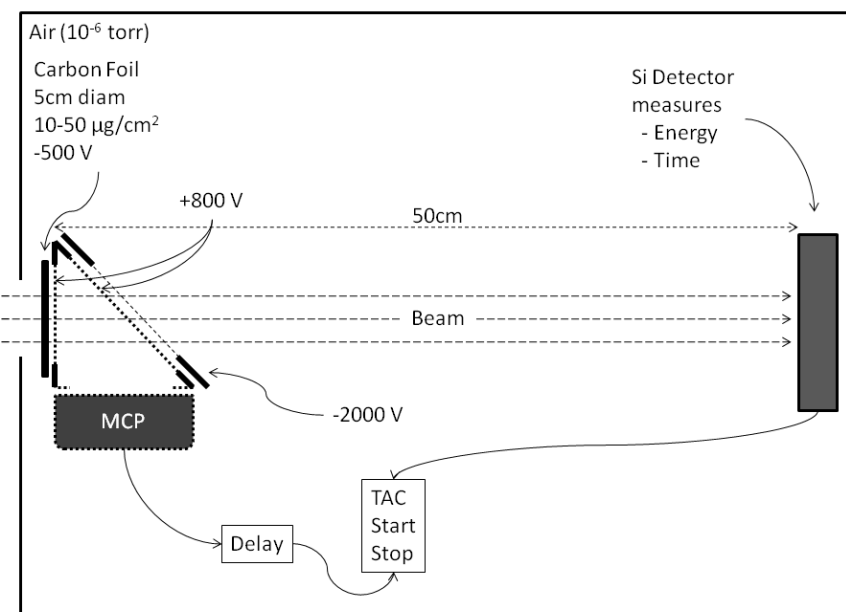
few reactions of interest to be studied.

Beam	Recoil	Beam $E_{lab}$ (MeV)	$E_{cm}$ (MeV)	Recoil $E_{lab}$ (MeV)	$E$ range ± %	Mom. $P$ (MeV/c)
$^{16}\text{O}$	$^{20}\text{Ne}$	5.8	1.16	4.64	2.8	415.7
		12.5	2.5	10.02	2.4	610.9
$^{18}\text{O}$	$^{22}\text{Ne}$	1.94	0.35	1.59	7.8	177.1
		3.3	0.60	2.70	6.2	332.6
$^{34}\text{S}$	$^{38}\text{Ar}$	10.0	1.05	8.95	2.1	795.7
		38.0	4.00	34.00	1.4	1551.0
$^{36}\text{Ar}$	$^{40}\text{Ca}$	12.5	1.25	11.25	1.8	915.3
		40.0	4.00	36.00	1.3	1638.0

Currently at IUSB a prototype detector system is in place for testing and proof of concept. It consists of a small alpha source, a thin carbon foil, a faraday cage, an electrostatic mirror, a MCP detector, and a silicon detector. The entire apparatus is under vacuum at about  $10^{-6}$  torr. Alpha particles are emitted from the source and pass through the carbon foil which is at -500 V. As the particles pass through the foil, they scatter electrons in all directions. As they exit, some of the electrons travel in the same direction as the particle. Both the alpha particles and the electrons enter the faraday cage and eventually exit the other side. There is a -2000 V electrostatic mirror on the other side which reflects the electrons downward because of electric force. These electrons reach the MCP

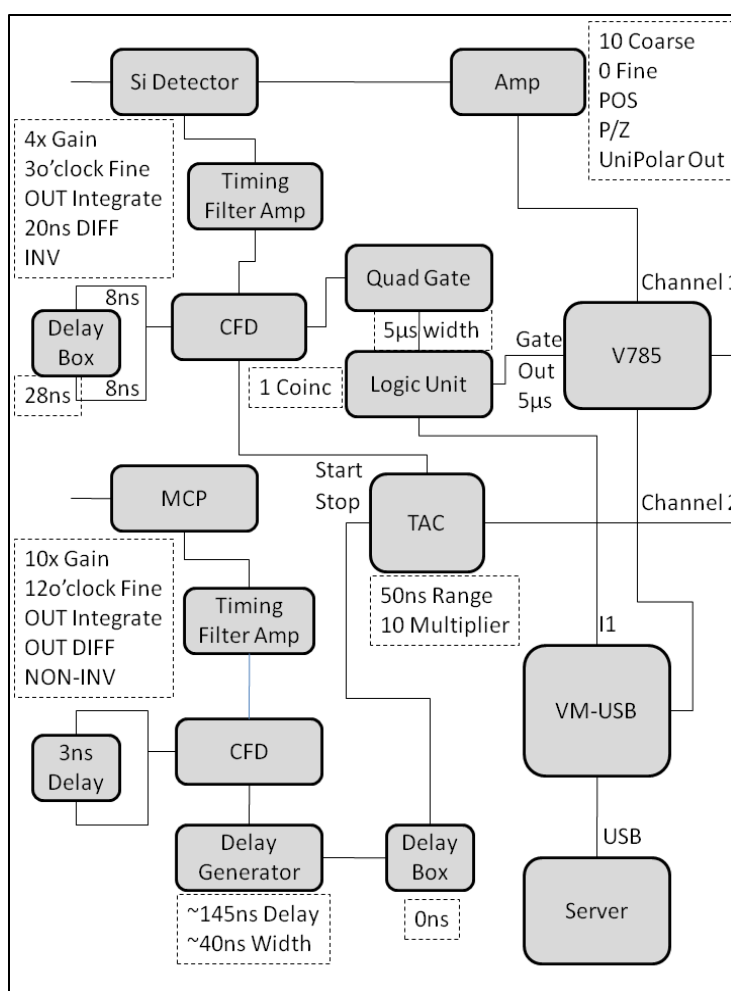
(microchannel plate)

detector which produces a signal corresponding to the event. This signal is amplified and shaped before it is fed to the Delay Generator. The Delay Generator delays the signal about 145



nanoseconds and gives it about a 40ns width. This signal is then fed into the TAC (time to amplitude converter) Stop gate.

The alpha particles in the prototype system, or the heavier ions in the upcoming St. George system, travel the 50cm from the foil to the silicon detector. The detector measures the energy of the particles and has two outputs. One output goes to an amplifier, which is fed to the CAEN V785 ADC (analog to digital converter) module. The input, however, needs to be gated, which is where the other output comes in. The other output from the Si detector is fed through a timing filter amplifier and then shaped with a slight delay. One output from the CFD (Constant Fraction Discriminator) is turned into a logic pulse with a width of 5 $\mu$ s. This logic pulse is used to gate both the ADC as well as the VM-USB module, which collects the data from the V785 module. The CFD also outputs to the TAC Start input.



The reason why the timer is started with the Si detector and stopped with the MCP signal is to reduce false positives. With the Si detector starting the timer, it will only go when a particle has actually hit the detector. These particles are spaced far enough apart that the signal from the MCP will be received, after the delay, before the next particle enters the chamber. The amplitude from the TAC is also fed to the V785 module, which digitizes the signal and passes it to the VM-USB module.

The VM-USB module is basically a buffer between the other modules in the VME crate and the server which collects the data. Both the server and the VME crate are part of the data acquisition (DAQ) system that will be used with St. George to collect and analyze data online. This system and its software were developed at Michigan State University (MSU) at the National Superconducting Cyclotron Laboratory (NSCL). Many of these DAQ systems use fiber optics to communicate directly between in the VME crate and the server. The VME crate controller for the St. George system is slightly different in that it uses a USB interface. USB offers faster transfer speeds than the traditional methods, but has a higher latency in setting up a connection. Therefore it is necessary to use a VM-USB module to collect the data from the other modules and then dump to the server as the buffers fill up. In the end the system is faster than the older systems and should lead to better performance.

Because of the latency, however, programming the modules is very different from the older method. With the fiber optic link, a user could write their own classes in C++ which instruct the modules how to behave when they receive a signal, what should be filtered out, and what data is significant

```
#Sample St. George DAQ config file

adc create V785 0xee000000
adc config V785 -smallthresholds on -thresholds [
    list 1 1 125 125 \
        125 125 125 125 \
        125 125 125 125 \
        125 125 125 125 \
        125 125 125 125 \
        125 125 125 125 \
        125 125 125 125 \
        125 125 125 125]

stack create event
stack config event -trigger nim1
stack config event -modules [list V785]

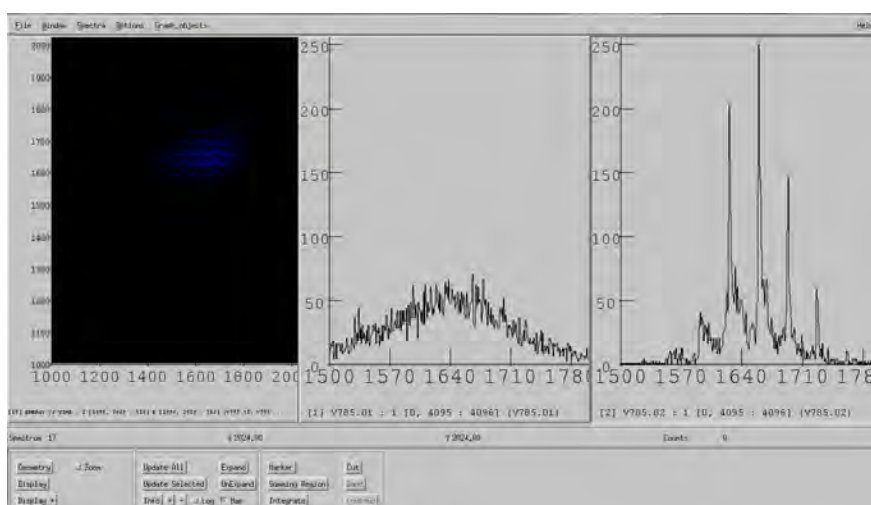
stack config event -delay 20

set adcChannels(V785) [
    list V785.01 V785.02 V785.03 V785.04 \
        V785.05 V785.06 V785.07 V785.08 \
        V785.09 V785.10 V785.11 V785.12 \
        V785.13 V785.14 V785.15 V785.16]
```

enough to be passed on to the DAQ server. For the VM-USB setup, all instruction must be stored in the VM-USB module, because it is acting as a gateway to the other modules. Instead of being in the form of C++ classes with the appropriate methods, instructions are stored in Tcl/Tk configuration files that interact with predefined classes for each module. These classes are specific to each module and were created at the NSCL. This allows a user to very easily specify how the modules should behave in a format that is easy to read and understand.

Here is a sample configuration file for using the prototype system. The create statement tells the VM-USB module to expect an ADC module of type V785 at the VME address 0xee000000 with the specified configuration. The smallthresholds option being on means the threshold values will be applied as is. The thresholds are then specified in list form for each of the 16 channels in the ADC. If the value received by the ADC is less than the threshold it will be discarded. The stack object is then created. Stacks are basically lists of instructions for the VM-USB module to follow. In this case an object called "event" is created and told to trigger on a signal from the input nim1, which was the gate provided by the Si detector via the logic unit. Next the modules to expect are listed, in this case only the V785 module will be used. Often it is necessary to delay a certain number of microseconds after the gate signal is received before retrieving data as some of it may still be being processed by the ADC module. Finally, in this configuration the 16 channels from the ADC are all named and the VM-USB module knows to expect values from each channel.

The setup is very much the same for other modules, each with their own predefined classes and methods. The configuration options correspond to the appropriate method calls behind the scenes. When an experiment is ready to be run, software has been provided by the NSCL to communicate with the VM-USB module and collect data when it is ready. Runs can be timed and terminated in the Readout program at any time. The user has the option to store the data recorded or just view it online.



The program for viewing online is called SpecTcl and is configurable for as many inputs as are needed. The Xamine program shows histograms of the data as it comes in. Additional spectra

may be created, including 2-d plots using existing spectra as the axes. Event files are all stored in the experiment directory in a central directory on the server, under the appropriate experiment name.

Above is a view of the SpecTcl/Xamine view of data as it is coming in. The 2-d plot is of energy vs. time. There are artifacts in the data that show up as the horizontal lines in the plot. This is most likely due to a misconfiguration of the CFD and will be investigated in the future.

These days, because of the complexity and cost of setting up detectors for nuclear physics experiments, it is often advantageous to simulate the detectors before any hardware is purchased. Once the simulation is in place various configurations can be tested for an optimal solution. To simulate the detector setup in the St. George system I used the Geant4 toolkit developed at CERN. Geant4 simulates the passage of particles through matter and is used in many areas of physics such as high energy, nuclear and accelerator physics, as well as medical and space science. To use Geant4, the user need only define a few required classes to control such things as detector construction and geometry, particles and physics processes to include, and beam characteristics. Many other modules may be loaded and defined to add functionality as Geant4 has a very robust set of tools to accomplish basically anything the developer needs.

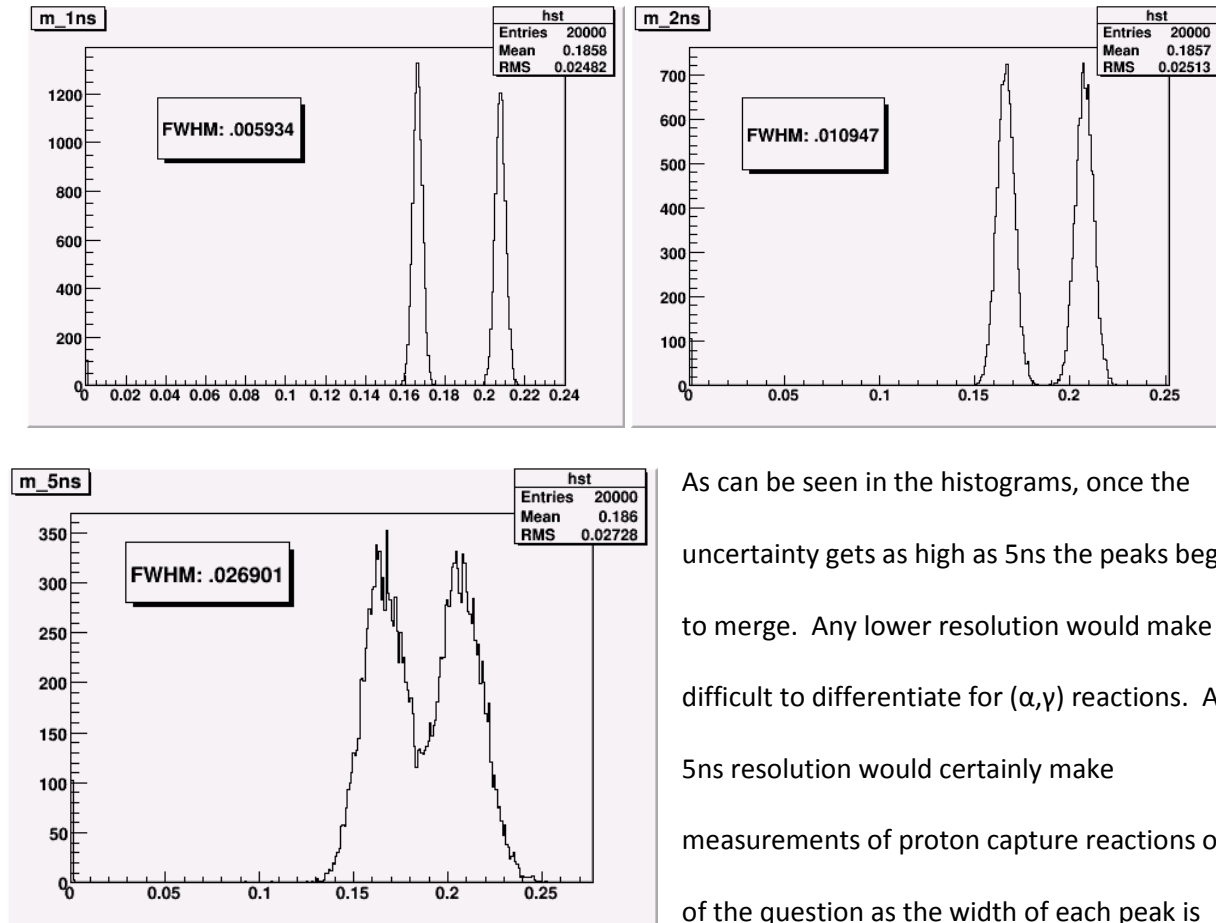
I set up the simulation in basically the same configuration as the prototype system, minus the faraday cage and MCP detector. The geometry consists of a world volume made of air at an extremely low density to mimic the vacuum conditions in the actual chamber, a very thin section made of carbon to simulate the carbon foil, and a larger section made of silicon to simulate the detector. Sensitive detectors were attached to both the foil and silicon regions to measure various attributes of the particles as they passed through. These hits were saved as the particle travelled and processed and stored after the event was completed. Initially, all incoming particles were alpha particles from a fixed point with a fixed energy. The starting position was later modified to be randomly distributed on a circular area such that all the particles would still pass through the foil.

The incident beam can be changed to be any particle, isotope or ion desired. As was shown in the table previously, one reaction of interest is  $^{16}\text{O}(\alpha,\gamma)^{20}\text{Ne}$ . Both  $^{16}\text{O}$  and  $^{20}\text{Ne}$  ions were run through the simulated chamber with various properties measured for each event. Deposited energy in the silicon detector, time-of-flight, and distance are the values of interest. Each was stored in the appropriate ROOT file. Each ROOT file contained about 10,000 events to be analyzed at a later time. As was described earlier, the distance from the carbon foil to the Si detector is 50cm. When a particle is traveling through the chamber, however, its path is always slightly longer as it is deflected as it passes through the carbon.

Once the data was collected it was imported into ROOT. Because it is data from a simulation, the values produced are too perfect to be compared to real world results. Hence the data needs to be spread out using a Gaussian distribution to better mimic the uncertainties and resolutions in real world detectors. Also, in the real world it can be difficult to differentiate between reacted and unreacted beam, especially at these relatively low energies. There was some discussion as to whether position-sensitive detectors would help. One aspect of this that can be easily tested in the simulations is the increased path length that can be measured with position-sensitivity. This translates into a longer time-of-flight. In ROOT, pseudo-parameters were created for these corrected values, adjusted based on the path length. Also, because of the relationship between kinetic energy and mass, individual masses per run can be computed using the pseudo-parameters again. When these are plotted against energy it should be easy to determine the values for reacted and unreacted beam. Because of the detector uncertainty, however, these areas can overlap, making it difficult to identify. Therefore, the goal was to compare the values for the position-sensitive and insensitive scenarios.

The resolution for the energy measurements in the silicon detector is well known from other experiments. Using a ratio, it was determined that for a 4.64MeV beam of  $^{20}\text{Ne}$ , the FWHM (full width half max) value should be 65.7KeV, likewise for  $^{16}\text{O}$ , the FWHM is about 73.5KeV. These values were

used to spread the energy distribution to mimic measured values. The resolution for the time is not well known, therefore a range of values were calculated. Currently the best timing resolution for the prototype system is about 1.2ns. For the simulated data values of 1ns, 2ns, and 5ns were used as the FWHM in the spreading. Below are the various plots of mass for each of the different timing resolutions.



As can be seen in the histograms, once the uncertainty gets as high as 5ns the peaks begin to merge. Any lower resolution would make it difficult to differentiate for  $(\alpha,\gamma)$  reactions. A 5ns resolution would certainly make measurements of proton capture reactions out of the question as the width of each peak is

already more than two atomic mass units wide. If the actual resolution of the final system is closer to 2ns,  $(\alpha,\gamma)$  reactions should be easily distinguishable and position-sensitivity should not be crucial. All analysis of the data from the simulation was done in ROOT and the peaks were fit with Gaussian functions.

There are several key improvements that can be made to the simulation and will be investigated in the future. First, the energies of the incoming particles in the real world are in no way uniform. Therefore, either an even or Gaussian distribution should be applied to the incoming energies within an

acceptable range. This will spread out the measured energies, better simulating real life. Secondly, the position of the particles as they enter the test chamber has an even angular distribution in the X, Y plane. But the smaller radii are more heavily favored. Therefore the distribution of incoming positions can be improved using different techniques such as Von Neumann rejection sampling. Thirdly, the angle to the z-axis is currently zero. In reality, particles have a variety of incoming angles. Varying these incoming angles would better simulate the beamline characteristics. Also the angles could be further improved knowing that the beam was passed through a focusing magnet before entering the test chamber. Finally, resolutions can be applied to the measured positions at the foil and Si detector to mimic real world uncertainties. The simulation should also be tested for the different reactions of interest at different energies for each reaction in a similar manner to the  $^{16}\text{O}(\alpha,\gamma)^{20}\text{Ne}$  scenario.

In conclusion, St. George is a recoil mass separator to be installed soon at the University of Notre Dame. It will be used in Nuclear Astrophysics research, specifically measuring the cross sections of various low energy ( $\alpha,\gamma$ ) reactions found in stars. These reactions are important to the helium burning process and stellar nucleosynthesis. This summer I participated in the commissioning of the DAQ system with a prototype detector setup and familiarized myself with data acquisition techniques. I also created a flexible simulation using the Geant4 toolkit and analyzed the data collected in these experiments. I will continue to improve these simulations in the future and share the expertise I have acquired with the students and professors at my university.

## Works Cited

Bennett, Jeffrey, Donahue, Megan, Schneider, Nicholas, & Voit, Mark. (2005). *The Essential cosmic perspective*. Addison-Wesley.

G. Christian, National Superconducting Cyclotron Laboratory report, *MoNA ROOT Guide*, 2010 (unpublished).

M. Couder, G.P.A. Berg, J. Gorres, P.J. LeBlanc, L.O. Lamm, E. Stech, M. Wiescher, J. Hinnefeld, Design of the recoil mass separator St. George, Nuclear Instruments and Methods in Physics Research Section A: Accelerators, Spectrometers, Detectors and Associated Equipment, Volume 587, Issue 1, 11 March 2008, Pages 35-45, ISSN 0168-9002, DOI: 10.1016/j.nima.2007.11.069.

R. Fox, National Superconducting Cyclotron Laboratory report, *VM-USB based Data Acquisition System*, 2010 (unpublished).

# Modeling and Visualizing Social Networks

LaTianna Sturrup  
Arizona State University

2010 NSF/REU Program  
Physics Department, University of Notre Dame

**Advisor:**  
Zoltan Toroczkai

**Collaborators:**  
Dr. Chris Sweet  
James Sweet  
Anthony Strathman

## **Abstract**

Social networks are complex physical systems, which are challenging to analyze. Our data set is a communication network that transpired over a time period of sixty-five days. The network is made up of more than seven million people and more than one billion communication events that occurred between them in this period. When the communication network is drawn as a graph, a node represents each actor. A communication event (e.g. a phone call) takes place between two nodes, which is represented by an edge that connects the two nodes. So how does one analyze a network that contains such a large data set? Our project strives to answer this question by developing techniques for modeling and visualizing the social communication network.

We have been developing an agent-based model to capture the coupling between individual relationship traits, such as reciprocity and degree assortativity. A networks degree assortativity refers to a preference for connection formation between like-degree nodes. Degree assortativity is a network structural property, observed for all social networks, but its origins have never been explained. We show that communication reciprocity is one such property that leads the formation of degree-assortative networks.

Along with creating models of our data, we are interested in creating visual representations of the communication network. Such a task can be completed through the use of graph drawing algorithms. Working with force-based, energy minimization algorithms (Kamada-Kawai and Fruchterman-Reingold force-fields minimized via Metropolis and Langevin dynamics) we produced spherical dynamic maps. Visualizing the community structures lying within segments of the social network.#

## **Description of Data**

The data we are currently analyzing is a complex physical-system consisting of 1,068, 151,513 communications events. The data was collected over a time period of sixty-five days. Within this time period 7,205,158 actors participated in the communication events. The communication events are divided into one of the following categories; voice calls, short message service (sms), and other. The cumulated airtime of the communication events lasted  $9.9707 \times 10^{10}$  seconds, approximately 3171 years. The median

call duration is fifty-three seconds and the maximum call duration is 45,901 seconds, approximately thirteen hours. The approximate cost incurred by the callers was six hundred million dollars (USD). The data originated from cell-phone trace logs, from which the caller's index, receiver's index, call date, call time, and duration of the called were recorded.

### **Network Assortativity and Reciprocity**

Assortativity is a network structural property observed in networks. A given network is said to show assortative mixing if like nodes have a propensity to form connections [1]. In this case, nodes are said to be alike if their degrees are similar. When measured social networks have been found to be assortative: higher-degree nodes form connections with nodes of higher-degree and lower-degree nodes with lower degree ones. Degree-assortative mixing in our model is measured by the Pearson coefficient of degree-degree correlations, first introduced by Newman (2003).

$$r = \frac{\sum_i j_i k_i - M^{-1} \sum_i j_i \sum_i k_i}{\sqrt{\left[ \sum_i j_i^2 - M^{-1} (\sum_i j_i)^2 \right] \left[ \sum_i k_i^2 - M^{-1} (\sum_i k_i)^2 \right]}} \quad [1]$$

Where  $j_i$  is the excess in degree,  $k_i$  is the excess out degree, and  $M$  is the number of edges. When  $r$  is measured to be  $r > 0$  the network is said to be assortative (social networks), and if  $r < 0$  the network is said to be disassortative (higher degree nodes form connections with lower degree nodes as seen in many biological and technological networks).

The origin of assortative mixing within social networks has never been explained. In my project we worked on the proposal that communication reciprocity is a key property that leads to assortative-degree mixing within social networks. Reciprocity is the social expectation that individuals will respond to one another in similar ways, hence it is a tendency to reduce imbalance of communication between people. Callers expect to have their calls reciprocated by receivers, according to the norm of reciprocity. Depending on how a pair (caller, receiver) reciprocates one another influences their relationship within the network. Social theory also says that un-reciprocal (unbalanced) links are typically short lived when compared to the reciprocated ones.

## Agent-Based Model

To test our hypothesis of “reciprocity leads to degree assortativity” in social networks, we develop an agent-based model of social communication, in which we parameterize reciprocity and provide a network evolution dynamics as function of this (and other) parameters. Agent-based modeling is a computer modeling technique in which autonomous decision-making agents are created. An agent has a unique set of characteristics that describes its state, perceived state of the environment, allowable actions, and strategies [2]. Each agent interacts with the other agents in the environment, performing allowable actions strategically. By giving agents decision-making capabilities complex entities, such as the actors in the communication network, can be modeled for analysis purposes.

In our model an agent establishes a communication relationships with other agents. An agent may have multiple agents, with whom it communicates, as long as the agent does not exceed its maximum communication potential. Two agents form a communication relationship when agent  $i(j)$  calls agent  $j(i)$ . According to the social norm of reciprocity agent  $i$  expects that agent  $j$  will return its call. Depending upon the level to which agent  $i$  is reciprocated by agent  $j$  determines what next action agent  $i$  performs. In the model agents can drop links (relationships) if they’re not being reciprocated, keep a link if the agent is happy with the relationship, and search for new agents to form relationships with. An agent’s decision to act in one of the three ways is made after measuring how happy an agent is with its relationships. Computationally, the algorithm is a Monte Carlo simulation.

### Construction of the agent-based model

Every agent's output rate towards the network is assumed to be the same value  $\omega$  for all agents. This is the gregariousness of the agent, assumed to be the same for all. One also assumes in this version of the model that this total out-flow is uniformly distributed amongst its network neighbors. Hence, if the degree of agent  $i$  is  $d_i$  then the outflow on any of its links is  $\omega/d_i$ . The in-flow from a neighbor  $j$  is then  $\omega/d_j$ . The difference:  $\Delta_{ij} = \omega/d_j - \omega/d_i$  is the “gain” of agent  $i$  coming from agent  $j$ . Agents are content with positive gains  $\Delta_{ij} > 0$ , but unhappy with negative ones. Hence given a network, every edge has a

directed weight going from the lower to the higher degree node (pointing into the agent receiving a positive activity gain). Agents (nodes) are unhappy with links directed away from them, with the degree of unhappiness increasing with the weight's absolute value. The total content of agent  $i$  with its network neighborhood could be interpreted by the sum:

$$H_i = \sum_{j \in \langle i \rangle} \Delta_{ij} = \omega \left( \sum_{j \in \langle i \rangle} \frac{1}{d_j} - 1 \right)$$

The larger this sum is, the more content the agent is with its overall current position in the network. A positive  $H_i$  means that it gets more contact activity (information) from its peers than it provides (although this is misleading somewhat, read below). This favors large-degree nodes to be connected to lower degree nodes. However, that can make many lower degree nodes unhappy. Our goal is to study dynamical models in which the agents try to change their network position such as to avoid unhappy positions as much as possible. Depending upon the degree distribution, there is inherent frustration in this system, and hence it promises non-trivial collective behavior. Where is this frustration coming from? An agent might have a number of very unhappy links and a number of very happy links such that they balance each other out, and even lead to a positive  $H_i$ . But this is not good, because it means that  $i$ 's communications towards some of its neighbors are hardly reciprocated, whereas he seriously does not reciprocate some neighbors. It seems as if  $i$ 's communications are misdirected. Behaving "undemocratically" would reduce the unbalance by directing the unreciprocated calls from his unhappy links towards the ones that he is making unhappy for others. In this version of the model we will operate under the assumption that this might not be enough and hence, for simplicity of treatment we exclude this possibility for now. We assume that the agent wants to minimize the non-reciprocity it suffers from its "negative links" ( $\Delta_{ij} < 0$ ). If a link is positive, it should not care about actively changing it (it is plentifully reciprocated). However, seriously positive links for an agent  $i$  are seriously negative for another one  $j$ , and that agent  $j$  will be trying to change it. For example, the other agent  $j$  might completely remove this link, in which case our agent  $i$  now has more outflow towards the remaining links possibly making some of them even more unbalanced, so it needs to work on its neighborhood again. We will insert some sort of "emphatic" behavior of the

agent towards its unreciprocated (by her) neighbors, when modifying its neighborhood composition. This basically models the tendency of the agent to stabilize her existing relations as much as she can. These are described in the next section.

There is one important but subtle aspect and needs emphasis. Note that  $H_i$  is NOT synonymous with profit or monetary gain. That is agents do not try to maximize  $H_i$  as a payoff would be maximized. If you call me more times than I call you, I am ok with that, and as long as this situation holds I don't even pay attention to it any more, because I am fully reciprocated. Even more so, if you are calling me way more than I call you that might actually bother me, so large positive imbalance on a link for an agent might have a negative effect. In this version of the model, however, we do not explicitly model this negative effect.

Let us define the “energy” variable associated with  $i$ ’s neighborhood.

$$E_i = \sum_{j \in \langle i \rangle} \Delta_{ij}^2$$

Which is larger the more unreciprocated links exists in  $i$ ’s immediate neighborhood. The case may exist in which, overall agent  $i$  is reciprocated by its peers ( $H_i \geq 0$ ); however, reciprocations are misdirected and  $E_i$  could be a large positive number. The way an agent can change its network neighborhood is by dropping links or by making new connections. When that happens, its degree might change and hence the weights  $\Delta_{ij}$  along its links will change as well. This generates a coupled dynamics between the link weights (communications) and neighborhood structure. Agents that have no negative  $\Delta_{ij} \geq 0$  links are content and will not actively try to change its network neighborhood. However, the positive links might have very large weights, meaning that it seriously under-reciprocates some of its neighbors who will want to change their neighborhood. The agent might find itself needing to work on its neighborhood again. The nice feature of the model is that it incorporates the observation that ones relationships with others do not only depend solely on his or her behavior.

Given that the outflow rate a neighbor of  $i$  receives is  $\omega/d_i$ , this can become arbitrarily small for an arbitrarily large neighborhood. A very small communication rate however, is meaningless in human

relationships. Extrapolating his studies from primates to humans (correlating neo-cortex size with a primate's group size), Dunbar estimated that human neighborhood sizes are limited by about  $D = 150$  and hence the smallest communication rate must be larger than  $\omega/D$ . The cell-phone network data gives 114 as maximum degree. The communication rate  $\omega/D$  is considered as a cutoff in the ABM in the sense that if it were to drop below this value, the rate of communication outflow from this agent is considered zero.

An agent  $i$  chosen to update its state will take its most negative link (if several have the same negative weight then it chooses uniformly at random from those) and drops it if  $d_i \geq 2$ . This can be threshold, namely, if the weight is below some threshold value (that is if it is negative enough), only then it will drop it. We will not consider isolated nodes, and the process is built such that if an isolated node appears momentarily, it will seek new links, constantly. Hence, the largest communication unit outflow is  $\omega$  (when the degree is unity), and the lowest is 0 (the lowest is  $\omega/D$  below which it is considered zero). Clearly,  $-\omega \leq \Delta_{ij} \leq \omega$ . A drop threshold would be modeled by  $\delta$  with  $-\omega \leq \delta < 0$ . This threshold also models the level of non-reciprocity below which an agent is not content and drops the link. An alternative way to model dropping the link is by using a soft, probabilistic method with dropping probability increasing the closer is  $\Delta_{ij}$  to  $-\omega$ . For simplicity, the first versions of the ABM will use a fixed, prescribed drop-threshold  $\delta$ .

Once the agent is dropping a link it does a computation. Since it dropped a link,  $d'_i = d_i - 1$  and recalculates the weights on all the other links. It also recalculates the new energy  $E'_i$  and the difference,

$$\Delta E_i = E'_i - E_i = \sum_{j \in \langle i \rangle} \left[ (\Delta'_{ij})^2 - \Delta_{ij}^2 \right].$$

If  $\Delta E_i \leq 0$ , then it redistributes its activity among the remaining neighbors and does not actively search for new links in that step. If  $\Delta E_i \geq 0$ , then it still can do the same redistribution of activity but with probability,  $e^{-\beta \Delta E_i}$  where  $\beta$  is an inverse temperature parameter. With probability  $1 - e^{-\beta \Delta E_i}$ , an agent does not redistribute its activity; instead it actively searches to add a new link.

Assume agent  $i$  decided to add a new link. In the simplest version of the model, she chooses uniformly at random another agent  $j$  not from her neighborhood and asks  $j$  if she will accept a new

contact. At this point  $j$  calculates the change in the energy  $\Delta E_j$  by increasing her degree by unity. If the change is negative,  $j$  accepts the link and both update their outflows towards their neighbors. If the change is positive, she might still accept the link, but with probability  $e^{-\beta \Delta E_j}$ , and with probability  $1 - e^{-\beta \Delta E_j}$  she will reject the offer. In the latter case agent  $i$  goes back to redistribute her activity amongst her existing neighbors (the friendship making process failed, so for now her neighbors have to take an increased activity from her).

### **Visualization Algorithms**

The ability to visualize complex networks is useful when analyzing complex physical-systems. With the use of graph drawing algorithms researchers are capable of creating visual representations of data. With the use of the force-based and minimization algorithms, subsets of the communication network were visualized as spherical dynamic maps. The forced-based algorithms Kamada-Kawai and Fruchterman-Reingold (Spring Algorithm) and the minimization algorithms Metropolis and Langevin were implemented to create these maps.

The Kamada-Kawai and Fruchterman-Reingold algorithms generate an energy  $E$  for the network. The Kamada-Kawai algorithm “is based on the idea to place the vertices on such places in the place with geometric distances correlated with topological distances”(Suvakov, 2008, p. 594).

$$E = \sum_{i,j} k_{ij} \left( |r_i - r_j| - l_{ij} \right)^2, [3]$$

In the Kamada-Kawai algorithm energy  $E$  is given by the preceding formula. Where  $K_{ij}$  is a parameter,  $r_i$  and  $r_j$  are vectors of position,  $|r_i - r_j|$  gives the physical distance between the two nodes, and  $l_{ij}$  is the shortest path between two nodes. In the Fruchterman-Reingold algorithm (Spring algorithm) edges act as springs between nodes, and nodes interact with a repulsive force.

$$E = \sum_{(i,j) \in E} k_{ij} \left( |r_i - r_j| - l_0 \right)^2 + \sum_{i,j} \frac{g}{|r_i - r_j|^\eta}, [3]$$

Using the spring model energy  $E$  is given by the preceding formula. Where  $K_{ij}$ ,  $l_0$ ,  $g$ ,  $\eta$  are parameters; and  $|r_i$  and  $r_j$  are vectors of position. The first term places neighbors the same distance apart, and the second term is the electrostatic repulsion for each pair of nodes.

Minimization algorithms attain the energy minimum for a graph. The metropolis algorithm picks a node at random, displaces it in a random direction by a random Gaussian distributed amount. The new energy  $E'$  is then calculated from  $\Delta E = E' - E$  [3]. The random move is accepted with probability  $\min\{1, e^{-\beta \Delta E}\}$  [3], if  $\beta$  is a high number the temperature is very low and if  $\beta$  is a low number the temperature is very high. The Langevin algorithm is a numerical time-integration in which the velocity of a node is calculated by  $\frac{dr_i}{dt} = -\nu \frac{\partial E}{\partial r_i}$  [3], where the parameter  $\nu$  is the viscosity measure.

Modified versions of these algorithms were implemented into a three dimensional viewer, more precisely with network nodes constrained to the surface of a sphere (written in Java). The reason behind the spherical layout is that there is convenient nonlinear relationship between the length of the connecting edges, appearing as chords of the sphere and the length of the arc between the two nodes, such, that for large chords (almost diametrical) the arc can vary considerably, which allows for a more relaxed positioning of far-away nodes, while close-by nodes are positioned with less freedom. This allows revealing clusters as compact “continents” separated by relatively large distances see figures. Using the software we were able to take a subset of our data and visualize it on a sphere. Figure 1 shows the initial placement of the nodes on the sphere. The forces are calculated between all node pairs, the corresponding total energy, and then the minimization algorithm takes over, and it keeps moving the nodes around the sphere until the total energy cannot be further minimized. Figure 2 shows an intermediate stage, while figure 3 shows the final stage for a high degree node’s 3-step network neighborhood. The nodes finally rearrange themselves according to their communication relationships.

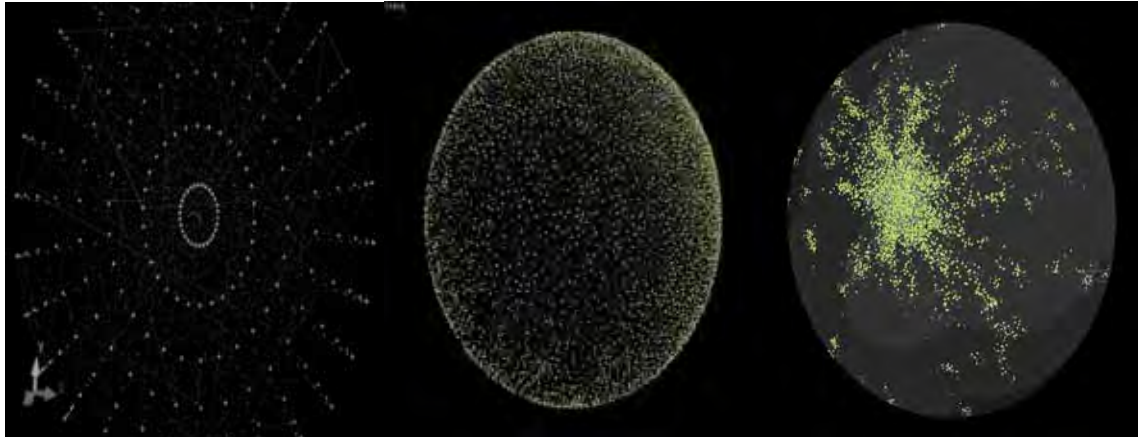


Figure 1.

Figure 2.

Figure 3.

## Conclusion

Researchers working with social networks are often left to analyze complex data sets. To be able to carry out this task researchers can now use computer modeling and visualizing techniques to analyze complex physical systems. With regards to our data set, we have been developing an agent-based model to test our hypothesis that “reciprocity is a property that leads to network assortativity” is indeed valid. Through the use of force-based and minimization algorithms we were able to create spherical dynamic maps of subsets of the data.

## Acknowledgments:

I would like to thank my advisor Dr. Toroczkai for working with me this summer, I am eternally grateful for your time and your patience. I would also like to thank Dr. Chris Sweet, Dr. Erika Camacho, James Sweet, and Anthony Strathman. To the REU organizers especially Dr. Garg and Sheri Herman, thank you for the time and effort you put into the REU program.

## References:

1. Newman, M.E.J.: Assortative Mixing in Networks, Phys. Rev. E 67, (2003) <http://pre.aps.org/pdf/PRE/v67/i2/e026126>.
2. Z. Toroczkai and S. Eubank. Agent-based Modeling as a Decision Making Tool: How to Halt a Smallpox Epidemic. Frontiers of Engineering, The National Academies, pp. 99 (2005); reprinted as feature article in The Bridge, 35(4), 22 (2005).
3. Suvakov, M.: Physics Based Algorithms for Sparse Graph Visualizations, Lecture Notes in Computer Science vol. 5102 (2008) <http://www.springerlink.com/content/7344k61j60422844/fulltext.pdf>

# **Distribution of Delay Times in Laser Excited CdSe-ZnS Core-Shell Quantum Dots**

Andrei Vajiac

Indiana University South Bend

Mathematics, Computer Science

Advisor: Pavel Frantsuzov, Physics

## Abstract

This project studies the distribution of delay times between laser excitation and photon emission for individual CdSe-ZnS core-shell quantum dots. The experimental data was obtained from Argon National Labs, where a Time Correlated Single Photon Counting device was used to detect the photon emissions from the quantum dots. The data was analyzed statistically, using Matlab, to determine what, if any, connections exist among the delay times that occur between laser excitation and photon detection and the on/off states of the quantum dots. This follows research performed by Wu, Sun, and Pelton on the distribution of recombination rates for quantum dots.

In this communication we present results from the statistical analysis of the delay times between laser excitation and photon emission in CdSe-ZnS Quantum Dots formed in colloidal solution. The data, obtained from Argonne National Laboratory, is the same as was used in “Recombination rates for single colloidal quantum dots near a smooth metal film” by X. Wu, Y. Sun, and M. Pelton.

### I. What is a Quantum Dot?

Quantum dots, discovered in the 1980s by Alexei Ekimov and Louis E. Brus are very small semiconductors whose properties and characteristics are closely tied to the size and shape of each individual crystal. To be able to understand the specifics of quantum dots, one must first have an understanding of excitons. An exciton is an electrically neutral quasi-particle existent in insulators, semiconductors, and some liquids. It is a bound state of an electron hole and an electron, which are attracted to each other by an electrostatic Coulomb force. Excitons form when an electron is excited from the valence band into the conduction band by a photon. This excitation leaves behind a ‘hole’ of opposite electric charge to which the electron is attracted by the Coulomb force. In this communication we wish to study the recombination rate of the electron and the electron hole within semiconductor nanocrystals (quantum dots). Now one can say that quantum dots are semiconductors who have their excitons confined in all three spatial dimensions. This quantum confinement effect occurs when the diameter of a particle is of the same magnitude as the wavelength of the electron wave function, hence causing quantum dots’ electronic and optical properties to be substantially different from those of bulk semiconductors. If the confining dimension is large enough, the bandgap between the valence band and the conduction band remains at its original energy. However, as the confining dimension decreases even further, the bandgap becomes dependent on size; this quantum confinement effect is generally used to explain the results from excitons being confined to a dimension that approaches a measurement known as the exciton Bohr radius. This type of quantum confinement leads to a few new electronic structures. Quantum Wells occur when the

electrons or holes are confined in one spatial direction and free propagation is allowed in the other two dimensions. Quantum Wires occur when the electrons or holes are confined in two spatial directions, allowing free propagation in the remaining direction. Finally, Quantum Dots are created when the excitons are confined in all three spatial directions. Since quantum dots can be relatively simply manufactured through many means at many different sizes, this bandgap can thus be altered to whatever size one may need. This allows quantum dots to be produced for various applications. For example, quantum dots have been used quite effectively in producing fluorescent dyes that can be used in medical applications.

## II. The Data

The data was obtained from Argonne National Laboratory and is the same as the data used in “Recombination rates for single colloidal quantum dots near a smooth metal film” by X. Wu, Y. Sun, and M. Pelton. Quantum Dots were excited using laser pulses and the photon emissions were detected using a Single Photon Counter. The laser used had a 400nm excitation wavelength and the repetition rate was 5MHz. Output pulses from the photon detector, as well as sync pulses from the laser, were sent to a Time Correlated Single Photon Counting (TCPSC) Machine. Since the exact times of the laser pulses is known, the data was comprised of two main parts. First, the time that has elapsed from the beginning of the experiment until the photon detection was known, henceforth referred to as true time. Also, the delay time between the previous laser excitation and the subsequent photon detection was also able to be recorded. Each dataset received contained the results from a different quantum dot being excited over a time span of 10 minutes. Each of these datasets contained anywhere between 2.5 million and 5.5 million detected photons and their respective true times and delay times.

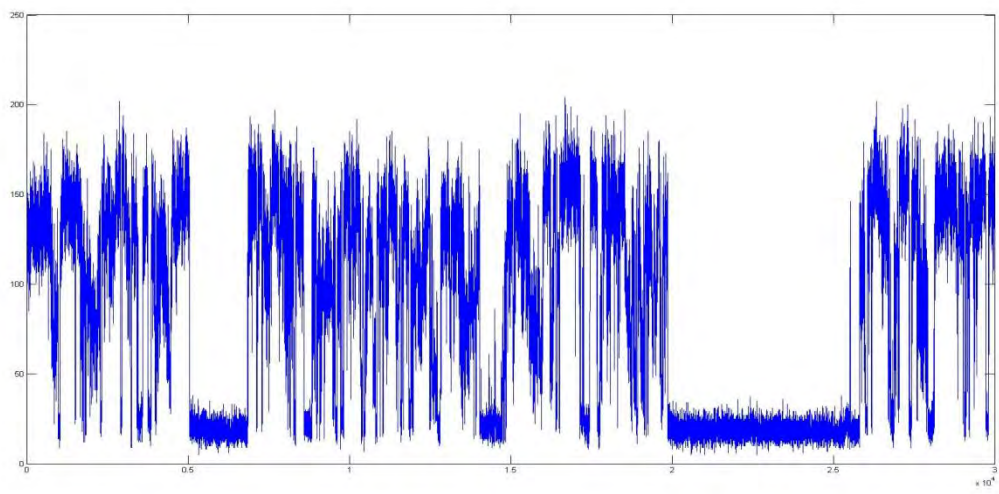
## III. Data Analysis Method

Since the datasets obtained are so large, the statistical toolbox within Matlab was used to analyze the data. Matlab has many different capabilities when it comes to analyzing data in

arrays and as such using Matlab required making a decision between iterative and boolean styles of programming. There are many distinct differences between these two styles, but in general, iterative programs are easier to write and understand. They are similar in style to conventional programming, in particular C++, however it is possible that iterative programs can cause the analysis to run very slowly, since they require actions to be performed in succession over every single data point in the dataset. Matlab also contains a boolean style of programming, which allows data points in an array to be interpreted as boolean values, which allows for much faster calculations. However, the issue with boolean programming is that the style is not as intuitive as the iterative style; the programs many times become harder to write if one does not have much experience with the Matlab system. It is also important to note that although in general one can say that the boolean style produces faster programs than the iterative style, it is not always the case. In particular, there was a program written to put the data in to different time bins which was able to be executed in a few seconds when the program was written iteratively, but when the program was translated to a boolean style, it took several minutes. Therefore much trial and error was required to be able to write the fastest, and best, programs to analyze the data.

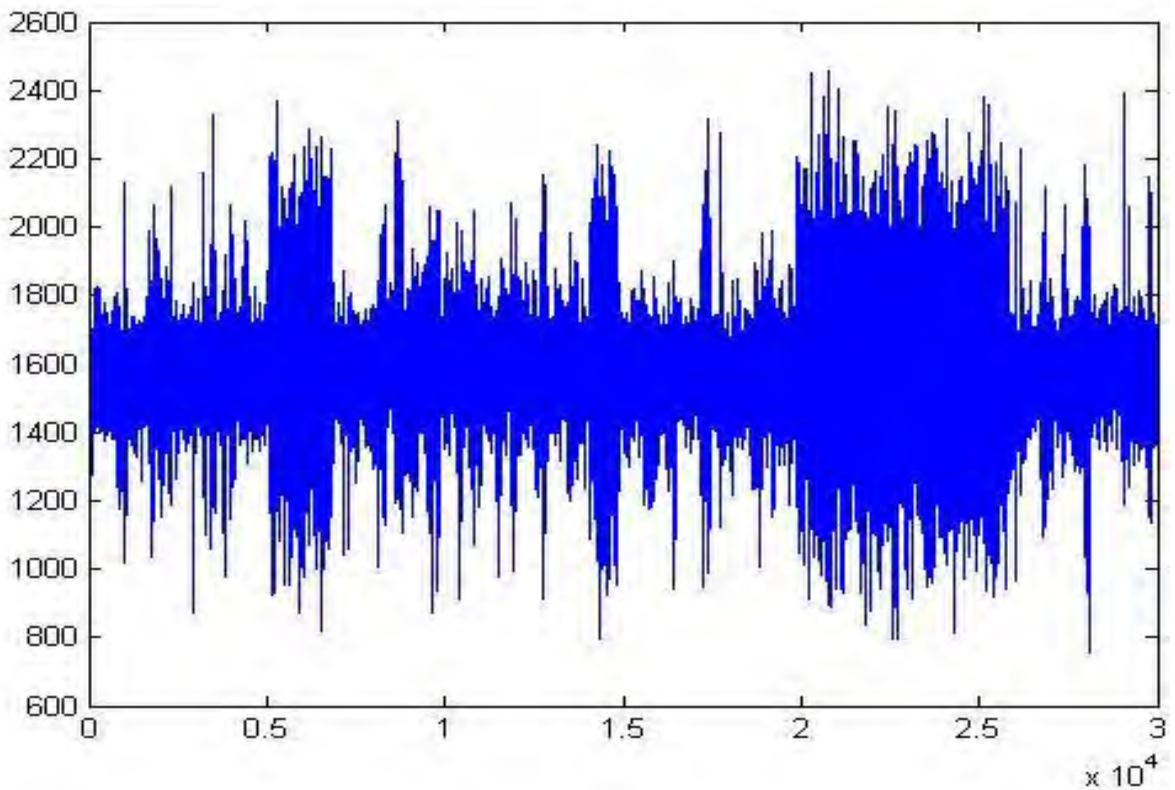
#### IV. Data Analysis

Initially, after extracting the data from the files received so that they could be imported into Matlab, the data needed to be binned by splitting the 10 minute experiment into smaller time intervals (bins) and then counting the number of detected photons in each bin (using the true time). This sort of analysis allows us to determine times of high photon emission from the quantum dot, known as “on-times” and times of low photon emission, known as “off-times”. An example of data binning is shown below:



This initial binning analysis provides us with a few questions. Firstly, we want to know why the quantum dot goes into “off” periods. The quantum dots exhibit the strange characteristic of being in an “on” state, or cycling from on to off quite rapidly, to going into an “off” state for periods up to two minutes, and then returning to the “on” state. This behavior is quite surprising, since quantum dots’ activity is usually measured on a nanosecond scale; thus an “off” state of up to two minutes is really a very long time for the dot to not be emitting very many photons. Another question that is raised is whether or not the delay times of the photons have any sort of connection to the “on” and “off” states. In general, we wish to discover whether there are any clues about the quantum dot behavior that can help us better understand and possibly to predict when “off” states will occur and how long they might last.

One attempt was to see if the range of delay times for photon detection that occurred in the “off” states for the quantum dot was smaller than the range of delay times occurring in the “on” states. We binned the delay times for the quantum dots in the same fashion as before, when we binned the true times, and obtained the following result:



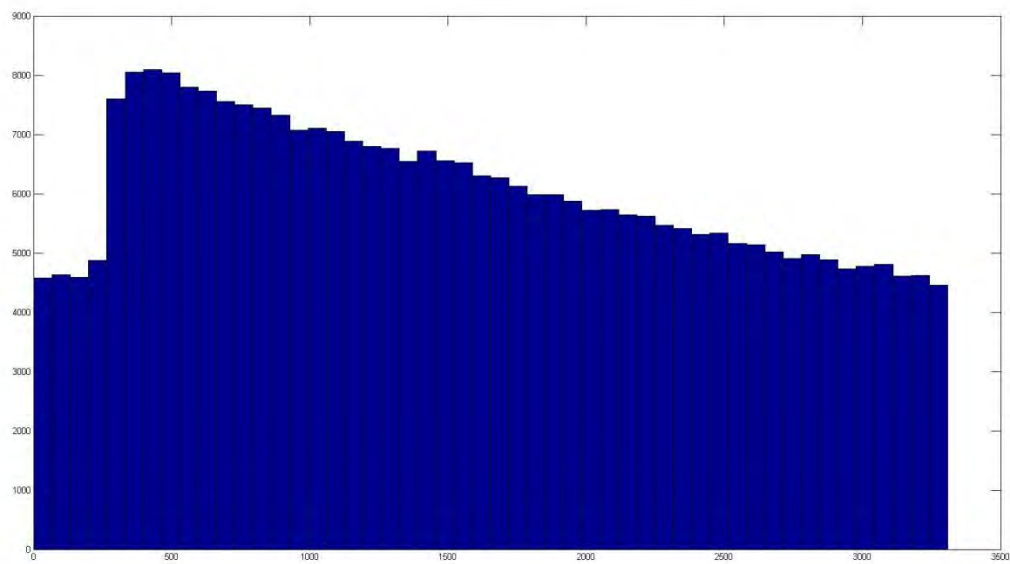
When comparing the above result from the graph of “on” and “off” times from before, we saw that our initial prediction was not correct; in fact we found that the range of delay times for the “off” states was significantly larger than the range of delay times for the “on” states.

From this point we are attempting to see if the distribution of delay times for the entire experiment (for each quantum dot) could be modeled using some sort of fit curve. We endeavor to fit the distribution using an exponential fit, accounting for background noise in the equation. A least-squares method is being used to calculate the best fit.

Our first idea for the data fit was to use the following model:

$$P(t) = Ae^{-\frac{t}{\tau}}$$

However, upon separating the delay times into photons emitted during “on” times and photons emitted during “off” times for each experiment, we obtained many similar graphs to the one below:



The above represents a histogram of the distribution of delay times for the “on” states of a particular quantum dot throughout the 10 minute experiment. As we can see, there is a significant amount of background noise in the data (it doesn’t seem to approach zero) and thus we need to change our predicted model.

We now wish to model the data using the function:

$$P(t) = Ae^{\frac{-t}{\tau}} + B$$

Where B represents the background noise in our data collection.

The least squares method is being used to model the data, so we wish to minimize:

$$S = \sum_{i=1}^m [(y_i - f(x_i))^2]$$

That is,

$$S = \sum_{i=1}^m \left[ (y_i - Ae^{\frac{-x_i}{\tau}} - B) \right]^2$$

Where, in the above, m represents our number of data points.

To minimize S, we need to take the partial derivatives with respect to our unknowns: A, B, and tau. After taking these partial derivatives and simplifying, we end up with:

$$\begin{aligned} \frac{\partial S}{\partial A} &= A \sum_{i=1}^m e^{\frac{-2x_i}{\tau}} - B \sum_{i=1}^m e^{\frac{-x_i}{\tau}} - \sum_{i=1}^m y_i e^{\frac{-x_i}{\tau}} \\ \frac{\partial S}{\partial B} &= A \sum_{i=1}^m e^{\frac{-x_i}{\tau}} - Bm - \sum_{i=1}^m y_i \\ \frac{\partial S}{\partial \tau} &= -A \sum_{i=1}^m x_i e^{\frac{-2x_i}{\tau}} + B \sum_{i=1}^m x_i e^{\frac{-x_i}{\tau}} + \sum_{i=1}^m x_i y_i e^{\frac{-x_i}{\tau}} \end{aligned}$$

By setting all of these partial derivatives to zero, we find the minimum of S, and thus our least squares estimate.

Obviously, the previous system of three nonlinear equations is not solvable manually; we are currently writing a Matlab program to be able to solve that linear system, and as such calculate the values of A, B, and tau.



# Project GRAND's Search for Sub-TeV Gamma Rays Coincident with Swift Gamma Ray Bursts

Taiyo Wilson

2010 NSF/REU Program  
Physics Department, University of Notre Dame

Advisor:  
Professor John Poirier

## Abstract

Project GRAND is a cosmic ray experiment located north of the University of Notre Dame campus. The detector array measures  $100\text{ m} \times 100\text{ m}$  and consists of 64 huts of proportional wire chambers used to detect charged secondaries. When high energy gamma rays strike the atmosphere, muon secondaries detectable by GRAND are produced. These muons act as signatures for gamma ray primaries and were used to find potential angular and temporal coincidences with gamma ray bursts (GRBs) detected by NASA's Swift satellite. A list of eight GRBs was arranged by likelihood of detection by GRAND. It was first determined which GRBs were in the visible sky for GRAND. Additional criteria for probable detection include a low zenith angle and high muon flux at GRAND (estimated from Swift data). For each GRB, GRAND's data during the T90 time interval and within roughly  $\pm 2.7^\circ$  of the GRB's direction were used. From this data, the deviation of the muon flux from the background rate was determined.

## Project GRAND

Project GRAND (Gamma Ray Astrophysics at Notre Dame) is a cosmic ray detector experiment located north of the University of Notre Dame campus at  $86^\circ 13' \text{ W}$ ,  $41^\circ 04' \text{ N}$  and 222 m elevation above sea level. GRAND studies cosmic rays in two energy bands: a lower energy band of range 30 - 300 GeV for detecting single muons and a higher energy band of range 100 - 100,000 TeV for detecting cosmic ray showers. The field measures  $100\text{ m} \times 100\text{ m}$  and contains 64 huts laid out in an  $8 \times 8$  grid. Each hut houses a detector system comprised of eight planes (four pairs) of proportional wire chambers (PWCs) [1].

Each PWC plane consists of a grid of 80 parallel wires which are held to a potential of 2600 V from the grounded metal casing. The chambers are filled with a mixture of 80% argon and 20% carbon dioxide gas which leaves a trail of ions and electrons if disturbed by an ionizing particle. The potential difference causes these ions to be accelerated toward the nearest wire, disturbing additional gas molecules and creating more ions in the process; this is called gas amplification. As a result, a small pulse of current is formed on the wires

nearest the ionizing particle's path, allowing the particle's position to be tracked.

Each pair of PWCs tracks a particle's two-dimensional location with an  $x$ -plane (eastward) and a  $y$ -plane (northward). Denoting the  $z$ -direction as vertical, the top three pairs of PWCs project the particle's path into the  $xz$  and  $yz$  planes with a precision of  $0.3^\circ$  [2]. The fourth PWC pair is separated from the top three by a 50 mm thick steel absorber plate used for particle discrimination of muons from electrons. On a basic level, muons can be thought of as heavier electrons due to their similar interactions. Because of their greater mass ( $105.7 \text{ MeV}/c^2$ ) muons are accelerated less through electromagnetic fields and do not emit as much bremsstrahlung radiation. This allows muons to penetrate through the 50 mm steel plate to the final PWC plane while the electrons are absorbed. Thus, GRAND recognizes a muon as aligned hits in all four PWC pairs, a method which is 96% accurate. Each PWC plane has an area of  $1.29 \text{ m}^2$ , yielding an effective area of  $83 \text{ m}^2$  for all 64 huts. GRAND's ability to identify particles and track their direction with high angular resolution make it ideal for tracking high energy cosmic rays.

## Gamma Ray Bursts

Gamma ray bursts (GRBs) are quick emissions, ranging from milliseconds to several minutes, of gamma rays associated with highly energetic explosions occurring in distant galaxies. These events are the most luminous electromagnetic events observed in the universe. Following the initial burst is a lower energy afterglow emitted at longer wavelengths, allowing the distance to the GRB to be known from the redshift of the light. The distance to GRBs is typically several billion light years. For these gamma rays to reach the Earth from this distance, they must be extremely energetic. (The energy released during a GRB is comparable to the amount the Sun will release in its 10 billion year lifetime.)

GRBs are categorized based on their duration. Long GRBs, those with duration greater than 2 s, are thought to be caused by the core collapse of massive, rapidly spinning, low-metallicity stars. These long GRBs are much more energetic, and thus easier to detect than short GRBs. When massive stars fuse their core to iron, they can no longer produce energy through nuclear fusion and collapse. This release of gravitational potential energy heats and expels the star's outer layers. If the star is spinning rapidly enough, the collapsing matter will cause the star to form a dense accretion disk which forces energy outwards at the rotational axis, due to a lower density, at relativistic speeds ( $0.99995c$ ). These narrowness and direction of these jets or beams ( $2 - 20^\circ$  from the rotational axis) explain the high intensity of the radiation and low detection rate on Earth.

If these relativistic jets are directed toward the Earth, the angular resolution of the direction of the GRB event is excellent. This is because cosmic gamma rays, unlike charged hadrons, are not deflected by the Earth's and

galactic magnetic fields. When cosmic gamma rays strike the Earth's atmosphere, they produce secondary pions which decay into muons which are subsequently detected by GRAND. These charged secondaries do undergo some deflection. Figures 1 - 3 and Table 1 show data taken from a FLUKA Monte Carlo simulation used to predict the properties of muons from cosmic ray primaries [3],[4]. Figure 1 shows the result of folding the multiplicity of muons at sea level ( $N_\mu/N_\gamma$ ) with the differential spectral index ( $d\Phi_\mu/dE_\gamma$ ) and half-maximum-height ( $\delta\Theta_{xz}$ ) as a function of the primary gamma energy (dashed line with diamond points). The maximum of this plot at  $\sim 10$  GeV means that of muons that reach the ground, the median energy of their gamma primaries is  $\sim 10$  GeV. Figures 2 and 3 show that most muons with 10 GeV gamma primaries are produced at  $\sim 17$  km above sea level and have an average energy  $\sim 4$  GeV. A height of 17 km corresponds to 0.87 atm or  $1131 \text{ g/cm}^2$ . The mean square deflection for a multiple scattered muon where  $v \approx c$  through the atmosphere is given by the equation [5]

$$\begin{aligned} <\theta^2> &= 0.157 \frac{Z(Z+1)z^2 t}{A(pv)^2} \ln[1.13 \cdot 10^4 Z^{4/3} z^2 A^{-1} t] \\ <\theta^2> &= 0.157 \frac{7(7+1)(1)^2 1131}{14(4000)^2} \\ &\quad \ln[1.13 \cdot 10^4 7^{4/3} 1^2 14^{-1} 1131] \end{aligned}$$

$$\theta = 1.54^\circ$$

where  $Z$  is the atomic number of nitrogen,  $z$  is the charge of a muons,  $t$  is the atmospheric pressure in  $\text{g/cm}^2$ ,  $A$  is the atomic weight of nitrogen, and  $pv$  is the energy of a muon in MeV.

The deflection of muons due to the Earth's magnetic field is given by the small angle approximation

$$\theta \approx \frac{l}{r} \quad r = \frac{pv}{qvB}$$

$$r = \frac{4 \cdot 10^9}{(3 \cdot 10^8)(0.186 \cdot 10^{-4})} = 7.17 \cdot 10^5$$

$$\theta \approx \frac{17 \cdot 10^3}{7.17 \cdot 10^5} = 1.36^\circ$$

where  $l$  is the length of the magnetic field traversed by the muon,  $r$  is the radius of curvature of the muon's path,  $pv$  is an approximation of the muon's energy due to its ultrarelativistic speed in eV,  $q$  is the charge of the muon,  $v$  the velocity of the muon, and  $B$  is the strength of the Earth's magnetic field in tesla at GRAND's location.

The deflection of the muon from the initial path of the pion due to pion decay can be calculated as the inverse tangent of the muons resultant transverse momentum divided by its forward momentum. This model assumes a maximum muon deflection angle perpendicular to the original direction of the pion [6].

$$\theta = \tan^{-1} \left( \frac{p_t}{p_f} \right)$$

$$p_t = \frac{1}{2M_\pi} [(M_\pi + M_\mu + M_\nu)(M_\pi - M_\mu - M_\nu) \cdot (M_\pi + M_\mu - M_\nu)(M_\pi - M_\mu + M_\nu)]$$

$$p_t = \frac{1}{2(139.6)} [2(139.6 + 105.7) \cdot 2(139.6 - 105.7)]$$

$$p_t = 29.8 \text{ MeV}/c$$

$$\theta = \tan^{-1} \left( \frac{29.8}{4000} \right) = 0.43^\circ$$

where  $p_t$  is the momentum of the muon in the reference frame of the pion (transverse momentum),  $p_f$  is the momentum of the muon in the original direction of the pion, and  $M_\pi$ ,  $M_\mu$ , and  $M_\nu$  are the masses of pion, muon, and neutrino respectively. Figure 4 shows a two-body decay from the both the pion and stationary reference frames.

The deflection angles for each of the previous calculations are added in quadrature for a total muon angle error of  $2.01^\circ$ . This compares

favorably with the estimated  $d\theta$  value estimated by the FLUKA Monte Carlo simulation in Table 1 [7].

$$d\theta_{total} = \sqrt{\delta\theta_s^2 + \delta\theta_b^2 + \delta\theta_\pi^2}$$

$$d\theta_{total} = \sqrt{1.54^2 + 1.36^2 + 0.43^2}$$

$$d\theta_{total} = 2.01^\circ$$

## Swift Satellite

Swift is a NASA satellite launched in late 2004 designed to detect and analyze GRBs. With higher energy sensitivity and better angular resolution than previous satellites such as BATSE, and the ability to swiftly point its telescopes at new events, Swift has revolutionized the detection of GRBs and increased detection rate to around one GRB per day. Swift's Burst Alert Telescope (BAT) automatically detects GRBs and is able to point its X-Ray Telescope (XRT) and Ultra-Violet/Optical Telescope (UVOT) in the right direction within 50 - 70 s and 80 - 100 s respectively [8]. By using Swift's data of the spatial coordinates and photon flux of each GRB, the most likely events to be observed by GRAND can be determined.

In order observe GRAND's data in the direction of a GRB, the right ascension and declination taken by Swift must be converted into local altitude and azimuth values. Altitude and azimuth are defined as [9]

$$alt = \sin^{-1} [\sin(lat) \cdot \sin(dec) + \cos(lat) \cdot \cos(dec) \cdot \cos(ha)]$$

$$az = \cos^{-1} [\sin(dec) - \sin(lat) \cdot \sin(alt) / \cos(lat) \cdot \cos(alt)]$$

and are solved using the following equations

$$ha = lst - ra$$

$$lst = [(6.6460556 + 2400.01512617 \cdot \frac{(jdate - 2415020)}{36525} + 1.0027379 \cdot UT - \frac{long}{15}) \bmod 24]$$

where lat and long are GRAND's geographic coordinates, *ra* and *dec* are the right ascension and declination, *ha* is the hour angle, *lst* is the local sidereal time, *jdate* is the Julian date, and *UT* is the Universal Time.

The altitude and azimuth are converted into angles projected into the *xz* and *yz* planes. The tangents of these angles are

$$TX = \sin(az) / \tan(alt)$$

$$TY = \cos(az) / \tan(alt)$$

There are 80 cells in each PWC plane. GRAND interprets these projected angles as differences in cell number, DX, between the top and bottom PWCs. Figure 5 shows a diagram of how the projected angles are converted into DX with an error window of  $2.7^\circ$ .

## Data Analysis

Swift GRBs considered were detected from January 2005 - June 2010. Preliminary analysis was conducted to determine which GRBs would most likely be detectable by GRAND. First, the GRBs must have been within  $62^\circ$  of the local zenith to be detectable by GRAND. The GRBs were chosen based on an acceptance factor and estimated fluence at GRAND. The acceptance factor is

$$Acc = \cos^2(zen) \cdot [\cos(zen)(1 - TX / \tan(1.0821)) \cdot (1 - TY / \tan(1.0821))]$$

where the term in brackets represents the acceptance of the detector and the cosine squared term represents the muon's path

through the atmosphere. The estimated fluence at GRAND is

$$\Phi_G = \Phi_s \left(\frac{E_G}{E_s}\right)^{-\gamma} = \Phi_s \left(\frac{20}{.05}\right)^{-\gamma}$$

where  $\Phi_G$  and  $\Phi_s$  are the fluence at GRAND and Swift respectively,  $E_G$  and  $E_s$  are the energy levels detected by GRAND and Swift respectively, and  $\gamma$  is the photon index measured by Swift which expresses how the fluence of gamma rays falls off for higher energies. The product of *Acc* and  $\Phi_G$  is used to determine the final list of eight GRBs listed in Table 2.

The signal of each GRB is calculated as the difference between the total counts inside the T90 interval minus the background counts normalized to the time of the T90. The background rate is the average count rate over the time interval  $24 \times T90$  before and after the signal. The signal and signal error are calculated as

$$N_\mu = S - B_s$$

$$dN_\mu = \sqrt{\delta(S - B_s)^2 + \delta B^2}$$

where  $S$  is the total counts during T90,  $B_s$  is the background count during T90, and  $B$  is the average background rate. Assuming the muon count rate is a Gaussian distribution, the *Z*-value, or statistical significance, of each signal is calculated as

$$Z = \frac{N_\mu}{dN_\mu}$$

where the *Z*-value represents the number of standard deviations away from the mean. These results are summarized in Table 2.

## Conclusions

The results do not indicate any meaningful detection of excess muons coincident with gamma ray bursts. The number of positive and negative deviations in muon signal were even. The event with the highest statistical significance,  $1.73\sigma$ , was expected to be the least likely out of the eight GRBs considered. The Z-value of this event corresponds to a probability of  $4.2 \times 10^{-2}$ , which is not even statistically significant as a single event.

An improvement that was considered was altering the size of the angular window to see if this would yield a better signal. Figure 6 shows a peak signal Z-value at  $1.5\sigma$  angular width. Assuming our calculated angular uncertainty of  $2.07^\circ$  corresponds to  $1\sigma$ , the optimal angular window size would be  $3.11^\circ$ , which is not significantly greater than the  $2.7^\circ$  window size used.

Additional uncertainty exists in the way the photon index measured by Swift. Three of the indices were determined by using a power law with an exponential cutoff. Because Swift measures energies much lower, 50 - 150 keV, than what GRAND detects, the exponential cutoff makes the value for the estimated fluence at GRAND more uncertain.

## Acknowledgements

First, I would like to acknowledge my research advisor Dr. John Poirier for making my first real research experience enjoyable. His expertise, willingness to help, and congenial nature made for a very comfortable working environment where I could develop my research skills. I would also like to thank Dr. Christopher D'Andrea for providing guidance throughout the summer.

Finally, I would like to thank the University of Notre Dame and the National Science Foundation for giving me the opportunity to experience basic research. Dr. Umesh Garg, Shari Herman, and many others in the Notre Dame Physics Department for making the summer both educational and enjoyable.

---

- [1] Project GRAND, <http://nd.edu/~grand/>.
- [2] J. Poirier, C. D'Andrea et al (2007), Status report on project GRAND, *30th International Cosmic Ray Conference (ICRC)*.
- [3] J. Poirier, S. Roesler, A. Fasso (2001), Distributions of secondary muons at sea level from cosmic gamma rays below 10 TeV, *Elsevier Science*.
- [4] J. Poirier, S. Roesler, A. Fasso (2001), Calculation of atmospheric muons from cosmic gamma rays, *26th International Cosmic Ray Conference (ICRC)*.
- [5] E. Segre, H. Staub et al (1953), Experimental Nuclear Physics Volume I, *John Wiley & Sons, Inc., New York*.
- [6] P. Trower (1965), High Energy Particle Data Volume III: Kinematics of Particles as a Function of Momentum, *Lawrence Berkeley National Lab*.
- [7] J. Poirier, S. Roesler, A. Fasso (2001), Muon angles at sea level from cosmic gamma rays below 10 TeV, *26th Cosmic Ray Conference (ICRC)*
- [8] Atteia, Jean-Luc, and Gilbert Vedrenne. "HETE-2 and Swift." Gamma-Ray Bursts: The brightest explosions in the Universe (Springer Praxis Books / Astronomy and Planetary Sciences). 1 ed. New York: Springer, 2009. 160. Print.
- [9] A. Henden, R. Kaitchuck (1990), Astronomical Photometry: Text and Handbook for the Advanced Amateur and Professional Astronomer, *Willmann-Bell*.

- [10] J. Poirier, C. D'Andrea (2003), Search for Sub-TeV Gamma Rays Coincident with BATSE Gamma Ray Bursts, *28th International Cosmic Ray Conference (ICRC)*.

## Appendix

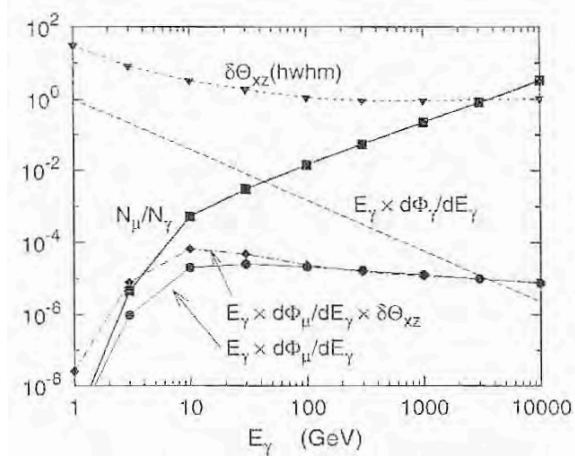


**Figure 1:** This graph shows the results of folding the multiplicity of muons at sea level per primary gamma ( $N_\mu/N_\gamma$ ) with the energy spectrum of primary gamma rays ( $N_\mu/N_\gamma$ ) with the energy spectrum of primary gamma rays ( $d\Phi_\mu/dE_\gamma$ ) and the half-maximum-height ( $\delta\Theta_{xz}$ ) as a function of the primary gamma energy (dashed line with diamond points).

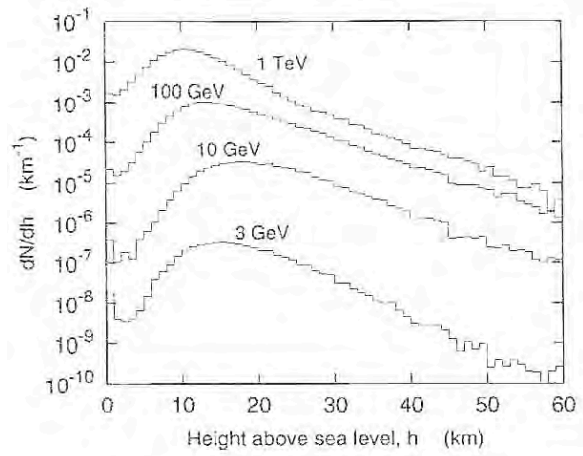


**Figure 2:** This graph shows the distribution of the production height of muons whose primary gammas have energy 3, 10, 100, and 1000 GeV.

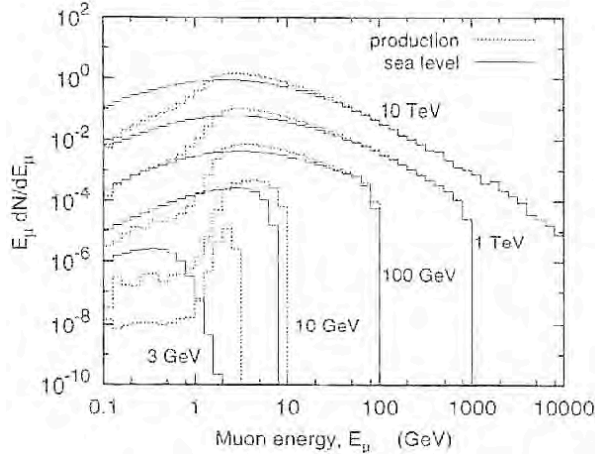


**Figure 3:** This graph shows the distribution of muon energy at their production height and at sea level for muons whose primary gammas have energy 3, 10, 100, and 1000 GeV.

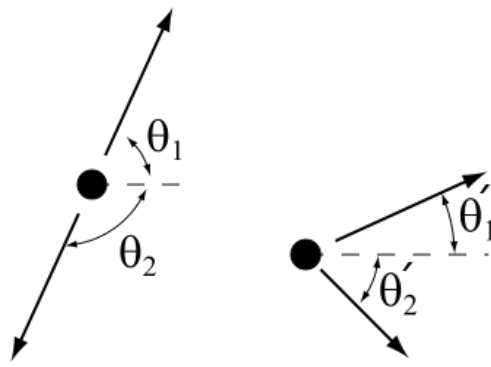


**Figure 4:** These diagrams show a two-body decay in the lab reference frame and in the reference frame of the incident particle, pion, decaying into a muon and muon neutrino.

## Appendix

	$E_\gamma$	$E_\mu > 0$		$E_\mu > 1$	$E_\mu > 2$	$E_\mu > 4$
		E-d.	E-d(b)	E-d.	E-d.	E-d.
n.f.	10	3.84	3.41	3.06	2.45	1.64
	1000	3.32	3.03	2.30	1.74	1.19
(1)	10	4.41	3.38	3.53	2.88	2.03
	1000	3.48	3.00	2.42	1.84	1.26
(2)	10	4.73	3.40	3.83	3.15	2.25
	1000	3.61	3.02	2.52	1.91	1.30
(3)	10	6.44	3.38	5.28	4.44	3.34
	1000	4.19	3.02	2.93	2.24	1.56

**Table 1:** This table shows the half-widths of the muon's sea level angular distribution due to varying magnetic field strengths, primary gamma energy, and secondary muon energy. Row (1) corresponds to the magnetic field strength for GRAND's geographic coordinates.

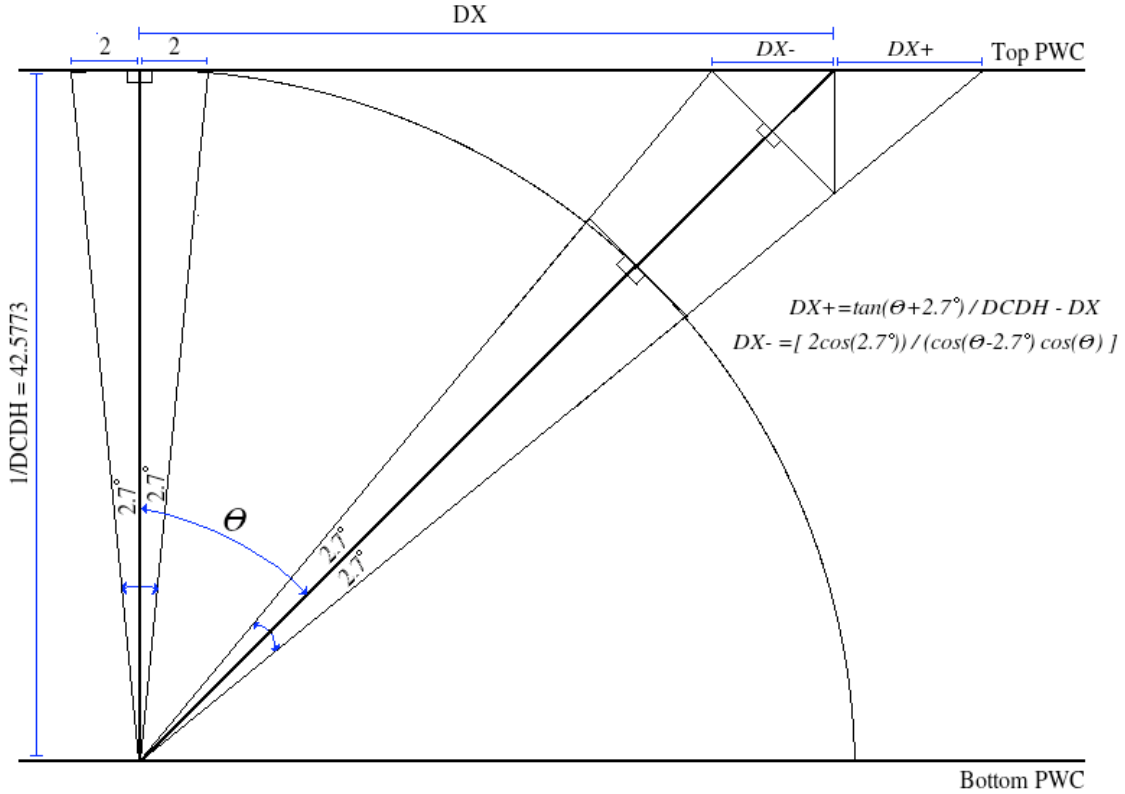


**Figure 5:** This diagram shows the projection of a muon path into the  $xz$  plane to be detected by GRAND's  $xz$  PWC planes. The angle of the muon ( $\theta$ ) is converted into a  $DX$  value which is the difference in cell number between the top and bottom planes (there are 80 cells). The angular window of  $\pm 2.7^\circ$  for a vertical angle varies with  $\theta$  and is also converted to a  $DX-$  and  $DX+$  value by the formulas above.

## Appendix

GRB	Time	T90	RA	Dec	Acc	$\Phi_G$	$100 \times \text{Acc} \times \Phi_G$	$N_\mu \pm dN_\mu$	Z
080319B	4396.3	45.124	14.5	36.3	0.6	1.59	91.23	$16.24 \pm 18.88$	$0.86\sigma$
060204B	34514	139.38	14.1	27.7	0.5	0.24	11.3	$6.54 \pm 12.15$	$0.538\sigma$
090618	12576	113.2	19.6	78.4	0.3	0.21	6.38	$-7.69 \pm 21.94$	$-0.351\sigma$
060428B	14112	96	15.7	62	0.6	0.07	4.11	$-15.06 \pm 25.80$	$-0.584\sigma$
061126	13710	70.84	5.77	64.2	0.6	0.02	1.44	$-17.5 \pm 22.42$	$-0.781\sigma$
081126	59660	55.8	21.6	48.7	0.8	0.02	1.22	$20.15 \pm 25.63$	$0.786\sigma$
06122A	80980	96	23.9	46.5	0.4	0.02	1.07	$-15.67 \pm 19.84$	$-1.055\sigma$
070616	41668	402.36	2.14	57	0.7	0.01	0.82	$100.53 \pm 58.24$	$1.73\sigma$

**Table 2:** This table is a summary of the eight GRBs analyzed. It lists the beginning of the T90 time, T90 duration, right ascension, declination, acceptance factor, estimated GRAND fluence, acceptance factor multiplied by fluence, signal and signal error, and the statistical significance or Z-value.

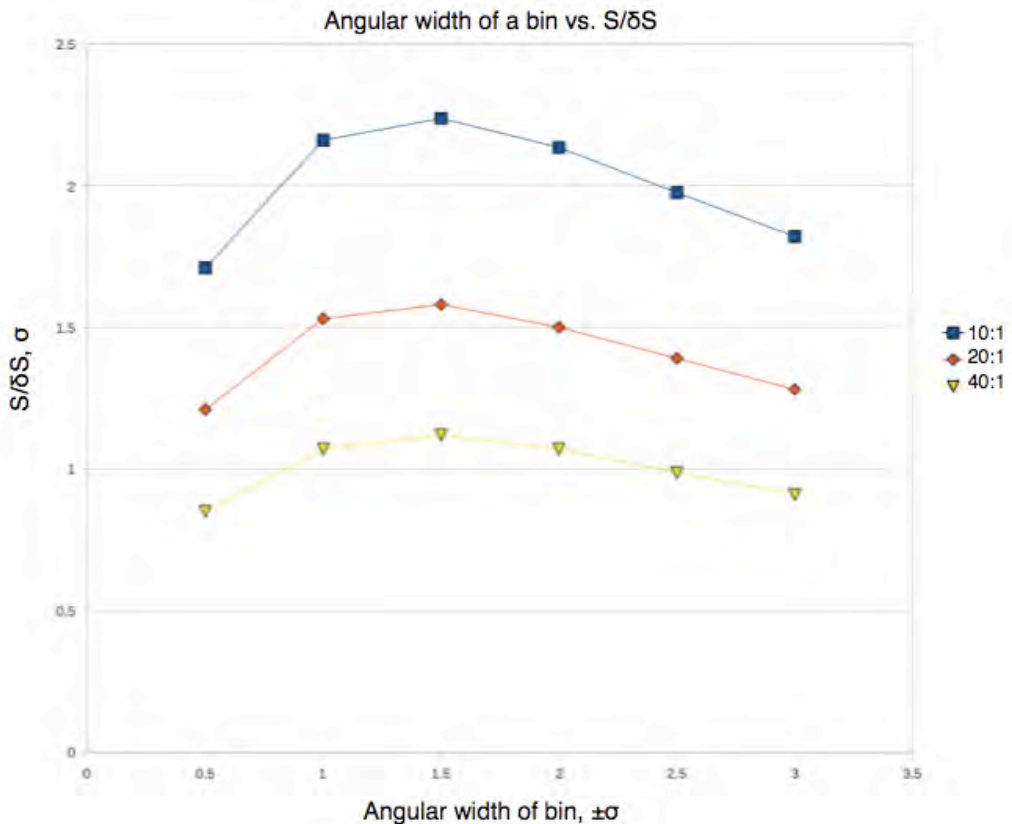


**Figure 6:** This graph shows the optimal angular window size for background to signal rates of 10:1, 20:1, and 40:1. The peak of this graph is  $\sim 1.5\sigma$ .